Collisional-radiative modelling for molecular hydrogen low-temperature and fusion edge plasmas

Richard Christian Bergmayr

Angaben zur Veröffentlichung / Publication details:

Bergmayr, Richard Christian. 2026. “Collisional-radiative modelling for molecular hydrogen low-temperature and fusion edge plasmas.” Augsburg: Universität Augsburg.

Collisional-Radiative Modelling for Molecular Hydrogen Low-Temperature and Fusion Edge Plasmas

Dissertation

zur Erlangung des akademischen Grades

Dr. rer. nat.

eingereicht an der

Mathematisch-Naturwissenschaftlich-Technischen Fakultät

der Universität Augsburg

von

Richard Christian Bergmayr

Augsburg, Juli 2025

Tag der mündlichen Prüfung: 15.12.2025

Erste Gutachterin: Prof. Dr.-Ing. Ursel Fantz

Zweiter Gutachter: Prof. Dr. Helmut Karl

Dritter Gutachter: Prof. Dr. Mathias Groth

Contents

1 Introduction

In nuclear fusion research it is aimed to develop a future carbon-emission free, sustainable, base-load energy source without producing any radiative waste with long decay times. While in future fusion power plants deuterium and tritium will be used as working gases, currently most magnetically confined fusion experiments operate with hydrogen or deuterium. In comparison to the hot inner plasmas with temperatures of above 100 000 000 K, the edge plasmas are rather cold with temperatures of 10 000 K. Nevertheless, among the open issues in nuclear fusion research is the plasma exhaust [1]: To reduce the heat load onto the plasma-facing materials, the edge plasma is directed to the divertor plates, where the particles recycle and form molecular hydrogen or deuterium [2]. The plasma can detach from the divertor plates building up a gas layer in-between, reducing the heat load onto the divertor plates. The exact role the molecules play in this process is still under discussion. While detachment is a standard operational scenario in todays experimental devices, achieving it in a stable manner and controlling its dynamics under reactor relevant conditions remain unresolved issues [1]. In detached plasmas, the parameters close to the divertor plates are typically comparable to the those of low-temperature plasmas [3].

Magnetically confined fusion experiment plasmas are usually (among other methods) heated through the injection of highly energetic particles of hydrogen or deuterium atoms. Through collision with the bulk plasma their energy is redistributed. Furthermore, in fusion devices based on the tokamak concept, the injected particles can contribute to driving the current in toroidal direction. The highly energetic particles are produced from ions extracted from ion source plasmas, that are subsequently accelerated and neutralized. The ion sources typically operate with low-temperature plasmas produced from molecular hydrogen or deuterium gas.

Low-temperature plasmas are also widely used for industrial applications such as the coating of surfaces, plasma etching of metals or silicon based materials and the conversion of electrical into chemical energy via gas conversion [4]. Often hydrogen is used as working medium or occurs as dissociation product [3].

For a fundamental understanding of fusion experiment plasmas, neutral beam injection plasmas and industrial plasmas, knowledge of the plasma parameters such as particle temperatures and densities is of crucial importance. These plasma parameters can be determined using various diagnostic methods. For instance the non-invasive technique of optical emission spectroscopy (of atomic and molecular hydrogen) records the radiation in the optical wavelength range emitted by the atoms and molecules in the plasma. Knowledge about the plasma parameters can be derived through analysis of the absolute emission intensities. The interpretation can be carried out for neutral particles in equilibrium plasmas through the Boltzmann distribution. Low-temperature plasmas are non-equilibrium plasmas, the neutrals do not follow the Boltzmann distribution. Instead, more appropriate population models such as collisional-radiative models (or corona models) are required for their interpretation.

Collisional-radiative (CR) models balance populating and de-populating process rates to predict excited state population densities in dependence on plasma parameters. The plasma parameters can be deduced by the comparison of excited state predictions with emission spectroscopy measurements. For high electron densities the solution approaches the Boltzmann distribution. Under certain conditions including low electron densities the corona equilibrium is applicable balancing solely excitation from the ground state with de-excitation via radiation. Note that CR models developed for low-temperature plasmas are not applicable to atmospheric pressure plasmas with strongly differing temperatures and densities. In addition to the interpretation of spectroscopic measurements, collisional-radiative models further enable various important applications: Population densities can be predicted for known plasma parameters and thus the photon fluxes towards surfaces [5]. Population models can be applied to calculate effective reaction rate probabilities (e.g. effective rate coefficients of dissociation and ionization of the molecules in plasmas) for use in neutral transport codes [6]. In such codes the energy loss of electrons and protons through collisions with H_2 in plasmas can be evaluated. For instance if the energy loss by ro-vibrational excitation is neglected, the energy loss of the plasma is underestimated and thus the plasma temperature and heat flux to the divertor plates overestimated [7].

Collisional-radiative modelling for atomic hydrogen has a long history starting with the pioneering works by Bates [8, 9] and Drawin [10]. The method was applied for the first time to molecular hydrogen in the works of Sawada and Fujimoto [11, 12]. For a more detailed overview of the history of CR modelling see e.g. [13].

The accuracy of CR models depends on the completeness of the model, the knowledge of the energy distribution functions (EDF) and the accuracy of the reaction probabilities provided as input to the model. Consequently, improvements in the field of atomic and molecular reaction probabilities are accompanied by improvements in CR modelling. Note that even if the uncertainty of all input reaction probabilities is known, no reliable uncertainty of the model result can be stated due to potentially missing processes. Instead, the excited state populations predicted by CR models are typically benchmarked with measurements. In the past, reaction probabilities from different works had to be combined and used as input for models, since measurements and calculations were usually solely performed for a small parameter range. This issue was improved by the works of Janev [14–16], which offer reviews and comparisons of collected data providing fits of recommended data. Recently the adiabatic-nuclei molecular convergent close coupling (MCCC) method [17] has been developed. It enables the calculation of consistent sets of fully quantal reaction probabilities for broad parameter ranges for collision processes between electrons and molecular hydrogen and its isotopologues. This improvement gives rise to a new era of CR modelling for molecular hydrogen and motivates to revisit this field also reviewing other reaction data that became available since the reviews by Janev as well as studying processes that have previously not been considered.

Due to its ro-vibrational structure, H_2 features several thousand ro-vibrational eigenstates. For a full CR model, the reaction probabilities coupling all these states through different types of reactions must be available. While the probabilities for transitions between ro-vibrational eigenstates induced by electron collisions are in the progress of being calculated with the MCCC method, the probabilities for other reactions between ro-vibrational eigenstates are still unknown or can merely be approximated. Consequently, a full CR model for H_2 is not feasible yet. The reaction probabilities available for hydrogen isotopologues in the literature are even more incomplete. Therefore, in this work a combined multi-stage approach is followed to develop and benchmark differently resolved models for H_2 for dedicated applications with the aim of providing CR models and state-of-the-art reaction probability databases for the plasma community and future fusion device predictions. For benchmarking these models the measurements from small scale laboratory experiments, the negative ion source test facility BATMAN Upgrade, the divertor plasma simulator Magnum-PSI and the DIII-D tokamak are applied.

This work is organized as follows: First the fundamental concepts of molecular hydrogen plasmas are discussed. This includes the quantum mechanical structure

of H_2, hydrogen emission, a more extensive distinction between different regimes of population modelling, the molecular reactions relevant for H_2 plasmas and specific properties of low temperature and divertor plasmas. Then diagnostics are discussed, the plasma experiment facilities and measurements from them applied for benchmarking are presented and utilized codes are described. Chapter 4 introduces the developed population models, their benchmarking and their application. The last chapter summarizes and concludes the implications learned from the developed models.

2 Fundamentals of molecular hydrogen plasmas

According to [18], a plasma is defined as a *quasineutral* gas consisting of charged and neutral particles that exhibit *collective behavior*.

The charged particles move around and generate local concentrations of positive or negative charge giving rise to electric fields. In addition, the motions of charges generate currents and thus magnetic fields. These fields in turn influence the motion of the charged particles. However, plasmas have the ability to shield out electric potentials that act on them. For instance, the potential emanating from a positive ion attracts electrons that can move more easily than the ion due to their lower mass and thus shield the potential. A measure for the shielding distance is given by the Debye length $\lambda_\mathrm{D} = \left(\frac{\varepsilon_0 k_B T_e}{n_\mathrm{e} e^2}\right)^{1/2}$ (with the electric constant ε_0, the Boltzmann constant k_B, the elementary charge e, the electron temperature T_e and the electron density n_e). If the dimensions of the system are much larger than λ_D, then whenever a local concentration of charge arises, it is shielded out, leaving the bulk of the plasma free of electric potentials or fields. As a result, the plasma can be considered to be quasineutral on a global scale (fulfilling $n_\mathrm{e} = \sum_i Z_i n_i$, with the charge number Z_i and the ion density n_i of each ion species involved)[18].

Collective behavior includes motions that depend not only on local conditions (e.g. collisions), but also on the state of the plasma in remote regions (e.g. forces due to the electromagnetic fields) [18].

Plasmas also consist of neutral particles (e.g. atoms and molecules) that undergo excitation and emit line emission. The heavy particle species that occur in hydrogen plasmas can include H, H^+, H^-, H_2, H_2^+ and H_3^+. The following chapter discusses the quantum mechanical principles for molecular hydrogen and hydrogen emission.

2.1 Quantum mechanical structure of molecular hydrogen

Molecular hydrogen (H_2) is a diatomic, homonuclear molecule consisting of two protons and two electrons. Since hydrogen or deuterium and deuterium-tritium plasmas are used in today's fusion experiments and in future fusion power plants respectively, the most prominent hydrogen isotopologues are D_2, T_2, HD and DT. While D_2 and T_2 additionally comprise of two and four neutrons respectively, HD and DT represent diatomic heteronuclear molecules. The focus of this work is on molecular hydrogen, several concepts will be discussed later for its isotopologues as well.

2.1.1 The Schrödinger equation for H_2

The Schrödinger equation for molecular hydrogen can be expressed as

$$\hat{H}\tilde{\Psi} = E\tilde{\Psi} \tag{2.1}$$

with the wavefunction $\tilde{\Psi}$ in dependence on the electron coordinates $\vec{r}_i$ and the coordinates $\vec{R}_a$ of the nuclei. The Hamiltonian [19]

$$\hat{H} = \hat{T}_\mathrm{e} + \hat{T}_\mathrm{N} + \hat{V}_\mathrm{e} + \hat{V}_\mathrm{N} + \hat{V}_\mathrm{eN} \tag{2.2}$$

with respect to an arbitrary origin in spherical coordinates consists of terms representing the kinetic energy of the electrons (with the electron mass m_e and the reduced Planck constant $\hbar$)

$$\hat{T}_\mathrm{e} = \sum_{i=1}^{2}(-\frac{\hbar}{2m_\mathrm{e}}\nabla_i^2), \tag{2.3}$$

the nuclear kinetic energy (with the proton masses m_p),

$$\hat{T}_\mathrm{N} = \sum_{\alpha=1}^{2}(-\frac{\hbar}{2m_\mathrm{p}}\nabla_\alpha^2), \tag{2.4}$$

the electron-electron interaction potential (with the electron coordinates $\vec{r}_1$,$\vec{r}_2$)

$$\hat{V}_\mathrm{e} = \frac{e^2}{4\pi\varepsilon_0}\frac{1}{|\vec{r}_1 - \vec{r}_2|}, \tag{2.5}$$

the nuclear potential (with the nuclei coordinates $\vec{R}_1$,$\vec{R}_2$)

$$\hat{V}_{\mathrm{N}} = \frac{e^2}{4\pi\varepsilon_0}\frac{1}{|\vec{R}_1 - \vec{R}_2|} \tag{2.6}$$

and the electron-nuclear interaction potential

$$\hat{V}_{\mathrm{eN}} = \sum_{\alpha=1}^{2}\sum_{i=1}^{2}\frac{e^2}{4\pi\varepsilon_0}\frac{1}{|\vec{R}_\alpha - \vec{r}_i|}. \tag{2.7}$$

In a first approximation, electron spin interaction and nuclear spin interaction are not accounted for.

2.1.2 The Born-Oppenheimer approximation

Since the electron masses are four orders of magnitude smaller than the nuclear masses, electrons are accelerated much faster and move much more quickly than the nuclei. Thus, for very short periods of time, electrons are moving and atomic nuclei are at rest [19].

This comparison motivates the Born-Oppenheimer approximation [20], which assumes that the electron distribution depends only on the instantaneous positions of the nuclei (and not on their velocities) [19]. Hence, the total wavefunction can be separated into electronic $\Psi_{\mathrm{e}}(\vec{r}_1, \vec{r}_2, R)$ and nuclear $\Psi_{\mathrm{N}}(\vec{R}_1, \vec{R}_2)$ parts, whereby the electronic part depends solely parametrically on the internuclear distance R [21]:

$$\tilde{\Psi} \approx \Psi^{\mathrm{BO}} = \Psi_{\mathrm{e}}(\vec{r}_1, \vec{r}_2, R)\Psi_{\mathrm{N}}(\vec{R}_1, \vec{R}_2). \tag{2.8}$$

As a consequence, the Schrödinger equation can be separated into two equations, with the solution of the equation for the electronic wavefunction yielding the energy $E_{\mathrm{e}}(R)$. This energy forms part of the potential to be inserted into the equation for the nuclear wavefunction in order to obtain the total energy [21]:

$$(\hat{H} - \hat{T}_{\mathrm{N}})\Psi_{\mathrm{e}}(\vec{r}_1, \vec{r}_2, R) = E_{\mathrm{e}}(R)\Psi_{\mathrm{e}}(\vec{r}_1, \vec{r}_2, R) \tag{2.9}$$

$$(\hat{T}_{\mathrm{N}} + E_{\mathrm{e}}(R))\Psi_{\mathrm{N}}(\vec{R}_1, \vec{R}_2) = E\Psi_{\mathrm{N}}(\vec{R}_1, \vec{R}_2). \tag{2.10}$$

When solving equation 2.9 for different values of R, the energy values obtained trace out potential curves that represent electronic eigenstates. The molecular hydrogen potential curves are well established in the literature. Since equation 2.9 has no nuclear mass dependence, they are valid for all isotopologues within

the Born-Oppenheimer approximation. The Born-Oppenheimer approximation breaks down for closely spaced or crossing electronic potential curves that arise from different excited electron configurations [21].

Furthermore, the nuclear wave function can be considered as the product of vibrational and rotational components, depending on the internuclear distance and orientation of the internuclear axis:

$$\Psi_{\mathrm{N}}(\vec{R}_1, \vec{R}_2) = \Psi_{\mathrm{vib}}(R)\Psi_{\mathrm{rot}}(\vec{R}_1, \vec{R}_2). \tag{2.11}$$

While the vibrational component represents the vibration along the internuclear axis, the rotational component represents the rotation of the molecule.

2.1.3 Electronic eigenstates

The electronic eigenstates are usually specified by the molecular term symbol [22]

$$^{2\mathrm{S}+1}\Lambda^{\pm}_{\mathrm{g/u}}. \tag{2.12}$$

The superscript $(2S+1)$ represents the *spin multiplicity* in dependence on the total electron spin S. For molecular hydrogen, the two electrons can have anti-parallel $(S = 0)$ or parallel $(S = 1)$ spin orientation giving rise to the *singlet* and *triplet* multiplet systems. The quantum number Λ represents the *projection of the coupled electronic orbital angular momentum onto the internuclear axis*. By convention it is labeled with Greek capital letters (e.g. Σ, Π, Δ for $\Lambda = 0, \pm 1, \pm 2$). The subscript g/u represent *even* and *odd electronic parity* describing the symmetry of the electronic wavefunction upon electron coordinate inversion through the center of the molecule. The superscript $\pm$ represent for Σ states, the *reflection symmetry* of the electronic wavefunction through a plane containing the internuclear axis [23]. For $|\Lambda| > 0$ states, the superscript $\pm$ is not part of the term symbol, since theses states occur in degenerate pairs with both specificities of the reflection symmetry. Nevertheless, $|\Lambda| > 0$ states are often written with the same superscripts, which, however, carry a different meaning to be expanded on later.

Electronic states of molecular hydrogen can also be characterized by the *effective quantum number* n in the united-atom limit [24]. The value assigned to the molecular state depends on the state of the electron (that is not in the ground state) to which it converges to as R increases. Sometimes the molecular term symbol is thus extended by the effective quantum number n (written with a capital letter): $N^{2\mathrm{S}+1}\Lambda^{\pm}_{\mathrm{g/u}}$.

Most molecular hydrogen states with $n \leq 4$ are typically labeled with historically assigned Latin letters, using capital letters for the singlet system and lower case letters for the triplet system. The ground state is labeled $X^1\Sigma_g^+$. Electronic states with potential curves having two minima are typically labeled with two letters (e.g. $GK^1\Sigma_g^+$). The state $b^3\Sigma_u^+$ is an example for a dissociative state: Since it does not have a potential well, it will dissociate into H atoms.

Figure 2.1 depicts the potential curves for molecular hydrogen for the first singlet and triplet states with the lowest corresponding E_e (plotted with data from the references given in [25]), whereby the potential energy is shown with respect to the potential minimum of the energetically lowest lying state.

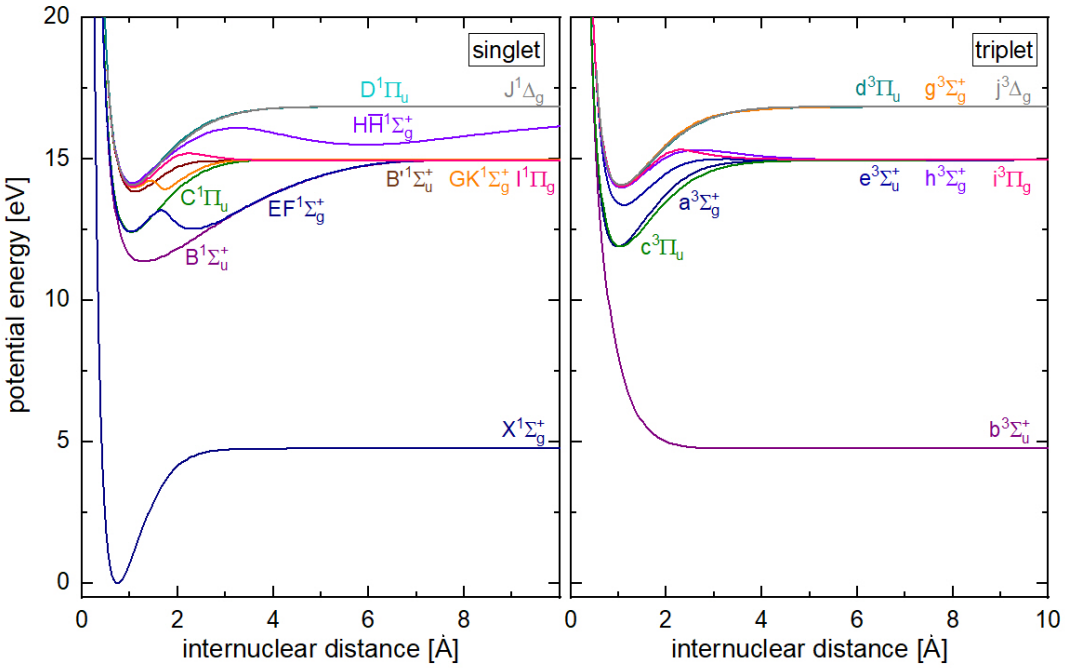

Figure 2.1: *Energetically lowest lying potential curves for H_2 singlet and triplet states (plotted with data from the references given in [25]).*

2.1.4 Vibrational and rotational levels

When inserting 2.11 into equation 2.10, two separate equations can be derived for the vibrational and rotational wavefunctions, since the vibrational wavefunction depends only on the internuclear distance R and the rotational wavefunction on its orientation, giving rise to the respective vibrational and rotational levels with the energies E_v and E_r^v.

The equation for the vibrational wavefunction can be brought into the shape of the wave equation for the *vibrating rotator* [19]. Expressions for the potential

energy term are well known for H_2 in literature (see e.g. the references in [25]).

The vibrational eigenfunctions are characterized by the quantum number $v \geq 0$ and the respective energy can be approximated by

$$E_v \approx \omega_e \left(v + \frac{1}{2}\right) - x_e\omega_e \left(v + \frac{1}{2}\right)^2 + y_e\omega_e \left(v + \frac{1}{2}\right)^3 + (...), \qquad (2.13)$$

with the harmonic vibrational frequency ω_e and the anharmonic constants x_e and y_e. The values of these constants for different electronic states and different molecules are given in e.g. [23].

Figure 2.2 depicts examples of potential curves and the corresponding vibrational eigenfunctions. It can be seen that the vibrational levels of a certain electronic state are closer together as v increases. For vibrational energies above the vibrational energy of the highest bound level, the molecule will dissociate.

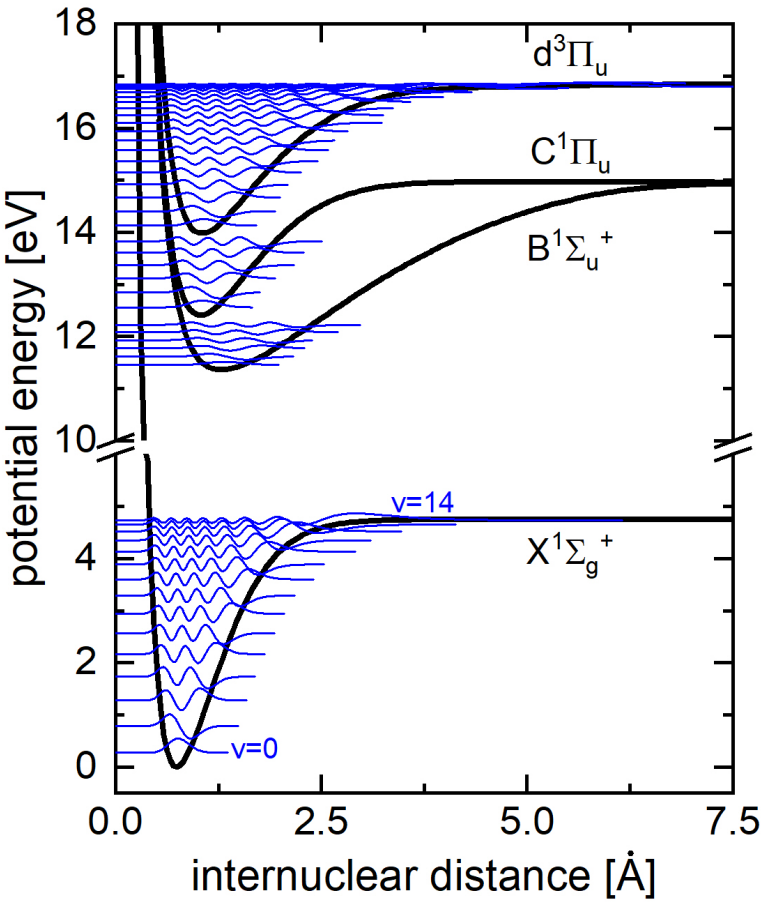

Figure 2.2: *Example of potential curves with the respective vibrational eigenfunctions (stemming from [25]) for the electronic ground state $X^1\Sigma_g^+$ and the electronically excited states $B^1\Sigma_u^+$, $C^1\Pi_u$ and $d^3\Pi_u$. To increase visibility, only the first few vibrational eigenfunctions are shown for the states $B^1\Sigma_u^+$ and $C^1\Pi_u$.*

In order to interpret the solution of the rotational part, the structure of the molecular rotation has to be clarified: The eigenvalues to the equation for the rotational wavefunction depend on the rotational quantum number N (not to be confused with the effective quantum number in the term symbol). The coupling of angular momenta in molecules is categorized by the *Hund's coupling cases* [26]. For molecular hydrogen, the spin is not strongly affected by the rotation of the molecule. Consequently, the vector $\vec{N}$ (corresponding to quantum number N) is formed from Λ with orientation along the internuclear axis and the vector representing the molecular rotation $\vec{J}_\mathrm{r}$. $\vec{N}$ subsequently couples with $\vec{S}$ and forms $\vec{J}$. For very light nuclei (e.g. such as in H_2), the influence of the spin is negligible and thus $\vec{J}$ plays no role [26]. Figure 2.3 illustrates this coupling scheme that classifies as Hund's coupling case (b).

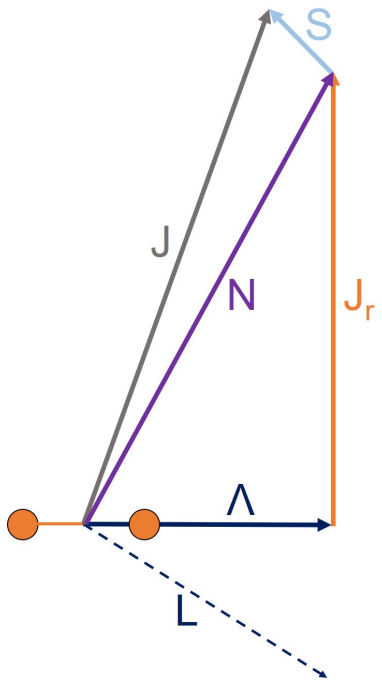

Figure 2.3: *Schematic of Hund's coupling case (b): $\vec{\Lambda}$, the projection of the coupled electronic orbital angular momentum onto the internuclear axis $\vec{L}$, and $\vec{J}_\mathrm{r}$ form $\vec{N}$ that subsequently couples with $\vec{S}$ to form $\vec{J}$. The connected circles represent the nuclei of the molecule.*

Since the structure of the measurements indicates that rotation and vibration occur simultaneously, the model of the vibrating rotator is applicable to describe molecular hydrogen. Therefore, the energy of a rotational level N for a vibrational

level v is expressed as

$$E_{\mathrm{r}}^{\mathrm{v}} \approx B_{\mathrm{v}} N(N+1) - D_{\mathrm{v}} \left[N(N+1)\right]^2 + (...), \tag{2.14}$$

with the rotational constant B_{v} and the centrifugal distortion constant D_{v} for the vibrational level v [23].

2.1.5 Molecular symmetries

If a molecule exhibits a certain symmetry, the effect of the associated operator can be used to characterize its wavefunctions and energy levels. However, it is crucial to always specify both the symmetry operation and the affected part of the wave function [22].

Table 2.1 summarizes the symmetries relevant for molecular hydrogen.

Table 2.1: *Summary of the molecular state symmetries relevant for H_2 and their symbols.*

Symbol	Symmetry
$\Sigma^{\pm}$	reflection symmetry of electronic wavefunction through plane containing internuclear axis
g/u	even/odd parity: symmetry under electron coordinate inversion through center of molecule
$+/-$	total parity: rotation level symmetry for origin reflection (at center of mass) of entire wavefunction
e/f	rotationless parity: total parity with the effect of rotation being factored out
s/a	symmetric/antisymmetric parity: nuclear permutation symmetry for rotational levels

- The superscript $\pm$ represents for Σ states the *reflection symmetry* of the electronic wavefunction through a plane containing the internuclear axis.
- *Even* or *odd parity* of an electronic state denotes the *symmetry under electron coordinate inversion through the center of the molecule* and is represented by subscript g/u.
- The *total parity* denotes the symmetry of a rotational level under origin reflection of the total eigenfunction. This reflection corresponds to the inversion of all coordinates of the particles (for both nuclei and electrons) in

the laboratory frame with the origin at the center of mass [22]. Depending on whether the total eigenfunction remains unchanged or changes sign, the corresponding rotational level is called *positive* or *negative*, commonly represented by a +/- label.

In addition, the effect of Λ-*doubling* must be considered for states with $\Lambda > 0$: Rotational levels occur pairwise, split into two states of opposite total parity with slightly shifted energies (as a consequence of the interaction between $\vec{L}$ and the rotation of the nuclei, whereby the occurring eigenstates represent combinations of the eigenfunctions corresponding to the two directions of rotation) [23]. The series of rotational levels in which even levels are *positive* and odd levels are *negative* is labeled Λ^+, the series of levels in which odd levels are *positive* and even levels are *negative* is labeled Λ^- (e.g. $d^3\Pi_u^+$ and $d^3\Pi_u^-$).

- *Rotationless parity* represents the total parity with the effect of rotation being factored out. Rotational levels with a total parity equal to $(-1)^N$ are called *e-band*, rotational levels with total parity equal to $(-1)^{N+1}$ are called *f-band* [22]. Since specifying the rotationless parity does not provide additional information, for given total parity and N, it will not be used in this work.

- The *nuclear permutation symmetry* represents the symmetry for exchange of the nuclei of homonuclear diatomic molecules. Whether the total wavefunction remains unchanged or changes sign, the state under consideration is *symmetric* (s) or *antisymmetric* (a) [23].

  The operation applied to the wavefunction is equivalent to inverting all electrons and nuclei through the origin in the laboratory frame ($\rightarrow$ depending on the total parity) and inverting back the electrons in the molecular frame ($\rightarrow$ depending on the g/u parity) [22]. As a consequence, all positive rotational levels are either even and symmetric or odd and antisymmetric, and all negative rotational levels are either even and antisymmetric or odd and symmetric. This observation is summarized in table 2.2.

Table 2.2: *Observed combinations of symmetries.*

	+	−
g	s	a
u	a	s

Since only transitions between the same nuclear permutation symmetry are observed, gases such as (ground state) molecular hydrogen can be regarded as a mixture of two modifications. While antisymmetric rotational levels are often referred to as *ortho* hydrogen (with symmetric nuclear spin function), symmetric levels are referred to as *para* hydrogen (with antisymmetric nuclear spin function) [27]. It will be discussed later that these two modifications of the rotational levels have different statistical weights depending on the nuclear spin alignment. Levels in the *ortho* modification have greater weights than levels in the *para* modification. Note that, for non-vanishing nuclear spin transitions between symmetric and antisymmetric levels can actually occur with a very small probability. The reciprocal transition probability amounts to the mean lifetime and is in the order of years [23].

In summary, table 2.3 depicts the first rotational levels for examples of electronic states (and arbitrary vibrational levels) and specifies the respective symmetry properties and modifications.

Table 2.3: *Rotational levels of the $X^1\Sigma_g^+$, $B^1\Sigma_u^+$, $a^3\Sigma_g^+$, $d^3\Pi_u^+$ and $d^3\Pi_u^-$ states (for arbitrary v) with their respective symmetry properties (e/f, $+/-$, s/a) and modification (o:ortho/p:para).*

N	$X^1\Sigma_g^+(v)$	$B^1\Sigma_u^+(v)$	$a^3\Sigma_g^+(v)$	$d^3\Pi_u^+(v)$	$d^3\Pi_u^-(v)$
0	$(e + s\ p)$	$(e + a\ o)$	$(e + s\ p)$	/	/
1	$(e - a\ o)$	$(e - s\ p)$	$(e - a\ o)$	$(e - s\ p)$	$(f + a\ o)$
2	$(e + s\ p)$	$(e + a\ o)$	$(e + s\ p)$	$(e + a\ o)$	$(f - s\ p)$
3	$(e - a\ o)$	$(e - s\ p)$	$(e - a\ o)$	$(e - s\ p)$	$(f + a\ o)$
4	$(e + s\ p)$	$(e + a\ o)$	$(e + s\ p)$	$(e + a\ o)$	$(f - s\ p)$

2.1.6 Statistical weight of molecular levels

Molecular states and levels have different kinds of statistical weights. The respective contributions are discussed separately below.

The electronic statistical weight

The statistical weight of electronic states g_e is the product of the spin multiplicity $(2S + 1)$ and the orbital angular momentum degeneracy. It can be expressed using

the Kronecker delta symbol:

$$g_{\mathrm{e}} = (2 - \delta_{0,\Lambda})(2S + 1). \tag{2.15}$$

The vibrational statistical weight

Vibrational levels in diatomic molecules are not degenerate. Therefore, their weight is equal to one [28] and will not be mentioned again.

The rotational statistical weight

The statistical weight of a rotational level g_N is for a fixed electronic state and vibrational level equal to [27]

$$g_N = (2N + 1). \tag{2.16}$$

The nuclear spin statistical weight

The nuclei of homonuclear molecules possess nuclear spin with the spin vector $\vec{I}$, respectively. The spin vectors $\vec{I}$ form the total nuclear spin of the molecule $\vec{T}$. The corresponding quantum number of total nuclear spin T has integer values between 0 and $2I$ [23]. The statistical weight arising from T amounts to $\Sigma_T(2T + 1)$, whereby the sum is taken over all even (for symmetric levels) and over all odd (for antisymmetric levels) values of T from 0 to I [28]. The resulting expressions for the nuclear spin statistical weight g_I are summarized in table 2.4.

Table 2.4: *Nuclear spin statistical weight g_I for homonuclear molecules.*

	integral I	half-integral I
s	$(2I + 1)(I + 1)$	$(2I + 1)I$
a	$(2I + 1)I$	$(2I + 1)(I + 1)$

Since the nuclei of H_2 consist of protons with $I = 1/2$ respectively, the symmetric levels have g_{I}=1 and the antisymmetric levels g_{I}=3.

2.1.7 The Franck-Condon principle

The Franck-Condon principle follows the idea that electronic excitation in a molecule occurs so rapidly compared to the vibrational motion that the nuclei still have nearly the same relative position and velocity immediately after excitation as they had before. [23]. The Franck-Condon factors measure the relative likelihood

of a transition between vibrational levels of electronic states and are defined as the squared overlap integral of the initial and final level vibrational wavefunctions:

$$q_{\mathrm{v,v'}}^{\mathrm{N}\Lambda_\sigma,\mathrm{N'}\Lambda'_{\sigma'}} = \left| \int_0^\infty \psi_{\mathrm{N}\Lambda_\sigma,\mathrm{v}}(r)\psi_{\mathrm{N'}\Lambda'_{\sigma'},\mathrm{v'}}(r)dr \right|^2 . \tag{2.17}$$

2.1.8 The molecular ions H_2^+, H_2^- and H_3^+

Figure 2.4 depicts the potential curves for the energetically lowest lying states of H_2, H_2^+ and H_2^-.

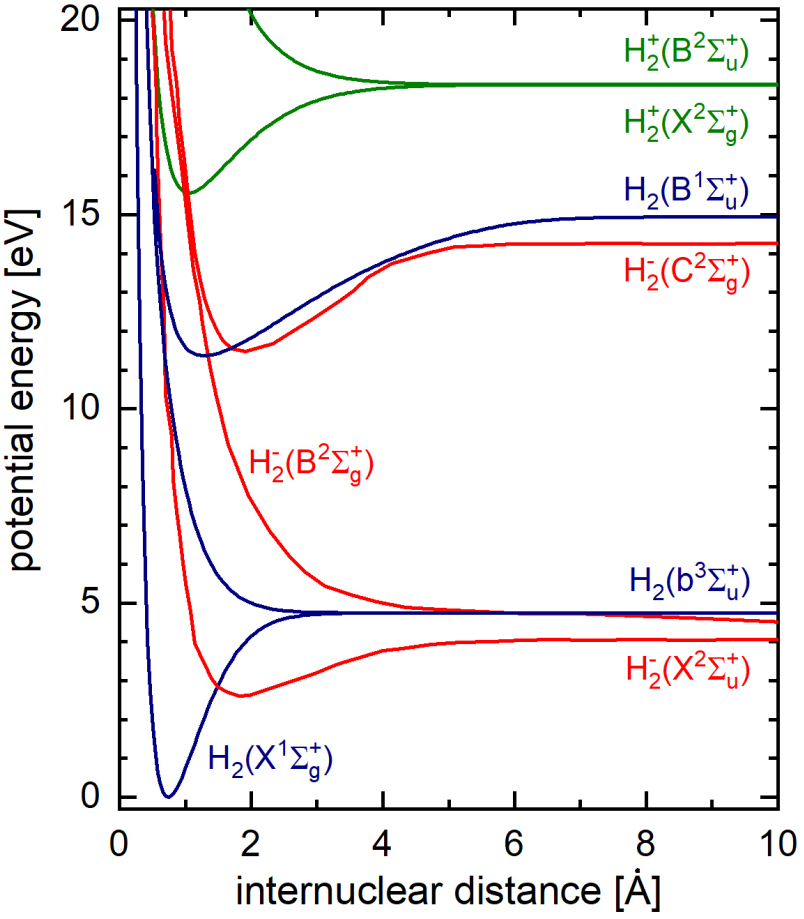

Figure 2.4: *Potential energy curves for the energetically lowest lying H_2 [29, 30], H_2^+ [31] and H_2^- states [32].*

The H_2^+ molecular ion

The molecular ion H_2^+ consists of two protons and an electron. For the rigid H_2^+, the corresponding Schrödinger equation can be solved exactly in dependence on the internuclear distance [33]. While the ground state $X^2\Sigma_g^+$ of H_2^+ is stable, the

excited state $B^2\Sigma_u^+$ is dissociative. Further states exist that have much higher excitation thresholds [31].

The H_2^- molecular ion

States of the H_2^- molecular ion are *resonances* (often also referred to as compound states or temporary negative ions). Resonances represent non-stationary states that are formed by the interaction of an incident electron with a target molecule in which the incident electron is temporarily captured [34]. The energetically lowest lying H_2^- states are $X^2\Sigma_u^+$ and $B^2\Sigma_g^+$ [16].

The H_3^+ molecular ion

H_3^+ is a stable triatomic molecular ion mainly produced by exothermic collisions between H_2^+ and H_2 ($H_2^+ + H_2 \rightarrow H_3^+ + H$). Due to its high dissociation energy ($\approx 4.4\,\mathrm{eV}$), it represents a rather stable species [35]. The potential energy of the system in dependence on the three internuclear distances is described by a three-dimensional potential surface [36].

2.2 Hydrogen emission

A measure for the amount of photons emitted by an atomic or molecular state through Spontaneous Emission is usually given in the form of *line emission intensities* (in units of photons (Ph) (s m^3)$^{-1}$). The line emission intensity depends both on the population density of the emitting state $n_{p'}$ (with $p' = (N'\Lambda'_{\sigma'}, v', N')$) and on the Einstein coefficient (for the transition between the states p' and q'') $A_{p'q''}$

$$I_{p'q''} = n_{p'} A_{p'q''} = \int_{peak} \varepsilon_\lambda d\lambda \tag{2.18}$$

and can be derived from the *spectral emission intensity* ε_λ (in units of Ph/(s m^3 nm)) by integration over the respective, measured emission peak. When radiative quantities are expressed in units of power, the energy per photon ($E = h\nu$ with the frequency ν and the Planck constant h) must be taken into account. It should be noted that the nomenclature of radiative quantities is not uniformly established in the literature. Therefore, an overview of the nomenclature used in this work is summarized in the Appendix A.

As a consequence of the uncertainty principle, emission lines experience natural broadening. The energy spread is inversely proportional to the temporal uncertainty associated with finding a particle in a particular state. For initial state

p' and final state q'' the temporal uncertainty can be represented by the mean lifetime of these states [21]:

$$\Delta\lambda_{\text{natural}} = \frac{\lambda_0^2}{c}\left(\frac{1}{2\pi\tau_p} + \frac{1}{2\pi\tau_q}\right). \tag{2.19}$$

When recording atomic or molecular emission, the observed spectral line shapes represent convolutions of the true line profiles with the apparatus function. The apparatus function depends on the measurement setup. The influences on the apparatus function for spectrometers are discussed in 3.1.1. The true line profile can be influenced in addition by different mechanisms [21] (e.g. Doppler broadening, Stark broadening, Zeeman broadening).

Doppler broadening is a consequence of the Doppler effect (describing the shift in wavelength of a signal emanating from a source apparently moving towards or away from an observer). In plasmas, the shift arises from the thermal motion of the emitting particles. If the particle motion is represented by a Maxwell-Boltzmann velocity distribution, the broadened line profile has Gaussian shape and its width is given by:

$$\Delta\lambda_{\text{Doppler}} = \frac{\lambda_0}{c}\sqrt{\frac{8\,\ln(2)\,RT}{M}} = 7.16\cdot 10^{-7}\sqrt{\frac{T}{M}}\lambda_0 \tag{2.20}$$

with the theoretical unshifted wavelength λ_0, the molar gas constant R and the mass number M. Although for emission in the visible range, the width due to Doppler broadening is typically two orders of magnitude higher than the width due to natural broadening [33], natural broadening can make a significant contribution to the wings of the line due to its Lorentzian shape [21].

Stark broadening is a consequence of the electric field of charged particles in the plasma perturbing emitting particles (due to the Stark effect) [21]. Typically, it only becomes relevant at electron densities above $10^{19}\,\text{m}^{-3}$ [37].

Broadening due to Zeeman splitting of degenerate states in magnetic fields is usually observed in fusion experiment plasmas due to the high magnetic fields present there [38].

For further information on other broadening mechanisms, see e.g. [33, 39].

2.2.1 Molecular line emission

The structure of molecular hydrogen emission can be understood by starting with the definition of Einstein coefficients expressing the probability for Spontaneous

Emission from state p' to state q'' [21]:

$$A_{p'q''} = \frac{16\pi^3\nu^3}{3\varepsilon_0 hc^3}|M_{p'q''}|^2. \tag{2.21}$$

Thereby, $M_{p'q''}$ represents the dipole matrix element for the transition between the molecular states with the wave functions (involving electronic, vibrational and rotational components) $\psi_{p'}$ and $\psi_{q''}$:

$$M_{p'q''} = \int\int \psi^*_{p'}\hat{p}\psi_{q''}d\tau_e d\tau_N, \tag{2.22}$$

whereby the integral extends over all $3(Z_\alpha + Z_{\alpha'})$ electronic coordinates and the six nuclear coordinates in dependence on the dipole operator, which comprises of contributions from the electrons $\hat{p}_\mathrm{e}$ and of the nuclei $\hat{p}_\mathrm{N}$:

$$\hat{p} = \hat{p}_\mathrm{e} + \hat{p}_\mathrm{N} = -e\sum_i \vec{r_i} + e(Z_\alpha\vec{R}_\alpha + Z_{\alpha'}\vec{R}_{\alpha'}), \tag{2.23}$$

again with the coordinates of the electrons $\vec{r_i}$, the coordinates of the nuclei $\vec{R}_\alpha$ and the respective charge numbers Z_α. For transitions between the same electronic state, it follows for orthonormal wavefunctions that the electronic part of the dipole operator in the matrix element becomes zero. Since $\vec{R}_\alpha = -\vec{R}_{\alpha'}$ applies to homonuclear molecules and the charge numbers of their nuclei are the same ($Z_\alpha = Z_{\alpha'}$), it follows that the nuclear component of the dipole operator cancels out ($\hat{p}_\mathrm{N} = 0$). Consequently, homonuclear diatomic molecules do not emit or absorb radiation for transitions within the same electronic state [33]. Hence, only transitions between different electronic states are observed for molecular hydrogen. Note that this argument only holds for homonuclear molecules, but not for heteronuclear molecules (e.g. HD or DT).

Within the Born-Oppenheimer approximation the total energy of a ro-vibrational level is (independent of the internuclear distance) the sum of the electronic, vibrational and rotational energy [33]:

$$E = E_\mathrm{e} + E_\mathrm{v} + E_\mathrm{r}, \tag{2.24}$$

whereby $E_\mathrm{e} \gg E_\mathrm{v} \gg E_\mathrm{r}$ [21]. The unshifted wavelength λ of a photon emitted from the transition between two states equals $\lambda = hc/\Delta E$ with

$$\Delta E = E_{N'\Lambda'_{\sigma'},v',N'} - E_{N''\Lambda''_{\sigma''},v'',N''} = \Delta E_\mathrm{e} + \Delta E_\mathrm{v} + \Delta E_\mathrm{r}. \tag{2.25}$$

Spectra emitted from molecular hydrogen appear therefore in the form of characteristic bands (e.g. $d^3\Pi_u^- \rightarrow a^2\Sigma_g^+$) with vibrational bands (e.g. $v' = 0 \rightarrow v'' = 0$) consisting of rotational lines (e.g. $N' = 1 \rightarrow N'' = 1$).

Optically allowed transitions obey the selection rules for dipole transitions. These selection rules can be derived by symmetry considerations regarding the matrix element of the dipole operator. The selection rules for molecular hydrogen (as a representative of Hund's angular momentum coupling case (b)) are summarized below. The rules applying to other coupling cases are given in e.g. [23].

For transitions involving dipole transitions, *positive* levels only combine with *negative* levels and *negative* levels solely combine with *positive* levels:

$$+ \leftrightarrow -, - \leftrightarrow +, + \nleftrightarrow + \text{ and } - \nleftrightarrow -. \tag{2.26}$$

For molecules with nuclei of equal charge, *even* electronic states combine only with *odd*:

$$u \leftrightarrow g \text{ but } u \nleftrightarrow u \text{ and } g \nleftrightarrow g. \tag{2.27}$$

Transitions (on timescales of less than months or years) occur exclusively between *ortho* and *ortho* levels or between *para* and *para* levels, so that it follows that:

$$antisym \nleftrightarrow sym. \tag{2.28}$$

For molecules the following rule regarding the quantum number Λ applies (equivalent to the selection rule for the magnetic quantum number for atoms in an electro-magnetic field):

$$\Delta\Lambda = 0, \pm 1. \tag{2.29}$$

Additionally, for Σ states the following rules apply:

$$\Sigma^+ \leftrightarrow \Sigma^+ \text{ and } \Sigma^- \leftrightarrow \Sigma^- \text{ but } \Sigma^+ \nleftrightarrow \Sigma^-. \tag{2.30}$$

However, both Σ^+ and Σ^- can still combine with Π states.

Since only states of the same multiplicity combine with another, transitions between different multiplet systems are optically forbidden:

$$\Delta S = 0. \tag{2.31}$$

Furthermore, the rotational quantum number N obeys

$$\Delta N = 0, \pm 1 \tag{2.32}$$

with the additional restriction:

$$\Delta N = 0 \text{ is forbidden for } \Sigma\text{-}\Sigma \text{ transitions.} \tag{2.33}$$

Thereby, the transitions with $\Delta N = N' - N'' = 0, +1, -1$ are typically referred to as *Q-*, *P-* and *R-lines* respectively [25]. It should be emphasized that transitions that are optically forbidden can still occur, but are much less likely.

With respect to the full molecular hydrogen spectra, several intense transition bands are prominently used for spectroscopic measurements. Figure 2.5 depicts the term scheme of the molecular hydrogen states with $n = 1 - 3$ and the transitions that are used in this work.

The most intense radiation in the VUV region are the Werner band (maximum emission below 130 nm) and the Lyman band (dominant part between 130−170 nm) originating from the resonant transitions $C^1\Pi_u \rightarrow X^1\Sigma_g^+$ and $B^1\Sigma_u^+ \rightarrow X^1\Sigma_g^+$ respectively [5].

Note that the effect of self-absorption in molecules is weak, since the transition probability of electronic states is distributed over the vibrational bands and rotational lines [3]. Hence, opacity is not relevant for the molecular radiation as the transition probability of an individual molecular line is too small [5].

For the transition between $a^3\Sigma_g^+ \rightarrow b^3\Sigma_u^+$ a broad continuum radiation between $120 - 600$ nm is emitted [5].

The Fulcher-α band between $d^3\Pi_u \rightarrow a^3\Sigma_g^+$ is typically the most intense band in the visible range [5]. Since the potential curves of these two states are almost unshifted in nuclear distance, the Franck-Condon Factors for diagonal vibrational transitions are high [3]. Its most intense structure lies around $600 - 640$ nm originating from the diagonal transitions with $v' = v'' = 0, 1, 2, 3$. The higher diagonal vibrational bands are less pronounced, as the respective emitting levels are mostly pre-dissociated (see below).

The transitions between $GK^1\Sigma_g^+ \rightarrow B^1\Sigma_u^+$ and $I^1\Pi_g \rightarrow B^1\Sigma_u^+$ can exhibit intense vibrational bands between $420 - 470$ nm and $390 - 460$ nm respectively, giving access to the population density of $n = 3$ singlet states through evaluation.

The intensities of rotational lines in a vibrational band can be specified in dependence on the *Hönl-London factors* $S_{P,Q,R}(N')$ describing the dependence on the rotational quantum numbers. The expression for P-, Q- and R-line transitions of diatomic molecules are given in [40].

For rotational lines of the same vibrational transition band of H_2, a 3:1 alternation in intensity is observed. This intensity alternation is a consequence

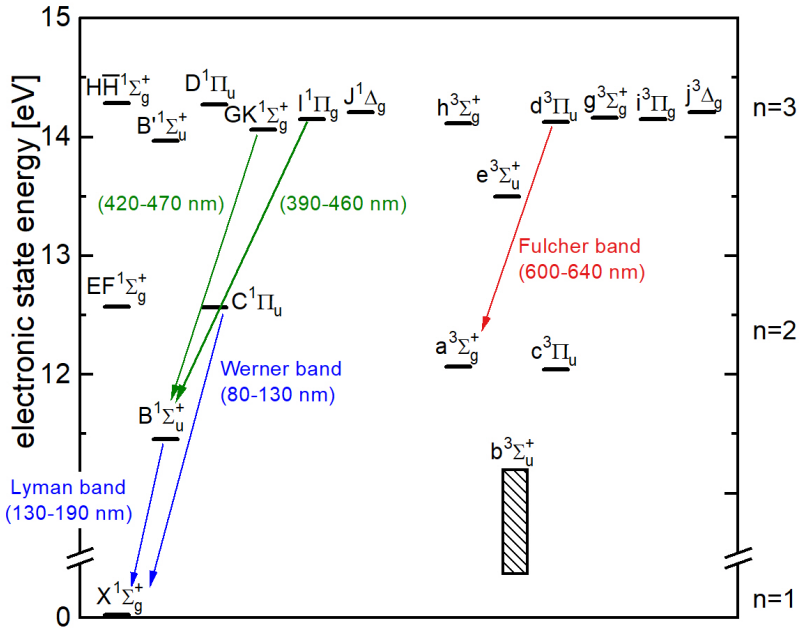

Figure 2.5: *Term scheme for the energetically lowest lying states of H_2 and the transitions between them that are used in this work. The color of the arrows gives an indication for the wavelength.*

of the nuclear statistical weight being g_I=1 for symmetric levels and g_I=3 for antisymmetric levels (see chapter 2.1.6).

2.2.2 Atomic line emission

The states of hydrogen atoms can be characterized (neglecting the hyperfine-structure) by the quantum numbers n (main quantum number), l (orbital angular momentum), m (magnetic quantum number) and m_s (component of spin in z-direction) [21].

States with different wave functions that have the same energy are called degenerate. In the absence of external fields, the respective energy depends only on the main quantum number n resulting in a degeneracy of $\sum_{l=0}^{n-1}(2l+1) = n^2$ without accounting for spin. Including the spin, the degeneracy amounts in total to $2n^2$ [21].

The energy for a hydrogen atom state in dependence on n is according to the semiclassical Bohr model:

$$E_n = \frac{\mu_0 e^4}{8\varepsilon_0^2 h^2}\frac{1}{n^2} = \frac{Ry^*}{n^2}, \tag{2.34}$$

with the magnetic constant μ_0 and $Ry^* = 13.6\,\mathrm{eV}$ equal to the ionization

energy of H [33].

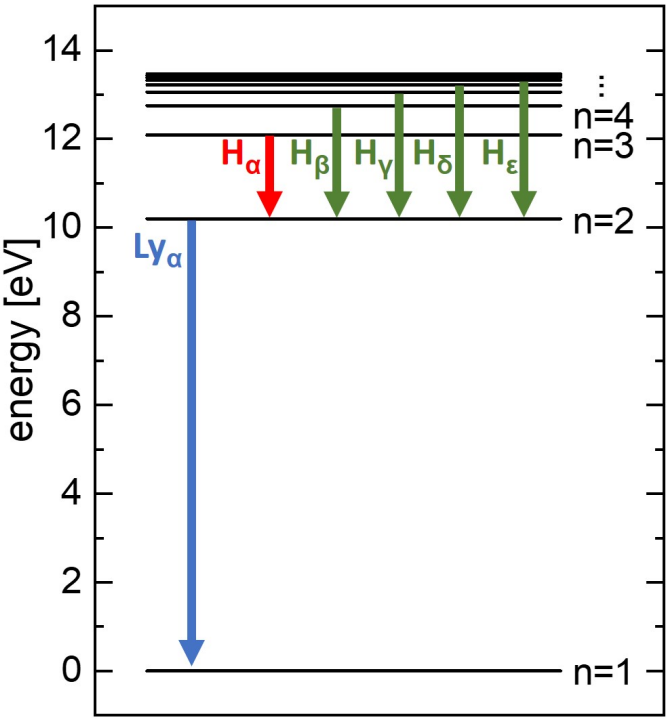

Figure 2.6: *States of the atomic hydrogen system and commonly recorded transitions. The color of the arrows gives an indication for the wavelength.*

Emission stemming from Spontaneous Emission transitions with final states $n = 1$ and $n = 2$ form the Lyman and Balmer line series respectively. The first transition of the Lyman series (Ly_α ($n = 2 \rightarrow n = 1$): 121.6 nm) lies in the vacuum ultraviolet spectral range. The Balmer line series lies in the visible range (H_α ($n = 3 \rightarrow n = 2$): 656.2 nm, H_β ($n = 4 \rightarrow n = 2$): 486.1 nm, H_γ ($n = 5 \rightarrow n = 2$): 434 nm, H_δ ($n = 6 \rightarrow n = 2$): 410.1 nm, H_ε ($n = 7 \rightarrow n = 2$): 397 nm) [33].

Optical thickness can play a role for the atomic hydrogen emission. In optically thick plasmas, excited states are de-populated by Spontaneous Emission, but not every emitted photon is measured due to the self-absorption of the photon from the plasma and the photon transport towards the position of the detector.

To account for the self-absorption in population models, the escape factor method can be applied. An overview of this method is given in [41]. Population escape factors Θ_{pop} are multiplied with the Einstein coefficients of the respective transitions in order to reduce the transition probabilities and thus increase the population densities of the respective excited states [42]. The relevance of the optical thickness depends on the plasma length (assuming isotropic emission), the density of the lower state of the respective transition, the gas temperature, the oscillator

strength of the transition and the reduced mass of the emitting particle [42].

The effect of self-absorption during the photon transport to the detector can be compensated for measurements using line escape factors Θ_{line} [43]. Since the emission from a plasma is reduced along its transport towards the detector, the measured emission intensity must be corrected by multiplication with the reciprocal line escape factor [44].

While both the population escape factor and line escape factor are important for the Lyman series, as they represent resonant transitions, opacity can often be neglected as a good approximation for the Balmer series (e.g. the factors are ≈ 1) [43]. However, the consideration of population escape factors for the Lyman series can also indirectly, due to redistribution, enhance the Balmer emission yield in population models [42].

2.3 A comment regarding other isotopologues

Since the nuclei of hydrogen isotopologues have higher masses compared to H_2, the ro-vibrational levels are spaced closer together, so that more vibrational levels are bound for a certain electronic state within the Born-Oppenheimer approximation. The differences in ro-vibrational levels have several consequences that are highlighted in the following using the example of D_2:

The reaction probabilities for the same reactions involving different isotopologues differ due to the different level energies, implying that individual population models are required and that the (ro-vibrationally resolved) models for H_2 should not simply be applied for D_2.

The ro-vibrational emission lines are spaced closer together and exhibit a different intensity alteration. Since the nuclei of D_2, consisting of a proton and a neutron respectively, have a nuclear spin $I = 1$, the symmetric levels have a statistical weight g_{I}=6 and the antisymmetric levels g_{I}=3. Consequently, an intensity alternation for rotational lines of 2:1 is observed [23].

Furthermore, it should be noted that the nuclei of molecular hydrogen follow Fermi statistics, while the nuclei of molecular deuterium follow Bose statistics. As a consequence, the symmetry properties discussed for H_2 cannot be transferred directly to D_2. Therefore, table 2.5 summarizes the symmetry combinations of the individual components of the total wavefunctions including the nuclear spin [23]. With the aid of this table, the rules for hydrogen isotopologues can be deduced.

Table 2.5: *Symmetry of entire wavefunction for $I \neq 0$*

nuclear statistic type	total function	total function without nuclear spin	nuclear spin function
Fermi	antisym.	sym.	antisym
Fermi	antisym	antisym.	sym.
Bose	sym.	sym.	sym.
Bose	sym.	antisym.	antisym.

2.4 Population models

As discussed above, the emission intensities depend on the excited state population densities. In plasmas the population densities themselves are again determined by collisional and radiative processes. The rates of collisional processes depend on the particle temperatures and densities in the plasma. Population models aim to predict population densities of excited states in dependence on the plasma parameters. For the inverse application of the population models, the plasma parameters can be deduced by comparison of the excited state predictions with emission spectroscopy measurements.

Typically three regimes for population modelling are distinguished in dependence on the electron density: the local thermodynamical equilibrium (LTE) at high densities, the corona regime at low densities and the intermediate regime that can be described by collisional-radiative models. Figure 2.7 shows the population density ratios for excited states in H_2 in dependence on the electron density indicating the different regimes.

2.4.1 Local thermodynamical equilibrium

A plasma and radiation field that are confined in a fictive box with an inner wall at constant temperature T is in thermodynamical equilibrium with the wall, and its physical state is entirely determined by T [45]. As a consequence, the radiation field follows the Planck blackbody law, the energy distribution of each species of particles corresponds to a Maxwell-Boltzmann distribution

$$f(E)dE = \frac{2}{\sqrt{\pi}} \frac{\sqrt{E}}{(k_\mathrm{B}T)^{3/2}} \exp\left(\frac{-E}{k_\mathrm{B}T}\right) dE\,. \tag{2.35}$$

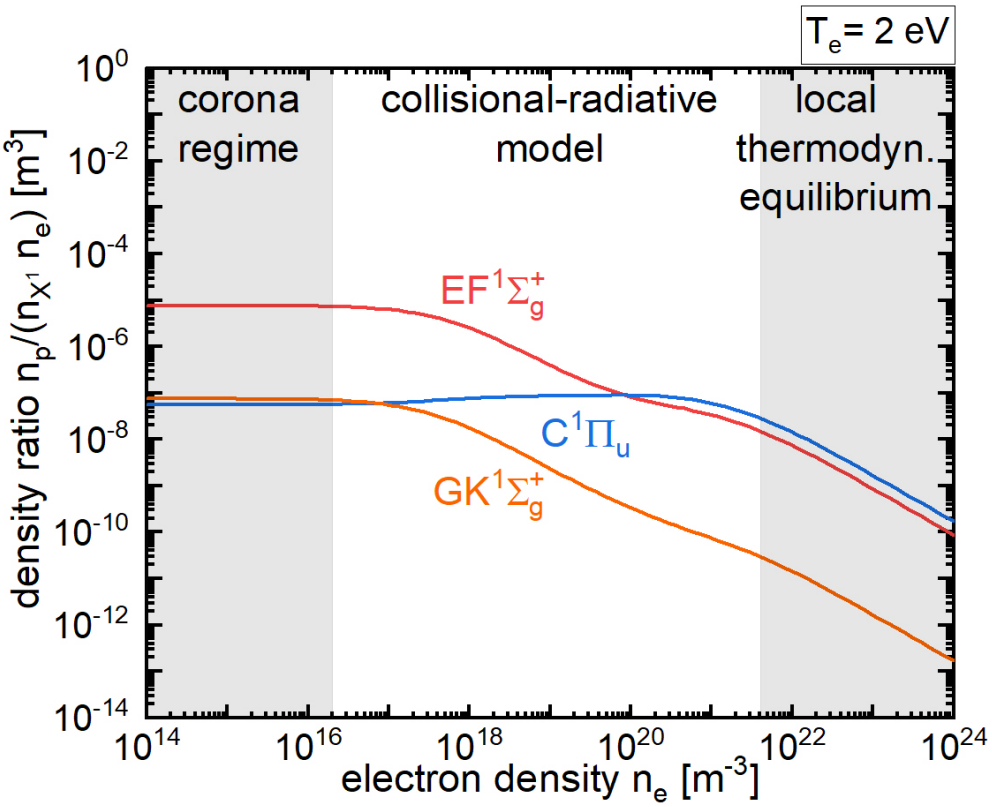

Figure 2.7: *Depending on the plasma parameters different regimes for population modelling can be distinguished: the local thermodynamical equilibrium for high electron densities, the corona regime for low electron densities and in-between the regime that can be described by collisional-radiative models.*

The population densities of excited atomic or molecular states follow the Boltzmann distribution

$$\frac{n_q}{n_p} = \frac{g_q}{g_p} \exp\left(-\frac{E_q - E_p}{k_\mathrm{B} T}\right), \tag{2.36}$$

the distribution between ions and neutrals obeys the Saha equation and each process is in equilibrium with its inverse [45] (e.g. for every photon emitted, a photon of the same frequency is absorbed [21]).

However, thermodynamical equilibrium is usually not reached in plasmas. Since radiation usually escapes from a plasma, the radiant field inside a plasma is below the Planck blackbody law [45]. Nevertheless, in collision-dominated plasmas (e.g. for sufficiently high electron densities) the excited state population densities follow the Boltzmann distribution and the ionization distribution is given by the Saha equation with Maxwell-Boltzmann energy distribution functions (EDFs) as prerequisites. Since electron collisions are much faster than ion collisions, the electrons establish the equilibrium [45]. The ion temperature can differ from the electron temperature, and both these temperatures can also

vary with location [21]. A plasma in such a state is characterized to be in the *local thermodynamical equilibrium (LTE)*. Note that low-pressure, low-temperature plasmas (see below) typically have not sufficiently high electron densities, thus the excited state population densities do not follow the Boltzmann distribution.

2.4.2 Corona equilibrium

For low electron densities, the corona equilibrium is often applicable, as collisional reactions between excited states are negligible. Consequently, the excited states are mainly populated by Electron Impact Excitation collisions directly from the ground state and de-populated by Spontaneous Emission

$$X^{\mathrm{e}}_{0p'} n_0 n_{\mathrm{e}} = \sum_{q''<p'} A_{p'q''} n'_p \tag{2.37}$$

with the rate coefficient for electron impact excitation from the ground state $X^{\mathrm{e}}_{0p'}$ and the ground state density n_0. The radiation field is typically so low that the absorption of photons is negligible as well. Each particle species is characterized by its own temperature (e.g. $T_{\mathrm{e}} > T_{\mathrm{ion}}$) [24]. In order to characterize a plasma in the corona equilibrium, the electron density and the excitation rates for electron impact processes in dependence on the electron temperature must be known [45].

2.4.3 Collisional-radiative modelling

Collisional-radiative (CR) models are the most general approach to predict excited state densities: Complete CR models inherently comprise corona models and for very high electron densities the population densities of the excited states calculated by CR models approach the (local) thermodynamic equilibrium distribution. However, in contrast to corona models the reaction probabilities for all types of collisional, radiative and spontaneous processes that (de-)populate the excited states of a particle (e.g. atom or molecule) need to be known. These processes are balanced in the form of coupled rate equations. For each excited state, an ordinary differential equation describes the temporal change of its population density

$$\frac{\mathrm{d}n_k}{\mathrm{d}t} = \sum_{ij} X^{\mathrm{j}}_{ik} n_i n_j + \sum_i A_{ik} n_i - n_k (\sum_{ij} X^{\mathrm{j}}_{ki} n_j + \sum_i A_{ki}), \tag{2.38}$$

applying the rate coefficient X^{j}_{ik} for collisions between species i and j populating species k (species representing particle species or (excited) state) depending on the temperature of the respective involved educt species and the Einstein

coefficient A_{ik} for Spontaneous Emission. Note that, as discussed above, the Einstein coefficients can be multiplied with population escape factors Θ_{pop} to account for self-absorption of radiation.

Since the relaxation times for the excited states are much shorter than the relaxation time for the ground state, the *quasi-steady state solution* [8, 9, 46] is applicable: In order to determine the excited state population densities, their temporal derivatives are set to zero, implying that all excited states instantaneously follow the variation in the ground state density [45]. This approach is motivated on the basis that the population of a particle changes over time until an equilibrium is reached in which the populating and de-populating processes counterbalance each other. Besides the ground state, ions or certain excited states (e.g. metastable states) can also have a much longer relaxation time compared to the other excited states, so that their density is determined by transport instead. Applying the quasi-steady state solution simplifies the set of coupled differential equations to a set of coupled linear equations. Hence, it is straightforward to consider the set of coupled linear equations in matrix representation and solve it by inverting the matrix that contains the rate coefficients. Alternatively, the equilibrium densities can also be determined by integrating the coupled linear equations.

It can be challenging to determine which states need to be treated as long-living and for which states the population must be calculated. Typically, the former are referred to as being in P-space and the latter as being in Q-space. Furthermore, *metastable states* can pose a particular challenge, since they are excited states that must be treated to be in P-space for small n_{e} and in Q-space for high n_{e}. The reason for this is that they can only be effectively de-populated by Electron Impact De-Excitation processes, which become increasingly relevant the higher n_{e}.

In [47, 48] the time-scale criterion for the quasi-steady state solution is universalized to criteria based on the characteristics of the matrix representing the equation system.

Instead of calculating excited state densities for given plasma parameters, CR models can be used in backward application to determine the plasma parameters for given excited state populations (derived from measured emission). In this case the solution is typically not unambiguous and a multi-dimensional solution space is found. However, the uncertainty can be reduced by considering the population densities (emission lines) from several states simultaneously.

The accuracy of CR models depends on the accuracy of reaction probabilities, the knowledge of the EDF and the completeness of the model. The following

chapter discusses the reactions that are accounted for in the CR-models developed within the scope of this work.

2.5 Molecular reactions (de-)populating H_2

2.5.1 Quantification of reactive processes

Quantification of collisional transitions

The probability for a particular collision process between two particles (A and B) is expressed in the form of a cross section $\sigma(E_{\mathrm{rel}})$ (or $\sigma(v_{\mathrm{rel}})$) $[m^2]$ in dependence on the relative kinetic energy (or relative velocity) of the two particles.

In practice it is essential to consider the specific energy frame in which the cross section is stated. The energy in the *center-of-mass frame* E_{CM} (center-of-mass being at rest throughout the collision) is related to the energy of particle A in the *laboratory frame* E_{A} (target particle B being at rest before the collision) given the respective particle masses (m_{A}, m_{B}) according to

$$E_{\mathrm{CM}} = \left(\frac{m_{\mathrm{B}}}{m_{\mathrm{A}} + m_{\mathrm{B}}}\right) E_{\mathrm{A}}. \tag{2.39}$$

For collisions between electrons and heavy particles with $m_{\mathrm{A}} = m_{\mathrm{e}} \ll m_{\mathrm{B}}$, the center-of-mass energy E_{CM} is approximately equal to the laboratory energy E_{A}.

A rate coefficient X $[m^3/s]$ is the quantitative measure for the effectiveness of a collision process [16] in dependence on the particle temperatures (T_{A},T_{B}) given the (normalized) velocity distribution $f(\vec{u})$ of the relative velocity $\vec{u} = \vec{v_A} - \vec{v_B}$ and can be derived from the cross section via

$$X = \langle \sigma v \rangle (T_{\mathrm{A}}, T_{\mathrm{B}}) = \int f(\vec{u})\, \sigma(\vec{u})\, u \, \mathrm{d}^3 u \,. \tag{2.40}$$

Thus the rate coefficient for a plasma with an isotropic stationary Maxwellian energy distribution function with $T^* = \frac{T_A m_B + T_B m_A}{m_A + m_B}$ and $m^* = \frac{m_A m_B}{m_A + m_B}$ is expressed as

$$X = \langle \sigma v \rangle (T_A, T_B) = \sqrt{\frac{2}{\pi}} \left(\frac{m^*}{T^*}\right)^{3/2} \int_0^\infty u^3\, \sigma(u)\, \exp\left(-\frac{m^* u^2}{2T^*}\right) \mathrm{d}u \,. \tag{2.41}$$

The collision rate Γ $[m^{-3}s^{-1}]$ is the product of the respective particle densities and the rate coefficient

$$\Gamma = n_{\mathrm{A}} n_{\mathrm{B}} X(T_{\mathrm{A}}, T_{\mathrm{B}}) \,. \tag{2.42}$$

Note that the relevance of a certain process involving specific states needs to be assessed based on the (collision) rate and not solely on the basis of the rate coefficient or cross section.

The *principle of detailed balance* (or *microscopic reversibility*) is a consequence of the symmetry of collision processes with respect to time reversal [16] holding at thermodynamical equilibrium for any pair of collisional processes that are inverse to each other [39]. It can be applied to derive the measure to the reverse process for a quantitatively known forward process. As an example it is applied to the (de-)excitation of particle B via the collision with particle A:

$$A + B(E_p) \leftrightarrow A + B(E_q) \text{ with } E_q > E_p \,. \tag{2.43}$$

corresponding to

$$n_{\mathrm{A}}\, n_{\mathrm{B(E_p)}}\, X_{\mathrm{pq}}(T) = n_{\mathrm{A}}\, n_{\mathrm{B(E_q)}}\, X_{\mathrm{qp}}(T) \,. \tag{2.44}$$

Since excited state populations follow a Boltzmann distribution in thermodynamical equilibrium, inserting 2.36 in 2.44 yields

$$X_{qp}(T) = \frac{g_p}{g_q} \exp\left(\frac{E_q - E_p}{k_{\mathrm{B}} T}\right) X_{pq}(T) \,. \tag{2.45}$$

The principle of the detailed balance can also be applied to cross sections in order to determine the cross section for the inverse process [39]. Doing so requires accounting for the energy threshold of the forward process (whereas there may not be a threshold for the backward process).

Quantification of spontaneous transitions

The inverse of the natural lifetime of a ro-vibrational level $\tau_{N'\Lambda'_{\sigma'},v',N'}$ $[s]$ is determined by the sum of all rates of spontaneous de-populating processes for this level. This sum may include besides Spontaneous Emission (characterized by the radiative lifetime $\tau^{\mathrm{SE}}_{N'\Lambda'_{\sigma'},v',N'}$) also other processes (e.g. Predissociation or Autoionization).

$$\begin{gathered}(\tau_{N'\Lambda'_{\sigma'},v',N'})^{-1} = (\tau^{\mathrm{SE}}_{N'\Lambda'_{\sigma'},v',N'})^{-1} + (\tau^{\mathrm{other}}_{N'\Lambda'_{\sigma'},v',N'})^{-1} \\ \text{with } \tau^{\mathrm{SE}}_{N'\Lambda'_{\sigma'},v',N'} = \left(\textstyle\sum_{N''\Lambda''_{\sigma''},v'',N''} A_{(N'\Lambda'_{\sigma'},v',N')(N''\Lambda'',v'',N'')}\right)^{-1}\end{gathered} \tag{2.46}$$

Effective quantities

Effective rate coefficients or Einstein coefficients represent reaction probabilities valid for specific population density distributions. An effective rate coefficient X^{eff}

is the sum of the respective rate coefficients X_p for each state $p = (N\Lambda_\sigma, v, N)$ weighted by the relative population of the respective state characterized by $\tilde{T}$:

$$X^{\text{eff}}(T) = \sum_p f(p, \tilde{T}) X_p(T) = \sum_p \frac{n_p}{n_{\text{total}}} X_p(T). \tag{2.47}$$

For instance the population of the vibrational levels of the electronic ground state $X^1\Sigma_g^+$ can be characterized by the vibrational temperature T_{vib}. An effective rate coefficient in dependence on T_{vib} may be of interest for processes in which the rate coefficient varies for different vibrational levels and for plasmas in which the population densities of vibrational levels are not negligible compared to the ground level.

An effective Einstein coefficient is the sum of the Einstein coefficients for each level weighted by the relative population of the respective level. Thereby, to derive for instance Einstein coefficients for transitions between purely electronically resolved states from vibrationally resolved coefficients, the coefficients are summed over the final levels:

$$\begin{gathered}(\tau^{\text{SE,eff}}_{N'\Lambda'_{\sigma'}})^{-1} = \textstyle\sum_{N''\Lambda''_{\sigma''}} \sum_{v'} A_{(N'\Lambda'_{\sigma'},v')(N''\Lambda''_{\sigma''})} n_{N'\Lambda'_{\sigma'},v'} \\ \text{with } \textstyle\sum_{v'} n_{N'\Lambda'_{\sigma'},v'} = 1 \text{ and } A_{(N'\Lambda'_{\sigma'},v')(N''\Lambda''_{\sigma''})} = \sum_{v''} A_{(N'\Lambda'_{\sigma'},v')(N''\Lambda''_{\sigma''},v'')}.\end{gathered} \tag{2.48}$$

2.5.2 Collision processes of electrons with hydrogen molecules

In the following the processes influencing the molecular hydrogen state population are discussed in detail. This discussion is restricted to the processes that are considered in the population models developed within the scope of this work. Note that even though the processes may partially feature a dependence on the rotational quantum number N, N-dependencies are not explicitly stated in this chapter.

Electron Impact (De-)Excitation

Electron Impact (De-)excitation characterizes the (de-)excitation of a molecule in initial state $H_2(N\Lambda_\sigma, v)$ to the energetically higher (lower), bound final state $H_2(N'\Lambda'_{\sigma'}, v')$ by electron collision at the cost of kinetic energy.

$$e^- + H_2(N\Lambda_\sigma, v) \rightleftarrows e^- + H_2(N'\Lambda'_{\sigma'}, v') \tag{2.49}$$

Transitions obeying the selection rules for optical transitions discussed above have higher probabilities than optically forbidden transitions. Examples for optically forbidden transitions are transitions between different multiplet systems (spin-mixing transitions with $\Delta S \neq 0$). Spin-mixing transitions are possible if the projectile electron takes the place of a bound electron repelling the latter.

Vibrational Electron Impact (De-)excitation of a vibrational level of the electronic ground state $X^1\Sigma_g^+$ is a two-step mechanism. Initially, most prominently the H_2^- resonance states $X^2\Sigma_u^+$ or $B^2\Sigma_g^+$ are formed by the collision process, which then decay by electron emission to a vibrational level of the electronic ground state [15, 32]:

$$e^- + H_2(X^1\Sigma_g^+, v) \rightarrow H_2^-(X^2\Sigma_u^+/B^2\Sigma_g^+) \rightarrow e^- + H_2(X^1\Sigma_g^+, v')\,. \tag{2.50}$$

Electron Impact Dissociation

Electron Impact Dissociation denotes Electron Impact (De-)excitation wherein the product is either part of the continuum ϵ' of a repulsive state (e.g. $H_2(b^3\Sigma_u^+,\epsilon')$ or energetically above the final bound level of a bonding state (e.g. $H_2(C^1\Pi_u, v > 13)$), causing the molecule to dissociate into an atom in the ground state H(1) and an excited atom H(n) [15, 32]:

$$e^- + H_2(N\Lambda_\sigma, v) \rightarrow e^- + H_2(N'\Lambda'_{\sigma'}, \epsilon') \rightarrow e^- + H(1) + H(n)\,. \tag{2.51}$$

Non-Dissociative Electron Impact Ionization

Non-Dissociative Electron Impact Ionization refers to the excitation of a molecule of initial state $H_2(N\Lambda_\sigma, v)$ to a bound vibrational level of H_2^+ via electron collision [15]:

$$e^- + H_2(N\Lambda_\sigma, v) \rightarrow 2e^- + H_2^+(X^2\Sigma_g^+, v')\,. \tag{2.52}$$

For this process only the ground state of H_2^+ ($X^2\Sigma_g^+$) is of relevance, since the first electronically excited state ($B^2\Sigma_u^+$) is repulsive and the other excited states lie energetically much higher, requiring higher electron energies [31, 49].

Dissociative Electron Impact Ionization

For Dissociative Electron Impact Ionization, a molecule of initial state $H_2(N\Lambda_\sigma, v)$ is excited to an unbound vibrational level of the ground state of $H_2^+(X^2\Sigma_g^+)$ or to the unbound continuum of the first excited, dissociative state of $H_2^+(B^2\Sigma_u^+)$ via electron collision, causing the dissociation of H_2^+ resulting in a ground state atom

and a proton [15].

$$e^- + H_2(N\Lambda_\sigma, v) \rightarrow 2e^- + H_2(X^2\Sigma_g^+, v') \rightarrow 2e^- + H(1) + H^+ \tag{2.53}$$

$$e^- + H_2(N\Lambda_\sigma, v) \rightarrow 2e^- + H_2^+(B^2\Sigma_u^+, \epsilon') \rightarrow 2e^- + H(1) + H^+ \tag{2.54}$$

Dissociative Electron Attachment

Dissociative Electron Attachment for a vibrational level of the electronic ground state proceeds via the H_2^- resonance states $X^2\Sigma_u^+$, $B^2\Sigma_g^+$ and $C^2\Sigma_g^+$ induced by electron collision [15, 32]. For sufficiently long resonance lifetimes the nuclei separate to such an extent that the electron cannot autodetach, resulting instead in the dissociation into an atom and H^- [50].

$$\begin{gathered} e^- + H_2(X^1\Sigma_g^+, v) \rightarrow H_2^-(X^2\Sigma_u^+/B^2\Sigma_g^+) \rightarrow H(1) + H^- \\ e^- + H_2(X^1\Sigma_g^+, v) \rightarrow H_2^-(C^2\Sigma_g^+) \rightarrow H(2) + H^- \end{gathered} \tag{2.55}$$

As a consequence of the respective energies of $X^2\Sigma_u^+$, $B^2\Sigma_g^+$ and $C^2\Sigma_g^+$ (see figure 2.4), the cross section for $H_2(X^1\Sigma_g^+)$ exhibits local maxima around the energies of 4, 10 and 14 eV [51].

Dissociative Electron Attachment for vibrational levels of initial electronically excited states proceeds via higher excited electronic resonance states $H_2^-(N_i^2\Lambda_\sigma)$ [15]:

$$e^- + H_2(N\Lambda_\sigma, v) \rightarrow H_2^-(N_i^2\Lambda_\sigma) \rightarrow H(n) + H^- \,. \tag{2.56}$$

2.5.3 Collision processes of protons with hydrogen molecules

Proton Charge Transfer

The process of Proton Charge Transfer converts atomic to molecular ions. If the molecular ground state is involved, the process can be endothermic ($v \leq 3$) or exothermic ($v \geq 4$) depending on the initial vibrational level [15]:

$$H^+ + H_2(X^1\Sigma_g^+, v) \rightarrow H(1) + H_2^+(X^2\Sigma_g^+, v') \,. \tag{2.57}$$

At low relative kinetic energies, the reaction proceeds in a quasiresonant two-step mechanism [52]: The vibrational excitation from the H_2 ground vibrational level to the excited ones $v = 3, 4$ is followed by the quasiresonant electronic nonadiabatic transition to the capture state dissociating into the products H and H_2^+ [53]. The

proton charge transfer cross section for initial $v = 0$ level exhibits a double-humped shape with two local maxima for the low energy region (below 100 eV) that is a consequence of non-reactive ($C^+ + AB(X^1\Sigma_g^+, v) \rightarrow C + AB^+$, for impinging proton C^+ and initial H_2 target AB) and reactive ($C^+ + AB(X^1\Sigma_g^+, v) \rightarrow A + BC^+$ or $B + AC^+$) reaction channels [53].

The process of Proton Charge Transfer for electronically excited molecular states

$$H^+ + H_2(N\Lambda_\sigma, v) \rightarrow H(n) + H_2^+ \tag{2.58}$$

is quite probable, since the electron binding energy of an electronically excited state in its vibrational ground level is close to the electron binding energy of the corresponding hydrogen atom excited state [15].

Proton Impact (De-)Excitation

Proton Impact (De-)Excitation denotes the vibrational (de-)excitation of molecular hydrogen via proton collision. For the reaction proceeding between vibrational levels of the molecular ground state

$$H^+ + H_2(X^1\Sigma_g^+, v) \rightleftarrows H^+ + H_2(X^1\Sigma_g^+, v') \tag{2.59}$$

the respective cross section for a fixed initial level has its local maximum for each final level for energies above its respective threshold, but decreases if the energy is high enough to exceed the subsequent higher threshold energy (enabling the excitation into the next higher lying final level), resulting in a local minimum [54].

Proton Impact Dissociation

Proton Impact Dissociation of the ground electronic state is driven by non-adiabatic coupling in the vibrational continuum of H_2 and H_2^+ [15].

$$H^+ + H_2(X^1\Sigma_g^+, v) \rightarrow H^+ + 2H(1) \tag{2.60}$$

This dissociative reaction can also involve charge transfer [15].

2.5.4 Collision processes between hydrogen molecules

Collisional Quenching

Collisional Quenching represents de-population of excited molecular states via heavy-particle collisions predominantly occurring through collisions with neutral

molecules [55]

$$H_2(N\Lambda_\sigma, v) + H_2(X^1\Sigma_g^+, v = 0) \rightarrow 2H_2(X^1\Sigma_g^+, v = 0)\,. \tag{2.61}$$

Hydrogen Molecule Impact (De-)Excitation

Hydrogen Molecule Impact (De-)Excitation in the electronic ground state can comprise of the transfer of kinetic energy to vibrational excitation (or the reverse) (VT transfer)

$$H_2(X^1\Sigma_g^+, v) + H_2(X^1\Sigma_g^+, w) \rightleftarrows H_2(X^1\Sigma_g^+, v') + H_2(X^1\Sigma_g^+, w) \tag{2.62}$$

or re-distribution of vibrational energy (VV transfer) by collisions between molecules in the electronic ground state [56]

$$H_2(X^1\Sigma_g^+, v) + H_2(X^1\Sigma_g^+, w) \rightarrow H_2(X^1\Sigma_g^+, v') + H_2(X^1\Sigma_g^+, w')\,. \tag{2.63}$$

The latter is most effective when the total vibrational energy before and after the collision is conserved (e.g. $\mid v' - v \mid = \mid w' - w \mid$) [15].

2.5.5 Collision processes involving H, H^-, H_2^+ and H_3^+

Hydrogen Atom Impact Dissociation

Hydrogen Atom Impact Dissociation refers to the dissociation of molecules by collisions with atomic hydrogen [15]

$$H(1) + H_2(X^1\Sigma_g^+, v) \rightarrow H(1) + 2H(1). \tag{2.64}$$

H^- Associative Detachment

H^- Associative Detachment induced by collisions between H^- and H typically proceeds via the H_2^- resonances $X^2\Sigma_u^+$ and $B^2\Sigma_g^+$ (with the main contribution from the former) decaying into the vibrational spectrum of H_2 [15].

$$H^- + H(1) \rightarrow H_2^-(X^2\Sigma_u^+/B^2\Sigma_g^+) \rightarrow e^- + H_2(X^1\Sigma_g^+, v') \tag{2.65}$$

Radiative Recombination

Non-dissociative Radiative Recombination of electrons and H_2^+ molecular ions results in the formation of (vibrationally excited) H_2 under the emission of an

photon with the energy $h\nu$

$$H_2^+ + e^- \rightarrow H_2(X^1\Sigma_g^+, v') + h\nu\,. \tag{2.66}$$

It is usually expected to be negligible in comparison to dissociative recombination of the same educts [16].

Collisional 3-Particle Recombination

Collisional 3-particle (three-body) Recombination of two electrons and H_2^+ forming (vibrationally excited) H_2 under the emission of an photon

$$H_2^+ + e^- + e^- \rightarrow H_2(X^1\Sigma_g^+, v') + e^- + h\nu \tag{2.67}$$

is also expected to be negligible in comparison to the corresponding dissociative recombination process [16].

H_3^+ Dissociative Recombination

Dissociative Recombination of H_3^+ with an electron proceeds via excited, unstable H_3^+ states (H_3^{+*}) resulting in the dissociation forming H_2 and H

$$e^- + H_3^+ \rightarrow e^- + H_3^{+*} \rightarrow H_2(X^1\Sigma_g^+, v) + H(n \geq 1)\,. \tag{2.68}$$

In an alternative reaction channel, three hydrogen atoms can also be produced by the recombination of the same educts [15].

2.5.6 Non-collisional processes for molecular hydrogen

Autoionization

Autoionization of excited H_2^* results in the formation of H_2^+ under emission of an electron occurring if the vibrational energy of a bound state is higher than the ionization energy of the vibrational ground level of that state. Non-adiabatic coupling of electronic and nuclear motion is presumably the driving mechanism [15].

$$H_2(N\Lambda_\sigma, v) \rightarrow H_2^+(X^2\Sigma_g^+, v') + e^- \tag{2.69}$$

Predissociation

Predissociation refers to the non-adiabatic coupling of two electronic states, whereby the potential curve for a stable electronic state is crossed by that for an unstable state or a state with lower dissociation energy, resulting in dissociation [21].

$$H_2(N\Lambda_\sigma, v) \rightarrow H_2(N'\Lambda'_{\sigma'}, \epsilon') + e^- \rightarrow H(1) + H(n > 1) + e^- \tag{2.70}$$

It can occur for bound, excited H_2 states that have an energy above the dissociation limit of an energetically lower excited state, with the strength being stronger the closer the states involved are to each other [15].

2.6 Specific molecular hydrogen plasmas

2.6.1 Low-pressure, low-temperature plasmas

Low-pressure plasmas are typically characterized by $p = 0.01 - 10\,000\,\mathrm{Pa}$ [3], $T_\mathrm{e} \approx 1 - 10\,\mathrm{eV}$, $n \approx 10^{14} - 10^{19}\,\mathrm{m}^{-3}$ and $T_i \ll T_\mathrm{e}$ [57]. Plasmas with electron temperatures in the range of eV are referred to as low-temperature plasmas [4].

Low-pressure plasmas are typically generated from neutral gas by applying an electric field, inductive (see chapter 3.2.1) or capacitive RF coupling or electromagnetic waves (see chapter 3.2.2). Thereby, already existing primary electrons are accelerated due to the electromagnetic field and thus ionize gas particles by collisions. A key feature of low-pressure and low-temperature plasmas is that due to the low collision frequency no equilibrium between the electron and heavy particle species temperatures is established [4, 57]: The applied power primarily heats the mobile electrons, while the heavier ions solely exchange energy efficiently through collisions with the background gas. Therefore, the electron temperature T_e is typically higher than the temperature of the background gas T_gas [57].

Plasmas from negative hydrogen ion sources for neutral beam injection (see 3.2.3) are generated by inductive RF coupling and comprise of both ionizing and recombining regions [58, 59]: In ionizing hydrogen plasmas ($T_\mathrm{e} \approx 10\,\mathrm{eV}$) the principal excitation channels for atomic emission are direct excitation from the ground state and dissociative excitation of H_2. In recombining plasmas ($T_\mathrm{e} \lessapprox 1\,\mathrm{eV}$), the (dissociative) recombination of positive ions (such as H^+, H_2^+ and H_3^+) and, if such plasmas are electronegative, the mutual neutralization of H^- with positive ions are crucial for the population of excited hydrogen atoms.

Due to the high collision frequency in low-temperature plasmas, the mean energy

of electrons is lower than the ionization energy of neutrals. Consequently, such plasmas typically have a low ionization degree ($\alpha = \frac{n_i}{n_n+n_i} \approx 10^{-3} - 10^{-6}$) and the heat transfer to surfaces such as chamber walls is dominated by the neutrals [3]. In [60] the ionization degree is correlated with the type of the EDF, according to which a Maxwellian electron distribution is typically justified for $\alpha \gtrapprox 10^{-4}$.

The plasma-wall interaction can give rise to the two-temperature distribution (sometimes called hockey-stick distribution), whereby the ro-vibrational levels of H_2 are observed to follow [61]:

$$n(X^1\Sigma_g^+(v,N)) \propto (1-\beta)\,\tilde{n}_{\mathrm{rot}}(T_{\mathrm{rot}\,1})\,\tilde{n}_{\mathrm{vib}}(T_{\mathrm{vib}\,1}) + \beta\,\tilde{n}_{\mathrm{rot}}(T_{\mathrm{rot}\,2})\,\tilde{n}_{\mathrm{vib}}(T_{\mathrm{vib}\,2}). \quad (2.71)$$

Thereby, $T_{\mathrm{vib}\,1}$ and $T_{\mathrm{vib}\,2}$ (and $T_{\mathrm{rot}\,1}$ and $T_{\mathrm{rot}\,2}$) represent vibrational (rotational) temperatures characterizing Boltzmann distributions according to which the respective vibrational (rotational) levels are populated [62]. $T_{\mathrm{vib}\,1}$ is determined by plasma processes. $T_{\mathrm{rot}\,1}$ has been found to amount to the gas temperature T_{gas} [63]. The population of both higher vibrational and rotational levels may depend on the surface recombination of atomic hydrogen [64], hence $T_{\mathrm{rot}\,2}$ and $T_{\mathrm{vib}\,2}$ are equated. $T_{\mathrm{vib}\,1}$ and $T_{\mathrm{rot}\,1}$ are typically lower than $T_{\mathrm{vib}\,2}$ and $T_{\mathrm{rot}\,2}$ respectively. The two distributions are each weighted by the factor β.

In order to characterize low-pressure, low-temperature plasmas through the interpretation of absolutely calibrated spectroscopic measurements, accurate CR models are essential.

2.6.2 Fusion edge plasmas

In magnetically confined fusion research, magnetic fields are used to confine a toroidal plasma. In *tokamaks* [65], in addition to the magnetic field generated by toroidal and helical coils, a magnetic field in poloidal direction is induced by a current flowing in toroidal direction [2]. The resulting helical magnetic field lines define nested flux surfaces of constant magnetic flux. The plasma itself is confined within the closed magnetic flux surfaces, whereby the last closed flux surface is called *separatrix* with the particle density n_u and temperature T_u. Outside the separatrix is the so-called *scrape off layer* (SOL), in which the plasma flows towards and interacts with solid surfaces called *divertor* target plates [65] with the particle density n_t and temperature T_t. Figure 2.8 illustrates the basic geometry of a poloidal cross section for a tokamak plasma.

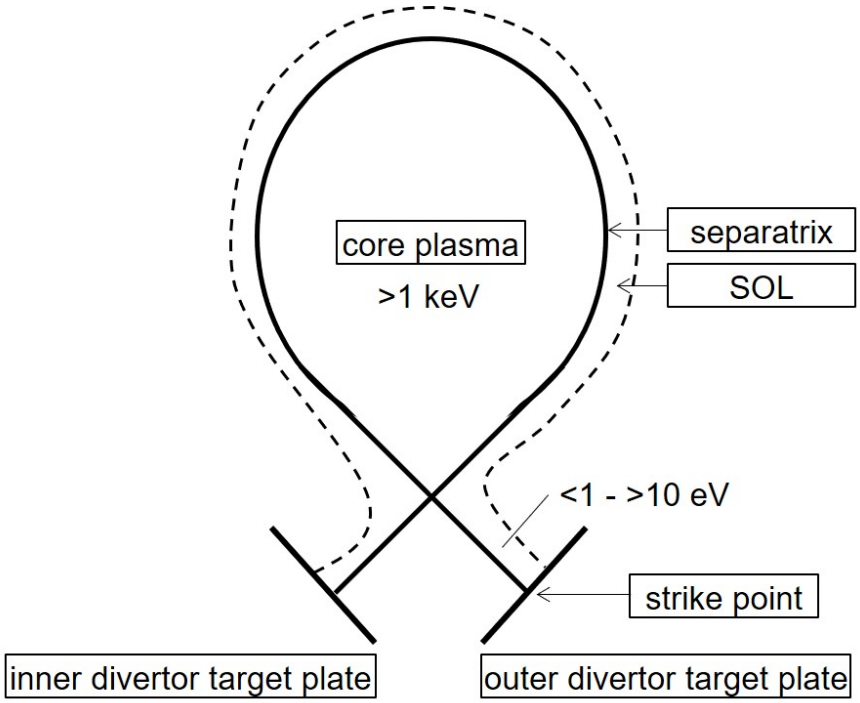

Figure 2.8: *Schematic of a poloidal cross section for a tokamak plasma.*

The aim of the divertor concept is to minimize the impurity content of the plasma (by having the plasma-surface interaction remote from the confined plasma), to design the particle flow towards the divertor (so that the impurities produced at the target cannot enter the confined region) and to remove the helium ash from fusion reactions (so that the reacting fuel is not diluted) [65]. In divertor discharges an operating regime with improved particle and energy confinement (called H-mode) can be achieved by increasing the input power starting from a conventional operational regime, the low-confinement mode (called L-mode) [66].

Among the key issues of plasma physics for a fusion power plant is *plasma exhaust* [1]: Since the power densities deposited at the divertor plates tend to be unacceptably high for reactor conditions (e.g. $150\,\mathrm{MW/m^2}$ [67]), attempts are made to achieve detached plasma regimes, in which the plasma partially detaches from the surface (so that a buffer layer of neutrals isolates the hot plasma from the surface), resulting in reduced erosion and melting of the edge structure [2]. The power reaching the edge can be dissipated by volumetric processes (e.g. radiation of hydrogen and impurities or charge transfer with hydrogen neutrals). Detachment can be achieved by increasing the plasma (electron) density in the midplane (upstream in the chamber) [2]. As a consequence, the power is deposited over large areas instead of being restricted to a small plasma wetted area.

Relevance of molecules for divertor detachment

Three different regimes of divertor operation are distinguished that depend not only on the main plasma parameters, but also on the divertor geometry [68].

The *low recycling regime* (or sheath-limited regime) is characterized by a linear dependency of the target density n_t on the upstream density n_u ($n_\mathrm{t} \propto n_\mathrm{u}$), while T_e at the target is $> 10\,\mathrm{eV}$ (with $T_\mathrm{e} > T_\mathrm{ion}$) [2]. The plasma is fully attached to the divertor plates.

An increase in the midplane density results in an increased upstream density and a decreased upstream temperature [3]. In the *high recycling regime* (or conduction-limited regime) the plasma temperature near the divertor target is lower, but the plasma is still attached and the possible overheating of the target is not yet solved [2]. The target density scales at least quadratic with the upstream density and large neutral densities are observed near the divertor [2]. The divertor plasma is sufficiently dense, so that the hydrogen particles in the divertor undergo several cycles of ionization in the divertor volume and subsequent neutralization on both the divertor targets or in the volume before they are pumped out or absorbed by the target material [69].

For further increasing upstream density the plasma starts to detach. The defining feature of the *detached regime* is the peaking and subsequent decrease (called rollover) of the ion saturation current while the H_α line radiation from the target regions continues to increase with n_e in the divertor region [2]. Typical features also include the rollover of the plasma flux on the target with increasing plasma density [70] accompanied by a large plasma pressure drop and low plasma temperatures in front of the target [69], and the high energy radiation losses from the SOL [71]. Due to the low temperature in the divertor plasma, the plasma bears resemblance to low-pressure laboratory plasmas and due to the high electron densities, the assumption of a Maxwellian electron EDF is typically justified [3].

Divertor detachment does not usually occur over the entire target and simultaneously in both the inner and outer divertors. Instead, the inner divertor usually detaches first, while the outer divertor detachment starts locally near the strike point [69]. Therefore, the outer divertor is usually the subject of detachment studies. For a more detailed description of divertor detachment see e.g. [72, 73].

Simple models like the closed-box approximation [74] demonstrate that two reasons for the rollover are likely: An increase in the impurity radiation and a progressive increase in the volumetric plasma recombination along with decreasing plasma temperature. In experiments both rollover mechanisms can work simultaneously [70]. However, while impurity radiation losses require relatively

high plasma temperatures of $\geq 10\,\mathrm{eV}$, radiative recombination and three body recombination (EIR), mostly of H^+, occur effectively only at temperatures below $1\,\mathrm{eV}$ [69]. For temperatures above $1\,\mathrm{eV}$ processes involving neutral molecules can be important for the plasma recombination.

The presence of neutral molecules in the divertor plasma gives rise to *molecular activated (assisted) recombination* (MAR). Several MAR channels can be distinguished. First, Proton Charge Transfer can be followed by Radiative Recombination

$$\begin{aligned} H_2(v) + H^+ &\rightarrow H_2^+ + H \\ H_2^+ + e^- &\rightarrow H + H. \end{aligned} \tag{2.72}$$

Second, Dissociative Electron Attachment can be followed by Mutual Neutralization

$$\begin{aligned} H_2(v) + e^- &\rightarrow H^- + H \\ H^- + H^+ &\rightarrow H + H. \end{aligned} \tag{2.73}$$

A third possible channel involves the formation and destruction of H_3^+ [75]

$$\begin{aligned} H_2 + H_2^+ &\rightarrow H_3^+ + H \\ H_3^+ + e^- &\rightarrow H_2 + H \text{ or } H + H + H. \end{aligned} \tag{2.74}$$

Due to the typically low H^- lifetime and small H_3^+ production yield for divertor conditions, the first channel has the highest relevance. Furthermore, the neutral molecules can undergo competing processes that do not contribute to the recombination: *Molecular Assisted Dissociation* (MAD) and *Molecular Assisted Ionization* (MAI). For MAD, Proton Charge Transfer is followed by electron collision induced dissociation of H_2^+:

$$\begin{aligned} H_2(v) + H^+ &\rightarrow H_2^+ + H \\ H_2^+ + e^- &\rightarrow H + H^+ + e^-. \end{aligned} \tag{2.75}$$

For MAI, Proton Charge Transfer is followed by electron collision induced dissociative ionization of H_2^+:

$$\begin{aligned} H_2(v) + H^+ &\rightarrow H_2^+ + H \\ H_2^+ + e^- &\rightarrow H^+ + H^+ + e^- + e^-. \end{aligned} \tag{2.76}$$

The relevance of MAI is typically negligible compared to MAR and MAD [76]. Note that molecules affect not only the plasma particle balance, but also the plasma momentum and power balance (e.g. momentum and energy are transferred to the molecules through elastic scattering of ions with recycled neutral molecules).

The effective MAR rates for the first two MAR channels (see 2.72 and 2.73) estimated in [77] are maximal for temperatures just above 1 eV. Numerous experiments (e.g. [78]) and simulations (e.g. [79]) have demonstrated that MAR can significantly contribute to the volumetric recombination of divertor plasmas. However, note that the simulations for effective MAR rates have been partially performed based on reaction probabilities derived from scaling laws. These statements may deviate for specifically selected state-of-the-art reaction data and current CR models and must be re-examined. For this purpose, benchmarked CR models are required, such as those developed within the scope of this work.

3 Plasma experiments and codes

In order to benchmark CR models, both the plasma parameters and the excited state population densities (via their emission) should be known from experiment. The population densities and plasma parameters from the measurements are compared with the population densities predicted by the model depending on the plasma parameters. Since different diagnostics give access to different quantities, typically several diagnostics have to be applied simultaneously. Furthermore, CR models should be benchmarked ideally across a wide operational space of plasma parameters. For this purpose, different plasma regimes need to be accessed at different experimental facilities.

In the following, the basic principles of diagnostics that are typically used to gain insights into the plasma parameters are discussed: These include optical emission spectroscopy, Langmuir probes and the laser diagnostics Thomson scattering, TALIF and CARS. Subsequently, several plasma experiment facilities and the measurements performed on them are described. The plasma parameters determined are later used for benchmarking purposes. The chapter concludes with an introduction to several codes that are relevant for the construction of the population models and benchmarking them.

3.1 Diagnostics

3.1.1 Optical emission spectroscopy

Optical emission spectroscopy (OES) is a non-invasive method for measuring the line-integrated, spectrally resolved plasma emission intensity. With the aid of atomic and molecular emission theory, it is possible to determine a vast number of population densities, particle densities and temperatures from the measured emission [24].

The experimental setup is rather simplistic consisting typically of an optical port, the fiber optics, a spectrometer and a detector. The spectrometer itself consists for instance of an entrance slit, a grating as a dispersion element, an

imaging mirror and an exit slit. The light from the slit parallel to the grooves of the grating is reflected. Thereby, the periodic structure of the grating behaves like a set of coherent sources forming secondary wavelets that interfere constructively and destructively depending on the wavelength and angle. As a consequence, one observes a spectrum at the detector plane [21]. The grating is characterized by the number of grooves per millimeter which influences the spectral resolution. The blaze angle of the grating sets the wavelength range with highest reflection efficiency and thus the sensitivity of the grating. The focal length of the spectrometer impacts the spectral resolution. Together with the size of the grating it defines the aperture and thus the light throughput. The width of the entrance slit influences the light throughput as well: the larger the entrance slit, the higher the intensity and the lower the spectral resolution. For the detector usually photomultipliers or charge coupled device (CCD) arrays are used. For the former, the width of the exit slit and for the latter the pixel size limit the spectral resolution of the system. The choice of detector entirely determines the temporal resolution of the system [24].

The wavelength calibration of the spectroscopic system can be performed using spectral lamps with known wavelengths of the lines emitted by the lamp. The intensity calibration can be performed relatively or absolutely: While a relative calibration solely accounts for the spectral sensitivity of the spectroscopic system along the wavelength axis, an absolute calibration links the measured signal (e.g. counts) with the emission intensity (e.g. $Ph/(m^3\,s)$). The absolute calibration is performed with a light source of known spectral radiance (e.g. Ulbricht sphere) [24].

For a more extensive description of spectroscopic systems see standard textbooks, such as e.g. [21]. The rather simple OES measurements require for quantitative analyses a complex interpretation, which is discussed below.

Boltzmann plot technique

The Boltzmann plot technique can be used to determine the rotational temperature, when fully resolved rotational lines are recorded [62].

Since the line emission intensity of a ro-vibrational level follows

$$I_{(N'\Lambda'_{\sigma'},v',N')(N''\Lambda''_{\sigma''},v'',N'')} \propto g_I(N'\Lambda'_{\sigma'},v',N')S_{\mathrm{P,Q,R}}(N'\Lambda'_{\sigma'},v',N')\exp\left(-\frac{E(N'\Lambda'_{\sigma'},v',N')-E(N'\Lambda'_{\sigma'},v',N'=1)}{k_{\mathrm{B}}T_{\mathrm{rot}}(N'\Lambda'_{\sigma'},v')}\right), \tag{3.1}$$

with the nuclear spin degeneracy g_I and the Hönl-London factor $S_{\mathrm{P,Q,R}}(N')$[23], the rotational temperature of the emitting excited state can be derived via the

slope of a linear fit by plotting $\ln(I/(g_I S))$ for the first rotational lines against $\Delta E_{\mathrm{rot}}(N')$.

The rotational temperature of the electronic and vibrational ground state can be derived from the rotational temperature of the excited state (deduced from the Boltzmann plot) via the ratio of the rotational constants $B_v(N\Lambda_\sigma, v)$ (see e.g. [80]) of these states [62]. If for instance the Fulcher-α band emission is measured and used to derive $T_{\mathrm{rot}}(d^3\Pi_{\mathrm{u}}^-, v')$, the rotational temperature in the ground state $X^1\Sigma_{\mathrm{g}}^+(v=0)$ is accessible via:

$$T_{\mathrm{rot}}(X^1\Sigma_{\mathrm{g}}^+, v=0) = \frac{B_v(X^1\Sigma_{\mathrm{g}}^+, v=0)}{B_v(d^3\Pi_{\mathrm{u}}^-, v')} T_{\mathrm{rot}}(d^3\Pi_{\mathrm{u}}^-, v'). \tag{3.2}$$

The rotational levels of the electronic ground state thermalize with the heavy particles, since the energy differences between rotational levels are so small that the energy transfer by collisions with gas particles suffices for excitation and hence it is usually observed that the determined $T_{\mathrm{rot}}(X^1\Sigma_{\mathrm{g}}^+, v=0)$ corresponds to the gas temperature T_{gas} [81]. In [82] it was demonstrated that the resulting $T_{\mathrm{rot}}(X^1\Sigma_{\mathrm{g}}^+, v=0)$ can differ depending on which v' is used for the back-projection and that the best agreement with an independently determined gas temperature is obtained from $v'=2$ for $\mathrm{H}_2(d^3\Pi_{\mathrm{u}}^-)$.

Comprehensive approach for the ro-vibrational population

In chapter 2 it has been discussed that a two-temperature distribution of the ro-vibrational level population densities (equation 2.71) is often observed in low-pressure, low-temperature plasmas. In order to evaluate the rotational and vibrational temperatures accounting for the two-temperature distribution and to estimate the total band emission based on upscaling the Q-line emission for the Fulcher-α band transition, a comprehensive approach is proposed in [61] and summarized below:

In equation 2.71, the quantities $\tilde{n}_{\mathrm{vib}}$ and $\tilde{n}_{\mathrm{rot}}$ are expressed as

$$\tilde{n}_{\mathrm{vib}} = \frac{n(v', T_{\mathrm{vib\,1}})}{\sum_{v'} n(v', T_{\mathrm{vib\,1}})} \text{ with } n(v', T) = \exp\left(-\frac{E(v') - E(v'=0)}{k_{\mathrm{B}} T}\right) \tag{3.3}$$

and

$$\tilde{n}_{\mathrm{rot}} = \frac{n(v', N', T_{\mathrm{rot}})}{\sum_{N'} n(v', N', T_{\mathrm{rot}})} \text{ with } n(v', N', T) = g_I g \exp\left(-\frac{E(v', N') - E(v', N'=1)}{k_{\mathrm{B}} T}\right), \tag{3.4}$$

whereby g represents the statistical weight equal to $(2N'+1)$. In the comprehensive approach, the parameters T_{vib}, $T_{\mathrm{rot\,1}}$, $T_{\mathrm{rot\,2}}$ and β are deduced by varying them, projecting the resulting ro-vibrational distribution of the $X^1\Sigma_g^+$ state into the $d^3\Pi_u^-$ state and matching the predictions with spectroscopic measurements of the experimental accessible first four vibrational levels of $d^3\Pi_u^-$. For the upward projection, vibrationally resolved electron impact excitation rate coefficients are used (assuming that the rotational excitation remains unchanged during the excitation). Since the rate coefficients depend on the electron temperature, T_e is required as additional input for the evaluation.

The indirect deduction of the parameters is performed in an iterative scheme: In a first step, a simultaneous least-square fit of the measured and projected rotational population in the first four vibrational levels of $d^3\Pi_u^-$ (from which the measured Q-lines originate) is performed by variation of $T_{\mathrm{rot\,1}}$, $T_{\mathrm{rot\,2}}$ and β in $X^1\Sigma_g^+$ for fixed T_{vib}. In a second step, the summation over the rotational population in each vibrational level of $d^3\Pi_u^-$ is performed, the respective vibrational distribution is normalized to $d^3\Pi_u^-(v'=0)$ and the result is compared to predictions by a simple corona model for the Fulcher-α band to deduce T_{vib}. The obtained value of T_{vib} is used as input for the first step and the procedure is repeated until convergence is achieved. Form the converged results of the relative ro-vibrational population of the $d^3\Pi_u^-(v'=0,1,2,3)$ and the absolute intensity of the Q1 emission lines, the absolute emission intensity of the four diagonal vibrational transitions with Δv=0 is determined. This emission intensity of the four diagonal vibrational transitions is multiplied by an upscaling factor from a simple population model (depending on the ro-vibrational population and the electron temperature between the values 1.08 and 6.5) to obtain the full Fulcher-α emission intensity (comprising P-branch, R-branch transitions and Q-branch transitions with $\Delta v \neq$0).

OES evaluation utilizing the *Yacora H model*

The plasma parameters T_e, n_e, n_H, n_{H_2}, n_{H^+}, $n_{H_2^+}$, $n_{H_3^+}$ and n_{H^-} can be obtained from the measured line emission intensities of the Balmer lines and the Fulcher-α band emission using the *Yacora H model* and a CR model for H_2 from [59, 83, 84]. The *Yacora H model* is a CR model for atomic hydrogen coupled to different heavy particle species that accounts for Electron Impact (De-)Excitation, Spontaneous Emission, Atomic Ionization, Recombination of H^+, Dissociation of H_2 and H_2^+, Dissociative Recombination of H_2^+ and H_3^+, Mutual Neutralization of H^- with H^+, H_2^+ and H_3^+ and Optical Thickness.

Since the plasma conditions (characterized by the respective plasma parameters)

determine the reaction rates and excited state densities (from which emission is emitted), the plasma parameters can be deduced from the strengths of the first five Balmer lines, the Fulcher-α band and the respective ratios. The particle densities used as input for the CR model are varied iteratively until the emission and emission ratios predicted by the models match the measurements within a selected uncertainty bar. Adequate initial values can simplify the procedure. Therefore, a starting value for the density of the hydrogen neutrals is estimated from the filling pressure (using the ideal gas law and T_{gas} determined with the comprehensive approach) and the gas composition of the experiment. The neutral densities determined can further be varied, since other effects (e.g. neutral depletion, see below) can occur. Prior knowledge of the typical dissociation degree is further helpful, but not necessary. If measurements are available for fewer than the first five Balmer lines, the result will typically have a high uncertainty bar due to the many unknowns.

Note that this evaluation determines T_{e} (among other quantities) and relies besides the Balmer line emission on the total Fulcher-α band emission (e.g. determined with the comprehensive approach). The comprehensive approach relies again on T_{e}. Therefore, these two evaluation schemes have to be applied iteratively to obtain self-consistent results.

$\mathbf{T_H}$ from the broadening of Balmer lines

The temperature of atomic hydrogen T_{H} can be deduced for highly resolved spectra (e.g. apparatus function in the magnitude of 10 pm) from the shape of the line profile of the measured Balmer lines. The following scheme is applicable, if the true line profile is mainly determined by natural and Doppler broadening and described by means of the Balmer-α transition: Due to the fine structure, the H_α transitions consists of the 7 constitutional transitions summarized in table 3.1.

The individual line transitions between the fine structure levels of the upper state and the fine structure levels of the lower state experience natural broadening according to equation 2.19, Doppler broadening according to equation 2.20 and broadening due to the apparatus function. The broadened line shape for each constitutional transition is the result of the convolution between the Lorentzian profile from natural broadening and the Gaussian profile from Doppler broadening and the apparatus function. The measured line profile is the sum of the individual line transitions between the fine structure levels. Lookup tables for the full width at half maximum (FWHM) from [86] are calculated based on these effects in dependence on varying T_{H} and different values of the apparatus function.

Table 3.1: *Fine structure components of the Balmer-a transition according to [85].*

upper state	lower state	wavelength [nm]
$3^2D_{3/2}$	$2^2P_{1/2}$	656.27097
$3^2P_{3/2}$	$2^2S_{1/2}$	656.272483
$3^2S_{1/2}$	$2^2P_{1/2}$	656.275181
$3^2P_{1/2}$	$2^2S_{1/2}$	656.277153
$3^2D_{5/2}$	$2^2P_{3/2}$	656.285177
$3^2D_{3/2}$	$2^2P_{3/2}$	656.286734
$3^2S_{1/2}$	$2^2P_{3/2}$	656.290944

The apparatus function can be approximately determined from spectroscopically closely spaced rotational lines of the Fulcher-α band, if it is known that apparatus broadening is the major broadening mechanism for these lines. By comparing the FWHM from the measured line profile with the lookup tables, T_H (for the excited state $n = 3$ state from which Balmer-α emission originates) can be deduced.

3.1.2 Langmuir probes

Langmuir probes represent a widely used intrusive diagnostic suited for spatially resolved measurements of n_e, T_e and the electron EDF. These probes are based on the pioneering works of Langmuir and Mott-Smith [87, 88]. A modern review is given in [89].

In the simplest form, a Langmuir probe consists of a single electrode that is inserted into a plasma. A variable voltage is applied to the probe with respect to the plasma vessel, the resulting current is measured and thus a current-voltage characteristic is obtained. The measured signal can be interpreted based on the theory of the electrostatic sheath that is established at the surface of the probe. With a sufficiently negative probe bias, all electrons are repelled and the measured, so-called *ion saturation current* (that would be independent of the voltage) can be linked to the ions. The *floating potential* is the potential at which the probe would float if it were electrically isolated. If an external potential is applied, the floating potential can be determined by the applied potential with a resulting net current of zero. When the probe potential equals the *plasma potential*, there is no sheath electric field and electron saturation is reached. Hence, the electrons flow to the probe surface with a thermal velocity distribution. The plasma potential characterizes the potential at which all charged particles reach the probe surface

without being accelerated or retarded [65].

The electron EDF can be determined from the second derivative of the current-voltage characteristic according to the Druyvesteyn formula [90]. The electron temperature T_e can be deduced from the slope of the current-voltage characteristic near the floating potential [91]. The electron density n_e is usually derived either from the ion saturation current assuming a Maxwellian electron EDF or the integral of the electron EDF [91].

3.1.3 Laser diagnostics

Thomson Scattering

Thomson scattering is a non-intrusive, spatially resolved laser diagnostic for measuring typically n_e and T_e.

A laser beam (e.g. Nd:YAG laser with <1 J) is scattered by electrons in the plasma, since they are accelerated as charged particles by the oscillating field of the electromagnetic beam [92]. Due to the velocity of the electrons, the re-radiated light is Doppler shifted and for incoherent scattering on an ensemble of electrons the spectrum obtained resembles the electron velocity distribution, from which T_e and n_e can be derived.

For collective Thomson scattering the electron density fluctuations on the scale of the Debye length can be observed that again are correlated with the movements of the ions and thus the ion temperature and ion velocity are accessible [93].

Due to the cumbersome alignment and challenges emanating from stray light, Thomson scattering is not available as a standard diagnostic.

For a more extensive description see standard textbooks, such as e.g. [92].

TALIF

Two-photon laser-induced fluorescence (TALIF) spectroscopy [94] is a non-intrusive optical diagnostic that can be applied to measure atomic ground state densities and temperatures. For atomic hydrogen, as an example, typically two photons of the wavelength 205 nm are absorbed simultaneously by the atomic hydrogen ground state, exciting it to the $n = 3$ state. The excited atom subsequently decays to the $n = 2$ state by fluorescent emission of a photon with the wavelength ≈ 656 nm (H_α emission) that is recorded [95]. The preference for two photons over one photon with half the wavelength is due to the fact that photons in the latter case have energies in the vacuum UV range and therefore necessitate an experimental setup involving vacuum equipment.

In calibrated systems, the measured H_α signal can be linked to the atomic hydrogen ground state density. The shape of the line profile yields information on the atomic hydrogen EDF and thus on T_H [96].

The calibration can be performed based on comparative measurements at a spectrally close two-photon resonance of a noble gas (e.g. krypton) with known density [97].

Owing to its complex setup, this diagnostic is typically not used as standard diagnostic.

CARS

Coherent Anti-Stokes Raman Scattering (CARS) is a non-intrusive optical diagnostic to determine the population density of specific quantum states, such as vibrational levels of the electronic ground state of H_2. Due to its very demanding setup and the need of a tunable laser, this diagnostic is typically only rarely available.

Two collinear light beams with the frequencies ω_L and ω_S ($\omega_\mathrm{L} > \omega_\mathrm{S}$) are employed to traverse a sample with a Raman active vibrational mode of frequency $\omega_v = \omega_\mathrm{L} - \omega_\mathrm{S}$. Thus, a new wave is generated with the frequency $\omega_3 = \omega_\mathrm{L} + (\omega_\mathrm{L} - \omega_\mathrm{S})$. This new wave stems from inelastic scattering of the wave with ω_L by molecular vibrations that are coherently driven by the waves with ω_L and ω_S. It is thus possible to perform quantum state-selected population density measurements by scanning the frequency ω_S with fixed ω_L and monitoring the signal amplitude at ω_3 [98].

3.2 Plasma experiment facilities

3.2.1 PlanICE (RF discharge)

The Planar Inductively Coupled Experiment *PlanICE* located at Augsburg University consists of a cylindrical stainless steel vessel of round profile (diameter 15 cm, height 10 cm). Plasma is created by inductive coupling of radio-frequency (RF) power (RF frequency 2 MHz, maximal power 2 kW) through a planar coil on the top of the vessel, inducing a magnetic field in radial-axial direction surpassing a dielectric window and an electric field in azimuthal direction, opposite to the coil current [57]. Both the vessel and a chamber containing the RF coil are pumped resulting in background pressures about 10^{-4} Pa. A matching network

consisting of two tunable capacitors adapting the overall impedance is used to achieve efficient power transfer from the generator to the discharge.

A schematic of *PlanICE* is depicted in figure 3.1. Quartz windows in radial direction give access to emission spectroscopy in the optical range. The Acton SP2750 spectrometer (1 800 lines/mm, CCD detector, Gaussian apparatus profile depending on the wavelength with FWHM $16 - 22$ pm) is calibrated with an Ulbricht sphere. A RF compensated Langmuir probe (compensating RF oscillations of the floating potential [99]) is radially movable through further vessel ports.

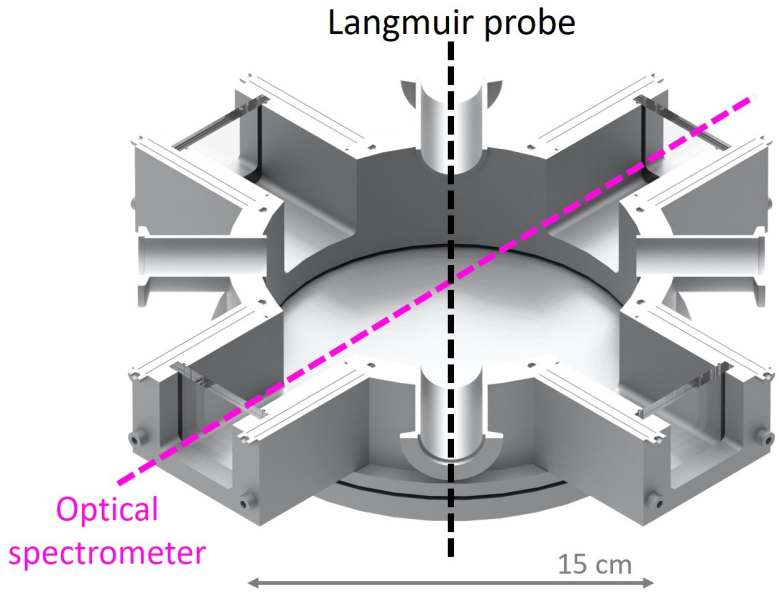

Figure 3.1: *Schematic cutaway view of the planar inductively coupled plasma experiment PlanICE and the position of the movable Langmuir probe and the spectroscopic line of sight.*

Within the scope of the work of [100], systematic measurements in hydrogen plasmas were performed varying the pressure between $1.1 - 10$ Pa at a constant RF power of 700 W. For each achieved pressure value the Langmuir probe was moved radially and measurements were conducted, observing T_e profiles constant over the radius that decrease close to the wall and n_e Bessel-shaped profiles. The spatially resolved T_e and n_e measurements were then averaged to mimic line of sight-based measurements, giving rise to uncertainty bars for the parameters from the standard deviation of the averaging. Furthermore, OES measurements of ro-vibrationally resolved Fulcher-α lines were performed and evaluated using the comprehensive approach discussed in chapter 3.1.1, revealing the typical two-temperature distribution of the electronic ground state $X^1\Sigma_\mathrm{g}^+$. n_{H_2} was derived from the filling pressure utilizing the ideal gas law. Table 3.2 summarizes the

plasma parameters determined from the measurements. Note that due to the height of the degree of ionization the assumption of a Maxwellian electron EDF is justified.

These measurements are compared in the chapters 4.1 and 4.3 to model predicted $d^3\Pi_u$ population densities and in chapter 4.4 to benchmark the rotational structure prediction of the corona model.

Table 3.2: *Plasma parameters determined at PlanICE from the pressure variation at constant input power P_{RF}=700 W.*

p [Pa]	T_e [eV]	n_e [m^{-3}]	T_{gas} [K]	T_{vib} [K]	$T_{rot\,2}$ [K]	β	n_{H_2} [m^{-3}]
1.1	8.8±0.7	(1.8±0.5) 10^{16}	500	4250	7565	0.14	$1.59 \cdot 10^{20}$
3	5.2±0.5	(1.9±0.4) 10^{16}	600	4500	6450	0.17	$3.65 \cdot 10^{20}$
5	4.2±0.2	(2.1±0.2) 10^{16}	630	4500	5960	0.15	$5.74 \cdot 10^{20}$
7	3.3±0.3	(2.4±0.4) 10^{16}	640	4000	5125	0.12	$7.89 \cdot 10^{20}$
10	2.7±0.2	(2.8±0.5) 10^{16}	670	3500	4830	0.08	$1.08 \cdot 10^{21}$

3.2.2 ECR discharge

The electron cyclotron resonance (ECR) reactor located at Augsburg University consists of a cylindrical vessel (diameter 15 cm, height 56 cm) with a glass plate separating a vacuum chamber from a chamber for microwave input coupling. The vessel is pumped continuously and the pressure is adjusted by the flow rate of an input gas resulting in typical pressures of $2 - 20$ Pa. A magnetron source at frequency 2.45 GHz supplies 100 W microwave power that is fed into the reactor via a coaxial transmission and a rod antenna. The reactor acts as cavity resonator and the top plate is movable in height to adapt the cavity. Cobalt samarium magnets below the base plate generate an inhomogeneous magnetic field (87.5 mT at a height of 1 cm above the base plate) orientated perpendicular to the electric field of the microwave [101]. The gyration frequency of the electrons propagating around the magnetic field lines is in this region in resonance with the microwave frequency ($2\pi f = eB/m_e$) [57]. The plasma is mainly produced there and spreads by diffusion and drifts in the inhomogeneous field [101].

The size of the plasma usually is smaller than the size of the chamber. Therefore, the plasma can change its size with changing input power, whereas n_e remains constant. Diagnostic windows are situated 3 cm above the bottom plate, where the magnetic field is negligible. Hence, the particle motion in this region is

dominated by diffusion and it can be assumed that the plasma is homogeneous in this area [3].

Within the scope of the work [102], a SPEX spectromter in Czerny-Turner configuration (focal length 1 m, 1 200 lines/mm, CCD detector) was used to study hydrogen-helium plasmas. Helium was added to achieve plasmas with increased T_e. The spectrometer was absolutely calibrated with a tungsten lamp. Ro-vibrational emission lines of the molecular hydrogen transition bands $B^1\Sigma_u^+ \rightarrow X^1\Sigma_g^+$, $C^1\Pi_u \rightarrow X^1\Sigma_g^+$, $GK^1\Sigma_g^+ \rightarrow B^1\Sigma_u^+$ and $I^1\Pi_g \rightarrow B^1\Sigma_u^+$ were measured and evaluated with the Boltzmann plot technique. The derived rotational temperatures were used to upscale the line emission from individual measured lines, in order to deduce the total band emission and thus the total population densities of the electronic states $B^1\Sigma_u^+$, $C^1\Pi_u$, $GK^1\Sigma_g^+$ and $I^1\Pi_g$. The gas temperature was determined to be T_{gas}=450±50 K from measurements of nitrogen bands. The electron density was determined to be $n_e = 1 \pm 10^{17}\,m^{-3}$ by means of interferometry and probe measurements. The electron temperature T_e (varying with the pressure and gas composition) was derived from the helium emission. The pressure was varied between $4 - 18$ Pa, resulting in electron temperatures between $1.8 - 3.8$ eV. Table 3.3 summarizes the plasma parameters of the measurements. The neutral molecular hydrogen density is derived from the filling pressure and the gas composition utilizing the ideal gas law. Note that due to the height of the degree of ionization the assumption of a Maxwellian electron EDF is justified.

Table 3.3: *Plasma parameters determined at the ECR experiment for varying pressure and gas composition.*

p [Pa]	(H_2:He)	T_e [eV]	n_e [m^{-3}]	T_{gas} [K]	n_{H_2} [m^{-3}]
18	(0.9:0.1)	1.77±0.09	(1±0.05) 10^{17}	450±50	2.35-2.93 10^{21}
10	(0.9:0.1)	2.15±0.17	(1±0.05) 10^{17}	450±50	1.3-1.63 10^{21}
4	(0.9:0.1)	3.07±0.25	(1±0.05) 10^{17}	450±50	5.22-6.52 10^{20}
10	(0.1:0.9)	3.43±0.34	(1±0.05) 10^{17}	450±50	1.45-1.81 10^{20}
10	(0.05:0.95)	3.77±0.41	(1±0.05) 10^{17}	450±50	7.25-9.06 10^{19}

These measurements are utilized in chapter 4.1 for comparison of model predicted excited state population densities.

3.2.3 BATMAN Upgrade (BUG)

BATMAN Upgrade (BAvarian Test MAchine for Negative ions, UpGrade (BUG)) located at the Max Planck Institute for Plasma Physics is a test facility using the prototype negative ion source for the neutral beam injection at ITER [103]. ITER [104] is the world's largest tokamak currently under construction. A schematic cutaway view of BUG is shown in figure 3.2.

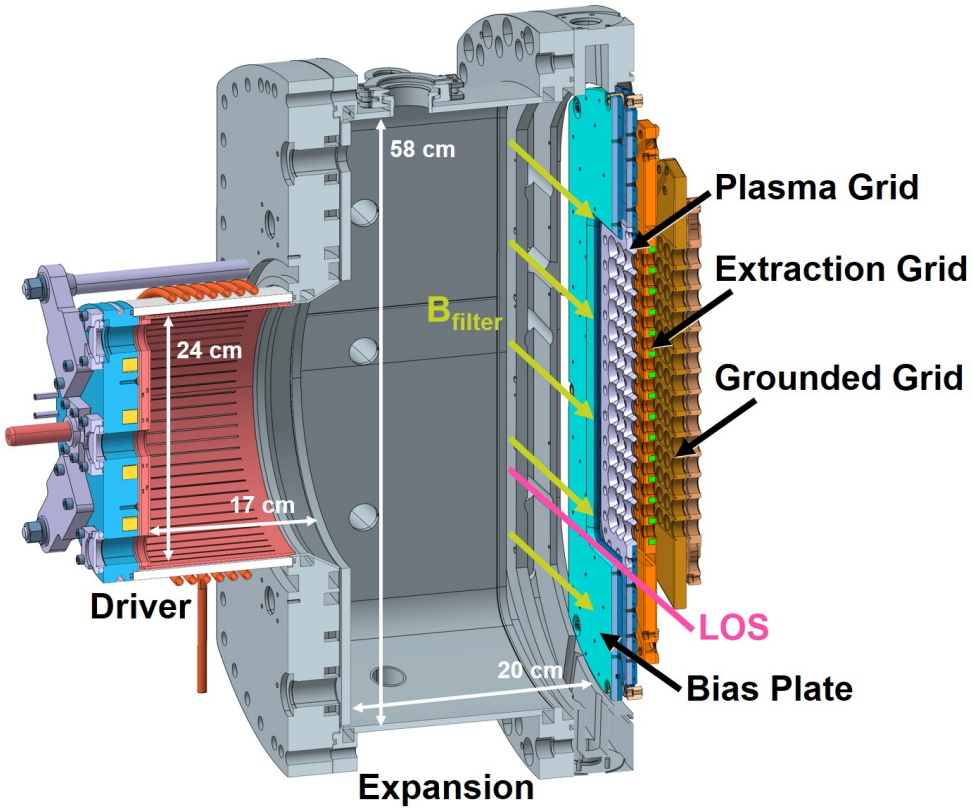

Figure 3.2: *Schematic of the ITER prototype negative ion source BATMAN Upgrade.*

At BUG the plasma is generated via inductive RF coupling (driving frequency 1 MHz, RF power up to 100 kW) in the so-called driver. The driver itself consists of a cylindrical dielectric vessel (diameter 24 cm, length 17 cm) with a Faraday screen between the plasma and the dielectric to avoid capacitive RF coupling and plasma erosion of the dielectric.

The plasma expands into the expansion region with a length of about 20 cm from the driver exit towards the extraction system. The extraction system is a grid system consisting of the plasma grid, the extraction grid (with embedded permanent magnets to deflect co-extracted electrons) and the grounded grid.

Caesium is evaporated from an oven located at the backplate, in order to

maintain a low work function at the plasma grid surface and hence to produce negative hydrogen ions by surface recombination processes [105].

The bias plate surrounds the plasma grid. Positive voltage can be applied to the plasma grid with respect to the bias plate and the source walls with the aim to reduce the amount of co-extracted electrons.

A magnetic filter field of a few mT (magnetizing the electrons but not the ions) is created in front of the plasma grid via a current of several kA flowing in vertical direction through it. A current of 1 kA amounts to a peak field value of 2.1 mT at 2 cm distance to the plasma grid. The magnetic filter field reduces the electron temperature and the electron density and thus the amount of co-extracted electrons as well as the destruction rate of negative ions by electron collisions [106]. Furthermore, the magnetic field causes a plasma drift in vertical direction.

The plasma pressure can deviate from the filling pressure (the gas pressure before ignition of the plasma) [107] for instance due to neutral depletion (the decrease of neutral gas density for high plasma density) [108].

For the ITER relevant filling pressure of 0.3 Pa, typically an ionizing plasma with $n_e \approx 10^{18}\,m^{-3}$ and $T_e \approx 10\,eV$ is observed in the driver. Contrarily, a recombining plasma with $n_e < 10^{18}\,m^{-3}$ and $T_e < 10\,eV$ is usually present in front of the plasma grid [109]. Utilizing OES T_{vib} was determined to be $3000 \pm 500\,K$ [81] independent of the magnetic filter field strength [81] and T_{gas} was determined to increase from 650 K at 0.3 Pa filling pressure to 820 K at 0.6 Pa (with no sensitivity to the magnetic filter field strength) [109]. A reasonable estimate for the positive ion contribution is 40% n_{H^+}, 40% $n_{H_2^+}$ and 20% $n_{H_3^+}$ [99].

For more details of recent progress and challenges in negative NBI development see [110, 111].

Measurements of the Fulcher-α band and the Balmer series have been performed within the scope of the work [81] using the bottom line of sight parallel to the plasma grid at a distance of 2.6 cm (shown in figure 3.2) and an absolutely calibrated Acton spectrometer (focal length 0.75 m, 1 800 lines/mm, CCD detector, Gaussian apparatus profile with FWHM < 20 pm) with no caesium present.

The measurements [102] are analyzed using the comprehensive approach to determine T_{vib} and T_{gas} and the *Yacora H model* to obtain the particle densities and T_e. T_H is determined from the broadening of the H_α line. The parameters evaluated for the measurement via the bottom line of sight close to the plasma grid for discharges with $p = 0.3\,Pa$, $P_{RF} = 40\,kW$ and PG current $I_{PG} = 1\,kA$ are summarized in table 3.4. T_{vib} is determined to be $3\,000 \pm 500\,K$. In chapter 4.2 the parameters from table 3.4 are used as input to a CR model to self-

consistently predict the vibrational population of the electronic ground state $X^1\Sigma_g^+$ and thus T_{vib}.

Table 3.4: *Plasma parameters determined at BUG for filling pressure p =0.3* Pa, *input power* P_{RF}*=40* kW *and* I_{PG} *=1* kA.

T_e [eV]	T_H [K]	T_{gas} [K]
2.5	8 000	640

n_e [m^{-3}]	n_H [m^{-3}]	n_{H_2} [m^{-3}]	n_{H^+} [m^{-3}]	$n_{H_2^+}$ [m^{-3}]	$n_{H_3^+}$ [m^{-3}]	n_{H^-} [m^{-3}]
$3.3 \cdot 10^{16}$	$7.3 \cdot 10^{18}$	$3.3 \cdot 10^{19}$	$1.5 \cdot 10^{16}$	$1.5 \cdot 10^{16}$	$3 \cdot 10^{15}$	10^{15}

3.2.4 Magnum-PSI

Linear devices are suited to simulate scrape off layer and divertor plasmas. Therefore, they are used to investigate edge plasma physics and the plasma material interaction in magnetically confined fusion devices [75].

The linear plasma generator *Magnum-PSI* [112] is located at the Dutch Institute For Fundamental Energy Research (DIFFER). The machine is unique in its ability to simulate ITER-relevant particle fluxes and heat loads.

The plasma is produced by a wall stabilized DC cascaded arc plasma source [113]. The source emits plasma into a vacuum vessel (consisting of the heating chamber and the target chamber) and a strong magnetic field (up to 2.5 T) confines the plasma into an intense plasma beam that is directed to the surface of a target mounted on a movable holder. The magnetic field is generated from superconducting NbTi magnets. The cascaded arc source can be operated in steady state and pulsed mode (utilizing a capacitor bank) to study power transients similar to *edge localized modes (ELMs)* [114]. The neutral pressure can be adapted by adjusting the speed of three pumps and by gas seeding into the target chamber (typically achieving background pressures <1 Pa). Thus, the plasma conditions can represent attached as well as detached divertor configurations. Both the position and inclination angle of the movable target holder can be changed with respect to the plasma beam [115].

Typical electron densities and temperatures are $n_e = 10^{19} - 10^{21}\,m^{-3}$ and $T_e = 0.1 - 10\,eV$. A full list of the design parameters is given in [116].

Radial Thomson scattering is available at a distance of 3 cm in front of the target and in the heating chamber downstream the source exit. The accuracy of n_e and T_e is 3 % and 6 % respectively at $n_e = 9.4 \cdot 10^{18}\,m^{-3}$ [93]. First OES

measurements are reported in [117]. CARS is in the progress of being implemented and performed to measure T_{vib} independently.

Within the scope of this work, OES measurements are performed along 30 radial lines of sight (within the same plane as the line of sight used for Thomson scattering) in the target chamber of Magnum-PSI with a tungsten target. A Jarrel-Ash 1m spectrometer in Czerny-Turner configuration (focal length 1 m, 2400 lines/mm, CCD detector) is absolutely calibrated utilizing an Ulbricht sphere. Figure 3.3 depicts the schematic diagnostic setup. During these OES measurements also TALIF measurements are performed utilizing the viewing window opposite to the OES window.

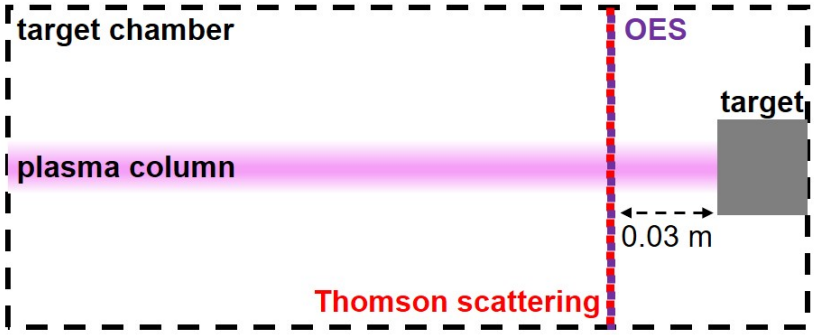

Figure 3.3: *Schematic of the Magnum-PSI target chamber and the position of the OES and Thomson scattering diagnostics.*

For the plasma source current of 120 A, the hydrogen flow of 8 slm, a constant magnetic field of 1.2 T and a target chamber background pressure of 0.4 Pa (without additional hydrogen puffing in the target chamber), the Balmer lines and the Fulcher-α band are measured. The electron temperature and density are measured through Thomson scattering. Since the quantities exhibit radial profiles, their peak values are used in a first approximation for further investigations. Additionally the profiles yield the plasma length of 0.03 m. The hydrogen atom density is determined from TALIF measurements stemming from [118]. While the comprehensive approach is used to determine $T_{\mathrm{vib}} = 4\,000 \pm 500\,\mathrm{K}$ and T_{gas}, the *Yacora H model* is used to obtain the molecular hydrogen and ion densities from the spectroscopic measurements of the central line of sight. Table 3.5 summarizes the plasma parameters determined. The values stated for $n_{\mathrm{H_3^+}}$ and $n_{\mathrm{H^-}}$ represent the upper limits possible according to the *Yacora H model*. These parameters from table 3.5 are used as input to a CR model to self-consistently predict the vibrational population of the electronic ground state $X^1\Sigma_g^+$ and thus T_{vib} in chapter 4.2.

Table 3.5: *Plasma parameters determined at Magnum-PSI for the plasma source current of 120* A *and the hydrogen flow of 8* slm *at a constant magnetic field of 1.2* T*.*

T_e [eV]	T_{gas} [K]
1.83	1620

n_e [m^{-3}]	n_H [m^{-3}]	n_{H_2} [m^{-3}]	n_{H^+} [m^{-3}]	$n_{H_2^+}$ [m^{-3}]	$n_{H_3^+}$ [m^{-3}]	n_{H^-} [m^{-3}]
$1.5 \cdot 10^{19}$	$5.6 \cdot 10^{18}$	$2.6 \cdot 10^{20}$	$1.49 \cdot 10^{19}$	$8.9 \cdot 10^{16}$	$3.4 \cdot 10^{18}$	10^{16}

3.2.5 Joint European Torus (JET)

The *Joint European Torus (JET)* [119, 120] was one of the largest tokamaks ever operated (to date) ceasing operations in 2023 located at the Culham Centre for Fusion Energy. JET had a tight aspect ratio (major radius $R = 2.96\,\mathrm{m}$, minor radius $a = 1.2\,\mathrm{m}$) and a D-shaped poloidal cross section [65]. The toroidal magnetic field B_t was operated up to 4 T, plasma currents up to 6 MA were achieved and an overall heating up to 37 MW could be provided [120]. Operation was pulsed with discharges lasting up to several tens of seconds.

Over the lifetime numerous modifications have been made to the tokamak. These include the change from a carbon interior to a mixture of beryllium and tungsten. This wall composition is typically referred to as ITER-like wall, even though in the currently proposed ITER baseline beryllium is replaced by tungsten for the first wall panels [121].

The last decade of experiments included investigations of magnetic configurations, impurity seeding experiments to achieve steady regimes at high density and low Z_{eff} with detached divertor, demonstrating successful plasma operation with the ITER-like wall, the development of plasma regimes operating in the same configurations as ITER [122] and the new world fusion energy record of 59 MJ achieved in a 50-50 deuterium-tritium hybrid scenario [123].

In the first study of the Fulcher-α band of deuterium plasmas with ITER-like wall in JET, higher rotational temperatures (up to about 3 000 K) were determined with Boltzmann plots in comparison to previous results for carbon wall machines and the vibrational distribution of $d^3\Pi_u$ was the largest for $v' = 0$ [124]. These findings were confirmed for hydrogen again with Boltzmann plots, determining rotational temperatures of about 3 700 K for $v' = v'' = 0$ [125].

The vast amount of diagnostics at JET contained divertor spectroscopy with multiple lines of sight. For detailed information of the system see e.g. [126].

In chapter 4.3.3, EDGE2D-EIRENE calculations (see below) from [127] for JET ITER-like wall L-mode plasmas are post-processed applying a vibrationally

resolved CR model to predict molecular emission bands.

3.2.6 DIII-D

The *DIII-D* tokamak is operated by *General Atomics* and is located in San Diego, California, United States. The device was commissioned in 1986 and is still in operation today. Its design evolved from the predecessor tokamaks *Doublet I*, *Doublet II* and *Doublet III*. A doublet is a two-lobed, toroidally symmetric plasma configuration with a cross section characterized by a number "8" shaped separatrix [128]. A summary of the doublet programme is given in e.g. [129]. DIII-D has a low aspect ratio (major radius $R = 1.66\,\mathrm{m}$, minor radius $a = 0.67\,\mathrm{m}$), a highly elongated D-shaped plasma chamber and a carbon divertor. The toroidal magnetic field B_t can reach up to $2.2\,\mathrm{T}$, the plasma current up to $5\,\mathrm{MA}$ and the heating system up to $26\,\mathrm{MW}$ [128].

The recent experimental program has included physical model validation studies and operational scenario development addressing processes from the core plasma to the divertor surfaces and the main chamber walls [130].

Over 60 diagnostics are installed [128] including divertor spectrometers [131], Thomsons scattering [132] and Langmuir probes (at the divertor plates) [133].

In chapter 4.3.4, EDGE2D-EIRENE calculations (see below) for a DIII-D deuterium L-mode plasma from [134, 135] are post-processed applying a vibrationally resolved CR model to predict the Fulcher-α band emission yield. Subsequently, the predicted Fulcher-α band emission yield is compared with measured DIII-D emission.

3.3 Codes

3.3.1 The Yacora solver

The Yacora code [136] is a solver for coupled sets of ordinary differential equations aimed for application in plasma physics. Since the rate equations of 0-dimensional CR models have such a mathematical structure, the solver is well suited for the development of population models based on it: The solver supports the definition of particles (e.g. eigenstates), processes (with specific particles as educts and products) and reaction probabilities in the form of cross sections, rate coefficients and transition probabilities for collisions and spontaneous processes. The collisional processes can involve both electron and heavy particle collisions. The solver can calculate rate coefficients from cross sections applying an arbitrary, user defined

energy distribution function for electrons and a Maxwellian energy distribution function for heavy particles [59]. The user can define temperatures, constant particle densities and initial values for the particle densities to be determined. The output of calculations can include calculated densities (of particles or excited state populations), equilibrium rates and the temporal development of the densities.

Since the typical timescales of collisional and radiative processes in plasmas are very different, the systems of rate equations is usually stiff, so that conventional solving techniques such as the Runge-Kutta method are quite slow [58]. Yacora therefore utilizes the CVODE package.

CVODE is part of the SUNDIALS package from the Lawrence Livermore National Laboratory [137] and includes backward differentiation formulas in fixed-leading coefficient form to solve initial value problems for stiff ordinary differential equation systems [138].

Since Yacora solves the coupled ordinary differential equations by integration of the equation system, the implementation of nonlinear and time-dependent processes (e.g. optical thickness) in the rate equations is possible and the solver is applicable not only for CR, but also for dissociation models [59]. Yacora is developed in C++.

The typical time for individual calculations represented by a combination of plasma parameters for atomic or electronically resolved molecular CR models is below 1 s [59].

Numerous CR models are built around the Yacora solver. These include (apart from the models for atomic and molecular hydrogen) models for He [58], Ar [139], Ar^+ [140], N_2 [141], C_2 [142], CH [142] and Cs [143].

The Yacors solver has been originally developed within the scope of [136] and has been continuously enhanced ever since. Some CR models based on the Yacora solver are available on the web framework *Yacora on the Web* [59].

3.3.2 EDGE2D-EIRENE

EIRENE is a 3D neutral gas transport Monte Carlo code applied worldwide for neutral particle transport problems in fusion devices [144]. This multi-species code can simultaneously solve a system of time dependent or stationary linear kinetic transport equations considering a background of other species particles [144]. Monte Carlo models typically do not solve the kinetic equations directly, but model trajectories of test particles and simulate their interactions with the solid background using pseudo-random numbers [73]. EIRENE is coupled to external

databases for atomic, molecular and surface reflection data, whereby the user can select the reactions to be included. A commonly used example is the atomic and molecular database *AMJUEL* [145].

The AMJUEL database contains effective rates and population coefficients for many elements. The data for molecular hydrogen has been derived from the pioneering CR model from [12]. Many assumptions made in this model can be avoided today due to the reaction probabilities now available. For instance, in the standard form of this model the electronic states are not vibrationally resolved and only the states with $n = 2$ are Λ-resolved. In addition, AMJUEL offers for a few processes effective rates from a modified version of the CR model from [12] with a vibrationally resolved ground state (e.g. H.2 3.2.3, H.4 2.2.5g).

EIRENE has been coupled with numerous plasma-fluid codes. Such codes solve the fluid equations that are approximated from the moments of the distribution functions of the plasma particles [73]. One of these is the 2D code EDGE2D that can discretize and thus solve the fluid equations by means of a hybrid approach between the Finite Difference and Finite Element methods [146]. A technical description of the coupling of EIRENE and EDGE2D to the EDGE2D-EIRENE code is given in [147]. Edge plasma transport codes coupled to neutral gas models are widely used for studying edge plasma phenomena, for the interpretation of measurements and for the prediction of edge plasma parameters and divertor heat loads in future devices [69].

3.3.3 The LEVEL code

The program *LEVEL* [148] can solve the radial Schrödinger equation for bound levels and resonances and thus calculate ro-vibrational eigenvalues and eigenfunctions for diatomic molecules. To do so, the user must supply potential curves as input. Furthermore, for instance Franck-Condon factors, matrix elements, rotational constants and radiative lifetimes (if electronic transition dipole operators are supplied) can be calculated.

4 The population models

The vast number of ro-vibrational levels in H_2 demands that a full CR model encompasses thousands of distinct reaction probabilities interconnecting these levels. Since these reaction probabilities are by far not available for fully ro-vibrationally resolved levels, a full CR model for H_2 is currently not feasible without rough approximations.

Instead, a combined multi-stage approach is followed in this work, to develop differently resolved models for specific applications without using overly simplified estimates of reaction probabilities. Thus, it is possible to study different aspects without having a fully ro-vibrationally resolved CR model for H_2.

In chapter 4.1 a purely electronically resolved CR model is used to compare different sources of input cross sections for the important process of Electron Impact Excitation involving different electronic states. Such a model is suited for basic investigations on the kinetics of populating and de-populating processes in the H_2 system.

In chapter 4.2 a vibrationally resolved model for the electronic ground state $X^1\Sigma_g^+$ is introduced with the aim of self-consistently predicting the vibrational population of the electronic ground state. In chapter 4.3 this model is extended to a vibrationally resolved model involving also the vibrational levels of the first 18 electronically excited states. The predictions from this model are compared to predictions from the AMJUEL database.

In chapter 4.4 a fully ro-vibrationally resolved corona model for the states of the Fulcher-α band system is developed to obtain insights regarding rotational excitation and to predict spectra in dependence on the plasma parameters.

4.1 The Yacora H_2 model

The first CR models for molecular hydrogen were purely electronically resolved [11, 12]. Based on the Yacora solver, there were previously separate CR models for the two multiplet systems of H_2: For the singlet system a model [142] could be switched between two sets of electron impact excitation cross sections (semiempirical cross sections from Miles [149] and a combination of cross sections from Janev [15] and cross sections based on calculations from Celiberto [150]). For the triplet system a Yacora model based on MCCC cross sections was presented in [84]. Therein it was shown that MCCC cross sections are the most consistent dataset compared to other cross section sets for the triplet system. Note that the AMJUEL database (see chapter 3.3) is based on the cross sections from Miles (for more details see 4.3.3).

Since no data on coupling processes between the two multiplet systems were previously available, a combined model for both multiplet systems could not be constructed. However, the MCCC cross sections now also enable to account for spin-mixing between electronically excited states. As an intermediate step toward the combined model discussed below, a singlet model based on MCCC cross sections was developed and published in [151].

4.1.1 Detailed model description

The *Yacora H_2 model* is a CR model aimed for basic investigations giving an overview of relevant reaction channels neglecting ro-vibrational resolution.

The model comprises separate electronic states for the singlet and triplet system up to $n = 10$. The states with $n \leq 3$ are resolved by the quantum number Λ. The energies of the respective electronic states are taken from [25] and thus the zero energy corresponds to the minimum of the potential curve of the $X^1\Sigma_g^+$ state. For the respective non-Λ resolved states with $n = 4 - 10$ the energies are approximated by $E_n = Ry^*(\frac{1}{0.94^2} - \frac{1}{n^2})$ using the ionization energy of the hydrogen atom Ry^*. The factor 0.94^2 represents the ratio of the ionization energy of the hydrogen atom and the ionization energy of the hydrogen molecule. Figure 4.1 depicts the included electronic states and their respective energies. For background information on the electronic states of H_2 see chapter 2.1.

Table 4.1 summarizes the processes included in the model. The input data utilized for this model is discussed in detail below. The process of spin-mixing between electronically excited states can optionally be disabled, so that calculations for the separate multiplet systems, singlet and triplet, are also possible.

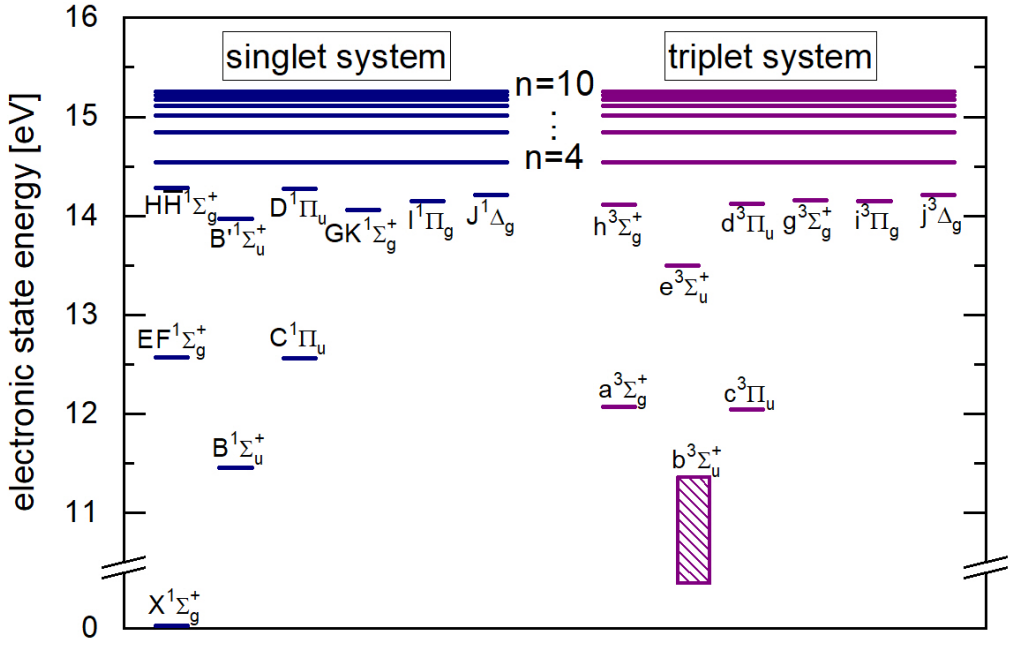

Figure 4.1: *Electronic state energies for H_2 (with respect to the minimum of the potential curve of the ground state $X^1\Sigma_g^+$) considered in the Yacora H_2 model. Note that only the states with $n < 4$ are resolved by quantum number Λ and that $b^3\Sigma_u^+$ is a repulsive state.*

Singlet system

- For Electron Impact Excitation $H_2(X^1\Sigma_g^+) \rightarrow H_2(n = 2, 3; \Lambda_\sigma)$, MCCC cross sections [152] are applied.

- Electron Impact Excitation cross sections for $H_2(X^1\Sigma_g^+) \rightarrow H_2(n = 4 - 10)$ are derived from MCCC cross sections for $H_2(X^1\Sigma_g^+) \rightarrow H_2(n = 3; \Lambda_\sigma)$ based on a scaling from [15]. This scaling is motivated by the fact that Electron Impact Excitation cross sections for collisions from the ground state are dependent on the dipole oscillator strength for dipole allowed transitions and on the generalized oscillator strength for symmetry-forbidden transitions:

$$\sigma(X^1\Sigma_g^+ \rightarrow N\Lambda_\sigma) = \left(\frac{N_0}{N}\right)^{(3+3\delta_{g\sigma})} \left(\frac{\Delta E_{0,N_0}}{\Delta E_{0,N}}\right) \sigma(X^1\Sigma_g^+ \rightarrow N_0\Lambda_\sigma)\,, \quad (4.1)$$

for $N > N_0$ with $\Delta E_{0,N_0} = E(N_0\Lambda_\sigma) - E(X^1\Sigma_g^+)$. Thereby, $N_0\Lambda_\sigma$ represent a Λ-resolved $n = 3$ states of the singlet system (and thus $N_0 = 3$). The individual cross sections for excitation to Λ-resolved $n = 3$ states are scaled to cross sections to the corresponding Λ-resolved $n > 3$ states, weighted by the statistical weight of the respective final electronic state and

Table 4.1: *Processes and corresponding reactions included in the Yacora H_2 model.*

Process	Reaction
Electron Impact (De-)Excitation	$H_2(N\Lambda_\sigma) + e^- \rightleftarrows H_2(N'\Lambda'_{\sigma'}) + e^-$
Electron Impact Dissociation	$H_2(N\Lambda_\sigma) + e^- \rightarrow H + H + e^-$
Non-Dissociative Electron Impact Ionization	$H_2(N\Lambda_\sigma) + e^- \rightarrow H_2^+ + e^- + e^-$
Dissociative Electron Impact Ionization	$H_2(N\Lambda_\sigma) + e^- \rightarrow H^+ + H + e^- + e^-$
Spontaneous Emission	$H_2(N\Lambda_\sigma) \rightarrow H_2(N'\Lambda'_{\sigma'}) + h\nu$
Dissociative Electron Attachment	$H_2(N\Lambda_\sigma) + e^- \rightarrow H + H^-$
Proton Charge Transfer	$H_2(N'\Lambda'_{\sigma'}) + H^+ \rightarrow H_2^+ + H$
Collisional Quenching	$H_2(a^3\Sigma_g^+, c^3\Pi_u) + H_2(X^1\Sigma_g^+) \rightarrow 2\,H_2(X^1\Sigma_g^+)$

summed to mimic excitation to the artificial non-Λ resolved states.

- For Electron Impact (De-)Excitation $H_2(n = 2; \Lambda_\sigma) \rightarrow H_2(n = 1, 2, 3; \Lambda_\sigma)$, MCCC cross sections [153] are utilized.

- Electron Impact Excitation cross sections for $H_2(n = 2; \Lambda_\sigma) \rightarrow H_2(n = 4-10)$ are derived from MCCC cross sections [153] using the scaling from [15] (analogously to the procedure described above for Electron Impact Excitation from $H_2(X^1\Sigma_g^+) \rightarrow H_2(n = 4 - 10)$).

- The rate coefficients for Electron Impact De-Excitation for $H_2(n = 3; \Lambda_\sigma) \rightarrow H_2(n = 1, 2; \Lambda_\sigma)$ are derived from the cross sections for the inverse process according to the principle of detailed balance.

- The rate coefficients for Electron Impact Excitation for $H_2(n = 3; \Lambda_\sigma) \rightarrow H_2(n = 4-10)$ stem from [12]. They follow the approximation recommended in [154] and average data for atomic hydrogen from [155] and [156].

- The rate coefficients for Electron Impact De-Excitation for $H_2(n = 4 - 10) \rightarrow H_2(n = 1, 2, 3; \Lambda_\sigma)$ are calculated from the cross sections for the inverse process according to the detailed balance principle.

- The rate coefficients for Electron Impact Excitation $H_2(n = 4 - 9) \rightarrow H_2(n = 5 - 10)$ stem from [12] based on the recommendation in [154]. The rate coefficients for the respective de-excitation processes are calculated according to the detailed balance principle.

- Electron Impact (De-)Excitation reactions for both initial and final states $H_2(n = 3; \Lambda_\sigma)$ are not included because such data are currently not available in the literature. Calculations for such reactions are due to the small energy differences of the involved states especially challenging.

- For Electron Impact Dissociation depopulating $H_2(n = 1, 2; \Lambda_\sigma)$ through (de-)excitation into the repulsive state $b^3\Sigma_u^+$ or unbound products energetically above the final bound level of a bonding state, MCCC cross sections [157] are utilized.

- For Non-Dissociative Ionization $H_2(n = 2, 3; \Lambda_\sigma)$, cross sections calculated with the Gryzinski method [158, 159] from [49] are applied. These semi-classical cross sections agree with the respective fully quantal MCCC cross sections for the states with $n = 1, 2$.

- The rate coefficients for Non-Dissociative Ionization for $H_2(n = 4 - 10)$ from [12] are used. They are based on the atomic data from [155] and [156].

- For Dissociative Ionization $H_2(n = 2; \Lambda_\sigma)$ cross sections calculated with the Gryzinski method from [49] are applied.

- Spontaneous Emission from initial $H_2(n = 2, 3; \Lambda_\sigma)$ is implemented via effective Einstein coefficients (see chapter 2.5) that are determined for room temperature ($T = 300\,\mathrm{K}$) from [25]. The A_{ik} therein are calculated with the TraDiMo code. This code solves the Schrödinger equation using Born-Oppenheimer potential curves to derive vibrational eigenstates and hence Einstein coefficients using electronic transition dipole operators. For more detailed information see [25].

- Spontaneous Emission from initial $H_2(n = 4 - 10)$ populating the states $H_2(n = 3; \Lambda_\sigma)$ and $H_2(n = 4 - 9)$ is accounted for via Einstein coefficients for atomic hydrogen from [155]. Spontaneous Emission from initial $H_2(n = 4 - 10)$ populating the states $H_2(n = 1, 2; \Lambda_\sigma)$ is included via Einstein coefficients for the helium atom scaled with n for H_2 after [160].

- Studies quantifying the probability of Dissociative Electron Attachment for electronically excited states are particularly scarce in the literature. The constant rate coefficients $X = 10^{-15}\,\mathrm{m^3/s}$ and $X = 6 \cdot 10^{-11}\,\mathrm{m^3/s}$ are applied for Dissociative Electron Attachment de-populating $H_2(n = 2; \Lambda_\sigma)$ and $H_2(n = 3; \Lambda_\sigma)$, $H_2(n = 4 - 10)$, respectively, and are motivated by

measurements in laser plasmas [161, 162]. These rather extraordinary high values are well known to be controversial in the literature [15, 163].

- For Proton Charge Transfer with $H_2(n = 2, 3; \Lambda_\sigma)$ and $H_2(n = 4 - 10)$, cross sections from the classical over barrier transport model adapted to molecules from [15] are applied

$$\sigma_{n^*}(E) = \frac{1.77\, n^{*4}}{1 + 0.42\,(n^{*2} E\, 10^{-3})^{0.2} + 0.52\,(n^{*2} E\, 10^{-3})^{0.5}} \cdot 10^{-19}\,[m^2]\,, \quad (4.2)$$

with the effective main quantum number $n^* = (13.6/(E(H_2^+ - H_2(N\Lambda_\sigma))))^{0.5}$. These cross sections are used for lack of alternatives, although they represent rather rough estimates. This statement is especially true for states with $n \leq 3$, since for these the classically forbidden electron under-barrier tunneling transitions are more important and may even shield the over-barrier transition mechanism [164].

Triplet system

The part of the *Yacora H_2 model* for the triplet system is largely based on the triplet model from [84]. Some changes are made to ensure consistency with the singlet part of the *Yacora H_2 model*. Firstly, the published MCCC cross sections for Electron Impact Excitation from [152, 153] are applied. Secondly, the energy values of the respective ground vibrational levels are used for the state energies instead of the energies of the minima of the respective potential curves. Furthermore, different energy differences are used for Electron Impact (De-)Excitation into the dissociative $b^3\Sigma_u^+$ state (see below). For Non-dissociative Ionization and Proton Charge Transfer more accurate input data are used. The effective Einstein coefficients for the $H_2(n = 2, 3; \Lambda_\sigma)$ states are calculated for $T_{vib} = 300\,K$ instead of $T_{vib} = 5\,000\,K$. Furthermore, the processes of Electron Impact Dissociation via other states than $b^3\Sigma_u^+$ and Dissociative Ionization are included. Even though the input data is often analogous to the data used for the singlet system, the source of the input data is specified in detail again for the reader's convenience.

- For Electron Impact Excitation $H_2(X^1\Sigma_g^+) \rightarrow H_2(n = 2, 3; \Lambda_\sigma)$, MCCC cross sections [152] are used.

- For Electron Impact (De-)Excitation $H_2(a^3\Sigma_g^+,\, c^3\Pi_u) \rightarrow H_2(n = 1, 2, 3; \Lambda_\sigma)$, MCCC cross sections [153] are utilized.

- Electron Impact De-Excitation rate coefficients for $H_2(n = 3; \Lambda_\sigma) \rightarrow H_2(X^1\Sigma_g^+, a^3\Sigma_g^+, c^3\Pi_u)$ are derived from the cross sections for the inverse process after the principle of detailed balance.

- Electron Impact Excitation rate coefficients for $H_2(X^1\Sigma_g^+, a^3\Sigma_g^+, c^3\Pi_u)$ and $H_2(n = 3; \Lambda_\sigma) \rightarrow H_2(n = 4{-}10)$ stem from [12] following the recommendation in [154].

- Electron Impact De-Excitation rate coefficients for $H_2(n = 4 - 10) \rightarrow H_2(n = 1, 2, 3; \Lambda_\sigma)$ are calculated from the data for the inverse process after the detailed balance principle.

- Electron Impact Excitation rate coefficients for $H_2(n = 4 - 9) \rightarrow H_2(n = 5{-}10)$ stem from [12] after the recommendation in [154]. The rate coefficients for the respective De-Excitation processes are calculated after the detailed balance principle.

- Electron Impact De-Excitation rate coefficients for $H_2(n = 3; \Lambda_\sigma)$ and $H_2(n = 4 - 10) \rightarrow H_2(b^3\Sigma_u^+)$ are calculated after the detailed balance principle from the rate coefficients from [12]. The $b^3\Sigma_u^+$ energy is determined individually for the respective energy difference: The potential minimum of the upper state is projected onto the $b^3\Sigma_u^+$ potential curve. For the artificial $H_2(n = 4 - 10)$ states, the average energy determined from the projection of the individual $H_2(n = 3; \Lambda_\sigma)$ is applied.

- For Electron Impact Dissociation originating from $H_2(a^3\Sigma_g^+, c^3\Pi_u)$ through (de-)excitation into the repulsive state $b^3\Sigma_u^+$ or unbound products energetically above the final bound level of a bonding state, MCCC cross sections [157] are utilized.

- For Non-Dissociative Ionization $H_2(a^3\Sigma_g^+, c^3\Pi_u, n = 3; \Lambda_\sigma)$, cross sections calculated with the Gryzinski method [158, 159] from [49] are applied.

- For Non-Dissociative Ionization for $H_2(n = 4 - 10)$, rate coefficients from [12] are used that are based on the atomic data from [155] and [156].

- For Dissociative Ionization $H_2(n = 2, 3; \Lambda_\sigma)$, cross sections calculated with the Gryzinski method from [49] are applied.

- Spontaneous Emission from initial $H_2(n = 2, 3; \Lambda_\sigma)$ is implemented through effective Einstein coefficients determined for room temperature ($T = 300\,\mathrm{K}$) from [25].

- Spontaneous emission from $H_2(c^3\Pi_u)$ to $H_2(X^1\Sigma_g^+)$ is optically forbidden. To account for magnetic dipole and electric quadrupole interactions, the transition rate $10^3\,1/s$ [15] is implemented.

- Spontaneous Emission from initial $H_2(n = 4 - 10)$ populating the states $H_2(n = 3; \Lambda_\sigma)$ and $H_2(n = 4 - 9)$ is accounted for via Einstein coefficients for atomic hydrogen from [155]. Spontaneous Emission from initial $H_2(n = 4 - 10)$ populating the states $H_2(n = 1, 2; \Lambda_\sigma)$ is included through scaled Einstein coefficients for the helium atom scaled with n of H_2 after [160].

- For Dissociative Electron Attachment for electronically excited states, again the constant rate coefficients $X = 10^{-15}\,m^3/s$ and $X = 6 \cdot 10^{-11}\,m^3/s$ after [161, 162] are applied, de-populating $H_2(a^3\Sigma_g^+,\ c^3\Pi_u)$ and $H_2(n = 3; \Lambda_\sigma)$, $H_2(n = 4 - 10)$ respectively.

- For Proton Charge Transfer de-populating $H_2(n = 2, 3; \Lambda_\sigma)$ and $H_2(n = 4 - 10)$, cross sections from the classical over barrier transport model adapted to molecules from [15] are applied.

- For Collisional Quenching from $H_2(a^3\Sigma_g^+,\ c^3\Pi_u)$ the experimentally determined rate constants from [165] are used. These are determined from laser absorption measurements. The rate coefficient for $c^3\Pi_u$ is found to be independent of vibrational and rotational quantum number with an average value of $1.88 \cdot 10^{-15}\,m^3/s$. For $a^3\Sigma_g^+$ the rate coefficient amounts to $1.15 \cdot 10^{-15}\,m^3/s$.

Spin-mixing

The singlet and triplet system are coupled via MCCC Electron Impact (De-)excitation (spin-mixing) cross sections from [153], coupling the non-dissociative $H_2(n = 2; \Lambda_\sigma)$ states of one multiplet system to the $H_2(n = 2, 3; \Lambda_\sigma)$ states of the respectively other multiplet system.

4.1.2 Benchmarking the model

The parameters determined from measurements at the ECR experiment discussed in chapter 3.2.2 are used as input for the *Yacora H_2 model* (with $n(X^1\Sigma_g^+) = n_{H_2}$) to benchmark the model predicted excited state population densities of singlet states with the densities derived from the measured emission. For the calculation of rate coefficients from cross sections, Maxwellian EDFs are assumed. In addition,

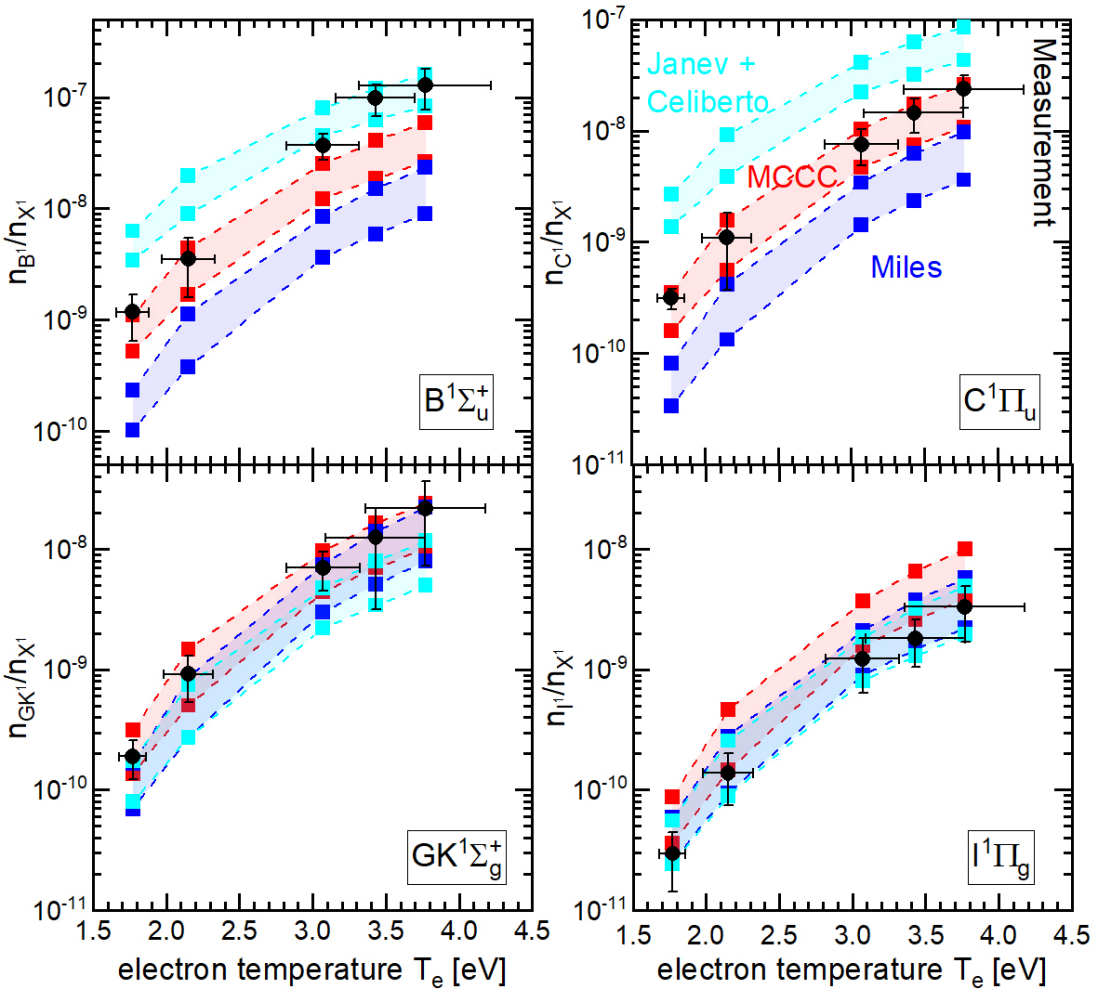

Figure 4.2: *Normalized population densities of the $B^1\Sigma_u^+$, $C^1\Pi_u$, $GK^1\Sigma_g^+$ and $I^1\Pi_g$ states calculated with different sets of input cross sections accounting for the uncertainty of the input parameters in comparison to measurements from the ECR experiment discussed in chapter 3.2.2.*

calculations are performed with the Yacora models for the singlet state based on the cross sections from Miles and the combined set of Janev and Celiberto. Figure 4.2 compares the predicted excited state densities from the three models (normalized with respect to the ground state density) with the densities derived from the measured emission in dependence on the electron temperature. The uncertainty ranges of the model results are a consequence of the uncertainties of the input plasma parameters estimated from the measurements.

Overall, the model applying the MCCC cross sections shows the best agreement with the measurements (note the logarithmic scale of the ordinate): For the $C^1\Pi_u$ state, it gives the best agreement with the measurements for all electron temperatures. For the $B^1\Sigma_u^+$ state, the model applying MCCC cross sections

shows the best agreement for the plasmas with low electron temperature, but underestimates the excited state densities for the plasmas with $T_e = 3.43$ and 3.77 K compared to the measurements. Since this trend increases with T_e, that was varied by changing the pressure, a pressure dependent effect may cause this discrepancy. For the $GK^1\Sigma_g^+$ and $I^1\Pi_g$ states the excited state densities are well predicted for each of the models used and cross sections applied.

The plasma parameters determined from measurements at the inductively coupled plasma experiment PlanICE described in chapter 3.2.1 are used as input for the *Yacora H_2 model* model (assuming Maxwellian EDFs again) and the predicted densities are compared with the densities derived from the measured Fulcher-α band emission. In the same way as described above, several model runs per measurement are conducted to account for the uncertainties of the plasma parameters estimated from the measurements (T_e, n_e and T_{gas}). The $d^3\Pi_u$ density predictions from the model (with and without accounting for the uncertainties of the plasma parameters) are shown in figure 4.3. All measurements lie within the simulation range that results from the uncertainty of the input parameters for the model.

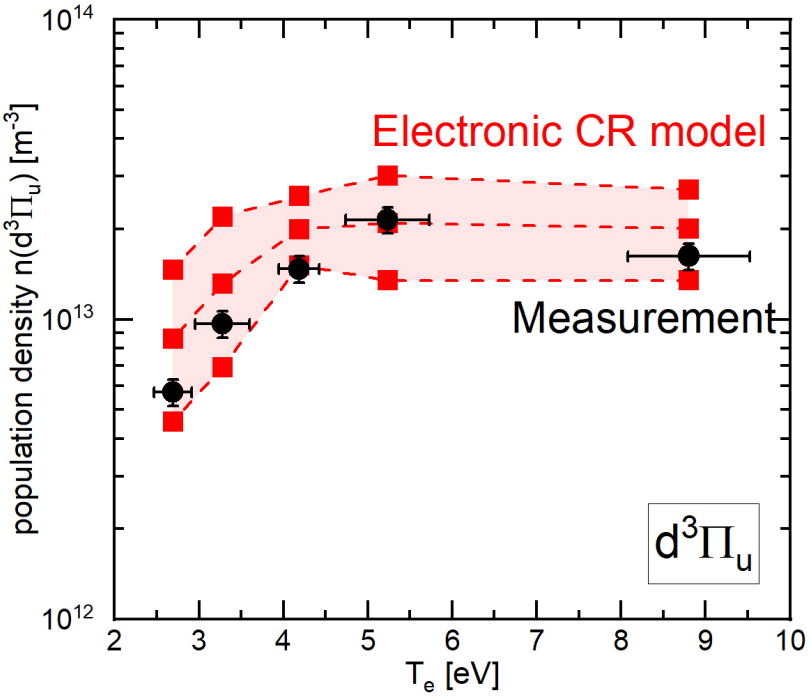

Figure 4.3: *Comparison of the $d^3\Pi_u$ population density predicted by the Yacora H_2 model with measurements from the Fulcher-α band at the inductively coupled plasma experiment PlanICE described in chapter 3.2.1.*

These benchmarks demonstrate that the *Yacora H_2 model* generally provides

accurate predictions and (like it was shown in [84] for solely the triplet system) that a model based on MCCC Electron Impact Excitation cross sections gives for the studied parameter range the most accurate predictions compared to models based on other input cross sections.

4.1.3 The general (de-)populating dynamics

The *Yacora H_2 model* can be used to investigate the extent to which the respective (de-)populating processes contribute to the excited state population densities. This application is particularly relevant in the context of the multi-stage approach (for CR model development) pursued in this work, in order to gain insights that can be used for other models with different state resolution.

The relative relevance of the populating rates is characterized by the respective contribution to the total (de-)populating rate. Calculations for a set of plasma parameters determined at the ECR plasma experiment ($T_e = 1.77\,\mathrm{eV}$, $T_{gas} = 450\,\mathrm{K}$, $n_{H_2} = 2.61 \cdot 10^{21}\,\mathrm{m}^{-3}$, see table 3.3) and varying $n_e = 10^{15} - 10^{22}\,\mathrm{m}^{-3}$ are performed with the *Yacora H_2 model* and the relative relevance of the respective populating and de-populating processes is shown in figures 4.4, 4.5 and 4.6 for the states $C^1\Pi_u$, $a^3\Sigma_g^+$ and $d^3\Pi_u$. These states are typical examples for the different (de-)population dynamics.

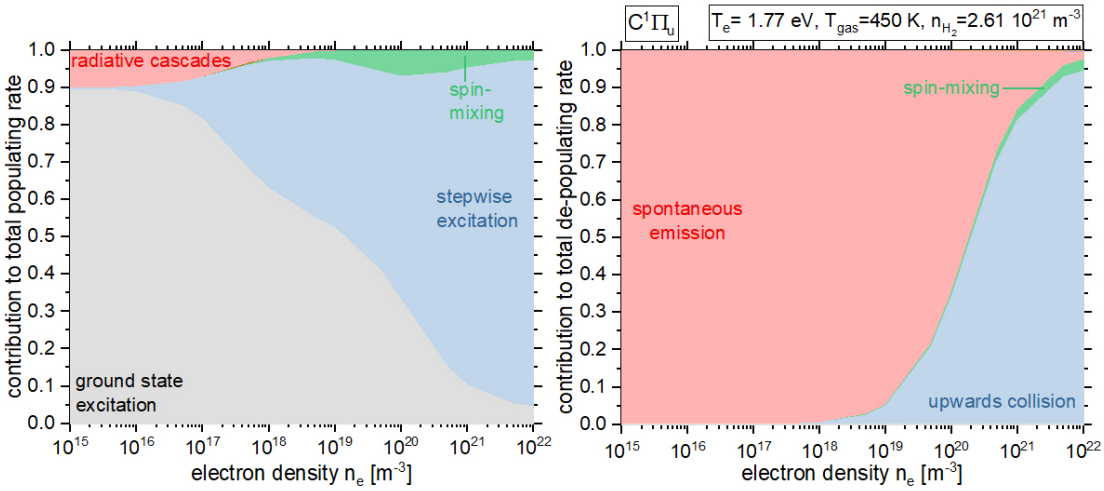

Figure 4.4: *Relative relevance of populating (left) and de-populating processes (right) of the $C^1\Pi_u$ state in dependence on n_e.*

According to figure 4.4, for low electron densities ($n_e \approx 10^{15} - 10^{16}\,\mathrm{m}^{-3}$), Electron Impact Excitation from the ground state (direct excitation) amounts to 89 % and radiation from higher states (radiative cascades) to 10 % of the total populating rate of the $C^1\Pi_u$ state. With increasing n_e, the relevance of direct

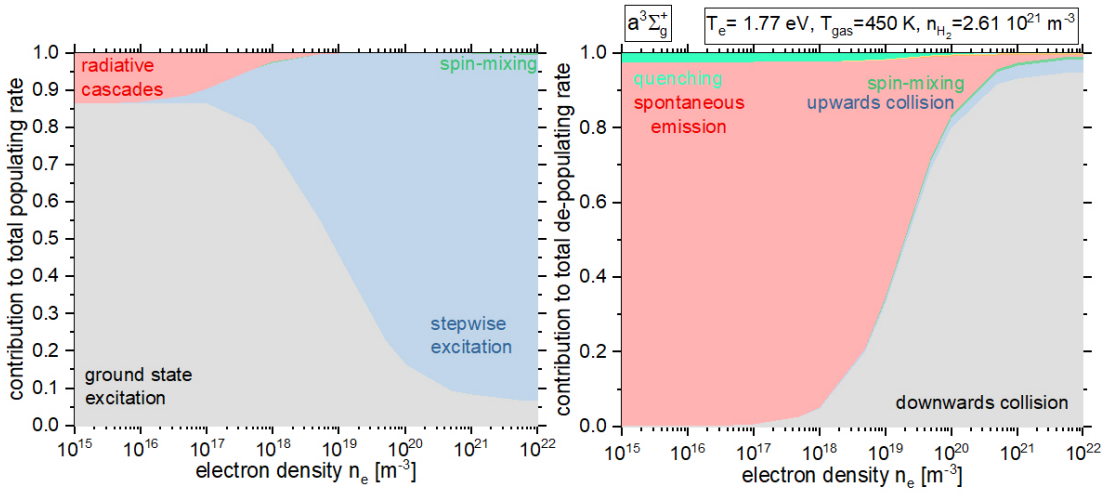

Figure 4.5: *Relative relevance of populating (left) and de-populating processes (right) of the* $a^3\Sigma_g^+$ *state in dependence on* n_e.

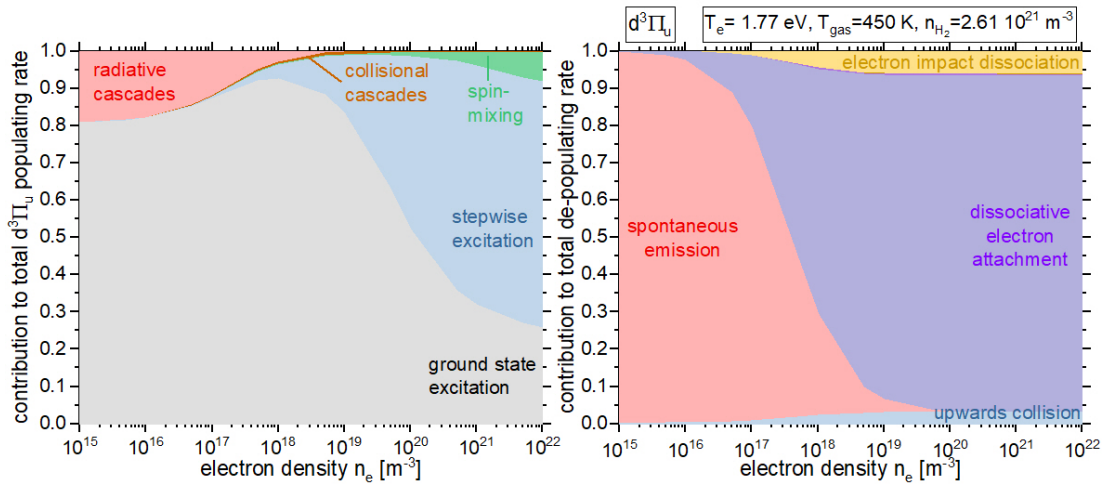

Figure 4.6: *Relative relevance of populating and de-populating processes of the* $d^3\Pi_u$ *state in dependence on* n_e.

excitation and radiative cascades decreases, while the relevance of population through Electron Impact Excitation proceeding via states with lower or same n (stepwise excitation) increases. This observation is not surprising, since the rates for radiative cascades depend only indirectly on n_e, the ground state excitation rate scales linearly with n_e, but the stepwise excitation rates scale stronger than linearly with n_e. For high electron densities ($n_e \approx 10^{20}\,\mathrm{m}^{-3}$), population by spin-mixing between electronically excited states amounts to about 7 % of the total populating rate. Population through Electron Impact De-Excitation from higher lying states (collisional cascades) is rather irrelevant as population mechanisms for any n_e.

For low electron densities ($n_e \approx 10^{15} - 10^{16}\,m^{-3}$), Spontaneous Emission determines almost the total de-populating rate. In this regime corona models are applicable. For $n_e \geq 10^{19}\,m^{-3}$ the relevance of Spontaneous Emission decreases strongly and the de-population is increasingly determined by Electron Impact Excitation to higher lying states. De-population through spin-mixing between electronically excited states amounts for high $n_e \gtrapprox 10^{21}\,m^{-3}$ to about 3 % of the total de-populating rate. Other de-populating processes (Electron Impact De-Excitation, Dissociative Electron Attachment, Ionization, Electron Impact Dissociation and Proton Charge Transfer) are rather irrelevant for the plasma parameters under consideration.

As can be seen in figures 4.5 and 4.6, the relative relevance of the populating processes for the $a^3\Sigma_g^+$ and $d^3\Pi_u$ states follows qualitatively similar trends as discussed for the $C^1\Pi_u$ state.

Contrarily, there are several differences regarding the de-population of these states: For $a^3\Sigma_g^+$ and high electron densities ($n_e \geq 2 \cdot 10^{19}\,m^{-3}$), downwards collision is the main de-populating mechanism. This observation is a consequence of the cross sections: The cross section for Electron Impact De-Excitation from $a^3\Sigma_g^+ \rightarrow c^3\Pi_u$ is almost for the entire energy range larger than the corresponding cross sections from $C^1\Pi_u \rightarrow B^1\Sigma_u^+$ and $C^1\Pi_u \rightarrow EF^1\Sigma_g^+$. In addition, Collisional Quenching contributes to the de-population, especially at low n_e (about 2.7 % of the total de-populating rate at $n_e = 10^{15}\,m^{-3}$). For $d^3\Pi_u$ and $n_e \gtrapprox 5 \cdot 10^{17}\,m^{-3}$, Dissociative Electron Attachment dominates the de-population. This observation is a consequence from the utilization of constant rate coefficients in the model (see above). Furthermore, the relevance of Electron Impact Dissociation increases with the electron density to 6.4 % of the de-populating rate at $n_e = 10^{22}\,m^{-3}$.

Since the rate coefficients utilized for Dissociative Electron Attachment are already under debate in the literature, the relevance study is repeated without this process and depicted for the $d^3\Pi_u$ state in figure 4.7. Compared to the standard case discussed above, differences are observed both in the population and de-population dynamics: At high n_e, electron impact dissociation is the most relevant de-population mechanism and the relevance of upwards collisions and ionization is increased. Regarding the population of the $d^3\Pi_u$ state, the relevance of collisional cascades is increased, since also the higher lying states are no longer de-populated by Dissociative Electron Attachment. The influence of Dissociative Electron Attachment on (vibrational levels) of electronically excited state is further studied in chapter 4.3.

The exact de-population dynamics of the other states included in the model are

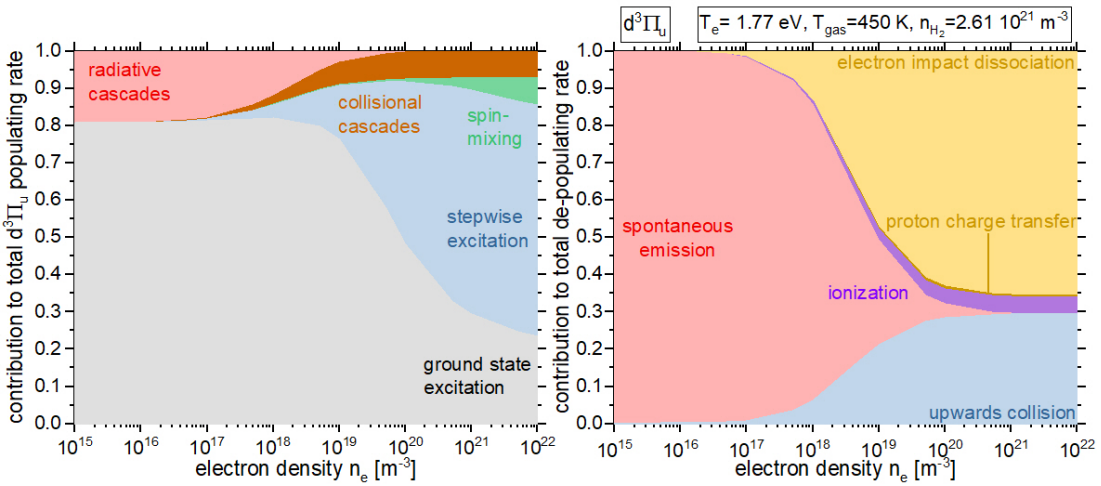

Figure 4.7: *Relative relevance of populating and de-populating processes of the* $d^3\Pi_u$ *state in dependence on* n_e *for calculations without Dissociative Electron Attachment.*

not discussed in detail here, since they are in general qualitatively similar to one of these examples. Exceptions are for instance the $c^3\Pi_u$ state: Since Spontaneous Emission into lower lying states is optically forbidden, Collisional Quenching dominates the de-population for low $n_e \lessapprox 10^{18}\,\mathrm{m}^{-3}$.

4.1.4 The influence of spin-mixing processes

Due to the previous lack of cross sections or rate coefficients for spin-mixing between electronically excited states, solely separate CR models for the singlet and triplet system have been available in the past. With the *Yacora* H_2 *model* it is possible for the first time to quantify the influence of spin-mixing between electronically excited states on population densities. Therefore, calculations for typical plasma parameters (varying values of $T_e = 1, 2, 5\,\mathrm{eV}$, $n_e = 10^{15} - 10^{20}\,\mathrm{m}^{-3}$ and fixed values of $T_{gas} = 1\,000\,\mathrm{K}$ and $n_{H_2} = 10^{20}\,\mathrm{m}^{-3}$) are performed. In addition, the calculations are repeated with deactivated spin-mixing between electronically excited states. As an example, the absolute population densities of again the $C^1\Pi_u$ and $a^3\Sigma_g^+$ states for the model runs with and without spin-mixing are depicted in figure 4.8. Additionally, the relative difference between the results of the two calculations are given as numbers. The difference in absolute population densities for the two model runs is most pronounced for small T_e and high n_e. This observation is not surprising, since, on the one hand, the spin-mixing cross sections have a low or no threshold and the corresponding rate coefficients are therefore much higher for low T_e than the rate coefficients for processes with a

large threshold energy (e.g. ground state excitation). On the other hand, the spin-mixing rates increase stronger than linearly with increasing n_e, since spin-mixing processes are induced by electron collisions and originate from electronically excited states. For a wide plasma parameter space ($n_e \lessapprox 10^{19}\,m^{-3}$), the influence of spin-mixing between electronically excited states is rather negligible. This study highlights that previous models treating the singlet and triplet system separately did not primarily lack the inclusion of spin-mixing reactions, but rather accurate and consistent cross sections in general.

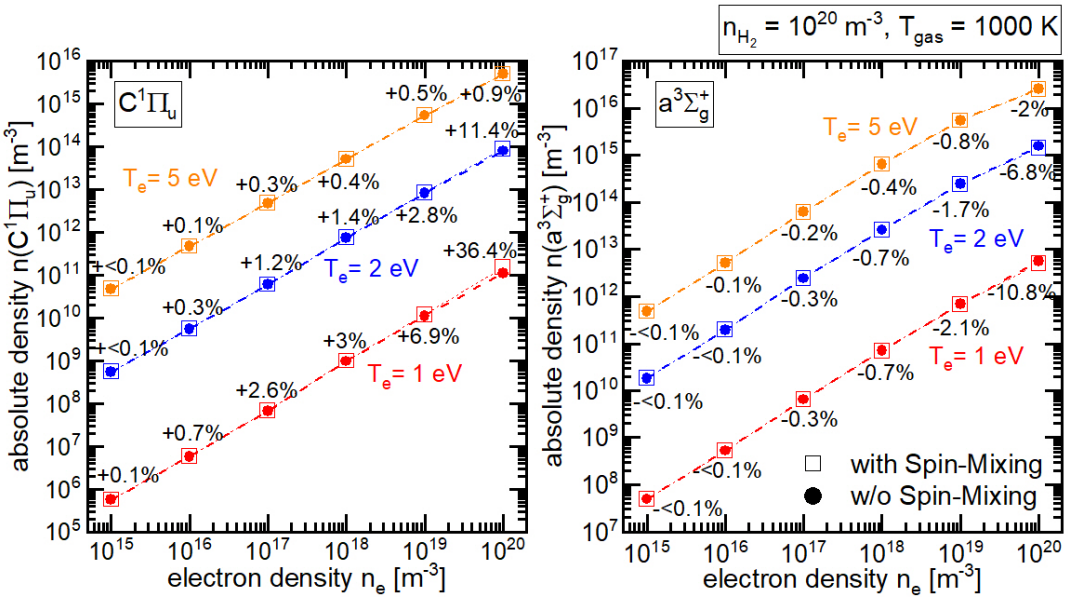

Figure 4.8: *Absolute population density of the states $C^1\Pi_u$ and $a^3\Sigma_g^+$ calculated applying the Yacora H_2 model with spin-mixing (squares) and without spin-mixing (circles) for varying n_e. The numbers give the relative difference ((n(with spin-mixing)-n(without spin-mixing))/n(without spin-mixing)) of the absolute population densities.*

4.1.5 The influence of the $n > 3$ states

In the *Yacora H_2 model*, the states with $n = 4 - 10$ are artificially combined states that are not resolved by the quantum number Λ. In order to investigate the influence of these states on the population densities of the Λ-resolved states with $n = 2 - 3$ by means of radiative and collisional cascades, modified versions of the CR model are constructed that exclude a range of the high n artificial states: models solely including the states with $n = 1 - 5$, with $n = 1 - 4$ and with $n = 1 - 3$.

Calculations with the standard *Yacora H_2 model* including the states with

$n = 1 - 10$ and the modified models are performed again for a set of plasma parameters determined at the ECR plasma experiment ($T_e = 1.77\,\mathrm{eV}$, $T_{gas} = 450\,\mathrm{K}$, $n_e = 10^{16}\,\mathrm{m}^{-3}$, $n_{H_2} = 2.61 \cdot 10^{21}\,\mathrm{m}^{-3}$). The ratio of the excited state population densities resulting from the modified models and the standard model are shown in figure 4.9. The more of the states with $n = 4 - 10$ and the respective cascading processes are neglected, the smaller are the excited state population densities for the Λ-resolved states with $n = 2 - 3$ and thus the smaller is the density ratio shown. The calculated population densities of the modified model including the states with $n = 1 - 5$ agree with the calculations of the standard model for all Λ-resolved states within 6 %. In contrast, the modified model with $n = 1 - 3$ yields much lower population densities for the Λ-resolved states (e.g. for $d^3\Pi_u$ a population density lower by 18 %). This observation is not surprising and can be visualized by means of the (de-)populating equilibrium rates for $d^3\Pi_u$ that are shown in figure 4.10: In the standard model, radiative cascades amount to 18 % of the populating rate for the investigated plasma parameters. In the modified models with $n = 1 - 5$, $n = 1 - 4$ and $n = 1 - 3$ radiative cascades amount to 17 %, 14 % and about 0.2 % of the populating rate. Hence, the majority of the radiative cascades in the standard model originate from the $n = 4 - 5$ states. With regard to the de-population of $d^3\Pi_u$, virtually no changes in the rates can be observed for the modified model versions. This is no surprise, since the processes of Spontaneous Emission and Dissociative Electron Attachment are the main de-populating mechanisms for the fixed plasma parameters in all tested versions of the model.

Since it is demonstrated that the states with $n = 4 - 5$ have a significant influence on the $d^3\Pi_u$ population density, it is to be expected that a physically more accurate treatment of these states by Λ-resolving them will further increase the accuracy of the model. However, there are currently no satisfactorily accurate (Λ-resolved) cross sections for any processes available in the literature.

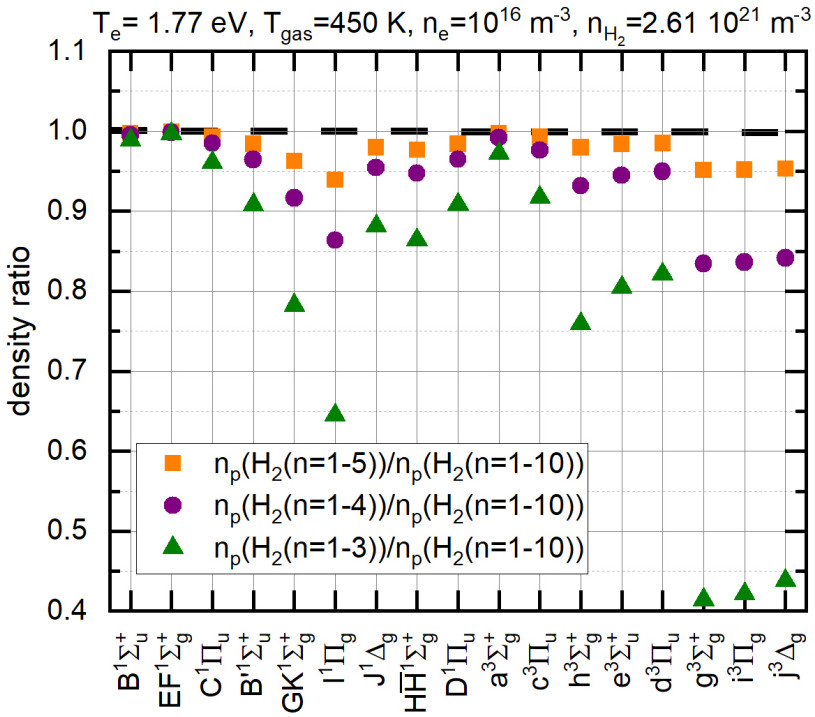

Figure 4.9: *Ratio of excited state population densities calculated with modified model versions (including the states with $n = 1 - 5$, $n = 1 - 4$ and $n = 1 - 3$) and the standard Yacora H_2 model (including the states with $n = 1 - 10$) for fixed plasma parameters.*

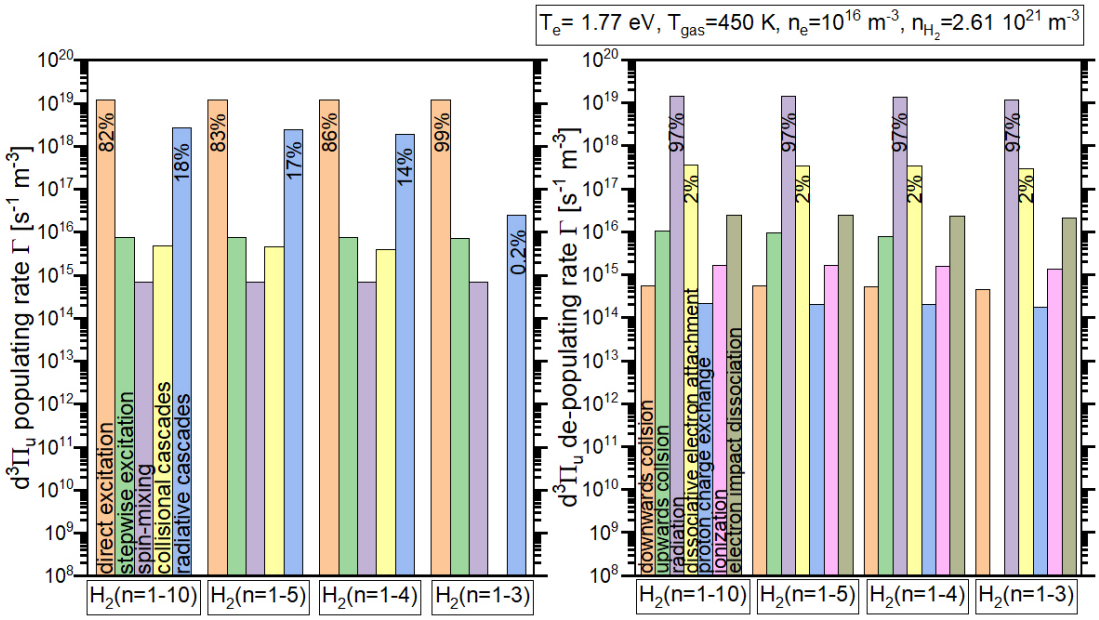

Figure 4.10: *(De-)populating rates of $d^3\Pi_u$ for the standard Yacora H_2 model (including the states with $n = 1 - 10$) and the modified model versions (including the states with $n = 1 - 5$, $n = 1 - 4$ and $n = 1 - 3$) for fixed plasma parameters. The printed numbers indicate the relative relevance of the respective (de-)population process.*

4.2 The Yacora $H_2(X^1,v)$ model

The *Yacora $H_2(X^1,v)$ model* is aimed to self-consistently predict the vibrational distribution of the electronic ground state $X^1\Sigma_g^+$. This goal is pursued by considering an extensive set of electron and heavy particle collisions based on state-of-the-art input data collected from literature. Vibrationally excited levels in $X^1\Sigma_g^+$ are of crucial importance, since they contribute for instance to MAR and thus may enhance divertor detachment.

Many other CR models for H_2 have been developed in the literature that include vibrational levels and vibrationally resolved reaction probabilities. For instance, the CR model in [166] includes the vibrationally resolved ground state. In [167] a vibrationally resolved CR model is used to calculate MAR rate coefficients. In [168] a vibrationally resolved CR model is part of a kinetic model for microwave H_2 plasmas. Since the CR model from [6] is partially ro-vibrationally resolved, this model tries to predict the vibrational ground state distribution too. The previous vibrationally resolved CR model based on the Yacora solver from [169] is aimed to calculate the vibrational population of the electronic ground state $X^1\Sigma_g^+$. This model is updated and extended in [58]. The model accounting for the processes of [169] (without wall interaction processes) through the reaction probabilities from [58] will be called *previous Yacora model* below. Results of the previous Yacora model will be first compared with a new model involving the same reactions with updated input reaction probabilities and second with an updated and extended model accounting for additional processes, in order to study the influence of both differences separately.

4.2.1 Detailed model description

The *Yacora $H_2(X^1,v)$ model* includes the vibrational levels of the molecular hydrogen electronic ground state $X^1\Sigma_g^+(v = 0-14)$ and the first two excited electronically excited states $B^1\Sigma_u^+(v = 0-36)$ and $C^1\Pi_u(v = 0-13)$ of the same multiplet system. Since Electron Impact (De-)Excitation between these states is optically allowed, it is highly probable. The energies of the respective levels are assigned according to [25].

Table 4.2 lists the processes and reactions considered in the model. The standard model version includes the processes Electron Impact (De-)Excitation, Electron Impact Dissociation, Dissociative Electron Attachment, Proton Charge Transfer, Non-Dissociative Electron Impact Ionization, Radiative Recombination, Collisional 3-Particle Recombination and the transitions via the vibrational levels of $B^1\Sigma_u^+$

and $C^1\Pi_u$ through Electron Impact (De-)Excitation and Spontaneous Emission. The extended model version accounts in addition for Dissociative Electron Impact Ionization, Proton Impact (De-)Excitation, Proton Impact Dissociation, H^- Associative Detachment, Hydrogen Atom Impact Dissociation, Hydrogen Molecule Impact (De-)Excitation, H_3^+ Dissociative Recombination, in order to test the relevance of these processes that are not included in the previous Yacora model. Each individual process can be flexibly switched on or off as required for instance for sensitivity studies. Note that plasma-surface interaction processes and the transport of vibrational levels are not accounted for in the *Yacora $H_2(X^1,v)$ model*. The reaction probabilities for plasma-surface interaction processes strongly depend on the respective surface material and temperature, and are merely partially known in the literature. In the following the input data utilized in this model is discussed in detail.

Standard model

- For Electron Impact Excitation $H_2(X^1\Sigma_g^+,v) + e^- \rightarrow H_2(X^1\Sigma_g^+,v') + e^-$ with $v = 0$ and $v' = 1, 2, 3$, cross sections from [16] are applied. These cross sections represent fits to different measurements. For other initial v and final v' (with $v' > v$), the *Greenland scaling* from [170] is applied to the rate coefficient calculated from the cross section for the $v = 0 \rightarrow v' = 1$ transitions:
$$X_{v,v'} = \frac{\exp(5E_v - 4.44E_{v'})}{0.121} X_{0,1}. \tag{4.3}$$
The scaling depends on the energies of the involved levels (E_v, $E_{v'}$) and is based on a fit to data from [171].

- Electron Impact De-Excitation $H_2(X^1\Sigma_g^+,v') + e^- \rightarrow H_2(X^1\Sigma_g^+,v'') + e^-$ (with $v' > v''$) rate coefficients are derived from the respective inverse process applying the detailed balance principle.

- For Electron Impact Dissociation $H_2(X^1\Sigma_g^+,v) + e^- \rightarrow H + H + e^-$, the MCCC cross sections from [172] are utilized. These cross sections account for excitation into dissociative levels in the vibrational continuum of electronically excited states and excitation to the bound vibrational spectrum of electronically excited states followed either by radiative decay to the dissociative vibrational continuum of $X^1\Sigma_g^+$ (excitation-radiative-decay dissociation) or predissociation.

- For Dissociative Electron Attachment $H_2(X^1\Sigma_g^+,v) + e^- \rightarrow H + H^-$, the

Table 4.2: *Processes and corresponding reactions included in the Yacora $H_2(X^1, v)$ model aimed to calculate the population densities of the vibrational levels $v = 1-14$ in the electronic ground state $X^1\Sigma_g^+$.*

	Process	Reaction
standard model	Electron Impact (De-)Excitation	$H_2(X^1\Sigma_g^+,v) + e^- \rightleftarrows H_2(X^1\Sigma_g^+,v') + e^-$
	Electron Impact Dissociation	$H_2(X^1\Sigma_g^+,v) + e^- \rightarrow H + H + e^-$
	Dissociative Electron Attachment	$H_2(X^1\Sigma_g^+,v) + e^- \rightarrow H + H^-$
	Proton Charge Transfer	$H_2(X^1\Sigma_g^+,v) + H^+ \rightarrow H_2^+ + H$
	Non-Dissociative Electron Impact Ionization	$H_2(X^1\Sigma_g^+,v) + e^- \rightarrow H_2^+ + e^- + e^-$
	Radiative Recombination	$H_2^+ + e^- \rightarrow H_2(X^1\Sigma_g^+,v') + h\nu$
	Collisional 3-Particle Recombination	$H_2^+ + e^- + e^- \rightarrow H_2(X^1\Sigma_g^+,v') + e^-$
	Electron Impact Excitation into $B^1\Sigma_u^+$ or $C^1\Pi_u$	$H_2(X^1\Sigma_g^+,v) + e^- \rightarrow$ $H_2(B^1\Sigma_u^+ \text{ or } C^1\Pi_u,v') + e^-$
	Electron Impact De-Excitation from $B^1\Sigma_u^+$ or $C^1\Pi_u$	$H_2(B^1\Sigma_u^+ \text{ or } C^1\Pi_u,v') + e^- \rightarrow$ $H_2(X^1\Sigma_g^+,v'') + e^-$
	Spontaneous Emission	$H_2(B^1\Sigma_u^+ \text{ or } C^1\Pi_u,v') \rightarrow$ $H_2(X^1\Sigma_g^+,v'') + h\nu$
	Dissociative Electron Impact Ionization	$H_2(X^1\Sigma_g^+,v) + e^- \rightarrow H^+ + H + e^- + e^-$
	Proton Impact (De-)Excitation	$H_2(X^1\Sigma_g^+,v) + H^+ \rightleftarrows H_2(X^1\Sigma_g^+,v') + H^+$
extending processes	Proton Impact Dissociation	$H_2(X^1\Sigma_g^+,v) + H^+ \rightarrow H + H + H^+$
	H^- Associative Detachment	$H^- + H \rightarrow H_2(X^1\Sigma_g^+,v') + e^-$
	Hydrogen Atom Impact Dissociation	$H_2(X^1\Sigma_g^+,v) + H \rightarrow H + H + H$
	Hydrogen Molecule Impact (De-)Excitation (VT)	$H_2(X^1\Sigma_g^+,v) + H_2(X^1\Sigma_g^+,w) \rightleftarrows$ $H_2(X^1\Sigma_g^+,v \pm 1) + H_2(X^1\Sigma_g^+,w)$
	Hydrogen Molecule Impact (De-)Excitation (VV)	$H_2(X^1\Sigma_g^+,v) + H_2(X^1\Sigma_g^+,w+1) \rightarrow$ $H_2(X^1\Sigma_g^+,v+1) + H_2(X^1\Sigma_g^+,w)$
	H_3^+ Dissociative Recombination	$H_3^+ + e^- \rightarrow H_2(X^1\Sigma_g^+,v') + H$

cross sections from [173] are applied. These calculations use a non-local resonance model based on ab initio data exclusively for the $X^2\Sigma_u^+$ shape resonance. Since a cross section for initial $v = 14$ is lacking, it is derived by scaling the cross section with initial $v = 13$ by a factor derived by extrapolating the decrease of the cross section maxima with increasing v for $v = 10 - 13$.

- For Proton Charge Transfer $H_2(X^1\Sigma_g^+,v) + H^+ \rightarrow H_2^+ + H$, a set of cross sections is compiled from several works: For initial $v = 0$ a combined cross section connecting the measurement from [174] and the calculation from [175] is constructed by a second order spline. For initial $v = 1 - 5$ the cross section fits from [15] are complemented by the calculated cross sections from [176] and connected by a second order spline. For initial $v = 6 - 14$ the cross section fits from [15] are applied.

  The measurements from [174] for collision energies for $E_{\mathrm{CM}} \lessapprox 9.5\,\mathrm{eV}$ are performed with a tandem mass spectrometer using a quadrupole mass filter and an electron multiplier. The calculations from [175] for $E_{\mathrm{H^+}} = 15 - 350\,\mathrm{eV}$ use the quantal vibrational-close-coupling method from [176] with ab initio electronic wave functions. For $E_{\mathrm{H^+}} = 350 - 5\,000\,\mathrm{eV}$ a semiclassical, eikonal method is used accounting for Coriolis couplings due to the rotation of the projectile position vector. These calculations agree with measurements from a proton beam experiment, confirming the existence of a local maximum of the cross section around 45 eV. The cross sections from [176] represent ab initio calculations at $E_{\mathrm{H^+}} = 10 - 10\,000\,\mathrm{eV}$ by vibronic close-coupling expansion in both quantal and semiclassical treatment. The cross section fits from [15] are based on the calculations from [177–180]. The calculations from [177, 178] are performed with the infinite order sudden approximation close-coupling formalism. The calculations from [179, 180] are performed using the trajectory-surface hopping method. It should be noted that this combined set of cross sections does not distinguish between non-reactive ($C^+ + AB(X^1\Sigma_g^+, v) \rightarrow C + AB^+$) and reactive electron capture ($C^+ + AB(X^1\Sigma_g^+, v) \rightarrow A + BC^+$ or $B + AC^+$). This distinction is irrelevant for CR modelling, but should be taken into account for application in neutral transport codes.

- For Non-Dissociative Electron Impact Ionization $H_2(X^1\Sigma_g^+,v) + e^- \rightarrow H_2^+ + e^- + e^-$, the cross sections from [49] are utilized, which are calculated with the semiclassical Gryzinski method.

- For Radiative Recombination $H_2^+ + e^- \rightarrow H_2(X^1\Sigma_g^+,v') + h\nu$, the rate coefficient from [58, 169] is used. This rate coefficient is calculated using the Gaunt factor assuming equal probability for the population of the 15 vibrational levels in $X^1\Sigma_g^+$. The Gaunt factor is a multiplicative so-called fudge factor that can be used to convert classical calculations into calculations with results corresponding to those obtained from quantum calculations [181].

- For Collisional 3-Particle Recombination $H_2^+ + e^- + e^- \rightarrow H_2(X^1\Sigma_g^+,v') + e^-$, the rate coefficient from [58, 169] is used assuming equal probability for population of the 15 vibrational levels of the electronic ground state $X^1\Sigma_g^+$. According to [169] this rate coefficient is calculated from the inverse for Electron Impact Ionization utilizing the Saha equation. Note that processes involving H_2^+ also depend on the vibrational level of H_2^+, this influence is however neglected here.

- For Electron Impact Excitation from the vibrational levels of $X^1\Sigma_g^+$ to the vibrational levels of $B^1\Sigma_u^+$ and $C^1\Pi_u$, the MCCC cross sections from [152] are applied.

- For Electron Impact De-Exciation from the vibrational levels of $B^1\Sigma_u^+$ and $C^1\Pi_u$ to the vibrational levels of $X^1\Sigma_g^+$, rate coefficients are derived from the inverse process applying the principle of detailed balance.

- Spontaneous Emission from the bound vibrational levels of $B^1\Sigma_u^+$ and $C^1\Pi_u$ to the vibrational levels of $X^1\Sigma_g^+$ is included through the Einstein coefficients from [25].

Extended model

- For Dissociative Electron Impact Ionization $H_2(X^1\Sigma_g^+,v) + e^- \rightarrow H^+ + H + e^- + e^-$, the cross sections from [49] are used, which were calculated with the semi-classical Gryzinski method.

- For Proton Impact (De-)Excitation $H_2(X^1\Sigma_g^+,v) + H^+ \rightarrow H_2(X^1\Sigma_g^+,v') + H^+$, a set of cross sections with $\Delta v \leq 4$ is used. These cross sections are derived combining the data from [177] and [182]. In [177] cross sections for $E_{CM} < 9.5\,eV$ are calculated using the fully quantal infinite order sudden approximation. In [182] cross sections for $E_{CM} < 20 - 100\,eV$ are calculated with the semi-classical impact parameter straight-line approximation. The cross sections are combined using a third-degree spline function to connect the different energy ranges.

- For Proton Impact Dissociation $H_2(X^1\Sigma_g^+,v) + H^+ \rightarrow H + H + H^+$, the cross section fits recommended in [15] are applied. These fits are based on the cross sections from [179] (calculations with classical trajectory-surface-hopping method) and [183] (calculations with the infinite order sudden approximation close-coupling formalism). The former calculations are made

with the trajectory-surface-hopping method, where the surface hop takes place on the point of the avoided crossing of two potential energy surfaces of H_3^+ and thus the surface hop is treated as a Landau-Zener type transition [179]. The latter formalism is applicable as long as the collision time is short compared to the typical rotation time, so that the rotation of a diatomic target may be considered frozen during the typical collision event. The validity of the fit is limited to about $E_{\mathrm{CM}} \lessapprox 20\,\mathrm{eV}$.

- For H^- Associative Detachment H^- Associative Detachment $H^- + H \rightarrow H_2(X^1\Sigma_g^+,v') + e^-$, the cross sections from [184] are used. These cross sections are calculated with a non-local resonance model to describe the H_2 collision complex. Since only cross sections populating $v' = 0 - 8$ are calculated, the cross section populating $v' = 8$ is also implemented for the population of $v' = 9 - 14$.

- For Hydrogen Atom Impact Dissociation $H_2(X^1\Sigma_g^+,v) + H \rightarrow H + H + H$, the rate coefficient fit from [16] is employed. It is based on the fit for rate coefficients [168] representing the data from [185]. The latter represent calculations based on the semi-classical trajectory method. The cross sections are obtained by running quasi-classical trajectories on the so-called Liu-Siegbahn-Truhlar-Horowitz [186] potential energy surface. The rate coefficients are calculated by integrating the cross sections over a Maxwell distribution. These rate coefficients are then averaged over a Boltzmann distribution function for rotational states.

- For Hydrogen Molecule Impact (De-)Excitation (VT) the fits from [56] that are based on the rate coefficients from [187] are applied. The latter are calculated with a semiclassical collision model.

- For Hydrogen Molecule Impact (De-)Excitation (VV) the approximation formula from [56] is applied, which is based on the rate coefficients from [188]. The rate coefficients are calculated with a semiclassical dynamical model.

- For H_3^+ Dissociative Recombination $H_3^+ + e^- \rightarrow H_2(X^1\Sigma_g^+,v') + H$, the cross section fit from [16] is scaled using the final level branching ratio from [189]. The cross section fit is derived by applying the channel branching ratio from [190] to the measurements of the total cross section from [191]. The channel branching ratio is determined in a storage ring experiment using an

electron cooler distinguishing between the channels producing $H_2(X^1\Sigma_g^+)$ + $H(n \geq 1)$ and $H(1s)$ + $H(1s)$ + $H(1s)$. The total cross section is measured in a merged beams experiment performed in an ion storage ring. The final level branching ratio is estimated based on statistical assumptions about the redistribution of the energy among the dissociating nuclei and about the population of the electronic potential surfaces.

4.2.2 Benchmarking the model at BUG

The BUG measurements discussed in chapter 3.2.3 are applied to benchmark the *Yacora $H_2(X^1,v)$ model*. The parameters T_e, n_e, T_H, n_H, T_{gas}, n_{H_2}, n_{H^+}, n_{H^-}, $n_{H_2^+}$ and $n_{H_3^+}$ are determined from the measurements and used as input for the model. Thereby, the population density of the vibrational ground level $v = 0$ is set to the constant density n_{H_2} and the gas temperature T_{gas} is used for the molecular hydrogen temperature T_{H_2}. Furthermore, the H^+ and H^- ion temperatures are assumed to match the atomic neutral temperature, since neutral hydrogen typically plays a role in the atomic ion formation (e.g. $T_{H^+} = T_{H^-} = T_H$). When calculating rate coefficients from cross sections, the EDF for each species is assumed to be Maxwellian.

From these input parameters the model calculates self-consistently the excited population densities of the vibrational levels of the electronic ground state $X^1\Sigma_g^+$. Figure 4.11 depicts the normalized densities $n(X^1\Sigma_g^+, v)/n(X^1\Sigma_g^+, v = 0)$ in dependence on the reduced level energy $(E_v - E_{v=0})$ calculated from the previous Yacora model, the standard *Yacora $H_2(X^1,v)$ model* and the extended *Yacora $H_2(X^1,v)$ model*. Additionally, the normalized densities of the spectroscopically accessible first levels corresponding to the measured $T_{vib} = 3\,000 \pm 500\,K$ are shown. Assuming a two-temperature distribution, the parameters $T_{vib\,1}$, $T_{vib\,2}$ and β are derived from fitting the normalized densities $n(X^1\Sigma_g^+, v)/\sum_{v=0}^{14} n(X^1\Sigma_g^+, v)$ of the respective model predictions.

It can be observed that the *previous Yacora model* overestimates the respective densities ($T_{vib\,1} = 7\,700\,K$, $T_{vib\,2} = 20\,000\,K$ and $\beta = 0.14$). Applying the updated input dataset using the standard Yacora model results in a better agreement with the measurement, but the respective densities are also overestimated ($T_{vib\,1} = 6\,700\,K$, $T_{vib\,2} = 20\,000\,K$ and β =0.02). The use of the extended Yacora model yields a considerably better agreement with the measurement, but some discrepancy still remains. The predicted densities follow a single Boltzmann distribution with $T_{vib} = 4\,400\,K$.

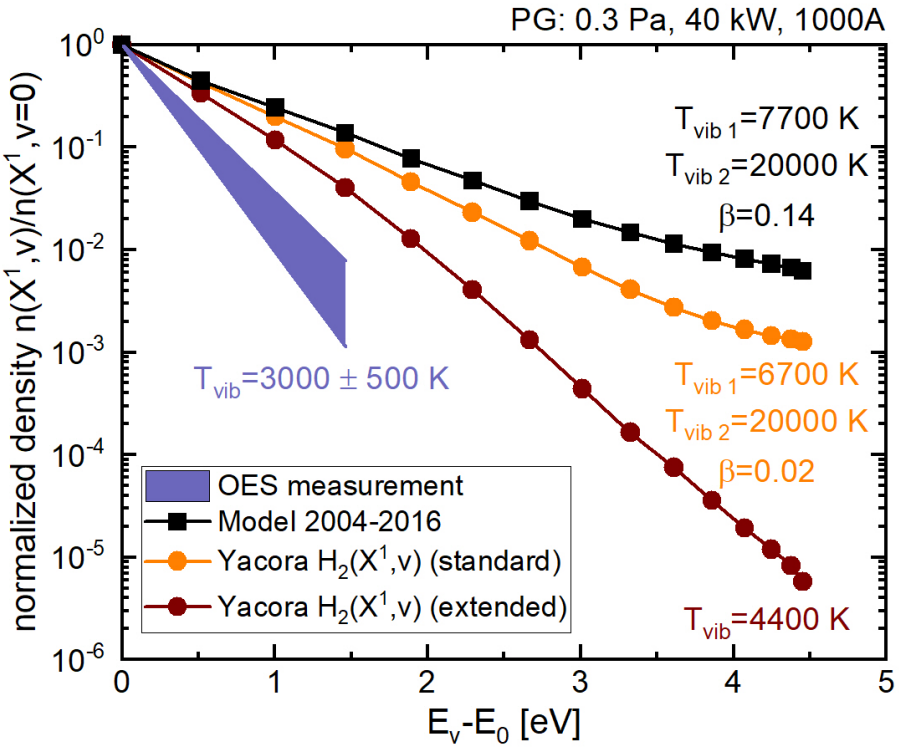

Figure 4.11: *Predictions of the previous Yacora model, the standard and the extended Yacora $H_2(X^1,v)$ model (for the input parameters from table 3.4) compared to the measurement in the form of the normalized level densities in dependence on the reduced level energy for the BUG plasma.*

Furthermore, in order to explain the remaining discrepancy, it is of interest to study, which processes are relevant for the vibrational distribution for the plasma parameters under consideration. To clarify this question, several runs of the *Yacora $H_2(X^1,v)$ model* are performed, whereby the individual processes are switched on or off. The results are depicted in figure 4.12, in addition to the result of the standard and the extended Yacora model for reference: A calculation is performed that solely takes into account Electron Impact Excitation (EIE). Subsequently, calculations are performed, in which additionally Proton Charge Transfer (PCX), Dissociative Electron Attachment (DEA) or Electron Impact Dissociation (EID) are included. It can be seen that the calculation with Electron Impact Dissociation is closest to the result of the standard Yacora model and thus this process has the greatest influence on the predictions of the standard Yacora model. Analogous studies are performed for the transitions via $B^1\Sigma_u^+$ and $C^1\Pi_u$ as well as for the processes of Non-Dissociative Ionization, Dissociative Ionization, Radiative Recombination and Collisional 3-Particle Recombination. However, these processes have little to virtually no influence on the vibrational population distribution. Moreover,

in addition to the processes of the standard Yacora model the processes of the extended Yacora model have been included separately to perform calculations. The processes of Proton Impact Excitation, Proton Impact Dissociation, H^- Associative Detachment, H_3^+ Dissociative Recombination and Hydrogen Molecule Impact Excitation have practically no influence on the vibrational population distribution. Contrarily, when including the process of Hydrogen Atom Impact Dissociation in addition to the standard model (Std+HAID), the results are almost identical to those of the extended Yacora model, demonstrating that Hydrogen Atom Impact Dissociation determines the vibrational population of the extended Yacora model for the investigated plasma parameters.

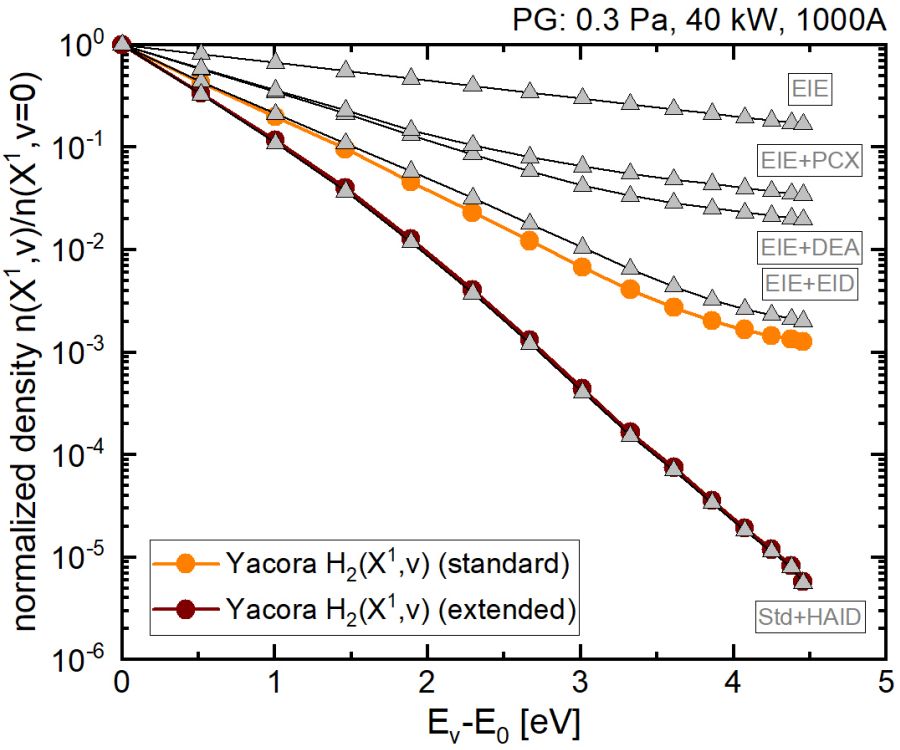

Figure 4.12: *Predictions of the standard and extended Yacora $H_2(X^1,v)$ model as well as individually combined processes in the form of the normalized level densities in dependence on the reduced level energy for the BUG plasma.*

In addition, a sensitivity study is performed to investigate, how sensitive the model results are to changes in input densities and temperatures. When the input temperatures and densities are varied by ±10 %, the qualitative conclusions are the same as those drawn from the investigation of the relevance of the respective processes. The T_{vib} predicted by the extended Yacora model only agrees with the measurement, if T_{H} is varied as model input from the measured 8 000 K to values above 11 000 and below 20 000 K. Note that it can not be ruled out that the

determination of T_H from the broadening of the Balmer-α line (used as input) is too inaccurate, since the supposed presence of different hydrogen atom populations [96] with different temperatures is not accounted for in the process of evaluating the measured line profile. Thus, also dedicated T_H measurements may help to resolve the discrepancy. TALIF measurements at BUG are planned with the aim of obtaining high-resolution T_H and n_H measurements.

On the other hand, the remaining discrepancy between the predictions of the extended model and the measurement may indicate that additional processes are missing in the model or that included processes need to be described with more accurate reaction probabilities. So far plasma-surface interaction processes are not accounted for in neither the standard nor the extended version of the *Yacora $H_2(X^1,v)$ model*. Thus, introducing plasma-surface interaction processes is recommended in the future and may resolve the discrepancy. In addition, the transport of vibrational levels may play a role, due to their long live times [192]. Furthermore, to date, only rate coefficients are available in the literature for the process of Hydrogen Atom Impact Dissociation that have been calculated for fixed, not specified H and H_2 temperatures. Since it has been demonstrated that this process basically determines the vibrational distribution according to the extended model, more accurate reaction probabilities in the form of dedicated cross sections are highly desirable. From such cross sections rate coefficients can be flexibly calculated for different EDFs and varying H and H_2 temperatures.

4.2.3 Benchmarking the model at Magnum-PSI

The Magnum-PSI measurements discussed in chapter 3.2.4 are applied to extend the benchmark of the *Yacora $H_2(X^1,v)$ model* to a different plasma regime (e.g. higher n_e and n_{H^+}). The plasma parameters T_e, n_e, n_H, T_{gas}, n_{H_2}, n_{H^+}, n_{H^-}, $n_{H_2^+}$ and $n_{H_3^+}$ obtained from the measurements are used as input for the CR model. Once again, the population density of the vibrational ground level $v = 0$ is set to the constant density n_{H_2} and the gas temperature T_{gas} is used for the molecular hydrogen temperature T_{H_2}. Since no information about T_H is available yet, two calculations are performed respectively: first, assuming stationary particles ($T_H = 1\,K$) and second, assuming high energy particles with a temperature corresponding to half the H_2 dissociation energy ($T_H = 27\,560\,K$). Note that the evaluation of T_H from the TALIF measurements is currently ongoing [118]. The temperatures of the atomic ions are assumed to be the same as the temperature of the neutral atoms (e.g. $T_{H^+} = T_{H^-} = T_H$). When calculating rate coefficients from

cross sections, the EDF for each species is assumed to be Maxwellian. Calculations are performed using the standard *Yacora $H_2(X^1,v)$ model*, the extended *Yacora $H_2(X^1,v)$ model* and the previous Yacora model.

Figure 4.13 depicts the normalized densities $n(X^1\Sigma_g^+, v)/n(X^1\Sigma_g^+, v = 0)$ in dependence on the reduced level energy $(E_v - E_{v=0})$ from the model calculations and the OES measurement. Note that solely one calculation is shown for the previous Yacora model, as this model is independent of T_H. Assuming a two-temperature distribution, the parameters $T_{vib\,1}$, $T_{vib\,2}$ and β are derived from fitting the normalized densities $n(X^1\Sigma_g^+, v)/\sum_{v=0}^{14} n(X^1\Sigma_g^+, v)$ of the respective model predictions. Analogous to the results from the BUG benchmark, the *Yacora $H_2(X^1,v)$ model* exhibits an improved agreement with the measurement ($T_{vib} = 4\,000 \pm 500\,K$) compared to the previous Yacora model ($T_{vib\,1} = 7\,800\,K$, $T_{vib\,2} = 20\,000\,K$ and $\beta = 0.07$): For calculations with $T_H = 1\,K$, the predictions of the extended model ($T_{vib\,1} = 6\,850\,K$, $T_{vib\,2} = 20\,000\,K$ and $\beta = 0.01$) are slightly closer to the measured values than the standard model ($T_{vib\,1} = 7\,160\,K$, $T_{vib\,2} = 20\,000\,K$ and $\beta = 0.01$). In contrast, for calculations with $T_H = 27\,560\,K$, the results of the standard model ($T_{vib\,1} = 6\,070\,K$, $T_{vib\,2} = 20\,000\,K$ and $\beta = 0.01$) are slightly closer to the measured values than the results of the extended model ($T_{vib\,1} = 6\,420\,K$, $T_{vib\,2} = 20\,000\,K$ and $\beta = 0.01$). This observation can be understood by analyzing the relevant processes for the plasma parameters under consideration.

The relevance of the individual processes for the standard model is shown in figure 4.14. In addition to the standard model predictions, calculations for which solely Electron Impact Excitation and the individual processes are activated are shown. For $T_H = 27\,560\,K$, the result of the calculation including Proton Charge Transfer (PCX) is very close to the result of the standard model (for the levels $v = 0 - 7$), indicating the high relevance of this process. Furthermore, the Electron Impact Dissociation (EID) and the processes involved in the transitions via $B^1\Sigma_u^+$ and $C^1\Pi_u$ are very relevant. Note that the results of the calculations labeled EIE+EID and EIE+B^1+C^1 are very close to each other and can hardly be distinguished in figure 4.14. In addition, Dissociative Electron Attachment (DEA) is more relevant than Proton Charge Exchange for $T_H = 1\,K$.

In order to investigate the relevance of the processes from the extended model, calculations are performed, in which in addition to the standard processes individual processes of the extended model are activated (not explicitly shown here). For $T_H = 1\,K$, Proton Impact (De-)Excitation (PIE) slightly reduces the population densities, while H_3^+ Dissociative Recombination (H_3^+DR) slightly increases the

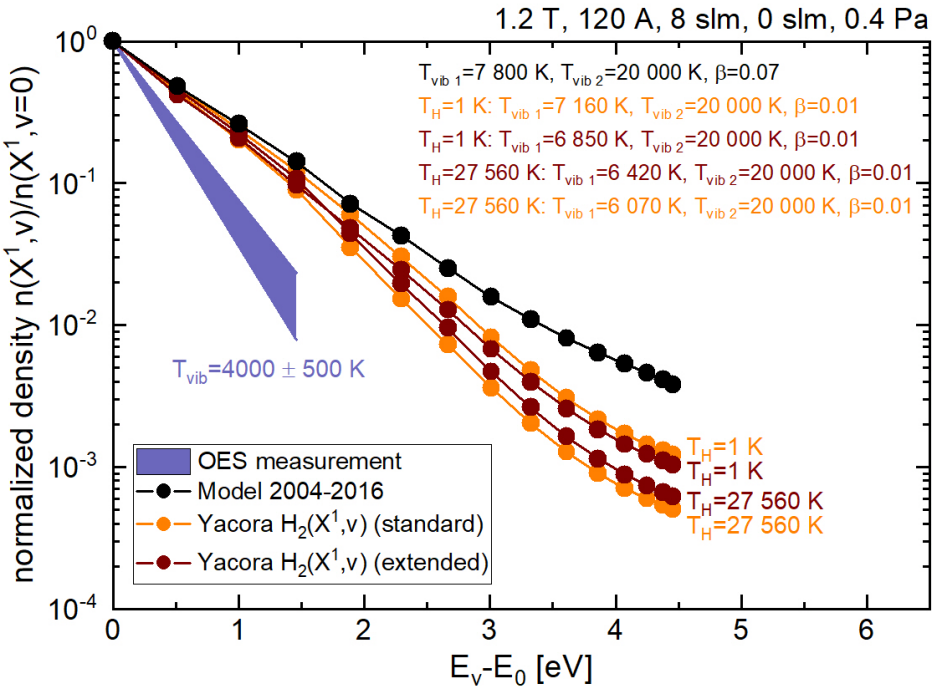

Figure 4.13: *Predictions of the previous Yacora model, the standard and the extended Yacora $H_2(X^1,v)$ model for the parameters from table 3.5 compared to the measurement in the form of the normalized level densities in dependence on the reduced level energy for the Magnum-PSI plasma.*

population densities. For $T_\mathrm{H} = 27\,560\,\mathrm{K}$, however, Proton Impact (De-)Excitation (PIE) increases the population densities, H_3^+ Dissociative Recombination slightly increases the population densities, and Hydrogen Atom Impact Dissociation (HAID) or Proton Impact Dissociation (PID) slightly reduce the population densities. These individual effects collectively result in higher population density predictions by the extended model than by the standard model for $T_\mathrm{H} = 27\,560\,\mathrm{K}$.

Overall, a discrepancy remains between the vibrational distribution determined from the Fulcher-α measurement evaluated with the comprehensive approach and the distribution predicted by either version of the *Yacora $H_2(X^1,v)$ model*. This discrepancy may be attributed to the nature of the different measurements: T_e and n_e are determined from the spatially resolved Thomson scattering measurements. These measurements reveal a strong radial profile for the plasma under examination. As mentioned above, the peak values are used as input for the 0-dimensional CR model calculations. The peak T_e values are also input for the evaluation of the line of sight averaged Fulcher-α band measurement using the comprehensive approach. When repeating the Fulcher-α band evaluation based on smaller T_e values, higher results for T_vib from the measurement are obtained and when repeating the *Yacora $H_2(X^1,v)$ model* calculations with either model version for

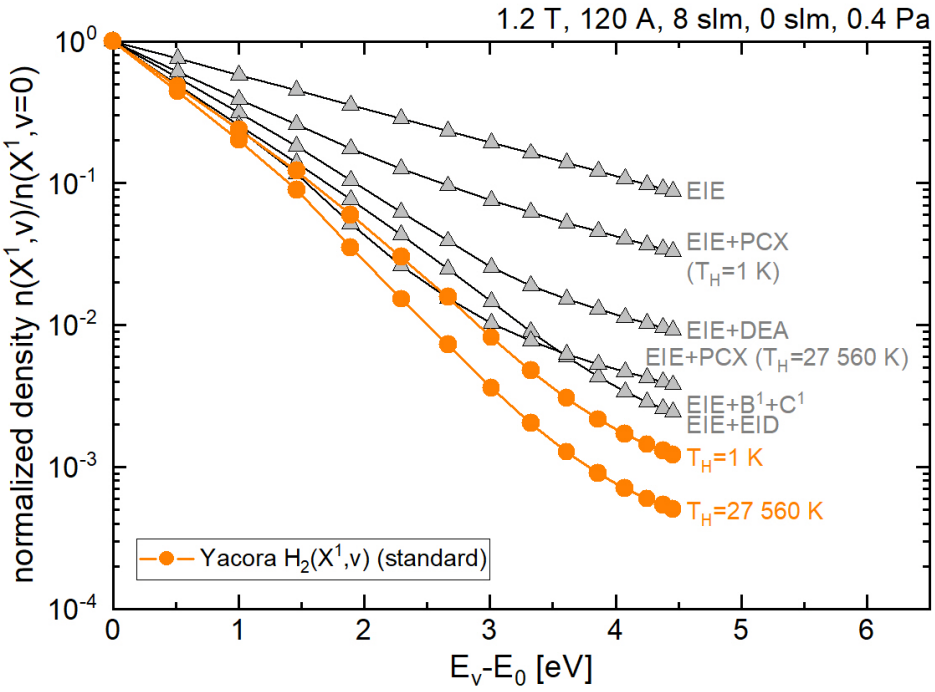

Figure 4.14: *Predictions of the standard Yacora $H_2(X^1,v)$ model and individually combined processes in the form of the normalized level densities in dependence on the reduced level energy for the Magnum-PSI plasma.*

the same plasma parameters with the exception of smaller T_e values, lower values of T_{vib} are predicted. In future work, the influence of the radial profile can be resolved by analyzing the data for further lines of sight from the OES measurements and performing an Abel inversion (see e.g. [45]) to obtain radially resolved emission profiles. Furthermore, again it is possible that the inclusion of surface processes or the transport of vibrational levels may play a role and must be checked in a future step. Finally, an upcoming CARS campaign at Magnum-PSI is aimed to determine T_{vib} independently, which may also help to resolve the remaining discrepancy between the present measurement and the *Yacora $H_2(X^1,v)$ model* predictions.

4.3 The Yacora H_2(v) model

The *Yacora $H_2(v)$ model* combines and extends certain aspects of the *Yacora $H_2(X^1,v)$ model* and the *Yacora H_2 model*: It fully comprises the levels and processes of the *Yacora $H_2(X^1,v)$ model* and contains in addition the processes and electronic states of the *Yacora H_2 model*, whereby the Λ-resolved electronic states with $n = 1 - 3$ and processes involving them are vibrationally resolved.

4.3.1 Detailed model description

Figure 4.15 depicts the states and levels contained in the *Yacora $H_2(v)$ model*. For the energies of the vibrational levels, the values determined from MCCC calculations (see below) are used.

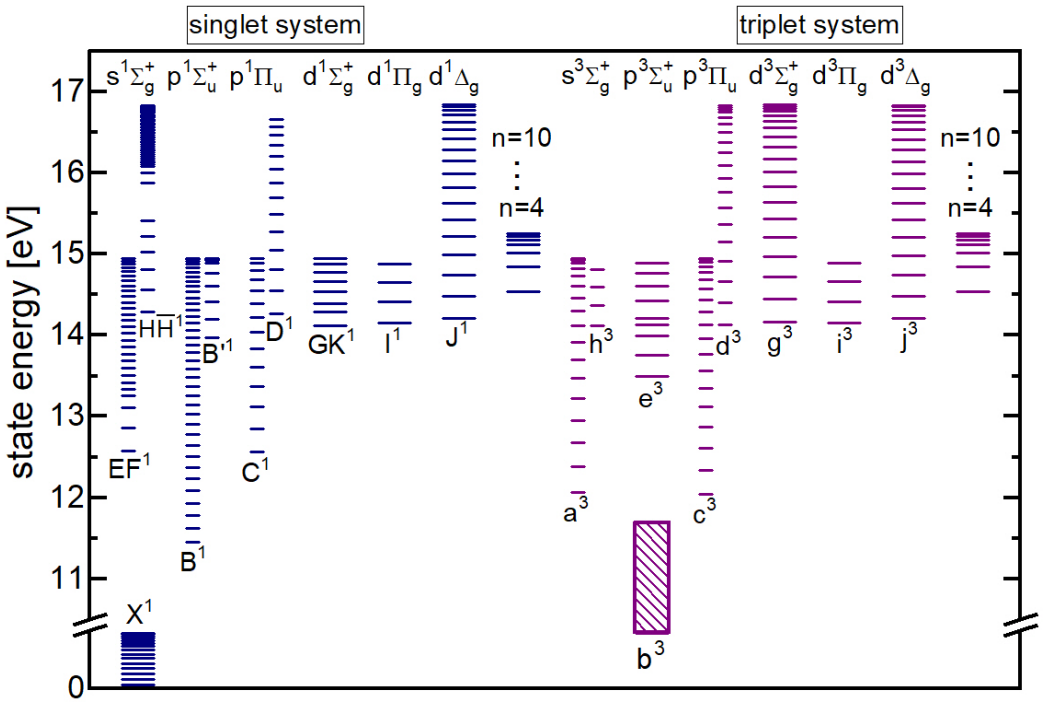

Figure 4.15: *Vibrational levels of H_2 considered in the Yacora H_2 model with respect to the minimum of the potential curve of the ground state $X^1\Sigma_g^+$. Note that only the states with $n < 4$ are Λ resolved and vibrationally resolved.*

Table 4.3 lists the processes and reactions considered in this model.

- For the description of the processes included in the *Yacora $H_2(X^1,v)$ model*, see the discussion in 4.2.
- For Electron Impact Excitation $H_2(X^1\Sigma_g^+,v) \rightarrow H_2(n = 2,3;\Lambda_\sigma,v')$ MCCC cross sections [157] are applied.

Table 4.3: *Processes and corresponding reactions included in the Yacora $H_2(v)$ model.*

Process	Reaction
$H_2(X^1,v)$ model	see the model
Electron Impact (De-)Excitation	$H_2(N\Lambda_\sigma,v) + e^- \rightleftarrows H_2(N'\Lambda'_{\sigma'},v') + e^-$
Electron Impact Dissociation	$H_2(N\Lambda_\sigma,v) + e^- \rightarrow H + H + e^-$
Non-Dissociative Electron Impact Ionization	$H_2(N\Lambda_\sigma,v) + e^- \rightarrow H_2^+ + 2\,e^-$
Dissociative Electron Impact Ionization	$H_2(N\Lambda_\sigma,v) + e^- \rightarrow H + H^+ + e^- + e^-$
Spontaneous Emission	$H_2(N\Lambda_\sigma,v) \rightarrow H_2(N'\Lambda'_{\sigma'},v') + h\nu$
Dissociative Electron Attachment	$H_2(N\Lambda_\sigma,v) + e^- \rightarrow H + H^-$
Proton Charge Transfer	$H_2(N\Lambda_\sigma,v) + H^+ \rightarrow H_2^+ + H$
Collisional Quenching	$H_2(a^3\Sigma_g^+$ or $c^3\Pi_u,v) + H_2(X^1\Sigma_g^+,v=0) \rightarrow 2\,H_2(X^1\Sigma_g^+,v=0)$

- For Electron Impact (De-)Excitation $H_2(n=2;\Lambda_\sigma,v) \rightarrow H_2(n=1,2,3;\Lambda_\sigma,v')$ MCCC cross sections [157] are used.
- Electron Impact De-Excitation rate coefficients for $H_2(n=3;\Lambda_\sigma,v) \rightarrow H_2(n=1,2;\Lambda_\sigma,v')$ are derived from the inverse process after the principle of detailed balance.
- To describe Electron Impact Excitation, Electron Impact De-Excitation and Non-Dissociative Ionization involving the states $H_2(n=4-10,v)$, the respective purely electronically resolved data from the *Yacora H_2 model* are used. Thereby, the lower excitation threshold of the excited vibrational levels within these electronic states is neglected.
- For Electron Impact Dissociation originating from $H_2(n=2;\Lambda_\sigma,v)$, MCCC cross sections [157] are utilized.
- For Non-Dissociative Ionization $H_2(n=2,3;\Lambda_\sigma,v)$, cross sections calculated with the Gryzinski method from [49] are applied.
- For Dissociative Ionization $H_2(n=2;\Lambda_\sigma,v)$, cross sections calculated with the Gryzinski method from [49] are applied.
- Spontaneous Emission from initial $H_2(n=2,3;\Lambda_\sigma,v)$ is implemented applying Einstein coefficients from [25].

- Spontaneous Emission from $H_2(c^3\Pi_u,v)$ to $H_2(X^1\Sigma_g^+,v)$ is optically forbidden. To account for magnetic dipole and electric quadrupole interactions, the transition rate $10^3\,s^{-1}$ [15] is implemented.

- Spontaneous Emission from initial $H_2(n = 4-10)$ is included applying scaled Einstein coefficients from the *Yacora H_2 model*. The Einstein coefficients linking electronically resolved states are scaled considering that Einstein coefficients are inversely proportional to λ^3, whereby λ corresponds to the energy difference of the states involved in the transition [136]. The Einstein coefficient $A_{v''}^{n',N''\Lambda''_{\sigma''}}$ for the transition of a non-Λ-resolved state into a vibrational level of a Λ-resolved state can be expressed as:

$$A_{v''}^{n',N''\Lambda''_{\sigma''}} = A^{n',N''\Lambda''_{\sigma''}} \frac{(\lambda_{v''}^{n',N''\Lambda''_{\sigma''}})^{-3}}{\sum_{v''}(\lambda_{v''}^{n',N''\Lambda''_{\sigma''}})^{-3}}\,. \tag{4.4}$$

- For Proton Charge Transfer with $H_2(n = 2,3;\Lambda_\sigma,v)$ and $H_2(n = 4-10)$, the cross sections from the *Yacora H_2 model* are applied. These are cross sections from the classical over barrier transport model adapted to molecules from [15]).

- Dissociative Electron Attachment for (vibrational levels of) electronically excited states is included applying the constant rate coefficients motivated by [161, 162]. For de-populating $H_2(n = 2;\Lambda_\sigma,v)$ the constant rate coefficient $X = 10^{-15}\,m^3/s$ and for de-populating $H_2(n = 3;\Lambda_\sigma,v)$ and $H_2(n = 4-10)$ the constant rate coefficient $X = 6\cdot10^{-11}\,m^3/s$ are applied. These rather extraordinary high values are well known to be controversial in the literature [15, 163].

- For Collisional Quenching of $H_2(a^3\Sigma_g^+$ or $c^3\Pi_u,v)$ the experimentally determined rate constants from [165] are used. These rate constants are used for all excited levels of the respective electronic state.

Note that all excited level and state densities are determined by the Yacora model under the quasi-steady-state approximation and n_{H_2} (e.g. determined from measurements or other calculations) is used as input to the model for the ground level of the electronic ground state (e.g. $n(X^1\Sigma_g^+, v = 0) = n_{H_2}$). As a consequence, the sum of the densities of the excited vibrational levels in $X^1\Sigma_g^+$ equals or exceeds (depending on the plasma parameters) n_{H_2}. Due to the simultaneous calculation of the vibrational levels in $X^1\Sigma_g^+$ and the vibrational levels of the electronically

excited states, it is also to be expected that the population densities of (vibrational levels of electronically) excited states are overestimated. Since the extent of the overestimation is not known prior to the calculation, it cannot be accounted for within the model. The influence of this overestimation is examined below. For the following analyses, solely the processes of the standard *Yacora $H_2(X^1,v)$ model* are activated in the *Yacora $H_2(v)$ model*.

4.3.2 Benchmarking the model

To investigate, how well the predictions of the *Yacora $H_2(v)$ model* agree with the measurements and the predictions of the electronically resolved model, the plasma parameters from the previously discussed inductively coupled plasma experiment PlanICE (from chapter 3.2.1) are applied. Thereby, $n_{\mathrm{H_2}}$ is utilized for $n(X^1\Sigma_g^+,v=0)$. Since $n_{\mathrm{H^+}}$ and $n_{H_2^+}$ are not determined from the experiment, $n_{\mathrm{H^+}} = n_{H_2^+} = 0.5\ n_e$ is assumed (according to the ratio suggested in [99]). This assumption affects the population of the vibrational levels in the electronic ground state and the de-population of the vibrational levels of the electronically excited states through Proton Charge Transfer.

Figure 4.16 shows the population density of the $d^3\Pi_u$ state for the electronically resolved *Yacora H_2 model* and the vibrationally resolved *Yacora $H_2(v)$ model* (that self-consistently predicts the vibrational population of the electronic ground state). The *Yacora $H_2(v)$ model* predicts population densities that are $1.4-2.1$ times higher than those of the electronically resolved model. This observation is a consequence of the simultaneous calculation of the population densities of the vibrational levels in the electronic ground state and in the electronically excited states: Since $n(X^1\Sigma_g^+, v=0) = n_{\mathrm{H_2}}$, it follows that the sum of the calculated population densities of all vibrational levels in the electronic ground state exceeds $n_{\mathrm{H_2}}$ (e.g. $\sum_v n(X^1\Sigma_g^+(v)) > n_{\mathrm{H_2}}$). Scaling the results of the *Yacora $H_2(v)$ model* by the factor $\frac{n_{H_2}}{\sum_v n(X^1\Sigma_g^+(v))}$ (to account for the higher model determined sum of vibrational levels in the electronic ground state compared to n_{H_2}) yields population densities close to the results of the electronically resolved model (e.g. $1.03-1.19$ times higher $d^3\Pi_u$ population densities than the electronically resolved model). The calculations of the *Yacora $H_2(v)$ model* with fixed, vanishing population densities of the excited vibrational levels of the electronic ground state (e.g. $n(X^1\Sigma_g^+,v=1-14)= 0\,\mathrm{m^{-3}}$, labeled as $T_{\mathrm{vib}}(X^1\Sigma_g^+)= 0\,\mathrm{K}$) yields comparable population densities too.

Consequently, for quantitative statements it should be kept in mind that due

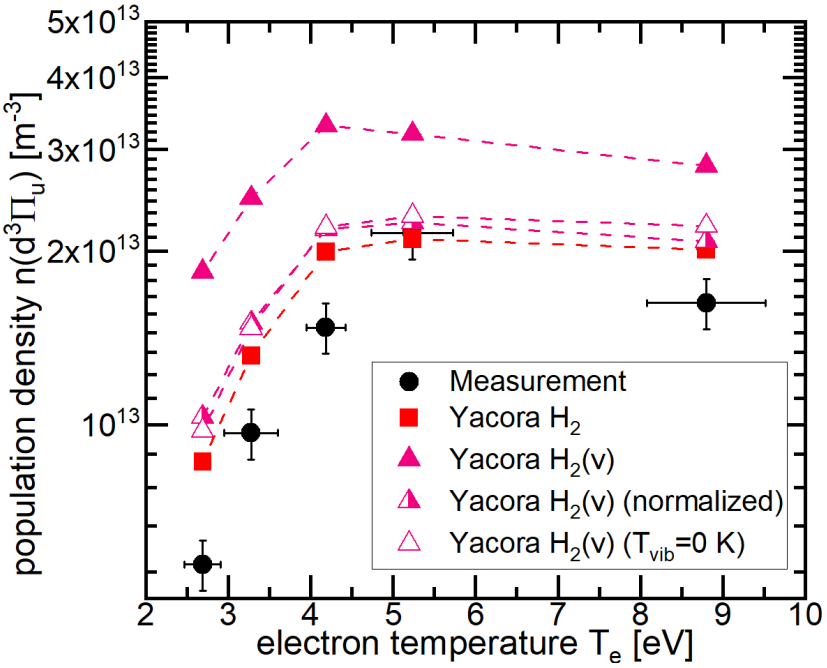

Figure 4.16: *Population density of the $d^3\Pi_u$ state predicted by the Yacora H_2 model, the Yacora $H_2(v)$ model, the Yacora $H_2(v)$ model scaled with a normalization factor and the Yacora $H_2(v)$ model keeping the population of the excited vibrational levels of $X^1\Sigma_g^+$ at 0. The measured densities from the PlanICE experiment are shown as well.*

to the overestimation of the ground state density, also the excited state density is overpredicted. When accounting for the evaluated factor in the vibrationally resolved model, the differently resolved models essentially agree with each other. Thereby, the advantage of the vibrationally resolved *Yacora $H_2(v)$ model* is, that reaction probabilities can be taken into account physically more accurately, namely individually for each vibrational level.

4.3.3 Post-processing EDGE2D-EIRENE JET profiles for comparison with AMJUEL

As already discussed in chapter 3.3, the AMJUEL database is usually utilized as input for EIRENE calculations. AMJUEL provides effective rates and population densities that are derived from the *Sawada 1995 CR model*. This CR model is again based on Electron Impact Excitation cross sections from [149] (Miles) and neglects processes such as Dissociative Electron Attachment and Proton Charge Transfer. Since it is demonstrated in chapter 4.1 that a CR model applying MCCC cross sections generally achieves the best agreement with measurements, the aim of this chapter is to compare predictions from the *Yacora $H_2(v)$ model*

with predictions from AMJUEL and to investigate how molecular data influences the interpretation of measurements. Main parts of the analysis described here have recently been published in [193].

For the comparison, 2D poloidal EDGE2D-EIRENE profiles of the plasma and neutral particle conditions from [127] are utilized. These profiles are calculated for JET ITER-like wall (tungsten in the divertor, berrylium in the main chamber) L-mode plasmas (plasma current $I_\mathrm{p} = 2.5\,\mathrm{MA}$, toroidal magnetic field $B_\mathrm{t} = 2.5\,\mathrm{T}$, core power $P_\mathrm{core} = 1.1\,\mathrm{MW}$) with hydrogen as the main plasma species and impurities of beryllium. Note that in these EIRENE calculations the transport of vibrationally excited levels or electronically excited states is not included. Typically, these omissions are made in EIRENE calculations to reduce the computational effort, although following the transport of vibrationally excited levels (in the electronic ground state) is due to their long lifetimes physically more accurate [192].

Figure 4.17 shows the total ion current to the low field side target plate $I_\mathrm{LFS,plate}$ in dependence on n_e adjacent to the separatrix low field side midplane position: The red line represents the EDGE2D-EIRENE calculations and the scatter stems from Langmuir probe measurements for JET pulse number 91284. Although, as stated in [194], the $n_\mathrm{e}^\mathrm{sep,LFS,mp}$ at which the predicted $\mathrm{I_{LFS,plate}}$ peaks, agrees with the measurements, the absolute value of $I_\mathrm{LFS,plate}$ and its relative dependence on $n_\mathrm{e}^\mathrm{sep,LFS,mp}$ differ. The different stages during detachment are characterized by the electron density at the outer midplane separatrix $n_\mathrm{e}^\mathrm{sep,omp}$. Three cases with distinct $n_\mathrm{e}^\mathrm{sep,omp}$ are utilized for the further analysis: $n_\mathrm{e}^\mathrm{sep,omp} = 0.7 \cdot 10^{19}\,\mathrm{m}^{-3}$ (for the low recycling regime), $n_\mathrm{e}^\mathrm{sep,omp} = 1.3 \cdot 10^{19}\,\mathrm{m}^{-3}$ (for the high recycling regime) and $n_\mathrm{e}^\mathrm{sep,omp} = 2.0 \cdot 10^{19}\,\mathrm{m}^{-3}$ (for the detached regime).

EDGE2D predicts 2D profiles of n_e and T_e. EIRENE predicts n_H, n_{H_2}, n_{H^+} and $n_{\mathrm{H}_2^+}$ on a 2D grid encompassing the EDGE2D grid and the halo plasma region between the outermost EDGE2D grid edge and the vessel wall. As an example, figure 4.18 depicts the n_{H_2} profile of the high recycling plasma ($n_\mathrm{e}^\mathrm{sep,omp} = 1.3 \cdot 10^{19}\,\mathrm{m}^{-3}$) for the entire simulation domain. It can be seen that the highest H_2 densities occur in the divertor region. In addition, the orientation of artificial lines of sight starting at the pivot point going to the divertor plates (used below as synthetic diagnostic) are indicated. The red box marks the divertor region for which plasma parameter profiles (n_{H_2}, n_H, n_e and T_e) are shown in figure 4.19. Therein, it can be noted that n_{H_2} is higher than n_H in the area close to the divertor plates. The position of the X-point can be determined from the T_e profile.

The plasma parameter profiles are post-processed with the *Yacora $H_2(v)$ model*:

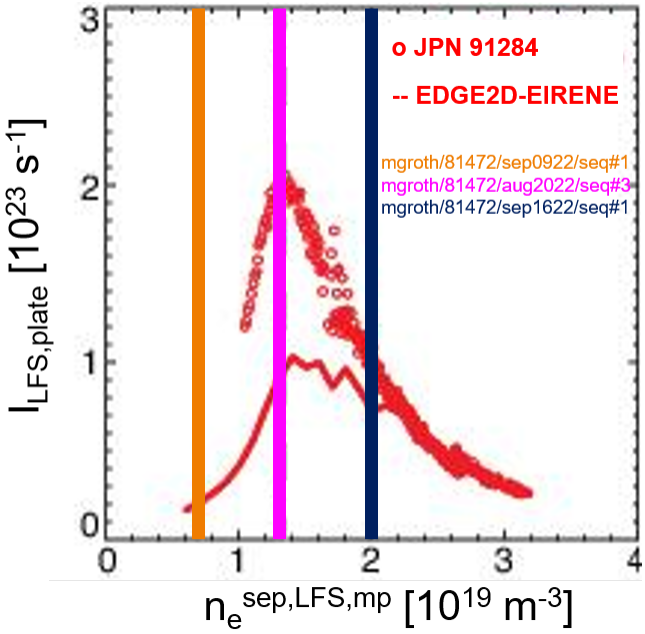

Figure 4.17: *Total ion current to the low field side target plate in dependence on n_e adjacent to the separatrix low field side midplane from measurements (JET pulse number 91284) and EDGE2D-EIRENE calculations. The vertical lines indicate the plasma regimes post-processed below. Figure adapted from [194].*

T_e, T_{H^+}, n_e, n_{H^+}, $n_{H_2^+}$, n_{H_2} are utilized as model input. For the calculation of rate coefficients from cross sections, Maxwellian EDFs are assumed. Since T_{H_2} is a necessary input parameter for the CR model, but it is not determined within EDGE2D-EIRENE, it is assumed to be small ($T_{H_2} = 1\,\mathrm{K}$). The influence of this assumption is tested and it is found that it has negligible effect on the emission prediction, as T_{H_2} is solely relevant for Proton Charge Transfer that again has low relevance for the set of plasma parameters under investigation. As stated above, n_{H_2} is utilized for $n(X^1\Sigma_g^+, v = 0)$. The excited level densities for the $d^3\Pi_u$, $B^1\Sigma_u^+$ and $C^1\Pi_u$ states are then multiplied by the respective individual Einstein coefficients and summed to obtain the entire Fulcher-, Lyman- and Werner band emission.

Figure 4.20 shows 2D profiles of the Fulcher band emission intensity for the high recycling plasma ($n_e^{sep,omp} = 1.3 \cdot 10^{19}\,\mathrm{m}^{-3}$) predicted by AMJUEL and the *Yacora $H_2(v)$ model*, as well as the respective ratio (Yacora/AMJUEL). The *Yacora $H_2(v)$ model* predicts generally lower Fulcher band emission than AMJUEL.

In order to compare the different model predictions also in a line of sight-integrated form in which emission measurements are obtained, synthetic lines of sight in the form of cones with finite etendue are introduced on the EIRENE

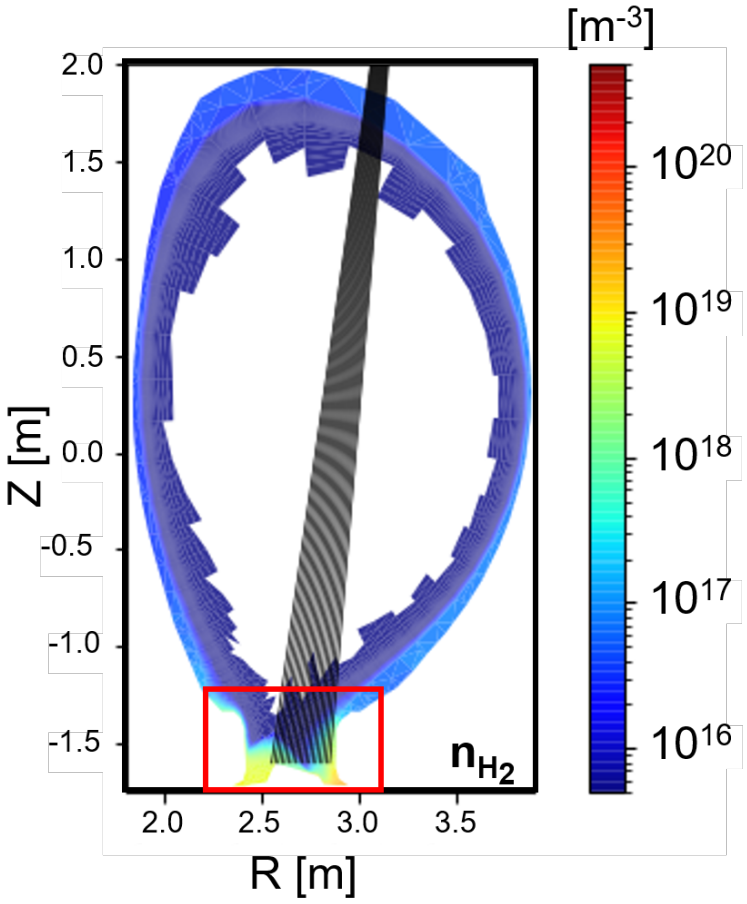

Figure 4.18: *n_{H_2} profile from EDGE2D-EIRENE for a JET ITER-like wall L-mode high recycling plasma ($n_e^{sep,omp} = 1.3 \cdot 10^{19}\,m^{-3}$). The black lines indicate the orientation of the artificial lines of sight. The red box marks the divertor region for which plasma parameter profiles are shown in figure 4.19.*

grid, pointing from the low-field side divertor to the pivot point in the tokamak top half (orientation shown in figure 4.18). For further comparison, the spatially resolved emission is integrated along the respective line of sight paths. The line of sight-integrated Fulcher-, Lyman- and Werner band emission for the three characteristic plasma regimes is shown in figure 4.21.

The *Yacora $H_2(X^1,v)$ model* predicts in comparison to AMJUEL line of sight-integrated about 2 times lower Fulcher band emission for the low recycling plasma ($n_e^{sep,omp} = 0.7 \cdot 10^{19}\,m^{-3}$), about 5 times lower emission for the high recycling plasma ($n_e^{sep,omp} = 1.3 \cdot 10^{19}\,m^{-3}$) and about 6 times lower emission for the detached plasma ($n_e^{sep,omp} = 2.0 \cdot 10^{19}\,m^{-3}$).

Furthermore, the *Yacora $H_2(X^1,v)$ model* predicts line of sight-integrated about 4 times higher Lyman band emission and about 2 times higher Werner band

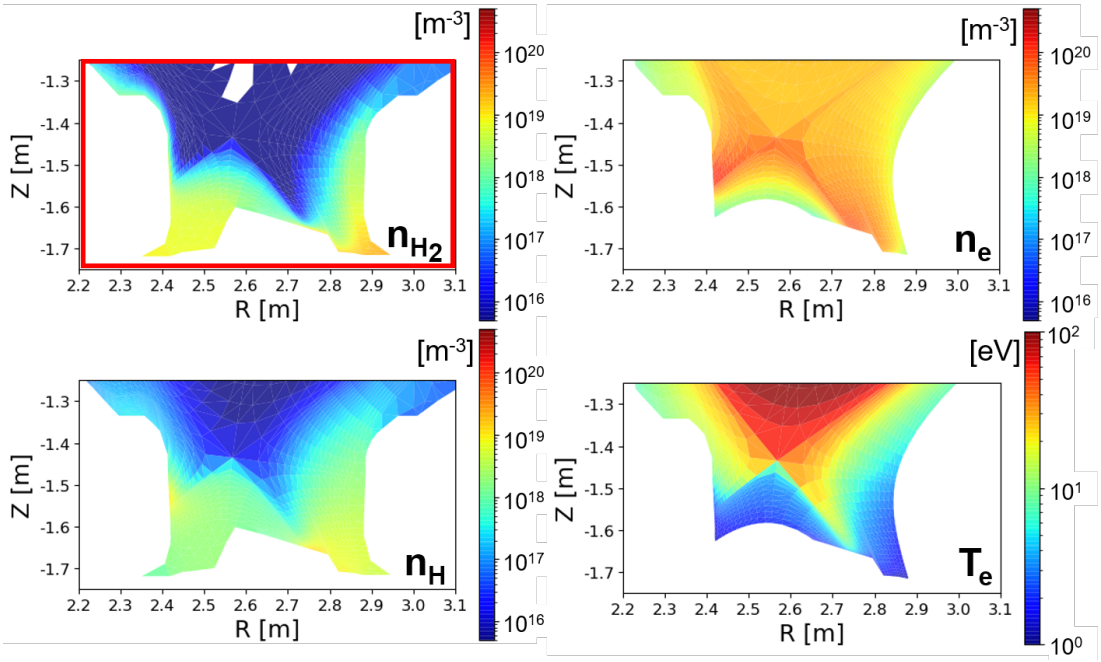

Figure 4.19: *Profiles for n_{H_2}, n_H, n_e and T_e from EDGE2D-EIRENE for a high recycling plasma ($n_e^{sep,omp} = 1.3 \cdot 10^{19}\,m^{-3}$).*

emission compared to AMJUEL, independent on the detachment stage.

The discrepancy in emission predictions between the *Yacora $H_2(v)$ model* and AMJUEL is a consequence of applying different reaction probabilities for the same processes and different sets of processes considered in the respective models. The Yacora model applies benchmarked MCCC cross sections for Electron Impact Excitation that are larger for the transitions from $X^1\Sigma_g^+$ to $B^1\Sigma_u^+$, $C^1\Pi_u$ and $d^3\Pi_u$ than the cross sections used in the Sawada 1995 model. The consequent increase in the rates would in itself result in higher Lyman-, Werner- and Fulcher band emission intensities.

Note that when accounting for the multiplicative factor $\frac{n_{H_2}}{\sum_v n(X^1\Sigma_g^+(v))}$ discussed in chapter 4.3.2 in the Yacora calculations, the emission ratio for the Fulcher band would be even smaller.

Dissociative Electron Attachment for (vibrational levels of) electronically excited states is included in the *Yacora $H_2(v)$ model* but not in the Sawada 1995 model. According to the model predictions this process dominates the de-population of the $d^3\Pi_u$ state (see e.g. figure 4.6) for high electron densities ($n_e \approx 10^{19}\,m^{-3}$). Since this process is not included in the Sawada 1995 model, lower $d^3\Pi_u$ densities are obtained overall from the *Yacora $H_2(v)$ model* compared to AMJUEL, despite the larger Electron Impact Excitation cross section in the *Yacora $H_2(v)$ model*. In contrast, for $B^1\Sigma_u^+$ and $C^1\Pi_u$ the respective constant Dissociative Electron

Attachment rate coefficient is several orders of magnitude smaller than that for the $d^3\Pi_u$ state (see chapter 4.3.1). Thus, Dissociative Electron Attachment does not dominate the de-population of these states (see e.g. figure 4.4 in chapter 4.1) and higher overall band emission is obtained.

The extent to which Dissociative Electron Attachment reduces the densities of vibrational levels of the $X^1\Sigma_g^+$ and $d^3\Pi_u$ states in the *Yacora H_2(v) model* is demonstrated in figure 4.22 for the plasma parameters of the marked cell in figure 4.21 ($T_e = 4.3\,\text{eV}$, $T_H = 5\,\text{eV}$, $n_e = n_{H^+} = 5.9{\cdot}10^{19}\,\text{m}^{-3}$, $n_{H_2^+} = 1.2{\cdot}10^{17}\,\text{m}^{-3}$, $n_{H_2} = 9.9 \cdot 10^{18}\,\text{m}^{-3}$). The population densities of the levels of the $d^3\Pi_u$ state calculated with a model run without Dissociative Electron Attachment for (vibrational levels of) electronically excited states results in population densities more than one order of magnitude higher than those of the standard model (see top part of figure 4.22). In contrast, the population densities of the levels of the $X^1\Sigma_g^+$ state are similar for the standard model and the calculations without Dissociative Electron Attachment for the vibrational levels of the electronic ground state (see bottom part of figure 4.22).

The constant rate coefficient for Dissociative Electron Attachment of electronically excited states from [162] is already under debate in the literature and known to be surprisingly high [15, 163]. In view of the high relevance of the Fulcher band for plasma diagnostics, studies on accurate cross sections for this process are highly desired.

The discrepancy in the emission predictions between the *Yacora H_2(v) model* and AMJUEL has further implications: Inconsistent results for the molecular density are expected when deriving it from the measured band emission, depending on which model and which molecular emission band is used (due to the anti-symmetric discrepancy for the different emission bands). For instance the overestimation of the molecular emission results in the underestimation of the n_{H_2} density and thus in the underestimation of MAR rates.

Based on the *Yacora H_2(v) model*, AMJUEL seems to overestimate the Fulcher band emission. This observation is in agreement with [195], where it is demonstrated that AMJUEL overestimates the Fulcher band emission for deuterium plasmas in DIII-D.

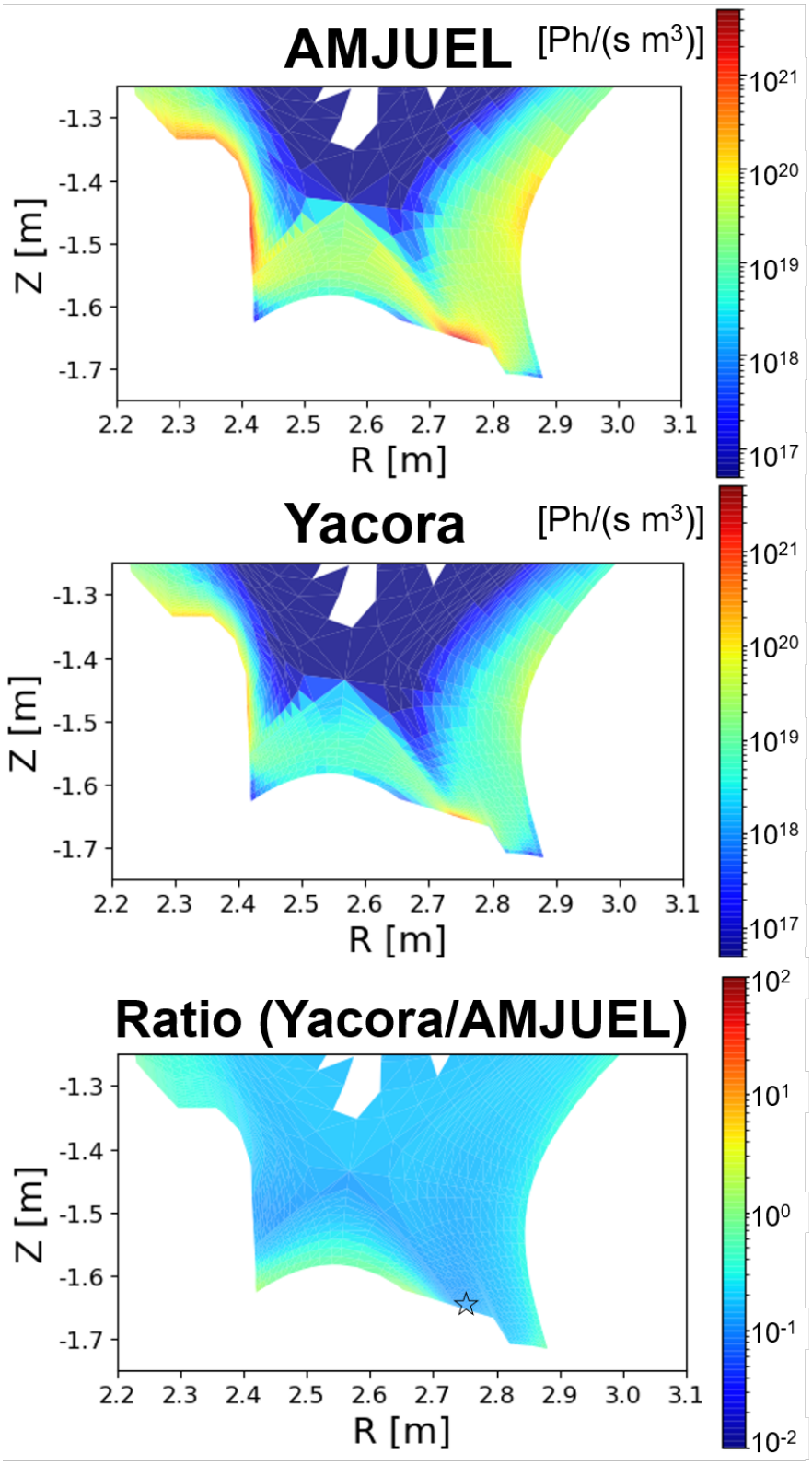

Figure 4.20: *Fulcher band emission intensity [Ph/(s m^3)] predicted by AMJUEL and the Yacora $H_2(X^1,v)$ model and their ratio for a high recyling plasma ($n_e^{sep,omp} = 1.3 \cdot 10^{19}\,m^{-3}$). Note the star in the ratio profile marking the position for which additional calculations are discussed below.*

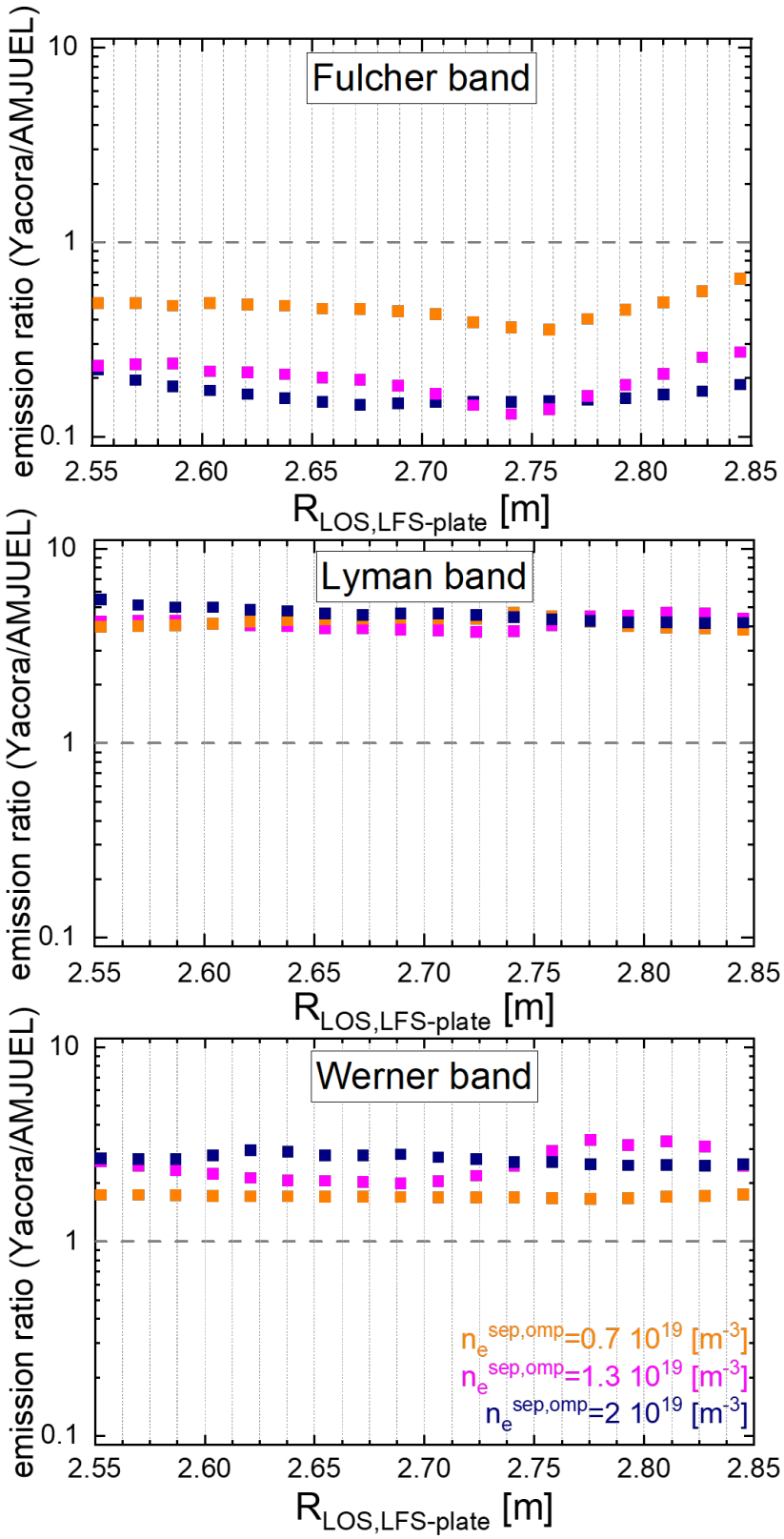

Figure 4.21: *Ratios of predicted Fulcher-, Lyman- and Werner band emission between Yacora and AMJUEL integrated over the synthetic line of sight directed to the LFS divertor.*

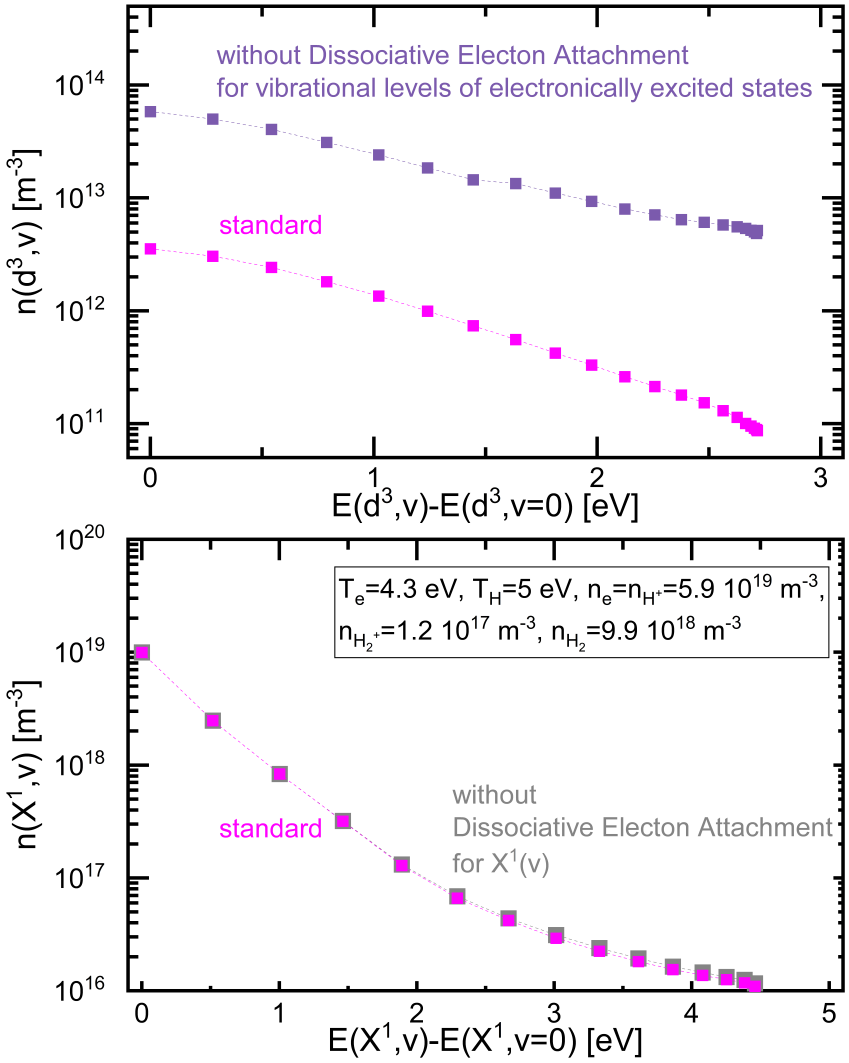

Figure 4.22: *Vibrational level population densities for $X^1\Sigma_g^+$ and $d^3\Pi_u$ predicted from the Yacora $H_2(X^1,v)$ model for the plasma parameters of a single grid cell of the high recycling plasma ($n_e^{sep,omp} = 1.3 \cdot 10^{19}\,m^{-3}$) in a standard model run, a calculation without dissociative electron attachment for electronically excited states and a calculation without dissociative electron attachment for the vibrational levels of the electronic ground state.*

4.3.4 Post-processing modified EDGE2D-EIRENE DIII-D deuterium plasma profiles

This chapter continues the comparison of the AMJUEL and *Yacora $H_2(v)$ model* predictions utilizing 2D poloidal profiles of the plasma and neutral particle conditions from EDGE2D-EIRENE for DIII-D deuterium plasmas. Since the vibrational levels in D_2 differ from the levels in H_2, this investigation may introduce a systematic error and should solely be regarded as first approximation and thus be repeated once a dedicated CR model for D_2 is available. The EDGE2D-EIRENE DIII-D L-mode profiles for a high-recycling deuterium plasma stem from [134, 135] and are based on previously established calculations from [195, 196] that are modified by imposing measured 2D T_e and n_e profiles (from Thomson scattering) and 1D ion saturation current j_{sat} profiles (from Langmuir probes). The previously established calculations are performed for deuterium with carbon as impurity (plasma current $I_p = 1.1\,\mathrm{MA}$, toroidal magnetic field $B_t = 2.1\,\mathrm{T}$, core power $P_{core} = 1.2\,\mathrm{MW}$, $n_e^{sep,omp} = 2 \cdot 10^{19}\,\mathrm{m}^{-3}$). The modification of these previously established EDGE2D-EIRENE calculations is motivated by their disagreement with measurements for high-recycling conditions (e.g. the calculations predict broader T_e and n_e profiles than observed by Thomson scattering measurements [195]). It should be noted that measurements to impose on the previously established calculations are not available for the entire EDGE2D-EIRENE profiles. Within the works of [195, 196], EIRENE is executed standalone for the modified profiles to predict the molecular emission yield according to AMJUEL.

The modified EDGE2D-EIRENE profiles for deuterium plasmas (T_e, T_{D^+}, n_e, n_{D^+}, $n_{D_2^+}$, n_{D_2}) are used as input for the *Yacora $H_2(v)$ model* to calculate the molecular emission yield. As the temperature of the molecular neutrals is not determined within EDGE2D-EIRENE, again it is assumed to be low ($T_{D_2} = 1\,\mathrm{K}$).

Analogous to the evaluation for the JET calculations, synthetic lines of sight are introduced at the EIRENE grid oriented towards the LFS divertor plate and the predicted emission (by AMJUEL or the Yacora model) is integrated along the lines of sight. The line of sight-integrated emission for the Lyman band, Werner band and Fulcher band is compared in figure 4.23 showing the emission ratio (Yacora/AMJUEL) in dependence on the detector angle. Yacora predicts higher emission yields for the Lyman band and Werner band and lower emission yield for the Fulcher band than AMJUEL. Note that this observation is consistent with the results of the JET calculations from the previous chapter. Hence, the discussion given there is also valid here.

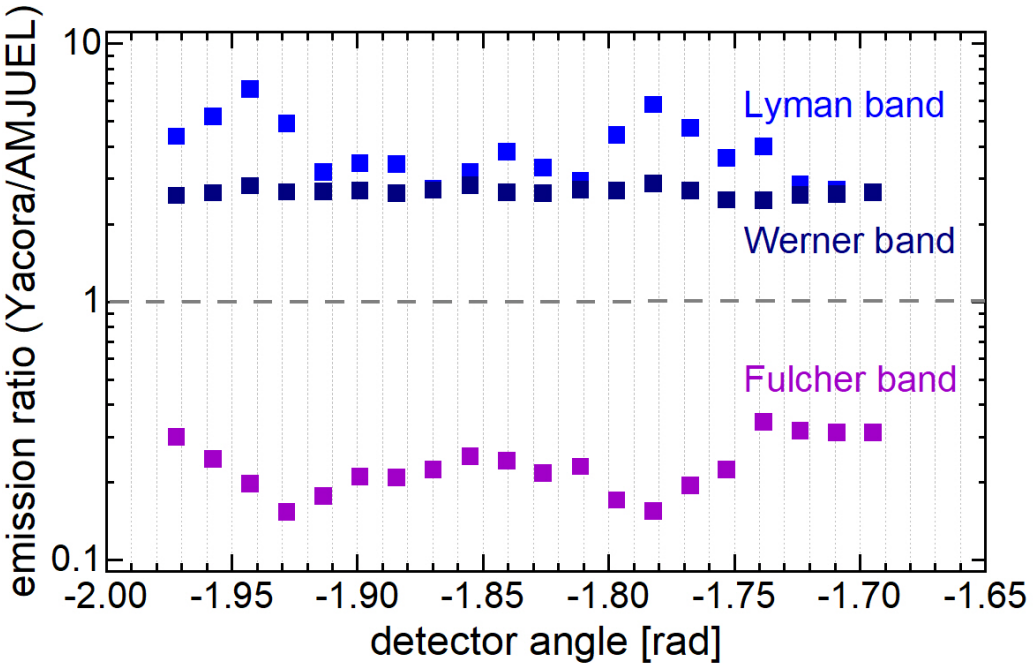

Figure 4.23: *Ratios of predicted Fulcher-, Lyman- and Werner band emission between Yacora and AMJUEL integrated over the synthetic lines of sight directed to the LFS divertor for the modified EDGE2D-EIRENE DIII-D profiles in dependence on the detector angle.*

Within the scope of the work [195], the Fulcher-α band was measured in the four identical DIII-D discharges 174243-174245 that represent plasmas comparable to the conditions in the EDGE2D-EIRENE calculations. Figure 4.24 shows the measured Fulcher-α band photon intensity in comparison to the line of sight-integrated predictions from AMJUEL and the *Yacora $H_2(v)$ model*. The Yacora predictions are closer to the measurement than the AMJUEL predictions and agree best in the detector angle range between -1.92 to -1.83 rad. This observation is a consequence of the availability of the imposed Thomson scattering and Langmuir probe measurements only in the central part of the divertor plasma (see [134, 135]). Since the Yacora predicted emission is in the central part slightly below the measurement, this may indicate that the probability for Dissociative Electron Attachment for vibrational levels of electronically excited states is slightly too high in the Yacora model. This observation would be, as already mentioned, in agreement with [15, 163]. However, it should be emphasized again that the application of the *Yacora $H_2(v)$ model* for post-processing deuterium profiles can cause a systematic error and must therefore be treated with caution. Nevertheless, the comparison demonstrates that the *Yacora $H_2(v)$ model* agrees better with the measurements than AMJUEL.

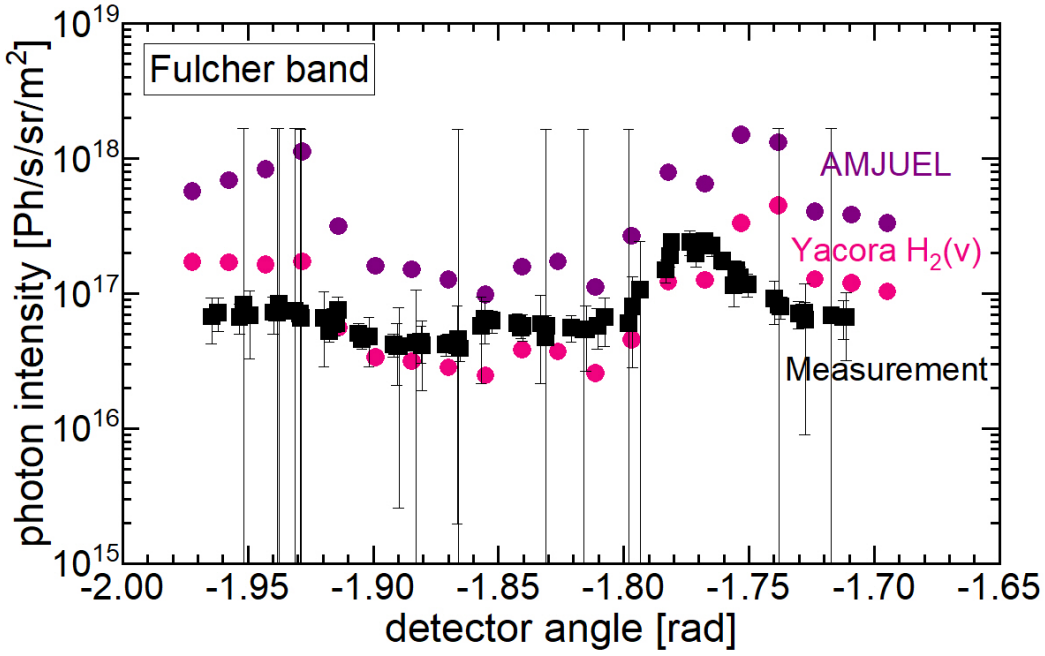

Figure 4.24: *Fulcher-α band photon intensity [Ph/(s sr m^2)] predicted by AMJUEL and the Yacora $H_2(v)$ model in comparison with DIII-D measurements in dependence on the detector angle.*

4.4 The Yacora H_2(v,N) Fulcher model

Since Lavrov's pioneering studies [197, 198], the Fulcher-α band emission is used to determine the ro-vibrational distribution of the H_2 electronic ground state $X^1\Sigma_g^+$.

The (relative) vibrational distribution is often derived under the assumption of the Franck-Condon principle (e.g. [76, 199, 200]): a vibrational distribution from $X^1\Sigma_g^+$ characterized by T_{vib} is projected into $d^3\Pi_u$ through Franck-Condon factors. Thus, the vibrational distribution of $d^3\Pi_u$ is obtained in dependence on T_{vib}. The calculation can be compared with measurement results (e.g. from optical emission spectroscopy) to deduce T_{vib} from experiment. If the absolute excited state population densities are of interest, de-excitation by Spontaneous Emission into $a^3\Sigma_g^+$ and the reduced energy threshold for excitation from excited vibrational levels in $X^1\Sigma_g^+$ are also accounted for. Note that non-Boltzmann vibrational ground state distributions (e.g. [201]) cannot be detected with such approaches, since they are only sensitive to the first vibrational levels in $X^1\Sigma_g^+$, as the Franck-Condon factors are highest for the lowest vibrational levels.

In [202] it is demonstrated for low-temperature plasmas that the excited state vibrational distributions deviate strongly, when T_{vib} is projected upwards from $X^1\Sigma_g^+$ based on Franck-Condon factors, compared to applying semi-classical Electron Impact Excitation cross sections. This deviation is caused by the fact that the variation of the electronic transition moment with diatomic inter-nuclear distance is not slow [203], and therefore the Franck-Condon approximation is not applicable.

Population models enable a more sophisticated analysis including in general the determination of the rotational distributions. Several corona models for the Fulcher-α band transition can be found in the literature: The models in [58] and [151] apply purely vibrationally resolved cross sections for Electron Impact Excitation between ro-vibrationally resolved levels of $X^1\Sigma_g^+$ and $d^3\Pi_u$ using either scaled cross sections via the Gryzinski method based on the cross sections from [15, 149] or MCCC cross sections [152] respectively:

$$X^{\mathrm{d}^3\Pi_u,\mathrm{v}',\mathrm{N}'}_{\mathrm{X}^1\Sigma_g^+,\mathrm{v},\mathrm{N}} = X^{\mathrm{d}^3\Pi_u,\mathrm{v}'}_{\mathrm{X}^1\Sigma_g^+,\mathrm{v}}. \tag{4.5}$$

While the ro-vibrational band structure agrees to some extent with measurements, the absolute emission of the models is always overestimated. For instance, the model from [151] overestimates the diagonal Q-lines typically by a factor greater than 2 compared to the measurements from the pressure variation at the PlanICE

experiment from chapter 3.2.1.

Other models (e.g. [202, 204, 205]) do not neglect the influence of rotational excitation and account for it by scaling vibrationally resolved cross sections via the factor $a_{\mathrm{NN'}}$ [206, 207]:

$$X^{\mathrm{d}^3\Pi_\mathrm{u},\mathrm{v'},\mathrm{N'}}_{\mathrm{X}^1\Sigma_\mathrm{g}^+,\mathrm{v},\mathrm{N}} = X^{\mathrm{d}^3\Pi_\mathrm{u},\mathrm{v'}}_{\mathrm{X}^1\Sigma_\mathrm{g}^+,\mathrm{v}}\, a_{\mathrm{NN'}} \tag{4.6}$$

with

$$a_{\mathrm{NN'}} = \sum_r \bar{Q}'_\mathrm{r}(2N'+1) \begin{pmatrix} N' & r & N \\ \Lambda' & \Lambda-\Lambda' & -\Lambda \end{pmatrix}^2 . \tag{4.7}$$

The last term in the brackets represents the Wigner 3-j symbol and $\bar{Q}'_\mathrm{r}(r = 1, 2, 3, 4)$ the normalized electron partial cross section (with the experimentally determined values 0.76, 0.122, 0.1 and 0.014). Note that this scaling implies that the rotational excitation is independent of the vibrational levels involved (e.g. $a_{\mathrm{NN'}}$ equivalent for arbitrary vibrational transitions).

While several of the mentioned models with and without accounting for $a_{\mathrm{NN'}}$ are capable to make accurate predictions of the relative excited state populations, predictions of the absolute excited state population density have previously not yet been presented. Within the scope of this work, a fully ro-vibrationally resolved corona model for the Fulcher-α band emission has been developed with the aim to make unprecedented absolute emission predictions. The chapter is structured as follows: First, the standard and extended versions of the *Yacora H_2(v,N) Fulcher model* are introduced. Second, the standard model is benchmarked demonstrating the accuracy of the applied ro-vibrationally resolved cross sections. Third, the influence of multipolar (de-)excitation (transitions with $|\Delta N| > 0$) is analyzed. Finally, the extended model version is discussed. Main parts of this chapter have recently been published in [208].

4.4.1 Detailed model description

The *Yacora H_2(v,N) Fulcher model* includes 1365 ro-vibrationally resolved levels of the electronic states $X^1\Sigma_\mathrm{g}^+$, $a^3\Sigma_\mathrm{g}^+$ and $d^3\Pi_\mathrm{u}$ (distinguishing $d^3\Pi_\mathrm{u}^-$ and $d^3\Pi_\mathrm{u}^+$ while treating them quasi-degenerate). For $X^1\Sigma_\mathrm{g}^+$ and $d^3\Pi_\mathrm{u}$ the levels and their energies include $v = 0-14$ and $v' = 0-20$ with N up to maximal N beneath the respective dissociation limit. The used energies of the ro-vibrational levels stem from ro-vibrationally resolved MCCC calculations (see below). For $a^3\Sigma_\mathrm{g}^+$ the levels with $v'' = 0-14$ and $N'' = 0-15$ are included, their energies stem from [209] calculated with the *LEVEL code* (see chapter 3.3).

As input, a 2-temperature distribution according to equation 2.71 is assigned to the ro-vibrational levels of the electronic ground state $X^1\Sigma_g^+$ (thus treating them to be in P-space, see chapter 2.4.3).

Table 4.4 summarizes the processes and reactions accounted for in the model.

Table 4.4: *Overview of processes and corresponding reactions included in the Yacora H_2(v,N) Fulcher model.*

Process	Reaction
Electron Impact Excitation	$H_2(X^1\Sigma_g^+, v, N) + e^- \rightarrow H_2(d^3\Pi_u, v', N') + e^-$
Spontaneous Emission	$H_2(d^3\Pi_u, v', N') \rightarrow H_2(a^3\Sigma_g^+, v'', N'') + h\nu$
Collisional Quenching	$H_2(d^3\Pi_u, v', N') + H_2(X^1\Sigma_g^+, v = 0, N = 0) \rightarrow 2\,H_2(X^1\Sigma_g^+, v = 0, N = 0)$
Autoionization	$H_2(d^3\Pi_u, v', N') \rightarrow H_2^+ + e^-$
Predissociation	$H_2(d^3\Pi_u, v', N') \rightarrow H + H$

A set of 45260 fully ro-vibrationally resolved MCCC cross sections for Electron Impact Excitation from $X^1\Sigma_g^+(v,N) \rightarrow d^3\Pi_u(v',N')$ including rotational excitation with $|\Delta N| \leq 5$ from [157] is applied. The transitions are being restricted to those with $|\Delta N| \leq 5$, since those with larger differences in the rotational quantum number N have cross sections effectively equal to zero within numerical tolerances.

The cross sections are utilized in the model to account for the transitions that are allowed according to the symmetry properties of the respective levels (see the bright blue arrows in figure 4.25 for transitions between the first 5 rotational levels of $X^1\Sigma_g^+$ and $d^3\Pi_u$ with arbitrary v). According to the selection rules for transitions between rotational levels, the total parity changes and the nuclear permutation symmetry for rotational levels remains unchanged. Therefore, an arbitrary level of $X^1\Sigma_g^+$ does not excite into each level of $d^3\Pi_u^+$ and $d^3\Pi_u^-$. For instance $X^1\Sigma_g^+(v, N = 0)$ solely excites into $d^3\Pi_u^+(v',N' = 1, 3, 5)$ and $d^3\Pi_u^-(v',N' = 2, 4)$. $X^1\Sigma_g^+(v,N = 1)$ solely excites into $d^3\Pi_u^+(v',N' = 2, 4, 6)$ and $d^3\Pi_u^-(v',N' = 1, 3, 5)$.

Spontaneous Emission for dipole transitions ($|\Delta N| \leq 1$) is included via Einstein coefficients stemming from [209] calculated with the *LEVEL code* based on dipole operators and potential curves from [29, 203]. According to the transition rules in effect, $d^3\Pi_u^+(v',N' = 1)$ only transitions into $a^3\Sigma_g^+(v'',N'' = 0, 2)$ and $d^3\Pi_u^+(v',N' = 2)$ only transitions into $a^3\Sigma_g^+(v'',N'' = 1, 3)$ by Spontaneous Emission. These P- and R-line transitions with $|\Delta N| = 1$ are represented by the dark blue arrows in figure 4.25. Furthermore, $d^3\Pi_u^-(v',N' = 1)$ only transitions into $a^3\Sigma_g^+(v'',N'' = 1)$ and $d^3\Pi_u^-(v',N' = 2)$ only transitions into $a^3\Sigma_g^+(v'',N'' = 2)$ by Spontaneous

Emission. These Q-line transitions are depicted by the pink arrows in figure 4.25.

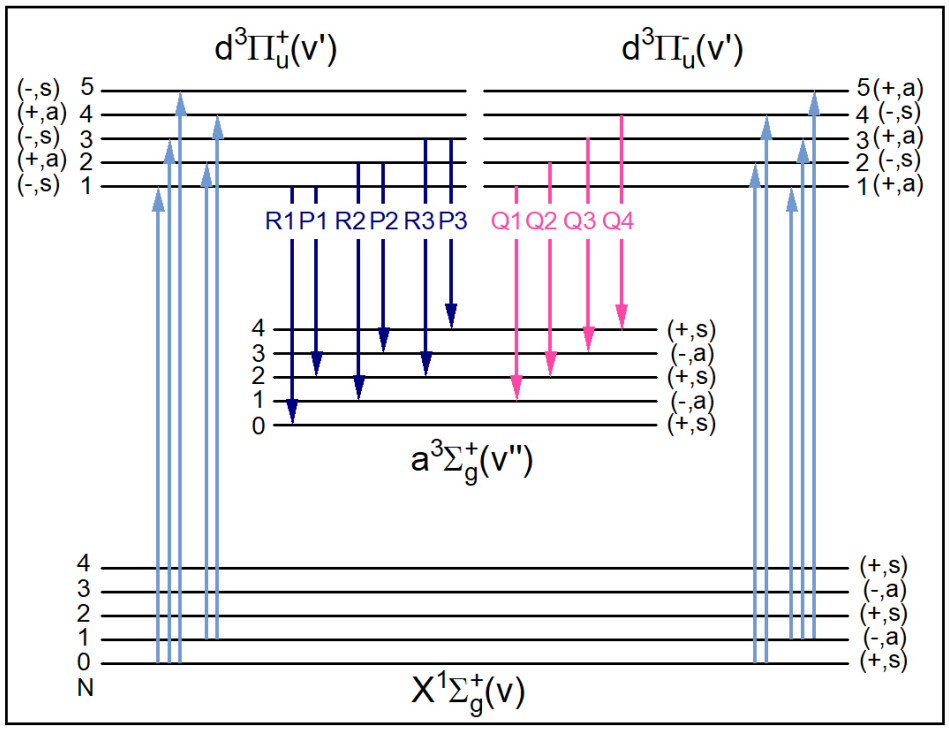

Figure 4.25: *Schematic of the ro-vibrational levels of the electronic states* $X^1\Sigma_g^+(v,N)$ *and* $d^3\Pi_u(v,N)$ *with arbitrary* v*. For each level the total parity and symmetry with respect to nuclear permutation (of the total wavefunction without nuclear spin) is given in brackets. The bright blue arrows depict transitions of Electron Impact Excitation, the pink and dark blue arrows represent Spontaneous Emission for* $\Delta N = 0$ *and* $\Delta N = \pm 1$*.*

In addition to these standard processes, the model includes as optional extensions the processes of Collisional Quenching, Autoionization and Predissociation.

Collisional Quenching rate constants [55] for individual ro-vibrational levels of $d^3\Pi_u^-(v' = 0, 1, 2, 3, 4, 5$ with $N' = 1$ and $v' = 6$ with $N' = 3)$ are applied. For the same v' and varying N', the same rate constants are applied owing to the lack of ro-vibrationally resolved data. For the levels with $v' > 6$, the rate constant for $v' = 6$ is utilized. The rate constants stem from measurements with the delayed-coincidence method for excitation by nanosecond near-threshold electron pulses in a gas filled cell. The data agree well with the less extensive measurements from [210] and [211], when accounting for the specifics of the different experimental setups.

For Autoionization of electronic H_2 states with $n = 4$, the calculated rate (inverse process dependent lifetime) $\tau^{-1}_{\text{autoionization}} = 10^7\,\text{s}^{-1}$ is given in [15]. For

lack of alternatives, this rate is implemented for all ro-vibrational levels of $d^3\Pi_u$ with an energy above the ionization threshold of H_2 ([31]). Table 4.5 summarizes the affected and thus autoionizing levels.

For Predissociation of $d^3\Pi_u^-$, predissociation lifetimes for $v' = 4 - 9$ calculated via the quantum defect theory [212] from [213] are applied. The study suggests that the predissociation rate rapidly increases with increasing v' and that it is rather independent of N' for fixed v'. For ro-vibrational levels with $v' < 4$ and an energy above the energy associated with the dissociation limit for H(2l)+H(1s) ([31]) the predissociation lifetime of $v' = 4$ is used. Table 4.6 summarizes the affected and thus predissociating levels of $d^3\Pi_u^-$. For ro-vibrational levels with $v' > 9$, the lifetime for $v' = 9$ is utilized.

For $d^3\Pi_u^+$ levels with an energy above the dissociation limit, a full Predissociation is expected and implemented. For $d^3\Pi_u^+$ levels with an energy below the dissociation limit, the predissociation lifetimes are deduced from experimental (total) lifetimes from [214] and calculated Einstein coefficients (thus neglecting the contribution of Autoionization to the experimental lifetime):

$$\tau_{\text{exp.}}^{-1} = \tau_{\text{SE}}^{-1} + \tau_{\text{prediss.}}^{-1} \text{ with } \tau_{\text{SE}}^{-1} = A_{\text{ik}}^{\text{eff}}. \tag{4.8}$$

Table 4.5: $d^3\Pi_u$ *levels with an energy above the ionization threshold.*

v'	0	1	2	3	4	5	6	7
N'	≥ 24	≥ 22	≥ 20	≥ 17	≥ 14	≥ 11	≥ 7	≥ 1

Table 4.6: $d^3\Pi_u$ *levels with an energy above the dissociation threshold.*

v'	0	1	2	3	≥ 4
N'	≥ 16	≥ 13	≥ 9	≥ 3	≥ 1

4.4.2 Benchmarking the standard model at PlanICE

The standard version of the *Yacora H_2(v,N) Fulcher model* is aimed to make accurate predictions of the population densities of the ro-vibrational levels of $d^3\Pi_u^-$ and thus through post-processing of the Fulcher-α band predictions of the Q-line emission. To benchmark this model, the measured emission and the

plasma parameters deduced from the pressure variation measurements at the inductively coupled plasma experiment PlanICE (see chapter 3.2.1) are applied. Since the accuracy of the MCCC Electron Impact Excitation cross sections is expected to be significantly higher than the accuracy of the reaction probabilities for the processes additionally considered in the extended model, this benchmark is explicitly performed for the standard model in order not to dilute its expected exceptionally good accuracy.

The parameters T_e, n_e, n_{H_2}, T_gas, T_vib, $T_{\mathrm{rot}\,2}$ and β are used as input for the corona model to predict the $d^3\Pi_\mathrm{u}$ level population densities. For the calculation of rate coefficients from cross sections, a Maxwellian electron EDF is assumed. To account for the uncertainty of T_e and n_e stemming from the Langmuir probe measurements, three separate simulations are performed for each pressure case (e.g. $(n_\mathrm{e},\, T_\mathrm{e})$, $(n_\mathrm{e} - \sigma_{n_\mathrm{e}},\, T_\mathrm{e} - \sigma_{T_\mathrm{e}})$ and $(n_\mathrm{e} + \sigma_{n_\mathrm{e}},\, T_\mathrm{e} + \sigma_{T_\mathrm{e}})$). The obtained excited level population densities are post-processed by multiplication with the respective Einstein coefficient to calculate the Fulcher-α emission intensity (see equation 2.18). For direct comparison with the absolutely calibrated measured spectra (spectral emission intensity in [Ph/(s m^3 nm)]), the line broadening is taken into account. The broadening is mostly given by the apparatus function that is Gaussian with a FWHM of $16 - 22\,\mathrm{pm}$ depending on the wavelength.

Figure 4.26 compares the measured and calculated spectral emission intensity in the range of $600 - 635\,\mathrm{nm}$ for the plasma at 1.1 Pa and 700 W plasma. The wavelength positions of the Q-lines for the first four diagonal vibrational transitions from literature [215] are indicated. The Q-lines agree in relative shape and general size very well between measurement and simulation. It should be noted that the standard version of the *Yacora H_2(v,N) Fulcher model* is solely aimed to accurately simulate the Q-lines. It is not surprising that the other lines including P- and R-lines originating from the $d^3\Pi_\mathrm{u}^+$ state are not well predicted by the standard model, since for the $d^3\Pi_\mathrm{u}^+$ state the additional de-populating mechanism of Predissociation has a large impact. Therefore, this process is accounted for in the extended version of the model discussed below.

A more accurate comparison between measurement and simulation is shown for the Q-lines with $v' = v'' = 0$ in figure 4.27: The simulated line emission intensity is compared with the line emission intensity derived from peakwise integrating the spectral emission intensity. Thus, the artificial broadening of the simulated emission intensities (where also the overestimated P- and R-lines contribute) is avoided. The measured line emission intensities are shown with their uncertainty. To account for the uncertainties of T_e and n_e (that result from

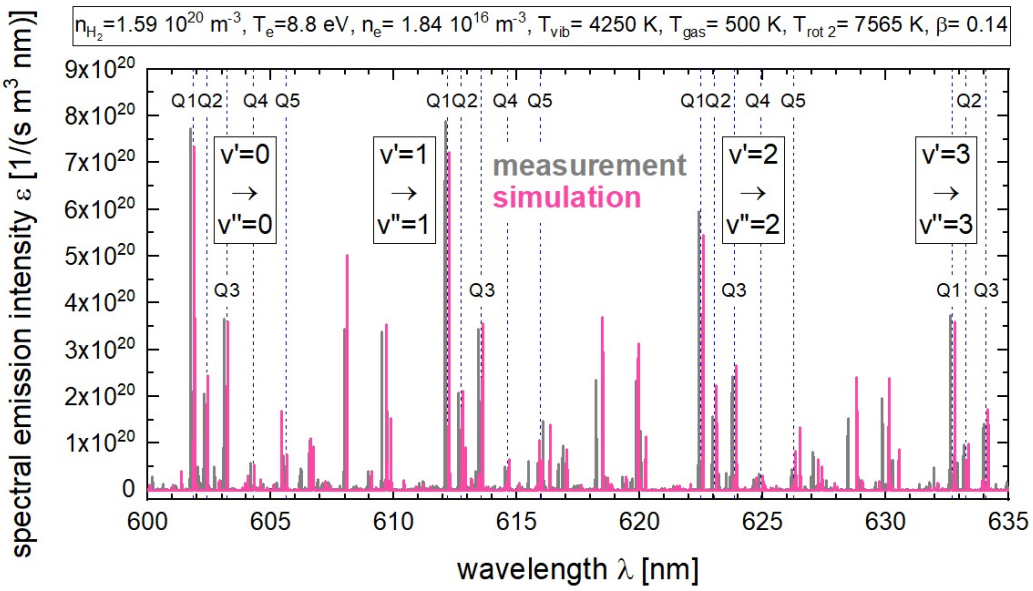

Figure 4.26: *Comparison of measured and simulated spectral emission intensity for the inductively coupled plasma at* $p = 1.1\,\mathrm{Pa}$ *and* $P_{\mathrm{RF}} = 700\,\mathrm{W}$. *The spectral emission intensities shown here are determined from the calculated line emission intensities by accounting for the line broadening. Note that the standard form of the corona model (applied here) is solely aimed to predict Q-line intensities and the complete spectrum section is shown solely for the reader's convenience.*

line of sight-averaging the spatially resolved Langmuir probe measurements), two model runs are shown with T_{e}=$T_{\mathrm{e}}^{\mathrm{Langmuir}}\pm\sigma_{T_e}$ and T_{e}=$n_{\mathrm{e}}^{\mathrm{Langmuir}}\pm\sigma_{n_e}$ as input respectively. The uncertainty bars of the measurements lie within the simulation range for each line.

The comparison is extended in figure 4.28 showing the line emission intensities for the Q-lines of $v' = v'' = 0, 1, 2$ for the plasmas of the entire pressure variation. For each Q-line and pressure, the measurements lie very well within the simulation range, only with certain exceptions independent of the pressure. Since the Q10($v' = 1$) and Q5($v' = 2$) lines usually overlap each other and cannot clearly be distinguished in the measurements, the same measured line emission intensity is depicted for both of them. The measured Q10($v' = 2$) and Q12($v' = 2$) lines usually are so weak that a clear distinction from the background is not possible.

The good agreement in absolute value of the Q-lines of the first three diagonal vibrational transitions of the Fulcher-α band between the measurement and the simulated line emission intensities of the *Yacora H_2(v,N) Fulcher model* demonstrates the unprecedented accuracy of the fully ro-vibrationally resolved MCCC Electron Impact Excitation cross sections.

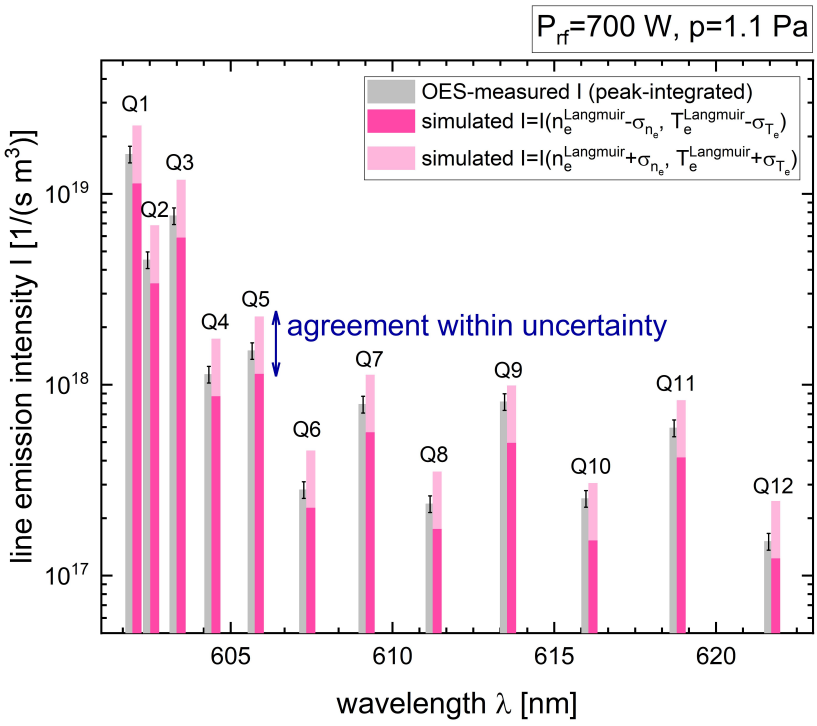

Figure 4.27: *Comparison of the measured and simulated Q-line emission intensities with $v' = v'' = 0$ for the plasma at $p = 1.1\,\mathrm{Pa}$, $P_{\mathrm{RF}} = 700\,\mathrm{W}$. The simulated data represents two model runs accounting for the uncertainties of the measured n_{e} and T_{e}.*

4.4.3 The influence of multipolar excitation

The relevance of multipolar (de-)excitation (transitions with $|\Delta N| > 0$) is a controversial topic on which no consensus has yet been reached in the literature.

Previously, it was believed that electrons are not capable to contribute significantly to the change in the rotational angular momentum of molecules due to their low mass. Consequently, the selection rule $\Delta N = 0$ would apply for Electron Impact Excitation. In the work of Otorbaev [207] it is indicated that a transfer of rotational momentum from electrons to molecules during collisional excitation occurs. Furthermore, spectra analyses [216] show that multipolar components beyond the dipolar contribution ($|\Delta N| > 1$) are necessary to model the excitation process. In [27] it is suggested that the contribution of quadrupole transitions ($|\Delta N| = 2$) amounts to 10 % of the total collisional excitation.

The influence of multipolar electron impact excitation for the ro-vibrationally resolved MCCC cross sections can be directly estimated from them. Figures 4.29 and 4.30 show the cross section for $X^1\Sigma_{\mathrm{g}}^+(v = 0, N = 0) \rightarrow d^3\Pi_{\mathrm{u}}(v' = 0, N')$ and

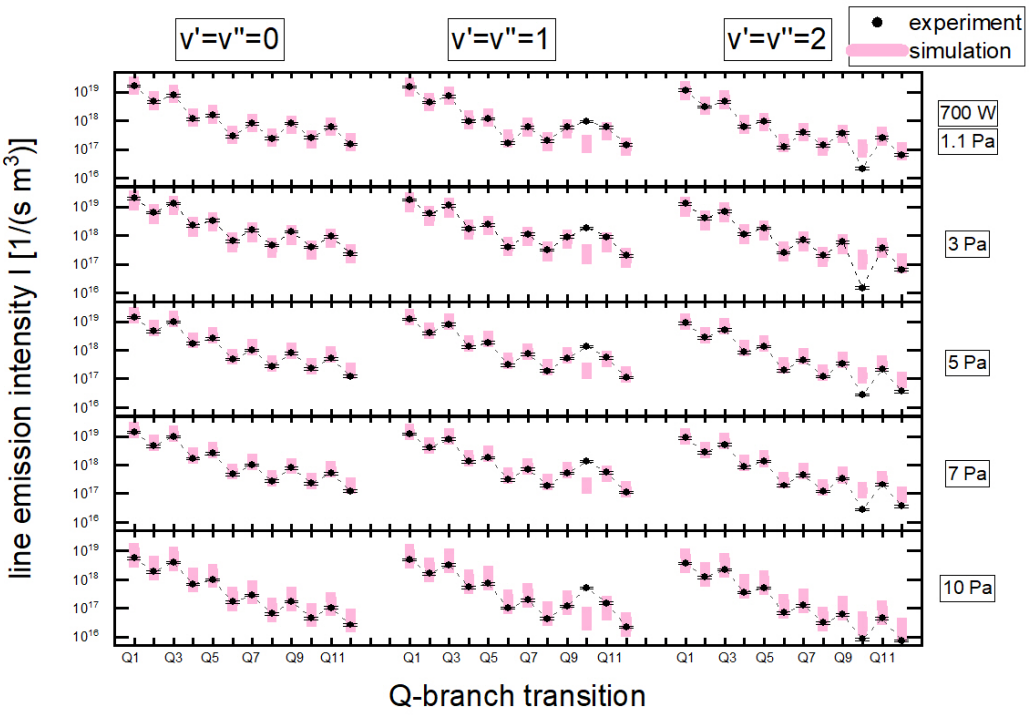

Figure 4.28: *Comparison of Q-line emission intensities from measurement and simulation for varying pressure* $p = 1.1 - 10\,\mathrm{Pa}$ *and* $P_{\mathrm{RF}} = 700\,\mathrm{W}$.

$X^1\Sigma_g^+(v = 0, N = 2) \rightarrow d^3\Pi_u(v' = 0, N')$ respectively and the comparison with the purely vibrationally resolved cross section $X^1\Sigma_g^+(v = 0) \rightarrow d^3\Pi_u(v = 0)$.

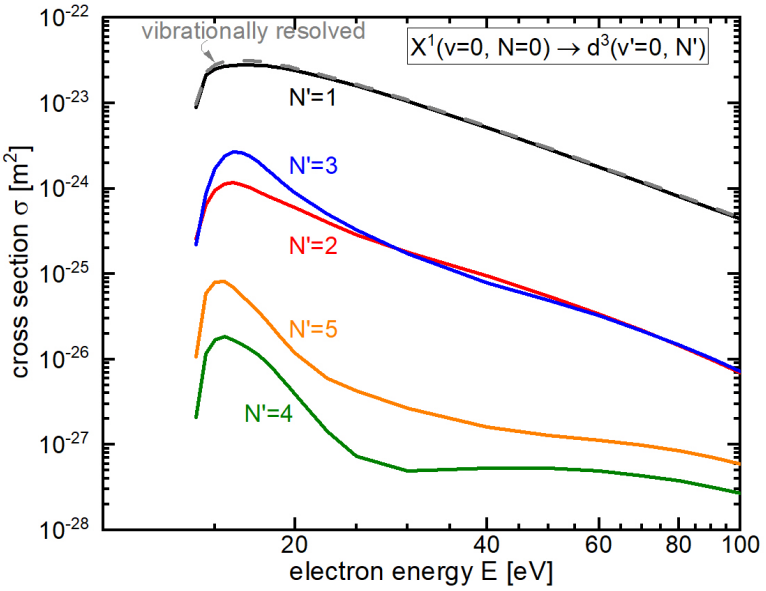

Figure 4.29: *Ro-vibrationally resolved MCCC electron impact excitation cross section for* $X^1\Sigma_g^+(v = 0, N = 0) \rightarrow d^3\Pi_u(v' = 0, N')$ *with* $\Delta N \leq 5$ *and the purely vibrationally resolved cross section calculated with the MCCC method.*

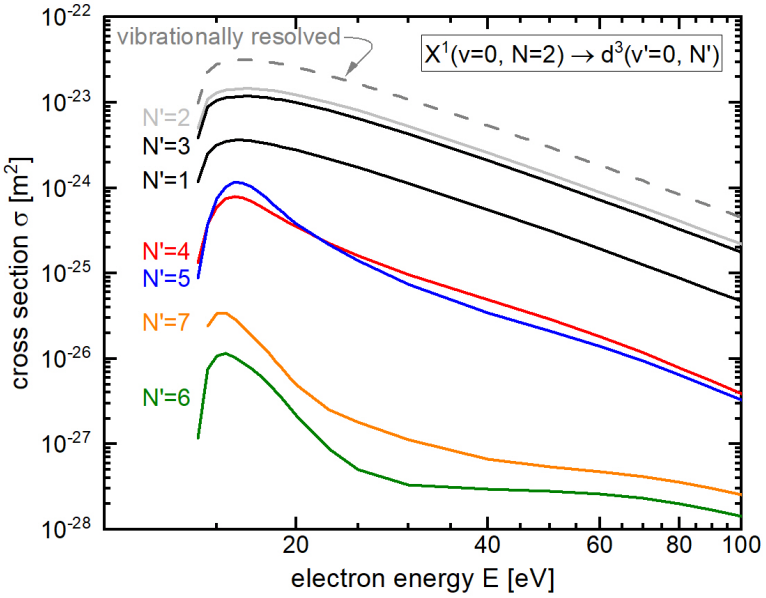

Figure 4.30: *Ro-vibrationally resolved MCCC electron impact excitation cross section for* $X^1\Sigma_g^+(v=0, N=2) \rightarrow d^3\Pi_u(v'=0, N')$ *with* $|\Delta N| \leq 5$ *and the purely vibrationally resolved cross section calculated with the MCCC method.*

In figure 4.29, the ro-vibrationally resolved cross section for excitation with $\Delta N = 1$ from initial $N = 0$ is similar in shape to the vibrationally resolved cross section, but slightly smaller. The ro-vibrationally resolved cross sections for excitation with $\Delta N = 2, 3$ from initial $N = 0$ amount for a broad energy range to less than 10 % of the cross section with $\Delta N = 1$. The ro-vibrationally resolved cross sections for excitation with $\Delta N = 4, 5$ from initial $N = 0$ are more than a factor 100 smaller than the cross section with $\Delta N = 1$ and should therefore be rather insignificant.

In figure 4.30 the ro-vibrationally resolved cross section for excitation with $|\Delta N| = 0, 1$ from initial $N = 2$ into $N' = 2, 3, 1$ are smaller about the factors 2,2.5,10 than the purely vibrationally resolved cross section, but similar in shape. The ro-vibrationally resolved cross section for excitation with $\Delta N = 2, 3$ from initial $N = 2$ are more than the factor 10 smaller than the cross with $\Delta N = 0$. The ro-vibrationally resolved cross sections for excitation with $\Delta N = 4, 5$ from initial $N = 2$ are negligible in comparison.

Although it is tempting to assume that the ro-vibrationally resolved cross sections decrease (for the entire energy range) monotonically with increasing N' for fixed N and $N' > N$, the depiction demonstrates that this dependency only exists between the levels along the same branch of excitation: The cross sections $X^1\Sigma_g^+(v=0, N=0) \rightarrow d^3\Pi_u(v'=0, N')$ decrease monotonically for excitation

into $d^3\Pi_u^+$ with final levels $N' = 1, 3, 5$ and into $d^3\Pi_u^-$ with final levels $N' = 2, 4$ respectively.

Figure 4.30 shows that the use of vibrationally resolved cross sections, as it was done in the already mentioned model from [151], overestimates Electron Impact Excitation between ro-vibrational levels even for transitions with $\Delta N = 0$.

Moreover, it is of interest to compare the rotational excitation accounted for in the ro-vibrationally resolved MCCC cross sections with the scaling based on the Wigner 3-j symbol from equation 4.7. The same quantity is derived from the fully ro-vibrationally and purely vibrationally resolved rate coefficients (that are determined from the respective MCCC cross sections for $v = v' = 0$ transitions applying Maxwellian electron energy distribution functions) according to equation 4.6. Figure 4.31 compares the factor $a_{NN'}$ estimated from equation 4.7 ($a_{NN'}^{Wigner}$) and derived from the MCCC cross sections ($a_{NN'}^{MCCC}$). Note that solely $a_{NN'}^{MCCC}$ has a dependency on T_e. The difference in absolute value is small for the excitation from $N = 0$ into $N' = 1$ ($a_{01}^{Wigner} = 0.76$ and $a_{01}^{MCCC} = 0.88 - 0.96$) and larger for excitation with $\Delta N \geq 1$. The factors $a_{NN'}^{Wigner}$ decrease for increasing ΔN. Contrarily, a_{03}^{MCCC} is for a broad electron temperature range larger than a_{02}^{MCCC}, and a_{05}^{MCCC} is larger than a_{04}^{MCCC}. From further analyses for transitions other than $X^1\Sigma_g^+(v = 0) \rightarrow d^3\Pi_u(v' = 0)$ (not explicitly shown here) it is found that the $a_{NN'}^{MCCC}$ has a low dependence on the vibrational levels involved in the excitation process, which is not the case for $a_{NN'}^{Wigner}$ and thus not accounted for in the scaling from equation 4.7.

In agreement with this discussion on the influence of rotational excitation in the ro-vibrationally resolved MCCC cross sections, the contribution of multipolar excitation to the levels from which the Q-lines originate is according to the corona model for the input parameters of the plasmas with $p = 1.1\,\mathrm{Pa}$ and $P_{RF} = 700\,\mathrm{W}$ and $p = 10\,\mathrm{Pa}$ and $P_{RF} = 700\,\mathrm{W}$ less than 15 %. This observation underlines that most importantly $\Delta N = 0$ cross sections must be correct in magnitude and excitation via multipolar components is only of secondary importance.

4.4.4 Insights from the extended model

The extended version of the fully ro-vibrationally resolved *Yacora H_2(v,N) Fulcher model* also includes the processes Collisional Quenching, Autoionization and Predissociation of $d^3\Pi_u$. Since the latter strongly depend on the respective (ro-)vibrational level, it is practical to implement theses processes in a (ro-)vibrationally resolved model only.

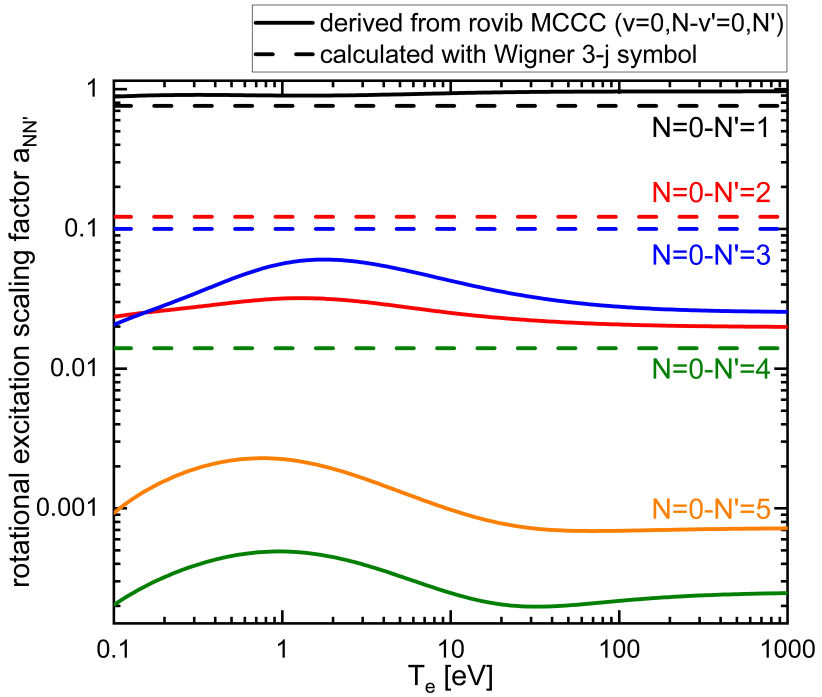

Figure 4.31: *Comparison of rotational excitation between scaling law from equation 4.7 and MCCC cross sections.*

For calculations of the standard *Yacora H_2(v,N) Fulcher model* solely extended by Collisional Quenching for the 1.1 Pa plasma with $n_{H_2} = 1.6 \cdot 10^{20}\,\mathrm{m}^{-3}$, the resulting excited $d^3\Pi_u$ level population densities practically do not differ from the results from the standard model. Individual Q-lines are reduced maximally $< 3\,\%$.

Since the Collisional Quenching rate depends on n_{H_2}, the relevance of this process is more pronounced for the 10 Pa plasma with $n_{H_2} = 1.1 \cdot 10^{21}\,\mathrm{m}^{-3}$. Individual Q-lines are reduced maximally $< 16\,\%$. When comparing the simulated Q-lines for the 10 Pa plasma to the measurements, the results from the extended corona model including Collisional Quenching are slightly in better agreement with the measurements than results from the standard model. Therefore, the inclusion of Collisional Quenching in the *Yacora H_2(v,N) Fulcher model* is recommended, when the calculation of Q-lines is of interest.

Both Autoionization and Predissociation do not affect $d^3\Pi_u^-(v' = 0-2, N' = 1-12)$ levels, with the exception of the $d^3\Pi_u^-(v' = 2, N' = 9-12)$ levels for which Predissociation is relevant. Therefore, the inclusion of theses processes does not affect the prior benchmark regarding the Q-lines. However, the implementation of these processes is of great importance for predictions of the total Fulcher-α band emission (diagonal and non-diagonal Q-, P-, R-lines combined). When comparing

the summed $d^3\Pi_u$ population density between the standard and the extended model, the predictions from the extended model are $\approx 30, 52, 52, 51, 32\,\%$ smaller for the parameters of the for $1.1, 3, 5, 7, 10$ Pa plasmas respectively. Figure 4.32 compares the line emission intensities for the entire spectrum simulated for the parameters of the 1.1 Pa plasma with the standard and the extended *Yacora $H_2(v,N)$ model* including Collisional Quenching, Autoionization and Predissociation. The $d^3\Pi_u^-(v' = 0-1, N' = 1-12)$ and $d^3\Pi_u^-(v' = 2, N' = 1-8)$ level population densities agree for both calculations within $3\,\%$, whereby this discrepancy is a consequence of the inclusion of Collisional Quenching.

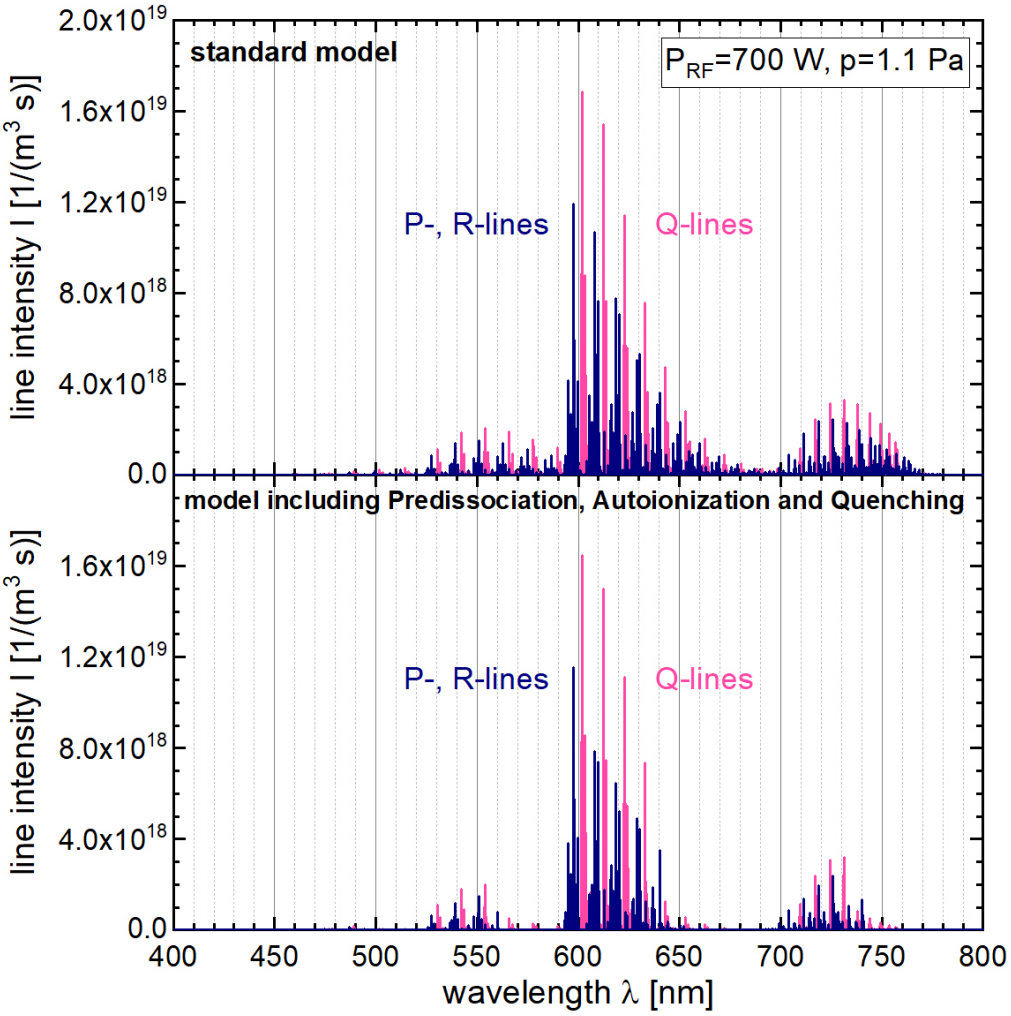

Figure 4.32: *Line emission intensities for entire Fulcher-α spectrum simulated with the Yacora $H_2(v,N)$ Fulcher model in its standard form and its extended version including Collisional Quenching, Autoionization and Predissociation for plasma parameters of 1.1* Pa *plasma discussed above.*

In order to deduce the inverse of predissociation lifetimes for the ro-vibrational levels of $d^3\Pi_u^+$ (see equation 4.8), the lifetimes recommended in [217] are also

test-wise implemented, as an alternative to the experimental lifetimes from [214]. Since the predictions by the extended model based on the data from [214] agree slightly better with the measurements, they are utilized in the extended model.

It can be seen from figure 4.32 that the *Yacora H_2(v,N) Fulcher model* is available to simulate entire Fulcher-α spectra (including also non-diagonal vibrational transitions). This application may especially be helpful to get an idea of a spectrum before the actual measurement is performed.

5 Conclusions

For a fundamental understanding of low-temperature molecular hydrogen plasmas, such as divertor plasmas of fusion experiments, negative hydrogen ion source plasmas for neutral beam injection and industrial plasmas, knowledge of the plasma parameters is crucial. This knowledge can be acquired through the non-invasive diagnostic of optical emission spectroscopy in combination with quantitative interpretation using CR models.

CR models are based upon systems of rate equations requiring reaction probabilities as input. The models predict excited state population densities in dependence on the plasma parameters. Atomic and molecular line emission is proportional to the excited state population densities. Therefore, the plasma parameters can be deduced from the model predicted excited state population densities together with emission spectroscopy measurements.

Improvements in the availability of (ro-vibrationally resolved) reaction probabilities have motivated to revisit the field of CR modelling for molecular hydrogen plasmas, resulting in the present work.

In this work, a muti-stage approach has been followed to develop and benchmark differently resolved models for H_2 based on the Yacora solver for different applications: the electronically resolved model *Yacora H_2*, the vibrationally resolved model for the electronic ground state *Yacora $H_2(X^1, v)$*, the vibrationally resolved model *Yacora $H_2(v)$* and the ro-vibrationally resolved corona model for the Fulcher-α band *Yacora $H_2(v,N)$ Fulcher*.

The electronically resolved CR model *Yacora H_2* is the very first model accounting for electron collision induced transitions between excited H_2 states of the different multiplet systems (singlet and triplet). This consideration is possible due to the recent availability of MCCC spin-mixing cross sections.

The model applying the MCCC cross sections for Electron Impact Excitation was compared with previous models based on other cross sections from Miles and a combined set from Janev and Celiberto. Note that the AMJUEL database, which is used as standard in the neutral transport code EIRENE, is based on a CR model

applying cross sections after Miles. The models based on the different sets of input cross sections were benchmarked with singlet state emission and plasma parameter measurements from an ECR experiment. The *Yacora H_2 model* applying the MCCC cross sections shows the best overall agreement with the measurements. This finding is in accordance with similar observations from previous work on a CR model for the triplet system based on MCCC cross sections. The influence of spin-mixing on the excited state population densities was studied and found to be negligible for $n_e \lessapprox 10^{19}\,m^{-3}$ and most pronounced at high electron densities combined with low electron temperatures. This study underlines that previous models (separate models for singlet and triplet) did not primarily lack the inclusion of spin-mixing reactions, but rather an accurate and consistent set of Electron Impact (De-)Excitation cross sections.

Studies on the relevance of population by cascades from energetically higher states performed using the *Yacora H_2 model* have demonstrated that the population densities of the H_2 states with $n = 2, 3$ agree with the full model (including the states with $n = 4 - 10$) within 94 %, if the Λ-unresolved excited states with $n = 6 - 10$ are neglected and the states with $n = 4, 5$ are kept. Consequently, the impact of cascades from states with $n = 4, 5$ is not negligible. In a next step, it is therefore of interest for a physically more accurate description of cascades, to resolve the states $n = 4, 5$ by the quantum number Λ, as it would enable a more precise treatment of Spontaneous Emission from these states towards lower lying states in the CR model. Since no satisfactorily accurate (Λ-resolved) Electron Impact Excitation cross sections for excitation into these states are currently available in the literature, especially MCCC calculations are desired.

In summary, it has been demonstrated that the purely electronically resolved *Yacora H_2 model* based on MCCC cross sections (for Electron Impact Excitation) makes more accurate predictions than a model using cross sections from Janev and Celiberto or Miles. This finding is particularly relevant, since the widely used AMJUEL database is based on cross sections from Miles. The *Yacora H_2 model* is ideally suited for fundamental investigations on the kinetics of populating and de-populating processes in H_2.

The vibrationally resolved CR model for the electronic ground state *Yacora $H_2(X^1, v)$* is aimed to self-consistently predict the distribution of the vibrational levels in the electronic ground state $X^1\Sigma_g^+$. So far, no other model has been presented in the literature that can accurately predict the vibrational population. Two different model versions have been developed within the scope of this work:

The standard model version includes the same reactions as a previous vibrationally resolved Yacora model, but applies the most accurate reaction probabilities currently available in the literature. The extended model version accounts for additional reactions including multiple heavy particle collision processes. Note that plasma-surface interaction processes are not accounted for, since they strongly depend on the respective surface material and temperature.

The comparison of the model predicted vibrational population densities with measurements from the ITER negative NBI prototype source at BATMAN Upgrade (BUG) recorded close to the plasma grid ($T_{\mathrm{vib}} = 3000 \pm 500\,\mathrm{K}$) have demonstrated that the standard model makes improved predictions ($T_{\mathrm{vib}\,1} = 6\,700\,\mathrm{K}$) in comparison to the previous model ($T_{\mathrm{vib}\,1} = 7\,700\,\mathrm{K}$) and that the extended model makes considerably closer predictions to the measurement ($T_{\mathrm{vib}} = 4\,400\,\mathrm{K}$). According to the standard model, the processes of Electron Impact Dissociation, Dissociative Electron Attachment and Proton Charge Transfer have the largest influence on T_{vib} (apart from Electron Impact Excitation). According to the extended model, additionally the process of Hydrogen Atom Impact Dissociation has a large influence on T_{vib}. The processes of Electron Impact Ionization, H_2^+ Recombination, Proton Impact (De-)Exciation, Proton Impact Dissociation, H^- Associative Detachment, Hydrogen Molecule Impact (De-)Exciation, H_3^+ Dissociative Recombination and transitions via the electronically excited states $B^1\Sigma_u^+$ and $C^1\Pi_u$ have a minor influence on T_{vib} for the investigated plasma parameters. The remaining discrepancy between the predictions of the extended model and the measurement could not be completely resolved. Since it has been demonstrated that the process of Hydrogen Atom Impact Dissociation basically determines the vibrational distribution according to the extended model, the accurate treatment of this process through accurate reaction probabilities and plasma parameters is especially crucial. To date, only rate coefficients for this process are available in the literature that have been calculated for fixed H and H_2 temperatures. More accurate reaction probabilities in the form of dedicated cross sections are highly desirable, as they would enable to calculate cross sections for different EDFs and varying H and H_2 temperatures. In addition, TALIF measurements at BUG are planned with the aim of obtaining high-resolution T_{H} and n_{H} measurements. Furthermore, as mentioned above, so far plasma-surface interaction processes and the transport of excited vibrational levels of the electronic ground state are not accounted for in the model. Studying their possible influence is recommended in the future as well.

The comparison of measurements from the divertor plasma simulator Magnum-

PSI ($T_{\mathrm{vib}} = 4\,000 \pm 500\,\mathrm{K}$) with the population densities predicted by the model have again demonstrated that the *Yacora $H_2(X^1, v)$ model* makes improved predictions (e.g. $T_{\mathrm{vib}} = 6\,420\,\mathrm{K}$ for the extended model and $T_{\mathrm{H}} = 27\,560\,\mathrm{K}$) in comparison to the previous Yacora model ($T_{\mathrm{vib}} = 7\,800\,\mathrm{K}$). Since the Magnum-PSI plasma investigated exhibits higher values for n_{e}, $n_{\mathrm{H^+}}$ than the BUG plasma, the relevance of the processes differs. According to the standard *Yacora $H_2(X^1, v)$ model* Proton Charge Transfer (for high T_{H}), Electron Impact Dissociation, transition via the electronically excited states $B^1\Sigma_{\mathrm{u}}^+$ and $C^1\Pi_{\mathrm{u}}$ and Dissociative Electron Attachment are most relevant (apart from Electron Impact Excitation) for the (de-)population of the vibrational levels of the electronic ground state $X^1\Sigma_{\mathrm{g}}^+$ in the Magnum-PSI plasma. From the extended *Yacora $H_2(X^1, v)$ model*, Proton Impact (De-)Excitation, H_3^+ Dissociative Recombination, Hydrogen Atom Impact Dissociation and Proton Impact Dissociation are most relevant for the vibrational population distribution in the Magnum-PSI plasma. Again, a discrepancy between the predictions of the *Yacora $H_2(X^1, v)$ model* and the measurement could not be completely resolved. Therefore, it is again recommended to include plasma-surface interaction processes and additionally the transport of excited vibrational levels in the electronic ground state in future work. Finally, further investigations of the OES measurements explicitly accounting for the radial plasma profile, further insights from the TALIF measurements (once these are fully analyzed) and an upcoming CARS campaign may help to explain or resolve the remaining discrepancy.

In summary, both the standard version and the extended version of the *Yacora $H_2(X^1\Sigma_{\mathrm{g}}^+, v)$ model* are able to make predictions with an improved agreement with measurements from different plasma parameter ranges. This improved agreement is achieved through both implementing state-of-the-art reaction probabilities and including additional processes that have been neglected in previous models.

The vibrationally resolved CR model *Yacora $H_2(v)$* extends the *Yacora $H_2(X^1\Sigma_{\mathrm{g}}^+, v)$ model* to (vibrational levels of) electronically excited states, accounting for the processes included in the *Yacora H_2 model*. Vibrationally resolved MCCC cross sections are applied for the process of Electron Impact Excitation.

The model is used to post-process EDGE2D-EIRENE JET ITER-like wall L-mode hydrogen plasma profiles for different detachment stages and to predict the molecular emission yields of the Fulcher-, Lyman- and Werner bands. The model predictions are line of sight-integrated and compared with the predictions from the AMJUEL database that is used as standard in EIRENE calculations. In

general, the Yacora model predicts lower Fulcher band emission and higher Werner and Lyman band emission than AMJUEL. The discrepancy in the emission yields is a consequence of different reaction probabilities for the same process and the inclusion of different sets of processes in the respective, underlying models. While the Yacora model applies MCCC cross sections for Electron Impact Excitation, AMJUEL is based on a CR model applying cross sections after Miles. This difference would in itself result in larger emission yields of the Yacora model for each of the transitions investigated. The Yacora model also includes the process of Dissociative Electron Attachment for (vibrational levels of) electronically excited states that is especially relevant at high electron densities resulting in a strongly reduced Fulcher band emission yield. Since the applied rate coefficients for this process are surprisingly high and already under debate in the literature, accurate cross sections for this process are desired. Switching off Dissociative Electron Attachment for (vibrational levels of) electronically excited states in the Yacora model results typically for divertor plasma calculations in population densities more than one order of magnitude higher than compared to standard calculations. The discrepancies between the predicted emission yields by the Yacora model and AMJUEL have the following implications: If the molecular density n_{H_2} is deduced from measurements on the basis of these predictions, inconsistent results are to be expected depending on which molecular emission band is used, due to the antisymmetric discrepancy for the different emission bands (e.g. the overestimation of the molecular emission results in the underestimation of n_{H_2} and thus the underestimation of MAR rates). AMJUEL overstimates the Fulcher band emission in comparison to the Yacora model for the profiles investigated. This observation is in agreement with previous studies of deuterium plasma at DIII-D, which compare AMJUEL predictions with measurements. Nevertheless, in order to be able to give an even clearer recommendation for the Yacora model, further benchmarks with measurements are required.

Therefore, the model is further used to post-process EDGE2D-EIRENE DIII-D L-mode high recycling deuterium plasma profiles to predict the molecular emission yields of the Fulcher-, Lyman- and Werner bands. Note that, since the vibrational levels in D_2 differ from the levels in H_2, this investigation should be repeated once a dedicated CR model for D_2 is available. The model predictions are again line of sight-integrated and compared with the predictions from the AMJUEL database showing results consistent with the JET calculations: lower Fulcher band emission and higher Werner and Lyman band emission predicted by Yacora than AMJUEL. In addition, the line of sight integrated, model predicted Fulcher-α band emission

is compared with DIII-D measurements demonstrating a better agreement of the *Yacora H_2(v) model* with the measurements than AMJUEL.

In summary, the *Yacora H_2(v)* model agrees better with measurements than AMJUEL. Therefore, it is recommended to apply the model for calculating AMJUEL-like lookup tables for use in neutral transport codes and ITER predictions. Thereby, ITER has already expressed interest in using this data.

The fully ro-vibrationally resolved corona model *Yacora H_2(v,N) Fulcher* can be used to derive T_{vib} and T_{rot} from Fulcher-α band measurements and the model predicted excited state population densities can be post-processed to simulate entire Fulcher-α band spectra. This application can be particularly useful to get an idea of a spectrum prior to a measurement. The model applies for the first time ro-vibrationally resolved MCCC Electron Impact Excitation cross sections for changes in the rotational quantum number $|\Delta N| \leq 5$.

The *Yacora H_2(v,N) Fulcher* corona model has been benchmarked with measurements from an inductively coupled RF plasma demonstrating unprecedented agreement of the absolute value for Q-line predictions within the uncertainty bars of the measurement. The model has been used to investigate the pending question regarding the significance of multipolar excitation (e.g. excitation with $|\Delta N| > 0$). According to the model, the contribution of multipolar excitation to the levels from which Q-line emission for the Fulcher-α band originate is less than 15 % for the investigated plasmas. This observation implies that most importantly $\Delta N = 0$ cross sections must be correct in magnitude for accurate model predictions and excitation via multipolar components is only of secondary importance.

The corona model has been extended for Collisional Quenching, Predissociation and Autoionization, in order to accurately predict P- and R-lines that originate from the perturbed $d^3\Pi_u^+$ state.

In summary, the *Yacora H_2(v,N) Fulcher* corona model makes unprecedentedly accurate predictions in absolute values and can be used as a starting point for the development of a fully ro-vibrationally resolved CR model. The model can be applied to predict entire Fulcher-α band spectra for plasmas in which the corona equilibrium is valid, whereby the validity of the corona equilibrium can be checked with the *Yacora H_2 model*.

In current fusion experiments and in future fusion power plants, hydrogen or deuterium and deuterium-tritium plasmas are used. Consequently, CR models are also required for H_2 isotopologues. Due to different nuclear masses, the H_2

isotopologues have different (ro-)vibrational level energies. As a consequence, the reaction probabilities for the same processes involving different isotopologues differ and dedicated CR models are necessary for the isotopologues. Insights gained from this work regarding H_2 can be transferred to the development of CR models for other isotopologues. For instance, a vibrationally resolved model for D_2 should be feasible straight away: MCCC cross sections for electron impact induced collision processes are available for all isotopologues. According to the standard version of the *Yacora* $H_2(X^1, v)$ model, the processes of Electron Impact Dissociation, Dissociative Electron Attachment and Proton Charge Transfer have the strongest influence on T_{vib}. Dedicated vibrationally resolved cross sections for these processes for D_2 are available in the literature too. Consequently, a vibrationally resolved model for molecular deuterium is feasible for the first time without introducing any questionable scaling laws based on H_2 reaction probabilities.

To sum up, the investigations presented in this work have demonstrated that the newly developed, differently resolved CR models are capable of significantly improved excited state predictions. The excited state densities are relevant for the molecular emission yields and (effective) reaction rates (e.g. dissociation rate). The improvements in the model predictions have been achieved through a critical review of data in the literature and, where necessary, through selection, resulting in the compilation of a database of recommended reaction data. Processes that had been neglected in previous models have been identified and included leading to improved model predictions resulting in better agreement with measurements. Since the developed models have been benchmarked against measurements from various experiments and different plasma parameter ranges, they are available for use in interpreting spectra as plasma diagnostics (e.g. for particle temperatures and densities) and can be applied for further applications. These applications include studying the role of molecules in volume recombination for divertor detachment, the compilation of an AMJUEL-like database of effective rate coefficients to be used in neutral transport codes for divertor plasmas and for ITER predictions. ITER has expressed interest in using this data.

Bibliography

[1] A. Fasoli, "Essay: Overcoming the obstacles to a magnetic fusion power plant," Physical Review Letters **130**, 220001 (2023).

[2] P. C. Stangeby, *The plasma boundary of magnetic fusion devices* (IOP Publishing Ltd, 2000).

[3] U. Fantz, *Atomic and molecular emission spectroscopy in low temperature plasmas containing hydrogen and deuterium*, IPP Report, Habilitationsschrift, Mathematisch-Naturwissenschaftliche Fakultät Universität Augsburg, 2002.

[4] A. von Keudell and V. Schulz-von der Gathen, "Foundations of low-temperature plasma physics-an introduction," Plasma Sources Science and Technology **26**, 113001 (2017).

[5] U. Fantz et al., "Quantification of the VUV radiation in low pressure hydrogen and nitrogen plasmas," Plasma Sources Science and Technology **25**, 045006 (2016).

[6] K. Sawada and M. Goto, "Rovibrationally resolved time-dependent collisional-radiative model of molecular hydrogen and its application to a fusion detached plasma," Atoms **4**, 29 (2016).

[7] K. Sawada, "Electron and proton energy loss via rovibrational excitation of molecular hydrogen in fusion detached plasmas," Plasma and Fusion Research **17**, 2403044 (2022).

[8] D. R. Bates, A. E. Kingston, and R. W. P. McWhirter, "Recombination between electrons and atomic ions, I. Optically thin plasmas," Proceedings of the Royal Society A **267**, 297–312 (1962).

[9] D. R. Bates and A. E. Kingston, "Recombination and energy balance in a decaying plasma I. H-H^+-e plasma," Proceedings of the Royal Society A **279**, 10–31 (1964).

[10] H. W. Drawin, "Collisional-radiative ionization and recombination coefficients for quasi-stationary homogeneous hydrogen and hydrogenic ion plasmas," Z. Physik **225**, 470–482 (1969).

[11] K. Sawada, K. Eriguchi, and T. Fujimoto, "Hydrogen-atom spectroscopy of the ionizing plasma containing molecular hydrogen: Line intensities and ionization rate," Journal of Applied Physics **73**, 8122–8125 (1993).

[12] K. Sawada and T. Fujimoto, "Effective ionization and dissociation rate coefficients of molecular hydrogen in plasma," Journal of Applied Physics **78**, 2913–2924 (1995).

[13] M. Capitelli et al., *Fundamental aspects of plasma chemical physics, Kinetics*, edited by G. W. F. Drake, Springer Series on Atomic, Optical, and Plasma Physics (Springer, 2016).

[14] R. K. Janev et al., *Elementary processes in hydrogen-helium plasmas* (Springer-Verlag Berlin Heidelberg New York London Paris Tokyo, 1987).

[15] R. K. Janev, D. Reiter, and U. Samm, *Collision processes in low-temperature hydrogen plasmas*, Report, 2003.

[16] R. K. Janev and D. Reiter, *Collision and radiative processes in hydrogen plasmas*, personal communication, 2015.

[17] M. C. Zammit et al., "Electron– and positron–molecule scattering: Development of the molecular convergent close-coupling method," Journal of Physics B: Atomic, Molecular and Optical Physics **50**, 123001 (2017).

[18] F. F. Chen, *Introduction to plasma physics and controlled fusion*, 3rd ed. (Springer, 2018).

[19] J. M. Brown and A. Carrington, *Rotational spectroscopy of diatomic molecules* (Cambridge University Press, 2003).

[20] M. Born and R. Oppenheimer, "Zur Quantentheorie der Molekeln," Annalen der Physik **84**, 457–484 (1927).

[21] A. P. Thorne, *Spectrophysics* (Chapman and Hall, 1988).

[22] P. F. Bernath, *Spectra of atoms and molecules* (Oxford University Press, 1995).

[23] G. Herzberg, *Spectra of diatomic molecules*, 2nd ed., Vol. I, Molecular Spectra and Molecular Structure (Van Nostrand Reinhold Company, 1950).

[24] U. Fantz, "Basics of plasma spectroscopy," Plasma Sources Science and Technology **15**, S137–S147 (2006).

[25] U. Fantz and D. Wünderlich, "Franck–Condon factors, transition probabilities, and radiative lifetimes for hydrogen molecules and their isotopomeres," Atomic Data and Nuclear Data Tables **92**, 853–973 (2006).

[26] F. Hund, *Quantentheorie*, 2nd ed., Vol. 24, Handbuch der Physik 561 (Verlag von Julius Springer, 1933).

[27] D. R. Farley et al., "Modeling of hydrogen ground state rotational and vibrational temperatures in kinetic plasmas," Journal of Quantitative Spectroscopy and Radiative Transfer **112**, 800–819 (2011).

[28] J. B. Tatum, "Interpretation of intensities in diatomic molecular spectra," Astrophysical Journal Supplement **14**, 388 (1967).

[29] L. Wolniewicz, "Relativistic energies of the ground state of the hydrogen molecule," The Journal of Chemical Physics **99**, 1851–1868 (1993).

[30] G. Staszewska and L. Wolniewicz, "Adiabatic energies of excited $^1\Sigma_u$ states of the hydrogen molecule," Journal of Molecular Spectroscopy **212**, 208 (2002).

[31] T. E. Sharp, "Potential-energy curves for molecular hydrogen and its ions," Atomic Data and Nuclear Data Tables **2**, 119–169 (1970).

[32] V. Laporta et al., "Vibrational excitation and dissociation of deuterium molecule by electron impact," Plasma Physics and Controlled Fusion **63**, 085006 (2021).

[33] W. Demtröder, *Atoms, molecules and photons, An introduction to atomic-, molecular- and quantum physics*, edited by R. Needs, W. T. Rhodes, and H. E. Stanley, 2nd ed. (Springer, 2006).

[34] G. J. Schulz, "Resonances in electron impact on diatomic molecules," Reviews of Modern Physics **45**, 423 (1973).

[35] P. C. Cosby and H. Helm, "Experimental determination of the H_3^+ bond dissociation energy," Chemical Physics Letters **152**, 71–74 (1988).

[36] C. Dykstra and W. Swope, "The H_3^+ potential surface," Journal of Chemical Physics **70**, 1–3 (1979).

[37] W. E. N. van Harskamp et al., "Detailed H(n = 2) density measurements in a magnetized hydrogen plasma jet," Plasma Sources Science and Technology **21**, 024009 (2012).

[38] J. Rosato, Y. Marandet, and R. Stamm, "A new table of Balmer line shapes for the diagnostic of magnetic fusion plasmas," Journal of Quantitative Spectroscopy and Radiative Transfer **187**, 333–337 (2017).

[39] I. I. Sobel'man, L. A. Vainshtein, and E. A. Yukov, *Excitation of atoms and broadeining of spectral lines*, edited by H. Lotsch, 2nd ed., Atoms+Plasmas 15 (Spinger, 1998).

[40] A. Hansson and J. K. G. Watson, "A comment on Hönl-London factors," Journal of Molecular Spectroscopy **233**, 169–173 (2005).

[41] F. E. Irons, "The escape factor in plasma spectroscopy—I. The escape factor defined and evaluated," Journal of Quantitative Spectroscopy and Radiative Transfer **22**, 1–20 (1979).

[42] K. Behringer and U. Fantz, "The influence of opacity on hydrogen excited-state population and applications to low-temperature plasmas," New Journal of Physics **2**, 23–23 (2000).

[43] K. Behringer, *Escape factors for line emission and population calculations*, IPP Report, 1998.

[44] D. Wünderlich et al., "Emission spectroscopy of negative hydrogen ion sources: From VUV to IR," Review of Scientific Instruments **92**, 1–13 (2021).

[45] H. J. Kunze, *Introduction to plasma spectroscopy*, Atomic, Optical, and Plasma Physics (Springer, 2009).

[46] R. W. P. McWhirter and A. G. Hearn, "A calculation of the instantaneous population densities of the excited levels of hydrogen-like ions in a plasma," Proceedings of the Physical Society **82**, 641–654 (1963).

[47] P. T. Greenland and D. Reiter, "Collisional-Radiative Models Re-examined," Contributions to Plasma Physics **38**, 302–306 (1998).

[48] P. T. Greenland, "Collisional-radiative models with molecules," Proceedings of the Royal Society A **457**, 1821–1839 (2001).

[49] D. Wünderlich, "Vibrationally resolved ionization cross sections for the ground state and electronically excited states of the hydrogen molecule and its isotopomeres," Atomic Data and Nuclear Data Tables **140**, 101424 (2021).

[50] A. Chutijan, A. Garscadden, and J. M. Wadehra, "Electron attachment to molecules at low electron energies," Physics Reports **264**, 393–470 (1996).

[51] E. Krishnakumar et al., "Dissociative electron attachment cross sections for H_2 and D_2," Phyiscal Review Letters **106**, 243201 (2011).

[52] G. Niedner et al., "Observation of vibrationally resolved charge transfer in $H^+ + H_2$ at E_{CM}=20 ev," The Journal of Chemical Physics **87**, 2685–2694 (1987).

[53] L. F. Errea et al., "Influence of nuclear exchange on nonadiabatic electron processes in $H^+ + H_2$ collisions," The Journal of Chemical Physics **133**, 244307 (2010).

[54] P. S. Krstić and D. R. Schultz, "Elastic and vibrationally inelastic slow collisions: H+ H_2, $H^+ + H_2$," Journal of Physics B: Atomic, Molecular and Optical Physics **32**, 2415–2431 (1999).

[55] M. L. Burshtein et al., "Measurement of the radiative lieftimes and collisional-quenching rate coefficients for the H_2-molecule $d^3\Pi_u$v,N levels," Optics and Spectroscopy **68**, 285–287 (1990).

[56] A. A. Matveyev and V. P. Silakov, "Kinetic processes in a highly-ionized non-equilibrium hydrogen plasma," Plasma Sources Science and Technology **4**, 606–617 (1995).

[57] M. A. Lieberman and A. J. Lichtenberg, *Principles of plasma discharges and materials processing* (John Wiley and Sons, 1994).

[58] D. Wünderlich and U. Fantz, "Evaluation of state-resolved reaction probabilities and their application in population models for He, H, and H_2," Atoms **4**, 26 (2016).

[59] D. Wünderlich et al., "Yacora on the Web: Online collisional radiative models for plasmas containing H, H_2 or He," Journal of Quantitative Spectroscopy and Radiative Transfer **240**, 106695 (2020).

[60] C. M. Ferreira and J. Loureiro, "Characteristics of high-frequency and direct-current argon discharges at low pressures: a comparative analysis," Journal of Physics D: Applied Physics **17**, 1175–1188 (1984).

[61] S. Briefi and U. Fantz, "A revised comprehensive approach for determining the H_2 and D_2 rovibrational population from the Fulcher-α emission in low temperature plasmas," Plasma Sources Science and Technology **29**, 125019 (2020).

[62] P. J. Bruggeman et al., "Gas temperature determination from rotational lines in non-equilibrium plasmas: A review," Plasma Sources Science and Technology **23**, 023001 (2014).

[63] S. Briefi, D. Rauner, and U. Fantz, "Determination of the rotational population of H_2 and D_2 including high-N states in low temperature plasmas via the Fulcher-α transition," Journal of Quantitative Spectroscopy and Radiative Transfer **187**, 135–144 (2017).

[64] P. Vankan, D. C. Schram, and R. Engeln, "High rotational excitation of molecular hydrogen in plasmas," Chemical Physics Letters **400**, 196–200 (2004).

[65] J. Wesson, *Tokamaks*, 2nd ed., Oxford Engineering Science Series 48 (Oxford University Press, 1997).

[66] F. Wagner et al., "Regime of improved confinement and high beta in neutral-beam-heated divertor discharges of the ASDEX tokamak," Physical Review Letters **49**, 1408–1412 (1982).

[67] R. P. Wenninger et al., "DEMO divertor limitations during and in between ELMs," Nuclear Fusion **54**, 114003 (2014).

[68] J. Boedo et al., "A review of direct experimental measurements of detachment," Plasma Physics and Controlled Fusion **60**, 044008 (2018).

[69] S. I. Krasheninnikov, A. S. Kukushkin, and A. A. Pshenov, "Divertor plasma detachment," Physics of Plasmas **23**, 055602 (2016).

[70] S. I. Krasheninnikov, "Fascinating physics at the edge of magnetic fusion devices," Plasma Physics and Controlled Fusion **64**, 124005 (2022).

[71] S. I. Krasheninnikov, A. Pigarov, and D. J. Sigmar, "Plasma recombination and divertor detachment," Physics Letters A **214**, 285–291 (1996).

[72] S. I. Krasheninnikov and A. S. Kukushkin, "Physics of ultimate detachment of a tokamak divertor plasma," Journal of Plasma Physics **83**, 155830501 (2017).

[73] S. Krasheninnikov, A. Smolyakov, and A. Kukushkin, *On the edge of magnetic fusion devices*, Springer Series in Plasma Science and Technology (Springer Nature Switzerland AG, 2020).

[74] S. I. Krasheninnikov et al., "Self-sustained oscillations in the divertor plasma," Nuclear Fusion **27**, 1805–1816 (1987).

[75] N. Ohno, "Plasma detachment in linear devices," Plasma Physics and Controlled Fusion **59**, 034007 (2017).

[76] U. Fantz, B. Heger, and D. Wünderlich, "Using the radiation of hydrogen molecules for electron temperature diagnostics of divertor plasmas," Plasma Physics and Controlled Fusion **43**, 907–918 (2001).

[77] A. S. Kukushkin et al., "Role of molecular effects in divertor plasma recombination," Nuclear Materials and Energy **12**, 984–988 (2017).

[78] K. Verhaegh et al., "Spectroscopic investigations of detachment on the MAST Upgrade Super-X divertor," Nuclear Fusion **63**, 016014 (2023).

[79] A. Terakado et al., "Reaction processes of molecular activated recombination leading to detachment of divertor simulation plasma in GAMMA 10/PDX," Nuclear Materials and Energy **20**, 100679 (2019).

[80] K. P. Huber and G. H. Herzberg, "NIST Chemistry WebBook, NIST Standard Reference Database Number 69," in, edited by P. Linstrom and W. Mallard, (online, last access May 26, 2025) (National Institute of Standards and Technology, Gaithersburg MD, 20899) Chap. Constants of diatomic molecules.

[81] S. Briefi, U. Fantz, and NNBI Team, "Spectroscopic investigations of the ion source at BATMAN Upgrade," AIP Conference Proceedings **2052**, 040005 (2018).

[82] U. Fantz, "Emission spectroscopy of molecular low pressure plasmas," Contributions to Plasma Physics **44**, 508–515 (2004).

[83] D. Wünderlich, S. Dietrich, and U. Fantz, "Application of a collisional radiative model to atomic hydrogen for diagnostic purposes," Journal of Quantitative Spectroscopy and Radiative Transfer **110**, 62–71 (2009).

[84] D. Wünderlich et al., "Application of molecular convergent close-coupling cross sections in a collisional radiative model for the triplet system of molecular hydrogen," Journal of Physics D: Applied Physics **54**, 115201 (2021).

[85] NIST ASD Team, *NIST Atomic Spectra Database (ver. 5.12)*, [Online], National Institute of Standards and Technology, Gaithersburg, MD., (last access April 30, 2025).

[86] R. Friedl and D. Rauner, *Personal communication*, 2025.

[87] I. Langmuir and H. M. Mott-Smith, "Langmuir probe technique," General Electric Review **27**, 449 (1924).

[88] H. M. Mott-Smith and I. Langmuir, "The theory of collectors in gaseous discharges," Physical Review **28**, 727–763 (1926).

[89] V. A. Godyak and V. I. Demidov, "Probe measurements of electron-energy distributions in plasmas: What can we measure and how can we achieve reliable results?" Journal of Physics D: Applied Physics **44**, 233001 (2011).

[90] M. J. Druyvesteyn, "Der Niedervoltbogen," Zeitschrift für Physik **64**, 781–798 (1930).

[91] V. A. Godyak, R. B. Piejak, and B. M. Alexandrovich, "Probe diagnostics of non-Maxwellian plasmas," Journal of Applied Physics **73**, 3657–3663 (1993).

[92] J. Sheffield, *Plasma scattering of electromagnetic radiation* (Academic Press, 1975).

[93] H. J. van der Meiden et al., "Incoherent and collective Thomson scattering for the determination of electron and ion properties in low-temperature plasma," Journal of Fusion Energy **39**, 251–260 (2020).

[94] G. D. Stancu, "Two-photon absorption laser induced fluorescence: rate and density-matrix regimes for plasma diagnostics," Plasma Sources Science and Technology **29**, 054001 (2020).

[95] J. Bokor et al., "Two-photon excitation of the n=3 level in H and D atoms," Physical Review A **24**, 612 (1981).

[96] F. Merk et al., "TALIF at H ion sources for the determination of the density and EDF of atomic hydrogen," Journal of Physics D: Applied Physics **56**, 155201 (2023).

[97] K. Niemi, V. Schulz-von der Gathen, and H. F. Döbele, "Absolute calibration of atomic density measurements by laser-induced fluorescence spectroscopy with two-photon excitation," Journal of Physics D: Applied Physics **34**, 2330–2335 (2001).

[98] M. Lefebvre, M. Pealat, and J. P. Taran, "Diagnostics of plasmas by CARS (coherent anti-Stokes Raman scattering)," Pure and Applied Chemistry **64**, 685–689 (1992).

[99] P. McNeely et al., "A Langmuir probe system for high power RF-driven negative ion sources on high potential," Plasma Sources Science Technology **18**, 014011 (2009).

[100] C. J. Fröhler-Bachus, *A portable diagnostic tool for the absolute determination of photon fluxes in low pressure plasmas down to the VUV region*, Dissertation, Mathematisch-Naturwissenschaftlich-Technische Fakultät, Universität Augsburg, 2022.

[101] U. Fantz, "Spectroscopic diagnostics and modelling of silane microwave plasmas," Plasma Physics and Controlled Fusion **40**, 1035–1056 (1998).

[102] M. Regler, *Messung ausgewählter Übergänge im Wasserstoffmolekül und Vergleich mit Rechnungen*, Diplomarbeit, Lehrstuhl für Experimentelle Plasmaphysik, Universität Augsburg, 2005.

[103] U. Fantz et al., "Advanced NBI beam characterization capabilities at the recently improved test facility BATMAN Upgrade," Fusion Engineering and Design **146**, 212–215 (2019).

[104] M. Shimada et al., "Chapter 1: Overview and summary," Nuclear Fusion **47**, S1–S17 (2007).

[105] M. Bacal and M. Wada, "Negative hydrogen ion production mechanisms," Applied Physics Reviews **2**, 021305 (2015).

[106] D. Wünderlich et al., "Achievement of ITER-relevant accelerated negative hydrogen ion current densities over 1000 s at the ELISE test facility," Nuclear Fusion **59**, 084001 (2019).

[107] P. McNeely, D. Wünderlich, and NNBI Team, "Neutral depletion in an H^- source operated at high RF power and low input gas flow," Plasma Sources Science and Technology **20**, 045005 (2011).

[108] A. Fruchtman, "Neutral gas depletion in low temperature plasma," Journal of Physics D: Applied Physics **50**, 473002 (2017).

[109] U. Fantz et al., "Negative hydrogen ion sources for fusion: From plasma generation to beam properties," Frontiers in Physics **9**, 1–17 (2021).

[110] B. Heinemann et al., "Towards large and powerful radio frequency driven negative ion sources for fusion," New Journal of Physics **19**, 015001 (2017).

[111] U. Fantz et al., "Contributions of the extended ELISE and BATMAN Upgrade test facilities to the roadmap towards ITER NBI," Nuclear Fusion **64**, 086063 (2024).

[112] J. Rapp et al., "Construction of the plasma-wall experiment Magnum-PSI," Fusion Engineering and Design **85**, 1455–1459 (2010).

[113] W. A. J. Vijvers et al., "Experimental and theoretical determination of the efficiency of a sub-atmospheric flowing high power cascaded arc hydrogen plasma source," Plasma Sources Science and Technology **19**, 065016 (2010).

[114] H. Zohm, "Edge localized modes (ELMs)," Plasma Physics and Controlled Fusion **38**, 105–128 (1996).

[115] M. J. van de Pol et al., "Operational characteristics of the superconducting high flux plasma generator Magnum-PSI," Fusion Engineering and Design **136**, 597–601 (2018).

[116] H. J. N. van Eck et al., "Operational characteristics of the high flux plasma generator Magnum-PSI," Fusion Engineering and Design **89**, 2150–2154 (2014).

[117] G. R. A. Akkermans et al., "The role of hydrogen molecular effects on detachment in Magnum-PSI," Phyiscs of Plasmas **27**, 102509 (2020).

[118] K. Loring, *Personal communication*, 2025.

[119] P.-H. Rebut, "The Joint European Torus (JET)," The European Physical Journal H **43**, 459–498 (2018).

[120] F. G. Rimini and JET Contributors, "JET: 40 successful years of fusion research," IEEE Transactions on Plasma Science **52**, 3561–3573 (2024).

[121] P. Barabaschi et al., "ITER progresses into new baseline," Fusion Engineering and Design **215**, 114990 (2025).

[122] F. Romanelli, "Overview of the JET results," Nuclear Fusion **55**, 104001 (2015).

[123] C. F. Maggi et al., "Overview of T and D–T results in JET with ITER-like wall," Nuclear Fusion **64**, 112012 (2024).

[124] G. Sergienko et al., "Molecular deuterium behaviour in tungsten divertor on JET," Journal of Nuclear Materials **438**, S1100–S1103 (2013).

[125] E. Pawelec et al., "Spectroscopic observations and analysis of the Fulcher bands of hydrogen an its isotopologues in divertor region of the ITER-like wall JET tokamak," 48th EPS Conference on Plasma Physics, EPS 2022 (2022).

[126] A. Meigs et al., "Enhancement of JET's mirror-link near-ultraviolet to near-infrared divertor spectroscopy system," Review of Scientific Instruments **81**, 10E532 (2010).

[127] M. Groth et al., "Impact of carbon and tungsten as divertor materials on the scrape-off layer conditions in JET," Nuclear Fusion **53**, 093016 (2013).

[128] J. Luxon, "A design retrospective of the DIII-D tokamak," Nuclear Fusion **42**, 614–633 (2002).

[129] M. Maisel et al., "The fusion power research programme at GA Technologies Inc," Nuclear Fusion **25**, 1113–1125 (1985).

[130] C. Holcomb et al., "DIII-D research to provide solutions for ITER and fusion energy," Nuclear Fusion **64**, 112003 (2024).

[131] N. Brooks et al., "Multichord spectroscopy of the DIII-D divertor region," Review of Scientific Instruments **63**, 5167–5169 (1992).

[132] F. Glass et al., "Upgraded divertor Thomson scattering system on DIII-D," Review of Scientific Instruments **87**, 11E508 (2016).

[133] J. Watkins et al., "High heat flux Langmuir probe array for the DIII-D divertor plates," Review of Scientific Instruments **79**, 10F125 (2008).

[134] M. Groth et al., *EIRENE predictions of deuterium emission in DIII-D L-mode plasmas constrained by 2D divertor Thomson scattering and Langmuir probe measurements*, 26th International Conference on Plasma Surface Interaction in Controlled Fusion Devices (PSI-26), Marseille, France, 2024.

[135] M. Groth et al., *EIRENE interpretation of divertor deuterium emission in DIII-D constrained by 2D divertor Thomson scattering and Langmuir probe measurements*, 51st EPS Conference on Plasma Physics, Vilnius, Lithuania, 2025.

[136] D. Wünderlich, *Berechnung von Teilchendichten für die Diagnostik an Niedertemperaturplasmen*, Shaker Verlag, Aachen, Dissertation, Mathematisch-Naturwissenschaftliche Fakultät, Universität Augsburg, 2005.

[137] A. C. Hindmarsh et al., "SUNDIALS: Suite of nonlinear and differential/algebraic equation solvers," ACM Transactions on Mathematical Software **31**, 363–396 (2005).

[138] S. D. Cohen, A. C. Hindmarsh, and P. F. Dubois, "CVODE, a stiff/nonstiff ODE solver in C," Computers in Physics **10**, 138–143 (1996).

[139] S. Dietrich, *Verifikation von optischen Diagnostikmethoden an H_2/D_2-Plasmen*, Dissertation, Mathematisch-Naturwissenschaftlich-Technische Fakultät, Universität Augsburg, 2010.

[140] F. Manaigo, *Creation, validation and application of a collisional radiative model for positive Argon ions*, Dipartimento di Fisica e Astronomia "Galileo Galilei", Universita degli studi di Padova, 2019.

[141] R. Friedl and U. Fantz, "Spectral intensity of the N_2 emission in argon low-pressure arc discharges for lighting purposes," New Journal of Physics **14**, 043016 (2012).

[142] U. Fantz and D. Wünderlich, "Atomic and molecular collisional radiative modeling for spectroscopy of low temperature and magnetic fusion plasmas," AIP Conference Proceedings **1344**, 204–216 (2011).

[143] D. Wünderlich, C. Wimmer, and R. Friedl, "A collisional radiative model for low-pressure hydrogen–caesium plasmas and its application to an RF source for negative hydrogen ions," Journal of Quantitative Spectroscopy and Radiative Transfer **149**, 360–371 (2014).

[144] D. Reiter, M. Baelmans, and P. Börner, "The EIRENE and B2-EIRENE codes," Fusion Science and Technology **47**, 172–186 (2017).

[145] D. Reiter, *The Data File AMJUEL: Additional Atomic and Molecular Data for EIRENE*, FZJ, Forschungszentrum Jülich GmbH, 2020.

[146] R. Simonini et al., "Models and numerics in the multi-fluid 2-D edge plasma code EDGE2D/U," Contributions to Plasma Physics **34**, 368–373 (1994).

[147] S. Wiesen, *EDGE2D-EIRENE code interface report*, JET ITC Report, 2006.

[148] R. J. Le Roy, "LEVEL: A computer program for solving the radial Schrödinger equation for bound and quasibound levels," Journal of Quantitative Spectroscopy and Radiative Transfer **186**, 167–178 (2017).

[149] W. T. Miles, R. Thompson, and A. E. S. Green, "Electron-impact cross sections and energy deposition in molecular hydrogen," Journal of Applied Physics **43**, 678–686 (1972).

[150] R. Celiberto et al., "Cross section data for electron-impact inelastic processes of vibrationally excited molecules of hydrogen and its isotopes," Atomic Data and Nuclear Data Tables **77**, 161–213 (2001).

[151] R. C. Bergmayr, D. Wünderlich, and U. Fantz, "Molecular data needs for advanced collisional-radiative modelling for hydrogen plasmas," The European Physical Journal D **77**, 136, 1–14 (2023).

[152] L. H. Scarlett et al., "Complete collision data set for electrons scattering on molecular hydrogen and its isotopologues: I. Fully vibrationally-resolved electronic excitation of $H_2(X^1\Sigma_g^+)$," Atomic Data and nuclear Data Tables **137**, 101361 (2021).

[153] L. H. Scarlett et al., "Convergent close-coupling calculations of electrons scattering on electronically excited molecular hydrogen," Physical Review A **103**, 032802 (2021).

[154] T. Fujimoto and R. W. P. McWhirter, "Validity criteria for local thermodynamic equilibrium in plasma spectroscopy," Physical Review A **42**, 6588–6601 (1990).

[155] L. C. Johnson, "Approximations for collisional and radiative transition rates in atomic hydrogen," Astrophysical Journal **174**, 227–236 (1972).

[156] L. Vriens and A. H. M. Smeets, "Cross-section and rate formulas for electron-impact ionization, excitation, deexcitation, and total depopulation of excited atoms," Physical Review A **22**, 940–951 (1980).

[157] L. H. Scarlett, *Personal communication*, 2024.

[158] M. Gryzinski, "Classical theory of atomic collisions. I. Theory of inelastic collisions," Physical Review **138**, A336–A358 (1965).

[159] E. Bauer and C. D. Bartky, "Calculation of inelastic electron—molecule collision cross sections by classical methods," The Journal of Chemical Physics **43**, 2466–2476 (1965).

[160] K. Sawada, *Personal communication with D. Wünderlich*, reference in IPP report 10/18 (see [169]), 2000.

[161] J. R. Hiskes, "Molecular Rydberg states in hydrogen negative ion discharges," Appl. Phys. Lett. **69**, 755–757 (1996).

[162] P. G. Datskos, L. A. Pinnaduwage, and J. F. Kielkopf, "Photophysical and electron attachment properties of ArF-excimer-laser irradiated H_2," Physical Review A **55**, 4131–4142 (1997).

[163] K. Fujii et al., "Experimental validation of a collision-radiation dataset for molecular hydrogen in plasmas," Physics of Plasmas **31**, 092512 (2024).

[164] R. K. Janev, C. J. Joachain, and N. N. Nedeljkovic, "Resonant electron transfer in slow collisions of protons with Rydberg hydrogen atoms," Physical Review A **29**, 2463–2469 (1984).

[165] A. B. Wedding and A. V. Phelps, "Quenching and excitation transfer for the $c^3\Pi_u^-$ and $a^3\Sigma_g^+$ states of H_2 in collisions with H_2," Journal of Chemical Physics **89**, 2965–2974 (1988).

[166] A. Y. Pigarov and S. I. Krasheninnikov, "Application of the collisional-radiative, atomic-molecular model to the recombining divertor plasma," Physics Letters A **222**, 251–257 (1996).

[167] K. Sawada and T. Fujimoto, "Effect of initial vibrational excitation of molecular hydrogen on molecular assisted recombination in divertor plasmas," Contrib. Plasma Phys. **6-7**, 603–607 (2002).

[168] K. Hassouni et al., "Chemical kinetics and energy transfer in moderate pressure H_2 plasmas used in diamond MPACVD processes," Plasma Sources Science and Technology **8**, 494–512 (1999).

[169] D. Wünderlich and U. Fantz, *Anwendung und Erweiterung eines Stoß-Strahlungsmodells für H_2 und H*, IPP Report, (Diplomarbeit, Lehrstuhl für Experimentelle Plasmaphysik, Universität Augsburg, November 2000), 2001.

[170] P. T. Greenland, *The CRMOL Manual: Collisional-radiative models for molecular hydrogen in plasmas*, JUEL-Report, 2001.

[171] J. N. Bardsley and J. M. Wadehra, "Dissociative attachment and vibrational excitation in low-energy collisions of electrons with H_2 and D_2," Physical Review A **20**, 1398–1405 (1979).

[172] L. H. Scarlett et al., "Electron-impact dissociation of vibrationally-excited molecular hydrogen into neutral fragments," Atoms **7**, 75 (2019).

[173] J. Horáček et al., "Dissociative electron attachment and vibrational excitation of H_2 by low-energy electrons: Calculations based on an improved nonlocal resonance model," Physical Review A **70**, 052712 (2004).

[174] M. G. Holliday, J. T. Muckerman, and L. Friedman, "Isotopic studies of the proton–hydrogen molecule reaction," The Journal of Chemical Physics **54**, 1058–1072 (1971).

[175] X. Urbain et al., "New light shed on charge transfer in fundamental $H^+ + H_2$ collisions," Physical Review Letters **111**, 203201 (2013).

[176] L. F. Errea et al., "Vibronic treatment of vibrational excitation and electron capture in $H^+ + H_2$ (HD, D_2 , ...) collisions at low impact energies," Physical Review A **75**, 032703 (2007).

[177] P. S. Krstić, "Inelastic processes from vibrationally excited states in slow $H^+ + H_2$ and $H+H_2$ collisions: Excitations and charge transfer," Physical Review A **66**, 042717 (2002).

[178] P. S. Krstić, D. R. Schultz, and R. K. Janev, "Charge transfer processes in slow collisions of protons with vibrationally excited hydrogen molecules," Physica Scripta **T96**, 61 (2002).

[179] A. Ichihara, O. Iwamoto, and R. K. Janev, "Cross sections for the reaction $H^+ + H_2$ (v = 0–14) $\rightarrow H + H_2^+$ at low collision energies," Journal of Physics B: Atomic, Molecular and Optical Physics **33**, 4747–4758 (2000).

[180] A. Ichihara, O. Iwamoto, and K. Yokoyama, *Atomic and plasma–material interaction data for fusion, volume 9*, p. 193, 2001.

[181] M. A. Dopita and R. S. Sutherland, *Astrophyiscs of the diffuse universe*, 1st ed., Astronomy and Astrophysics Library (Springer Berlin, Heidelberg, 2003).

[182] P. S. Krstić, "Vibrationally resolved collisions in cold hydrogen plasma," Nuclear Instruments and Methods in Physics Research B **241**, 58–62 (2005).

[183] P. S. Krstić and R. K. Janev, "Inelastic processses from vibrationally excited states in slow $H^+ + H_2$ and $H + H_2^+$ collisions. ii. Dissociation," Physical Review A **67**, 022708 (2003).

[184] M. Cízek, J. Horáček, and W. Domcke, "Nuclear dynamics of the H_2- collision complex beyond the local approximation: associative detachment and dissociative attachment to rotationally and vibrationally excited molecules," Journal of Physics B: Atomic, Molecular and Optical Physics **31**, 2571–2583 (1998).

[185] F. Esposito, C. Gorse, and M. Capitelli, "Quasi-classical dynamics calculations and state-selected rate coefficients for $H + H_2(v,j) \rightarrow 3H$ processes: application to the global dissociation rate under thermal conditions," Chemical Physics Letters **303**, 636–640 (1999).

[186] D. G. Truhlar and C. J. Horowitz, "Functional representation of Liu and Siegbahn's accurate ab initio potential energy calculations for $H+H_2$," The Journal of Chemical Phyiscs **68**, 2466–2476 (1978).

[187] M. Cacciatore and G. D. Billing, "State-to-state vibration-translation and vibration-vibration rate constants in H_2-H_2 and HD-HD collisions," Journal of Chemical Physics **96**, 217–223 (1992).

[188] M. Cacciatore, M. Capitelli, and G. D. Billing, "Vibration-to-translation energy exchanges in H_2 colliding with highly vibrationally excited H_2 molecules," Chemical Physics Letters **157**, 305–308 (1989).

[189] D. Strasser et al., "Branching ratios in the dissociative recombination of polyatomic ions: the H_3^+ case," Physical Review A **65**, 010702 (2001).

[190] S. Datz et al., "Branching processes in the dissociative recombination of H_3^+," Physical Review Letters **74**, 896–899 (1995).

[191] M. Larsson et al., "Direct high-energy neutral-channel dissociative recombination of cold H_3^+ in an ion storage ring," Physical Review Letters **70**, 430–433 (1993).

[192] D. Reiter et al., "Detailed atomic, molecular and radiation kinetics in current 2D and 3D edge plasma fluid codes," Journal of Nuclear Materials **363-365**, 649–657 (2007).

[193] R. C. Bergmayr et al., "Demonstrating the impact of ro-vibrationally excited H_2 on divertor detachment via population modelling," Nuclear Materials and Energy **42**, 101895 (2025).

[194] M. Groth et al., "Impact of H, D, T and D-T hydrogenic isotopes on detachment in JET ITER-like wall low-confinement mode plasmas," Proc. of the 29th IAEA Fusion Energy Conference 2023, London, UK, IAEA-CN-316-2021, manuscript submitted to Nuclear Fusion (2023).

[195] M. Groth et al., "EDGE2D-EIRENE predictions of molecular emission in DIII-D high-recycling divertor plasmas," Nuclear Materials and Energy **19**, 211–217 (2019).

[196] M. Groth et al., "Validation of EDGDE2D-EIRENE predicted 2D distributions of electron temperature and density against divertor Thomson scattering measurements in the low-field side divertor leg in DIII-D," Nuclear Materials and Energy **34**, 101372 (2023).

[197] B. P. Lavrov, "Determination of the gas temperature of a low-pressure plasma from the intensities of the H2 and D2 molecular bands. Relationship between the intensity distribution in a band and the gas temperature," Opt. Spectrosc. (USSR) **48**, 680–689 (1978).

[198] B. P. Lavrov, V. N. Ostrovskii, and V. I. Ustimov, "Determination of the gas temperature of a low-pressure plasma from the intensities of the H2 and D2 molecular bands; rotational transition under electron-impact excitation," Opt. Spektrosk. **47**, 55–62 (1979).

[199] U. Fantz and B. Heger, "Spectroscopic diagnostics of the vibrational population in the ground state of H_2 and D_2 molecules," Plasma Physics and Controlled Fusion **40**, 2023–2032 (1998).

[200] U. Fantz et al., "Optical emission measurements of H_2 and D_2 molecules in the divertor region of ASDEX Upgrade," Journal of Nuclear Materials **266-269**, 490–494 (1999).

[201] T. Mosbach, H. M. Katsch, and H. F. Döbele, "In situ diagnostics in plasmas of electronic-ground-state hydrogen molecules in high vibrational and rotational states by laser-induced fluorescence with vacuum-ultraviolet radiation," Physical Review Letters **85**, 3420–3423 (2000).

[202] B. Xiao et al., "Rovibrational distribution determination of H_2 in low temperature plasmas by Fulcher-band spectroscopy," Plasma Physics and Controlled Fusion **46**, 653–668 (2004).

[203] G. Staszewska and L. Wolniewicz, "Transition moments among $^3\Sigma$ and $^3\Pi$ states of the H_2 molecule," Journal of Molecular Spectroscopy **198**, 416–420 (1999).

[204] T. Shikama et al., "Construction of coronal models for H_2 $d^3\Pi_u$ - $a^3\Sigma_g^+$ and $I^1\Pi_g$ - $B^1\Sigma_u^+$ transitions for the evaluation of ro-vibrational temperatures," Nuclear Instruments and Methods in Physics Research A **623**, 744–746 (2010).

[205] D. Bruno, B. Zaniol, and I. Mario, "Rotational and vibrational temperatures of hydrogen nonequilibrium plasmas from Fulcher band emission spectra," Physica Scripta **98**, 015614 (2022).

[206] P. L. Rubin, "Probabilities of population of rotational levels by electron excitation of diatomic molecules," Soviet Journal of Experimental and Theoretical Physics **65**, 1375–1381 (1974).

[207] D. K. Otorbaev et al., "Electron-excited molecules in nonequilibrium plasma," in, edited by N. N. Sobolev (New York: Nova Science, 1989) Chap. Electron-impact excitation levels of the rotational levels of molecular electron states in gas discharges, pp. 121–173.

[208] R. C. Bergmayr et al., "A ro-vibrationally resolved corona model for the molecular hydrogen Fulcher-α system," Journal of Quantitative Spectroscopy and Radiative Transfer **338**, 109414 (2025).

[209] D. Wünderlich, *Personal communication*, 2023.

[210] J. Bretagne, J. Godart, and V. Puech, "Time-resolved study of the H_2 continuum at low pressures," Journal of Physics B: Atomic and Molecular Physics **14**, L761–L765 (1981).

[211] B. P. Lavrov and V. P. Prosikhin, "Electronic excitation in hydrogen gas-discharge low-pressure plasma," Opt. Spektrosk. **64**, 498–502 (1988).

[212] C. Jungen and O. Atabek, "Rovibronic interactions in the photoabsorption spectrum of molecular hydrogen and deuterium: An application of multichannel quantum defect methods," Journal of Chemical Physics **66**, 5584–5609 (1977).

[213] T. Kiyoshima et al., "Competition between predissociative and radiative decays in the $e^3\Sigma_u^+$ and $d^3\Pi_u$ states of H_2 and D_2," Physical Review A **60**, 4494–4503 (1999).

[214] T. Kiyoshima and H. Sato, "Perturbation effects on lifetimes of $d^3\Pi_u$ states in H_2 and D_2," Physical Review A **48**, 4771–4774 (1993).

[215] H. M. Crosswhite, *The hydrogen molecule wavelength tables of Gerhard Heinrich Dieke* (New York, Wiley-Interscience, 1972).

[216] X. Liu et al., "Spectra, emission yields, cross sections, and kinetic energy distributions of hydrogen atoms from H_2 excitation by electron impact," The Astrophysical Journal **818**, 120 (2016).

[217] S. A. Astashkevich and B. P. Lavrov, "Lifetimes of vibro-rotational levels in excited electronic states of diatomic hydrogen isotopologues," Journal of Physical and Chemical Reference Data **44**, 023105 (2015).

List of publications

Printed publications as first author

- **R.C. Bergmayr**, L.H. Scarlett, D. Wünderlich, D.V. Fursa, M.C. Zammit, I.Bray and U. Fantz, *A fully ro-vibrationally resolved corona model for the molecular hydrogen Fulcher-α system*, Journal of Quantitative Spectroscopy & Radiative Transfer **338** (2025), 109414.

- **R.C. Bergmayr**, D. Wünderlich, M. Groth, L.H. Scarlett, D.V. Fursa, M.C. Zammit, I. Bray and U. Fantz, *Demonstrating the impact of ro-vibrationally excited H_2 on divertor detachment via population modelling*, Nuclear Materials and Energy **42** (2025), 101895.

- **R.C. Bergmayr**, D. Wünderlich and U. Fantz, *Molecular data needs for advanced collisional-radiative modelling for hydrogen plasmas*, Eur. Phys. J. D **77** (2023), 136.

Miscellaneous

- **R.C. Bergmayr**, D. Wünderlich and U. Fantz, *About recent progress in collisional-radiative modelling of molecular hydrogen plasmas*, DPG-Frühjahrstagung der Sektion Materie und Kosmos (SMuK), Göttingen, Germany, (2025) Oral.

- J. Bryant, K. McKay, J.R. Harrison, D. Moulton, K. Verhaegh, C. Cowley, **R.C. Bergmayr**, U. Fantz and D. Wünderlich, *Impact of Yacora evaluated molecular effective rate coefficients on detached SOLPS-ITER simulations*, Nuclear Fusion **65** (2025), 036025.

- U. Fantz, **R.C. Bergmayr** and D. Wünderlich, *Challenges in the analysis of spectra of atomic and molecular hydrogen particles in low temperature plasmas*, NWO Physics 2025, Veldhoven, The Netherlands, (2025) Oral.

- U. Fantz, **R.C. Bergmayr** and D. Wünderlich, *Recent progress of collisional radiative modelling of H_2 with Yacora and steps needed for D_2*, The Decennial IAEA Technical Meeting on Atomic, Molecular and Plasma-Material Interaction Data for Fusion Science and Technology (AMPMI 2024), Helsinki, Finland, (2024) Oral.

- **R.C. Bergmayr**, D. Wünderlich, M. Groth, L.H. Scarlett, D.V. Fursa, M.C. Zammit, I. Bray and U. Fantz, *Demonstrating the impact of ro-vibrationally excited H_2 on divertor detachment via population modelling*, 26th International Conference on Plasma Surface Interaction in Controlled Fusion Devices (PSI 26), Marseille, France, (2024) Poster.

- **R.C. Bergmayr**, D. Wünderlich, L.H. Scarlett, M.C. Zammit, I. Bray, D.V. Fursa and U. Fantz, *Ro-vibrationally resolved corona modelling for the Fulcher-α band of H_2 plasmas: a powerful tool for spectra analysis*, DPG-Frühjahrstagung der Sektion Materie und Kosmos (SMuK), Greifswald, Germany, (2024) Oral.

- D. Wünderlich, **R.C. Bergmayr** and U. Fantz, *Vibrationally and ro-vibrationally resolved collisional radiative modelling of molecular hydrogen: current status and outlook*, 2nd Technical Meeting on the Collisional-Radiative Properties of Tungsten and Hydrogen in Edge Plasma of Fusion Devices, Vienna, Austria, (2023) Oral.

- **R.C. Bergmayr**, D. Wünderlich, L.H. Scarlett, M.C. Zammit, I. Bray, D.V. Fursa and U. Fantz, *Corona modelling for ro-vibrationally resolved spectra analysis in low temperature hydrogen plasmas*, 35th International Conference on Phenomena in Ionized Gases (ICPIG 2023), Egmond aan Zee, The Netherlands, (2023) Poster.

- **R.C. Bergmayr**, D. Wünderlich and U. Fantz, *Collisional radiative modelling for molecular hydrogen plasmas applying MCCC cross sections*, 86. Jahrestagung der DPG und DPG-Frühjahrstagung der Sektion Materie und Kosmos (SMuK), Dresden, Germany, (2023) Oral.

- **R.C. Bergmayr**, D. Wünderlich and U. Fantz, *Collisional radiative modelling for molecular hydrogen plasmas*, International Plasma School on "Low Temperature Plasma Physics: Basics and Applications", Bad Honnef, Germany, (2022) Poster.

- D. Wünderlich, **R.C. Bergmayr** and U. Fantz, *Collisional radiative modelling of hydrogen using the flexible solver Yacora: overview and features*, 12th International Conference on Atomic and Molecular Data and Their Applications (ICAMDATA 2022), Mola di Bari, Italy, (2022) Oral.

- **R.C. Bergmayr**, D. Wünderlich and U. Fantz, *Relevance of molecular data in collisional radiative modelling of molecular hydrogen plasmas*, 12th International Conference on Atomic and Molecular Data and Their Applications (ICAMDATA 2022), Mola di Bari, Italy, (2022) Oral.

Acknowledgments

I would like to express my gratitude to everyone who has supported me on this journey or contributed to this thesis in any way.

I am grateful to Prof. Ursel Fantz for the opportunity to pursue this dissertation at the Max Planck Institute for Plasma Physics, as well as for the outstanding support throughout the entire project.

I thank Prof. Helmut Karl for his willingness to take on the role as second reviewer.

My thanks go to Dirk Wünderlich for your support as scientific supervisor, your previous work that I could built upon and the great freedom you have given me.

Within the scope of this project, I have had the privilege of working with several scientist from all over the world. My thanks go to Liam Scarlett, Mark Zammit, Igor Bray and Dmitry Fursa for the fruitful collaboration and the opportunity to be one of the first to test and apply your most fundamental cross sections.

Furthermore, I would like to express my gratitude to Mathias Groth for the joint projects, discussions and doors you have opened. I extend my appreciation to Detlev Reiter for any scientific exchange we have had and for sharing your profound knowledge about so many relevant topics for this work.

I convey my thanks to Ivo Classen, Hennie van der Meiden, Kaden Loring, Kay Schutjes and Jordy Vernimmen for the opportunity and your contribution to our joint measurements at Magnum-PSI and for the great atmosphere during my stay at DIFFER.

In addition, I extend my thanks to many experts in their fields, who have discussed with me or replied to my mails (even without knowing each other), or have helped me getting leads to previously available cross section data that had been removed from the web.

Furthermore, my thanks go especially to Roland Friedl, Arne Meindl, Stefan Briefi, David Rauner and Christian Wimmer for the support in your respective

fields of expertise.

I would like to thank Thomas Pütterich for fulfilling your role as scientific counsel in an exemplary manner.

I further thank Karin Eisenträger, Waltraud Sinz and Kurt Ritter for your administrative or IT support.

I thank Elisabeth Wolfrum, if you hadn't given me first access to fusion research, I wouldn't be writing this right now.

Sometimes fundamental work can be exhausting during the day to day business. Being reminded of the big picture, can be an enormous motivator. Therefore, I would like to thank Ingrid Kaufmann for organizing and giving me the opportunity to hold science communication tours on the institute, as well as all visitors who, with their interest and reactions to our work, re-fueled my enthusiasm for realizing the harnessing of energy from a burning star on Earth.

Moreover, a doctorate also thrives on the experiences of others further along the path and the pleasant time with them. I am grateful to Freddy Merk, Adrian Heiler, Max Lindqvist, Christian Kiefer, Daniele Mussini, Vinzenz Wolf, Nikolas Klose, Julian Hörsch and Joey Rubin. I further thank Dimitar Yordanov, Araceli Navarro Fernandez, Anil Cherukulappurath, Jasper Knaack, Rodrigo Mendes Antunes, Niek den Harder and all other (former) not explicitly mentioned colleagues!

Finally, I want to thank my family, especially Gerda and Christian for encouraging me from early on to pursue my curiosity and all your support in every way. I am deeply grateful to Eugenie, for all your understanding, backing and love.

After all, I thank the public for funding this endeavor. We will deliver.

Appendix

A Nomenclature of radiative quantities

While the nomenclature of the radiometry units is well established, the denomination for quantities expressed in the form of $\frac{Ph}{s}$ ($W \cdot \frac{\lambda}{hc} \widehat{=} \frac{Ph}{s}$) varies in the literature. Table A.1 summarizes the nomenclature of radiative quantities used in this work.

Table A.1: *Nomenclature of radiative quantities.*

Radiative quantity	Unit
radiant flux	W
spectral flux	W/nm
radiant intensity	W/sr
spectral intensity	W/(m sr)
radiance	W/ (m^2 sr)
flux density (irradiance)	W/m
spectral irradiance	W/m^3
spectral emission intensity	Ph/(s m^3 nm)
emission intensity	Ph/(s m^3)
line emission intensity	Ph/(s m^3) (for single emission lines)
photon intensity	Ph/(s m^2 sr)

B Applied cross sections and rate coefficients

For the reader's convenience, a selection of cross sections and rate coefficients applied in the electronically resolved *Yacora H_2 model* and the vibrationally resolved *Yacora $H_2(X^1, v)$ model* are depicted in the following. Please see the extensive model descriptions in chapters 4.1 and 4.2 and the references therein for the origin of the data.

B.1 The Yacora H_2 model

Electron Impact Excitation

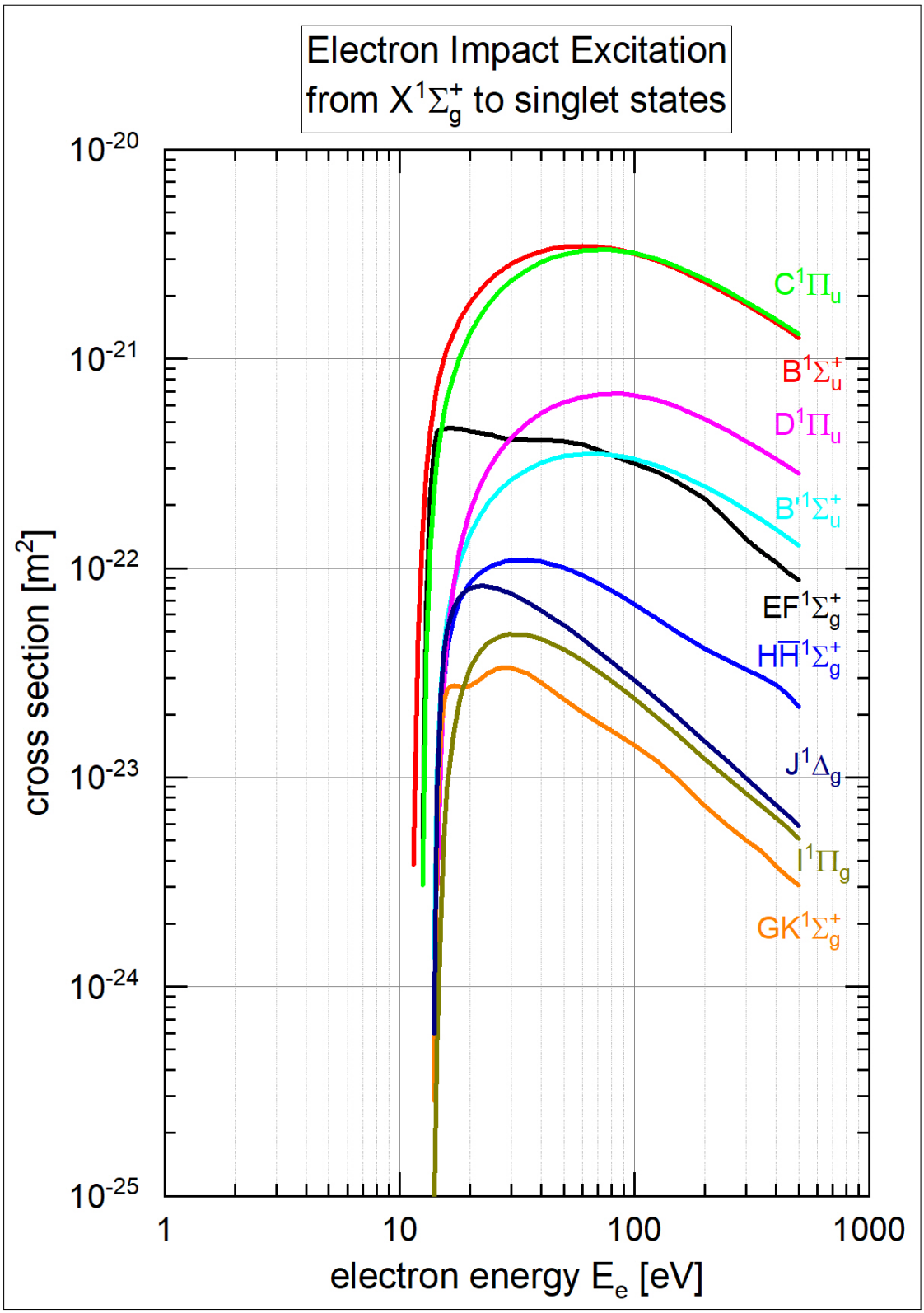

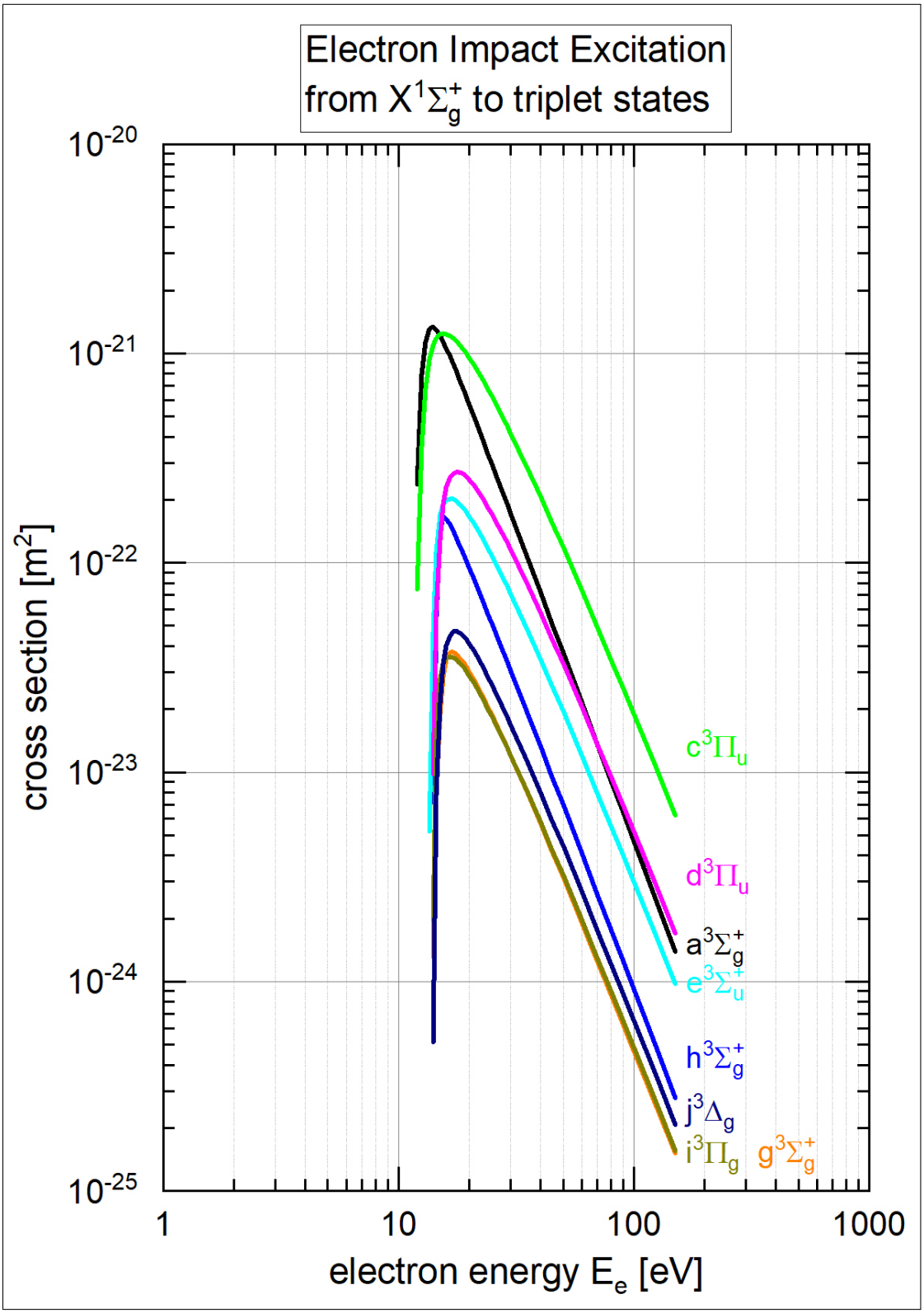
Electron Impact Excitation
from X$^1\Sigma_g^+$ to triplet states
cross section [m^2]
10^{-20}
10^{-21}
10^{-22}
10^{-23}
10^{-24}
10^{-25}
1
10
100
1000
electron energy E_e [eV]
$c^3\Pi_u$
$d^3\Pi_u$
$a^3\Sigma_g^+$
$e^3\Sigma_u^+$
$h^3\Sigma_g^+$
$j^3\Delta_g$
$i^3\Pi_g$
$g^3\Sigma_g^+$

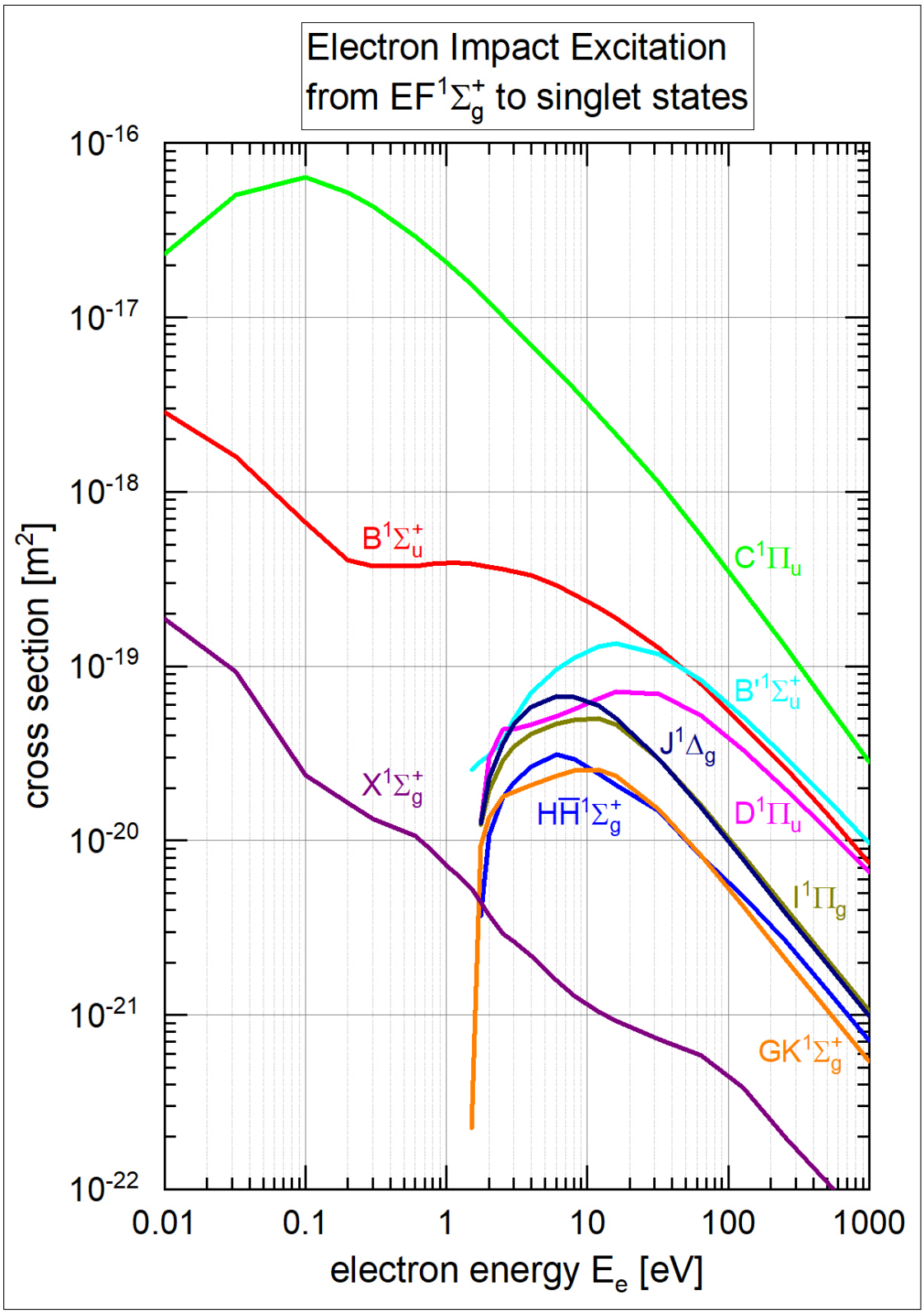
Electron Impact Excitation
from EF$^1\Sigma_g^+$ to singlet states
cross section [m^2]
electron energy E_e [eV]
10^{-16}
10^{-17}
10^{-18}
10^{-19}
10^{-20}
10^{-21}
10^{-22}
0.01
0.1
1
10
100
1000
$B^1\Sigma_u^+$
$C^1\Pi_u$
$B'^1\Sigma_u^+$
$J^1\Delta_g$
$X^1\Sigma_g^+$
$H\bar{H}^1\Sigma_g^+$
$D^1\Pi_u$
$I^1\Pi_g$
$GK^1\Sigma_g^+$

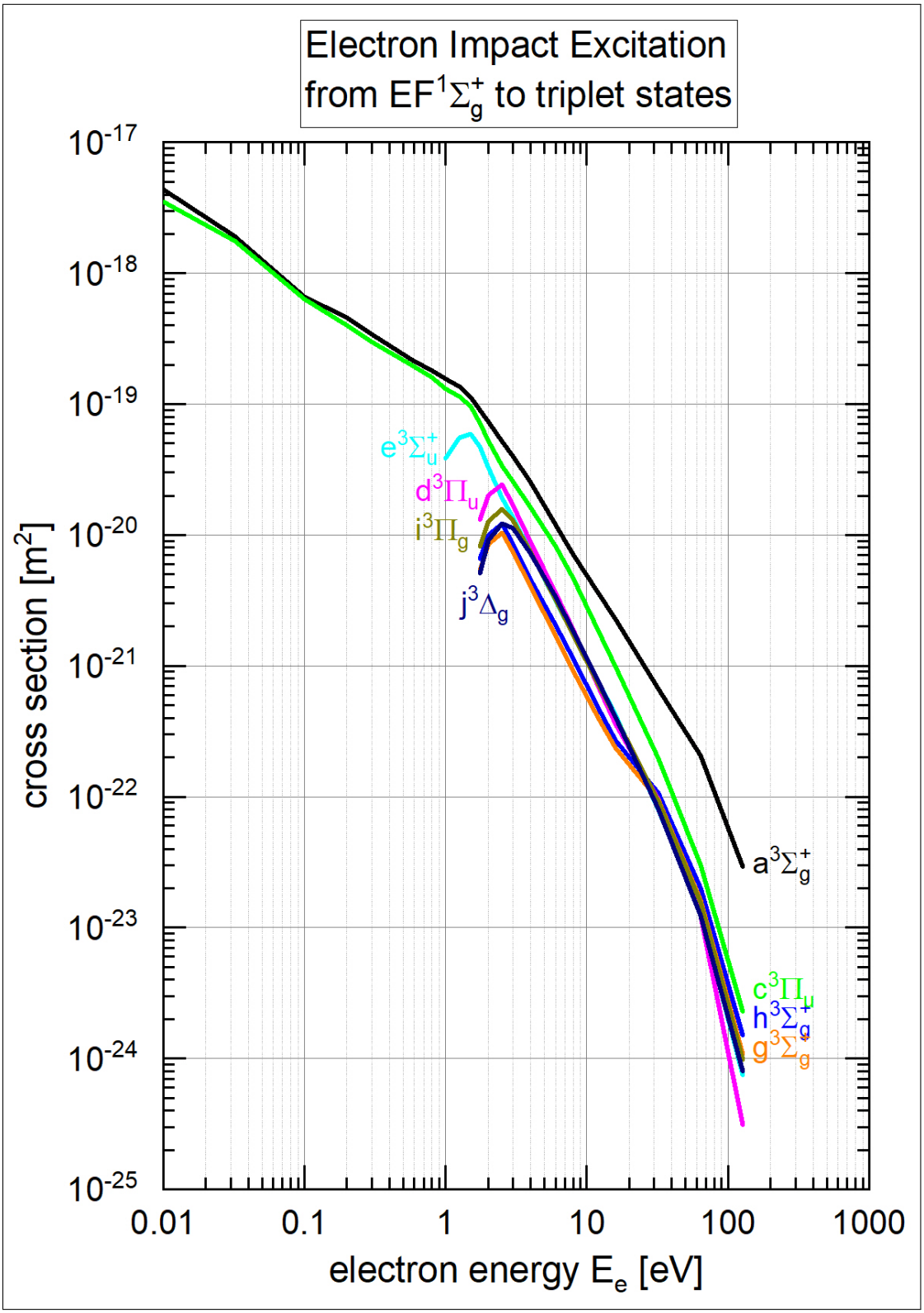
Electron Impact Excitation
from EF$^1\Sigma_g^+$ to triplet states
cross section [m^2]
electron energy E_e [eV]
10^{-17}
10^{-18}
10^{-19}
10^{-20}
10^{-21}
10^{-22}
10^{-23}
10^{-24}
10^{-25}
0.01
0.1
1
10
100
1000
$e^3\Sigma_u^+$
$d^3\Pi_u$
$i^3\Pi_g$
$j^3\Delta_g$
$a^3\Sigma_g^+$
$c^3\Pi_u$
$h^3\Sigma_g^+$
$g^3\Sigma_g^+$

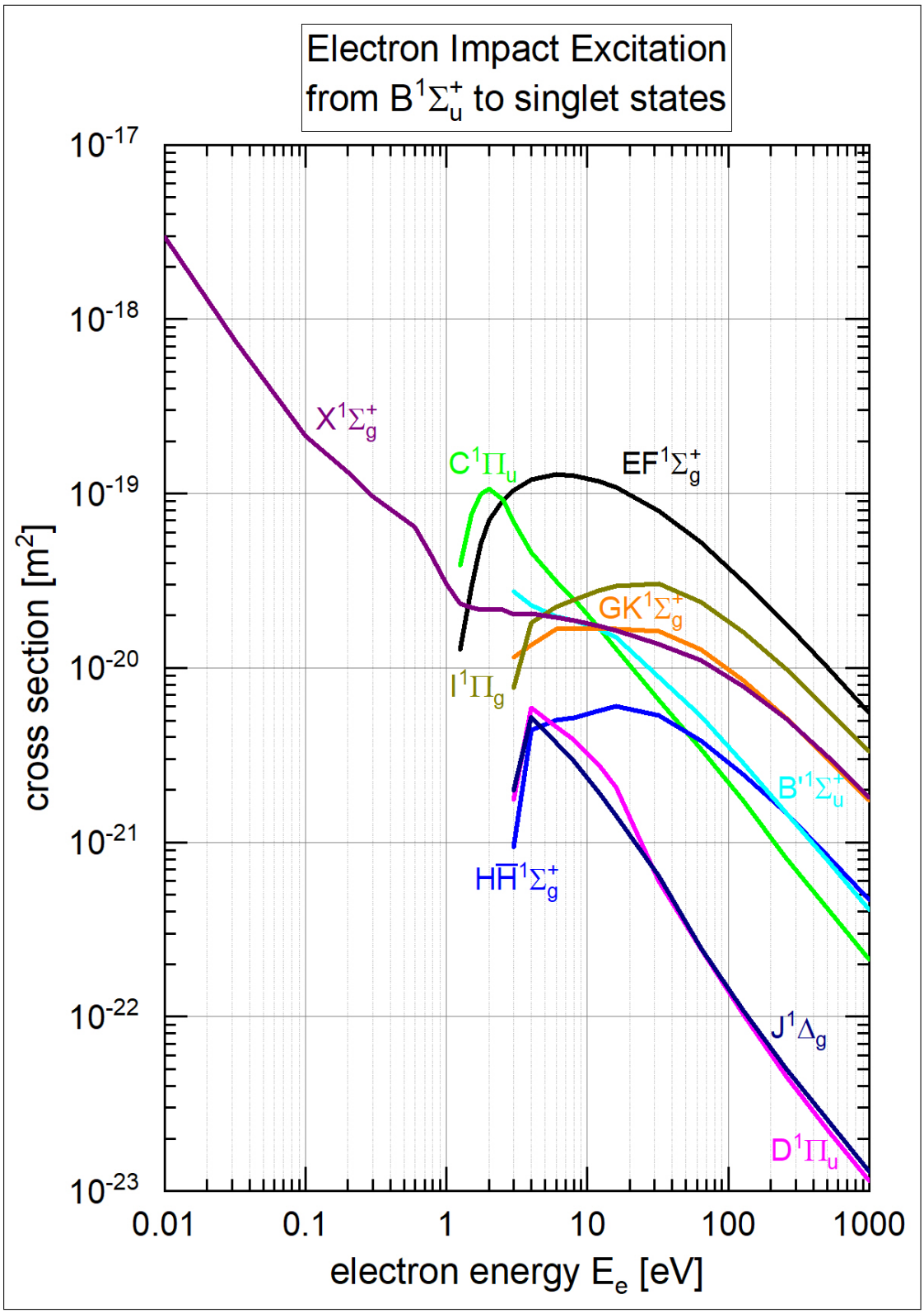
Electron Impact Excitation
from B$^1\Sigma_u^+$ to singlet states
cross section [m^2]
electron energy E_e [eV]
10^{-17}
10^{-18}
10^{-19}
10^{-20}
10^{-21}
10^{-22}
10^{-23}
0.01
0.1
1
10
100
1000
$X^1\Sigma_g^+$
$C^1\Pi_u$
$EF^1\Sigma_g^+$
$GK^1\Sigma_g^+$
$I^1\Pi_g$
$B'^1\Sigma_u^+$
$H\overline{H}^1\Sigma_g^+$
$J^1\Delta_g$
$D^1\Pi_u$

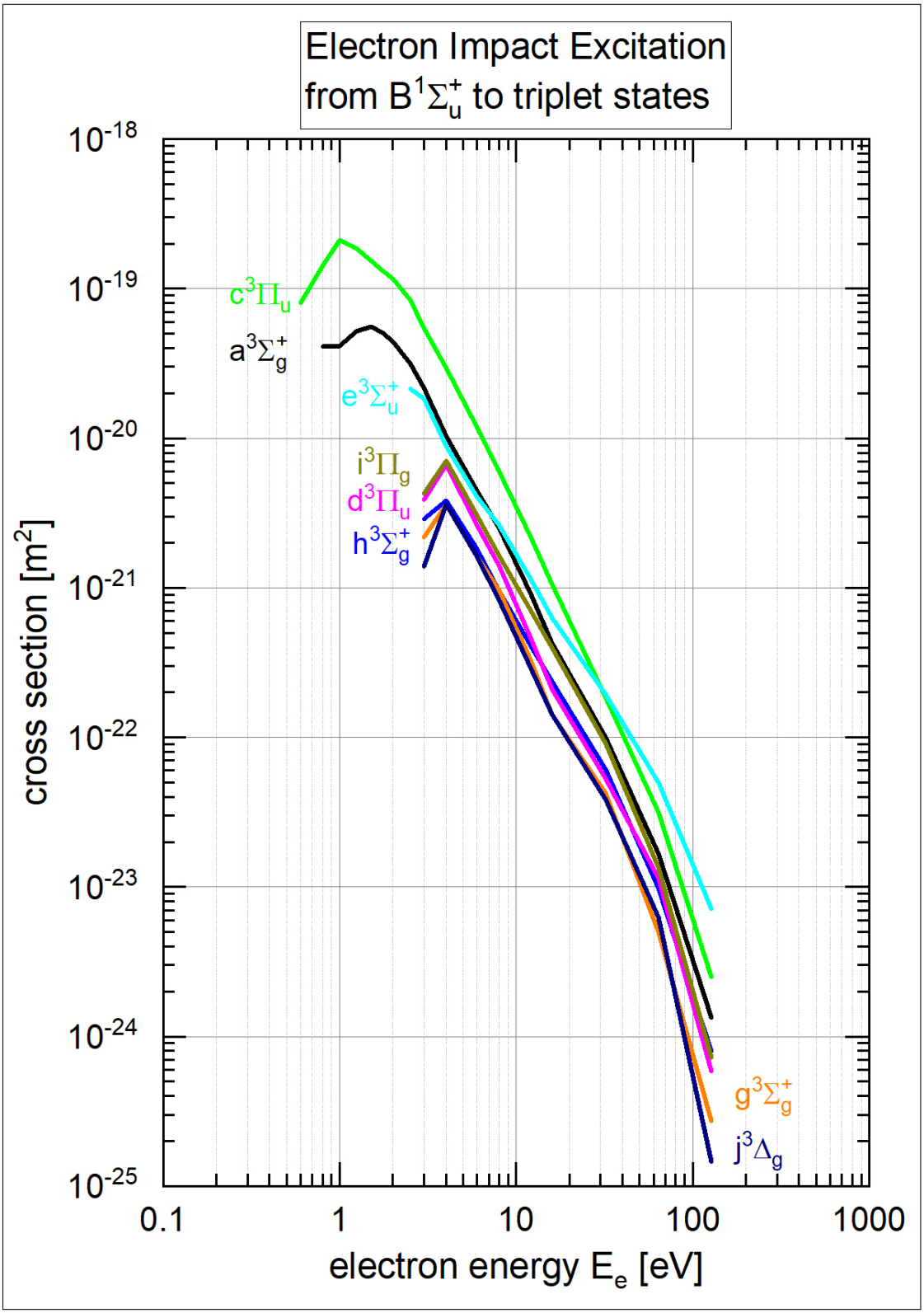
Electron Impact Excitation
from B$^1\Sigma_u^+$ to triplet states
cross section [m^2]
electron energy E_e [eV]
10^{-18}
10^{-19}
10^{-20}
10^{-21}
10^{-22}
10^{-23}
10^{-24}
10^{-25}
0.1
1
10
100
1000
$c^3\Pi_u$
$a^3\Sigma_g^+$
$e^3\Sigma_u^+$
$i^3\Pi_g$
$d^3\Pi_u$
$h^3\Sigma_g^+$
$g^3\Sigma_g^+$
$j^3\Delta_g$

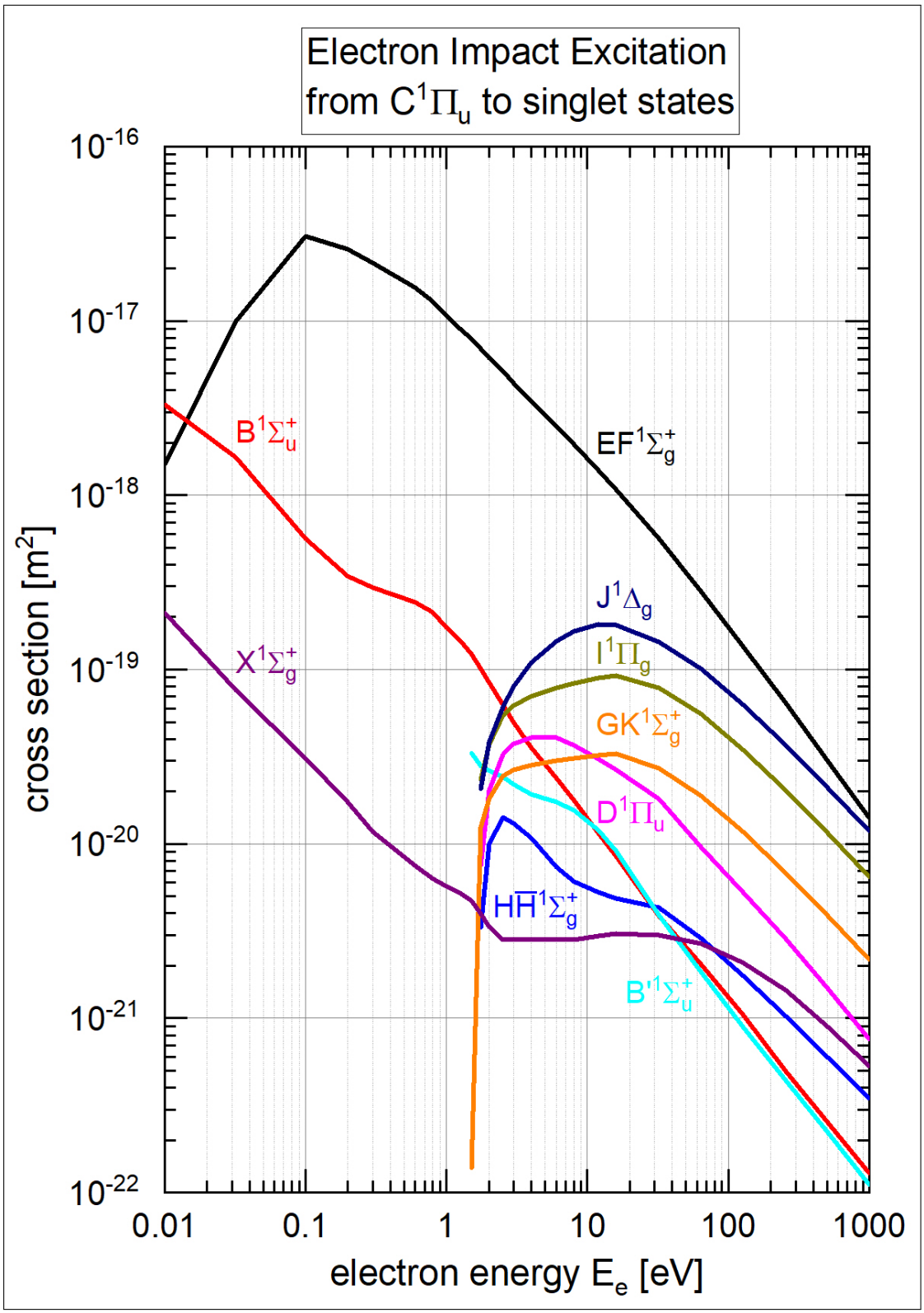
Electron Impact Excitation
from C¹Πu to singlet states
cross section [m²]
electron energy Ee [eV]
10-16
10-17
10-18
10-19
10-20
10-21
10-22
0.01
0.1
1
10
100
1000
B¹Σu+
X¹Σg+
EF¹Σg+
J¹Δg
I¹Πg
GK¹Σg+
D¹Πu
HH̄¹Σg+
B'¹Σu+

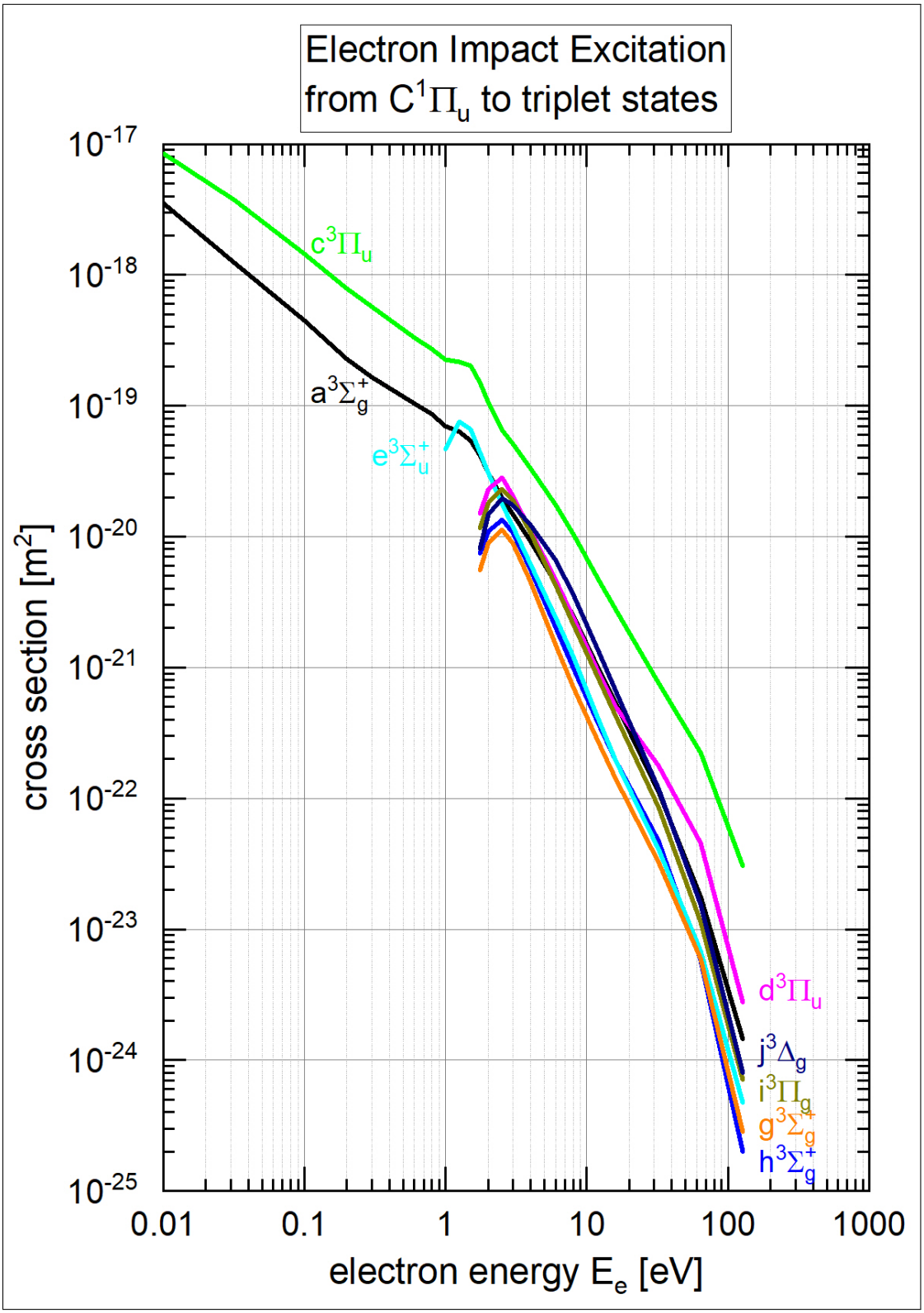
Electron Impact Excitation
from C¹Πu to triplet states
cross section [m²]
electron energy Ee [eV]
10-17
10-18
10-19
10-20
10-21
10-22
10-23
10-24
10-25
0.01
0.1
1
10
100
1000
c³Πu
a³Σg+
e³Σu+
d³Πu
j³Δg
i³Πg
g³Σg+
h³Σg+

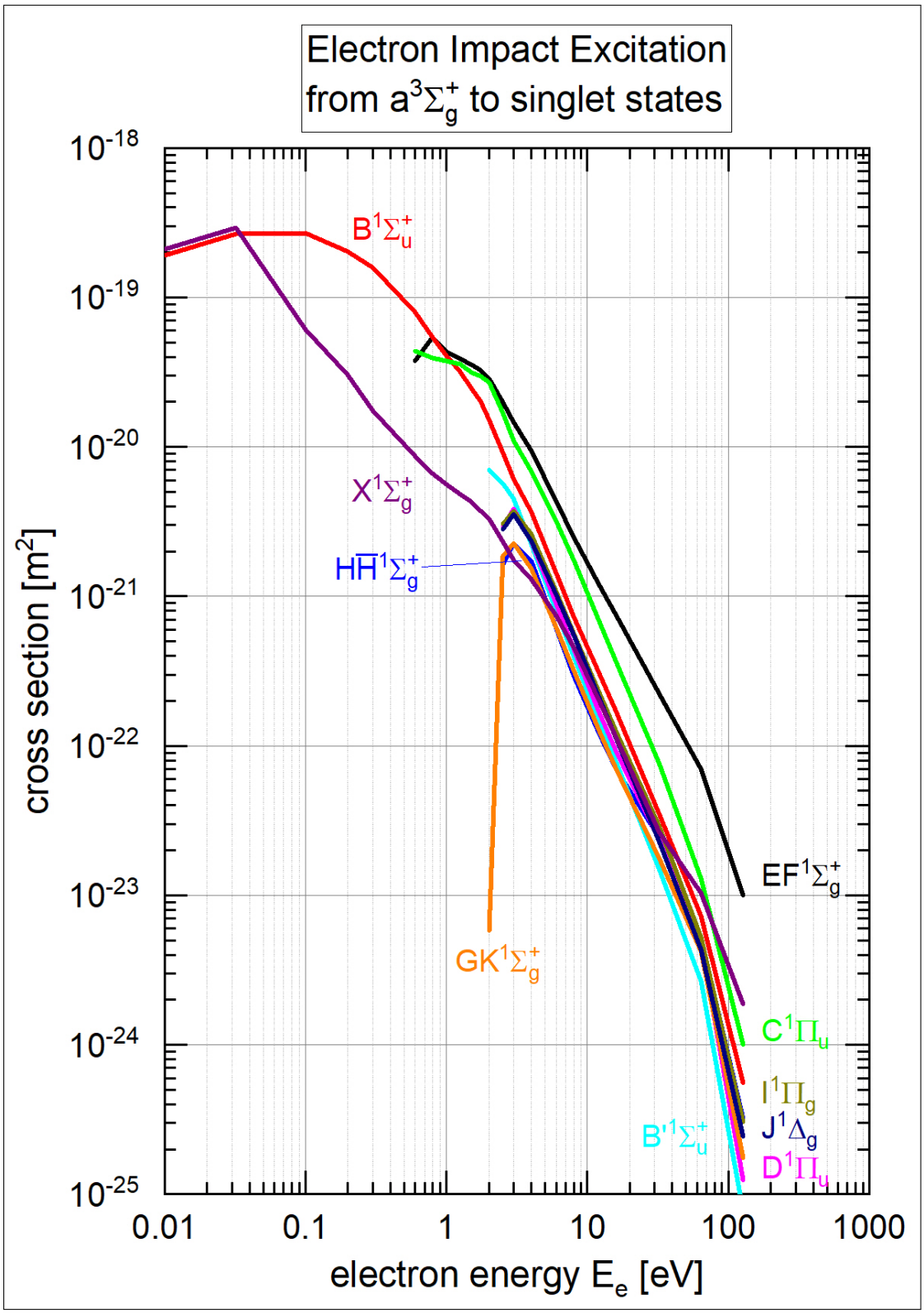
Electron Impact Excitation
from a$^3\Sigma_g^+$ to singlet states
cross section [m^2]
electron energy E_e [eV]
10^{-18}
10^{-19}
10^{-20}
10^{-21}
10^{-22}
10^{-23}
10^{-24}
10^{-25}
0.01
0.1
1
10
100
1000
$B^1\Sigma_u^+$
$X^1\Sigma_g^+$
$H\overline{H}^1\Sigma_g^+$
$GK^1\Sigma_g^+$
$EF^1\Sigma_g^+$
$C^1\Pi_u$
$I^1\Pi_g$
$J^1\Delta_g$
$D^1\Pi_u$
$B'^1\Sigma_u^+$

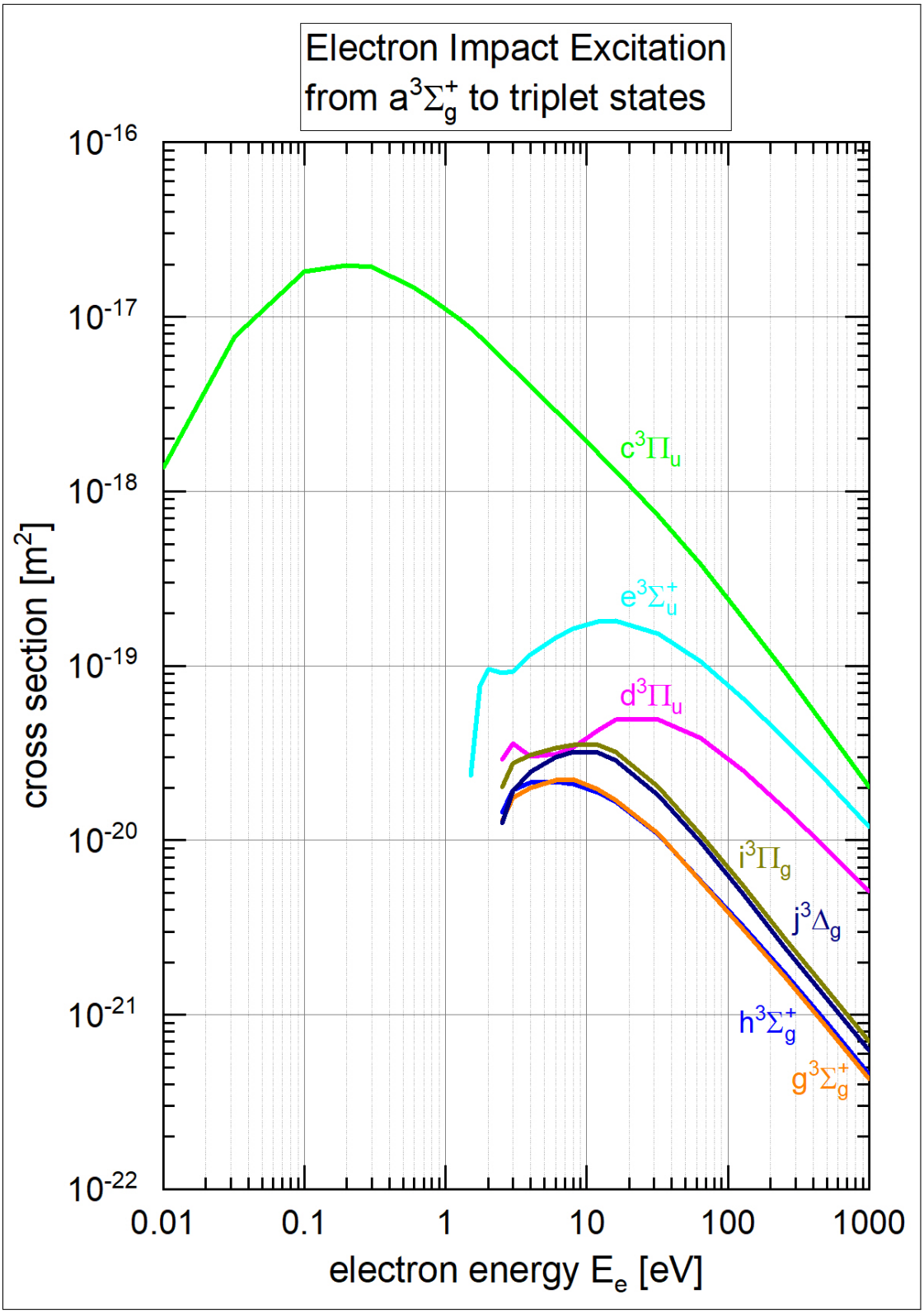
Electron Impact Excitation
from a$^3\Sigma_g^+$ to triplet states
cross section [m^2]
electron energy E$_e$ [eV]
10^{-16}
10^{-17}
10^{-18}
10^{-19}
10^{-20}
10^{-21}
10^{-22}
0.01
0.1
1
10
100
1000
c$^3\Pi_u$
e$^3\Sigma_u^+$
d$^3\Pi_u$
i$^3\Pi_g$
j$^3\Delta_g$
h$^3\Sigma_g^+$
g$^3\Sigma_g^+$

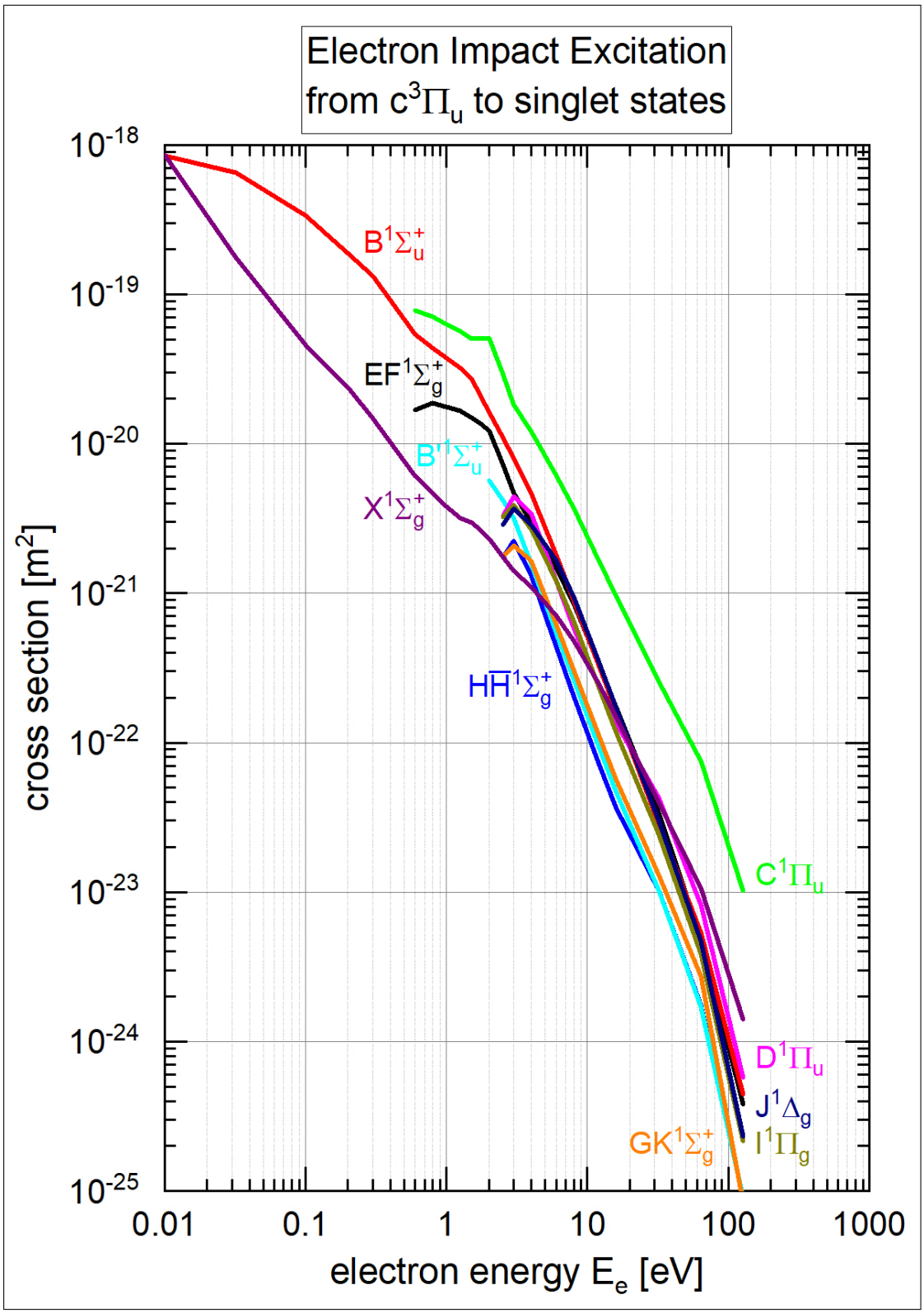
Electron Impact Excitation
from c³Πu to singlet states
cross section [m²]
electron energy Ee [eV]
10-18
10-19
10-20
10-21
10-22
10-23
10-24
10-25
0.01
0.1
1
10
100
1000
B¹Σu+
EF¹Σg+
B'¹Σu+
X¹Σg+
HH̄¹Σg+
C¹Πu
D¹Πu
J¹Δg
GK¹Σg+
I¹Πg

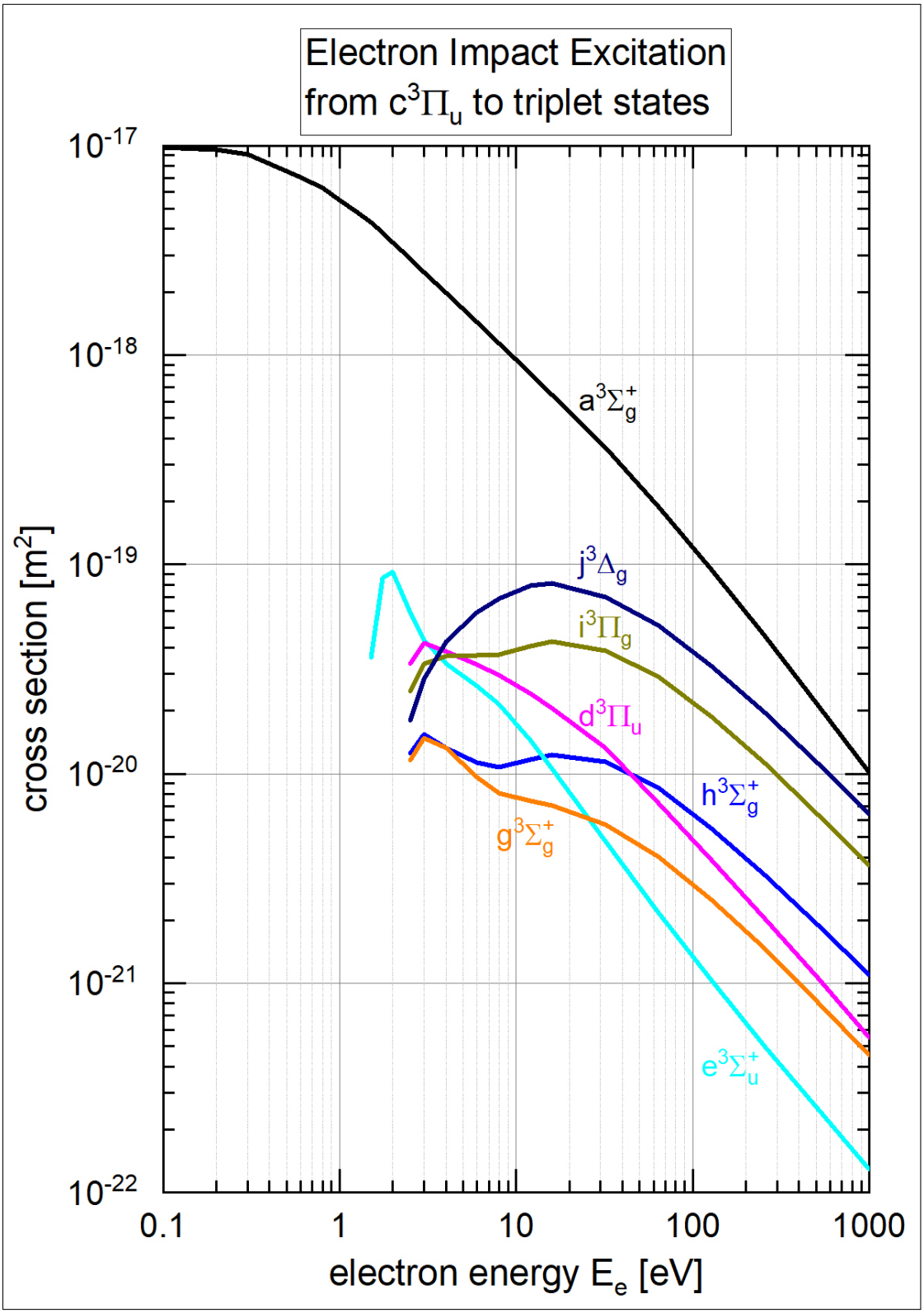
Electron Impact Excitation
from c³Π_u to triplet states
cross section [m²]
10^-17
10^-18
10^-19
10^-20
10^-21
10^-22
0.1
1
10
100
1000
electron energy E_e [eV]
a³Σ_g⁺
j³Δ_g
i³Π_g
d³Π_u
h³Σ_g⁺
g³Σ_g⁺
e³Σ_u⁺

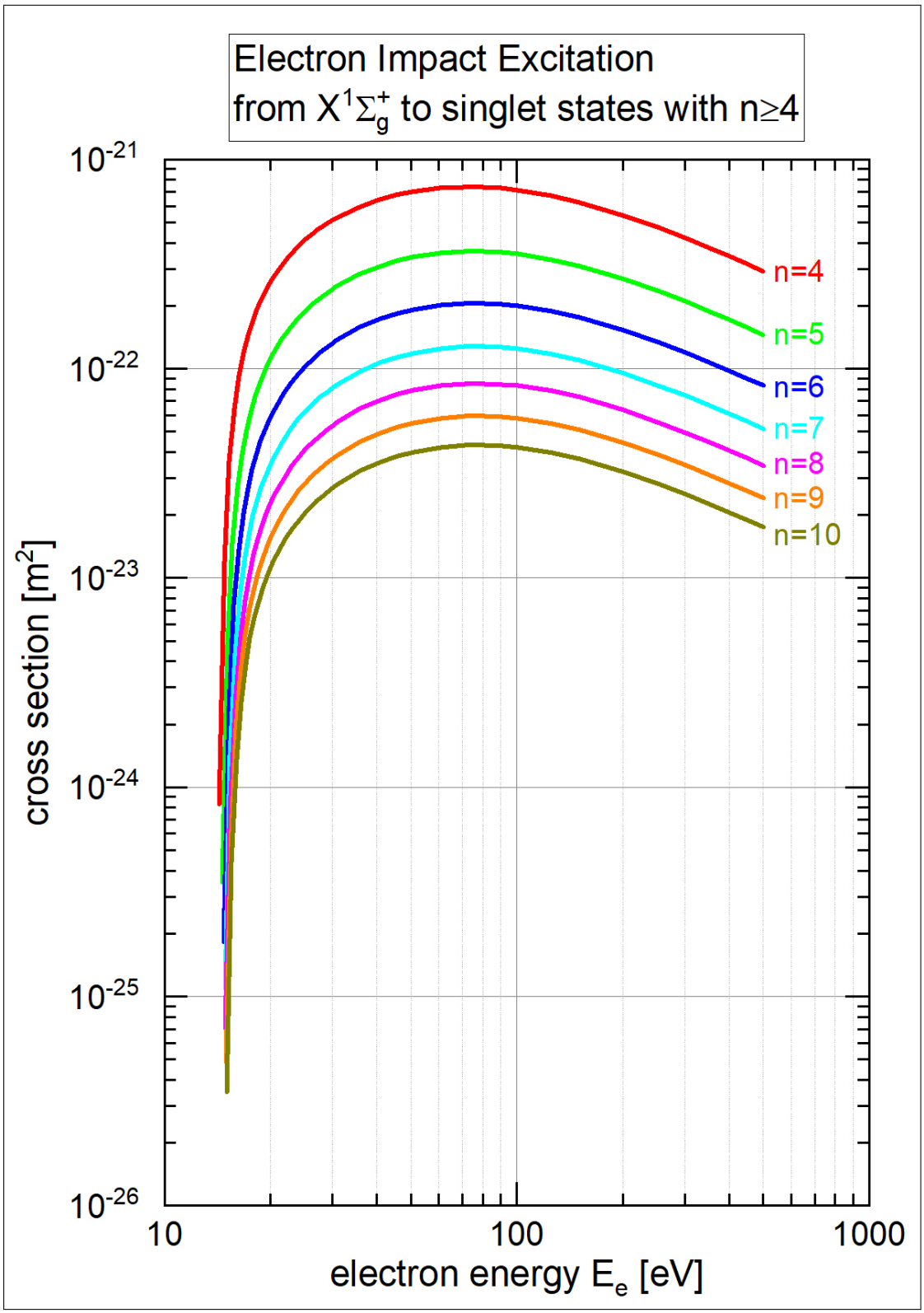
Electron Impact Excitation
from X$^1\Sigma_g^+$ to singlet states with n≥4
cross section [m^2]
10^{-21}
10^{-22}
10^{-23}
10^{-24}
10^{-25}
10^{-26}
10
100
1000
electron energy E_e [eV]
n=4
n=5
n=6
n=7
n=8
n=9
n=10

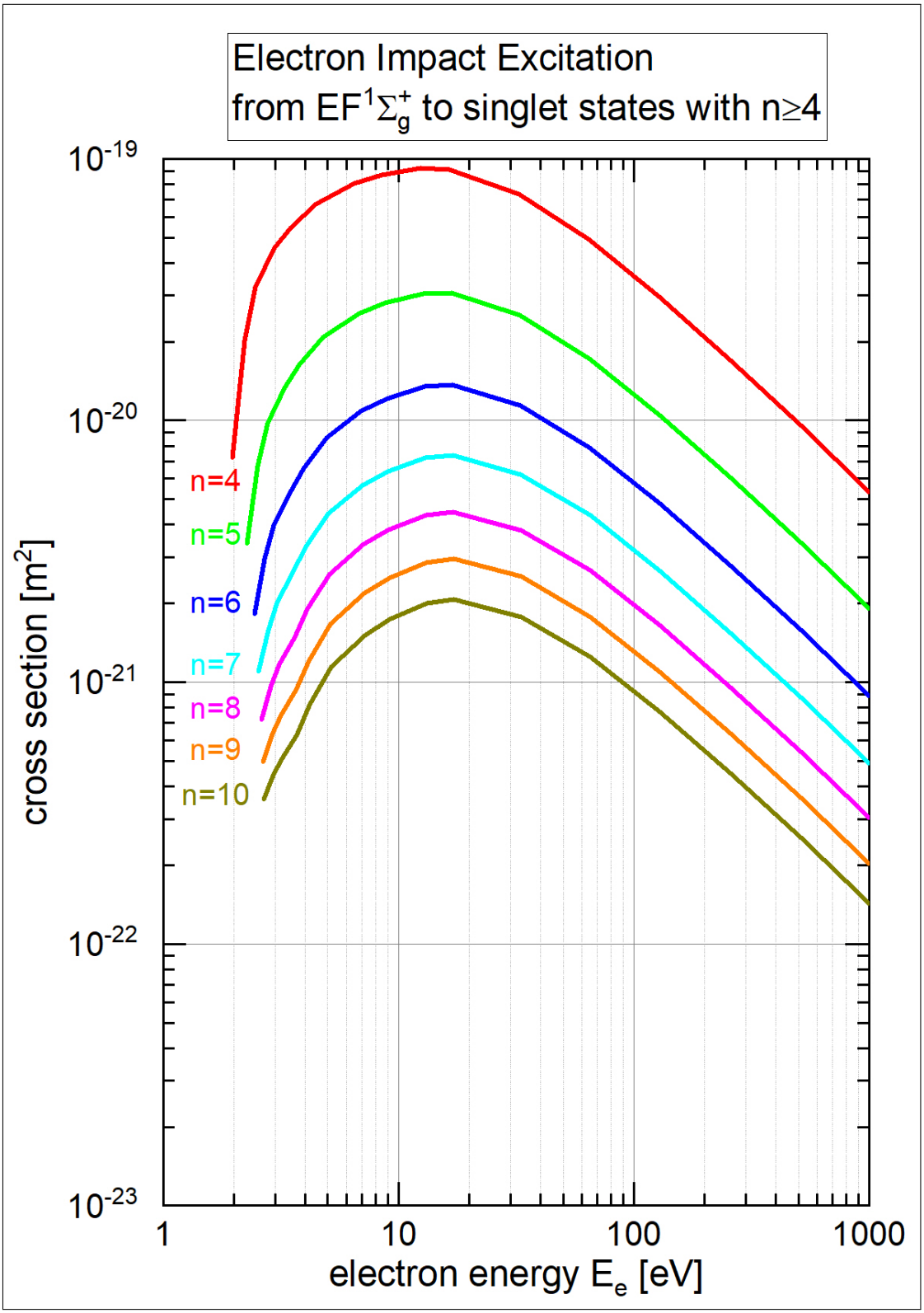
Electron Impact Excitation
from EF$^1\Sigma_g^+$ to singlet states with n≥4
cross section [m^2]
10^{-19}
10^{-20}
10^{-21}
10^{-22}
10^{-23}
n=4
n=5
n=6
n=7
n=8
n=9
n=10
1
10
100
1000
electron energy E_e [eV]

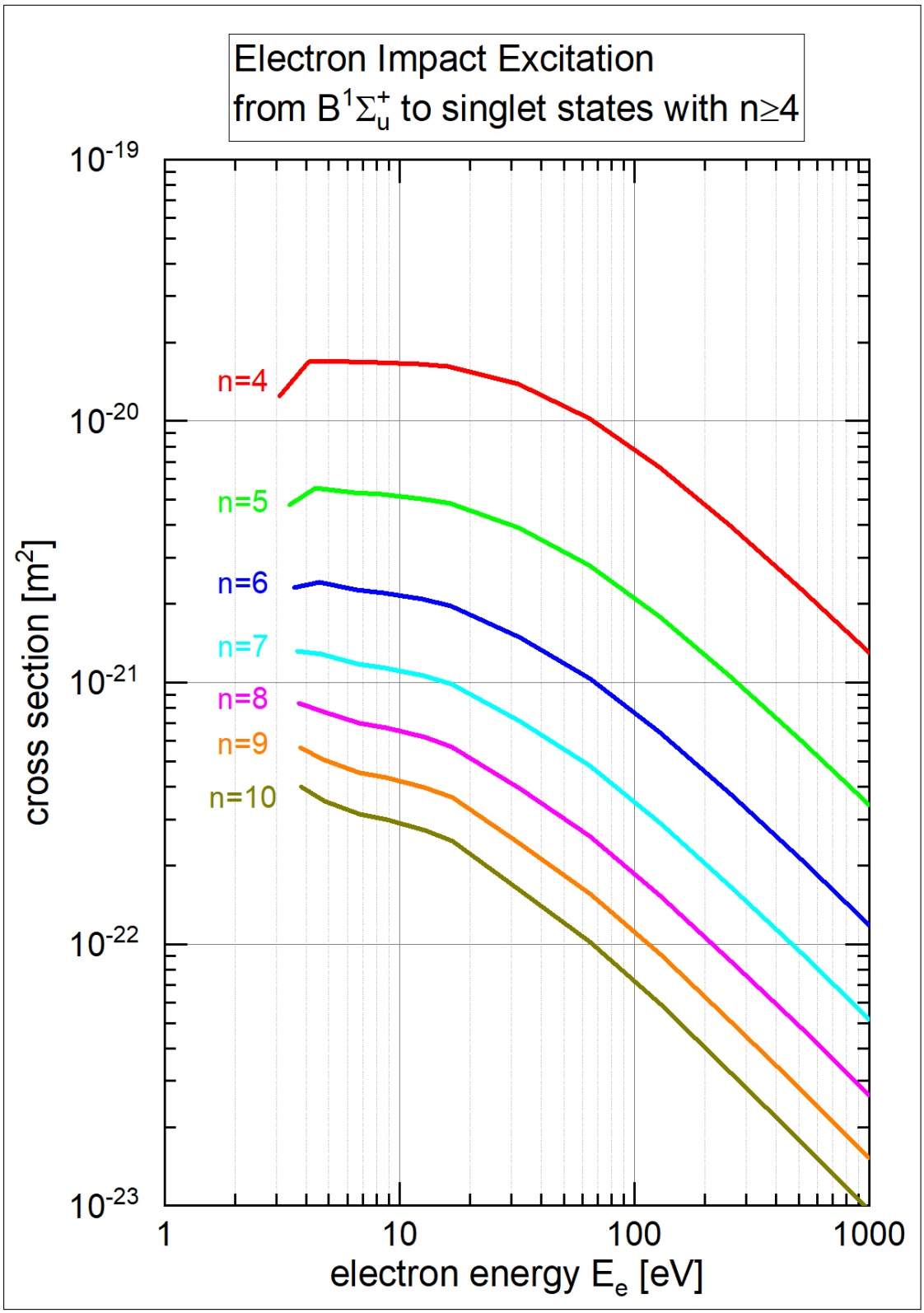
Electron Impact Excitation
from B$^1\Sigma_u^+$ to singlet states with n≥4
cross section [m^2]
electron energy E$_e$ [eV]
10^{-19}
10^{-20}
10^{-21}
10^{-22}
10^{-23}
1
10
100
1000
n=4
n=5
n=6
n=7
n=8
n=9
n=10

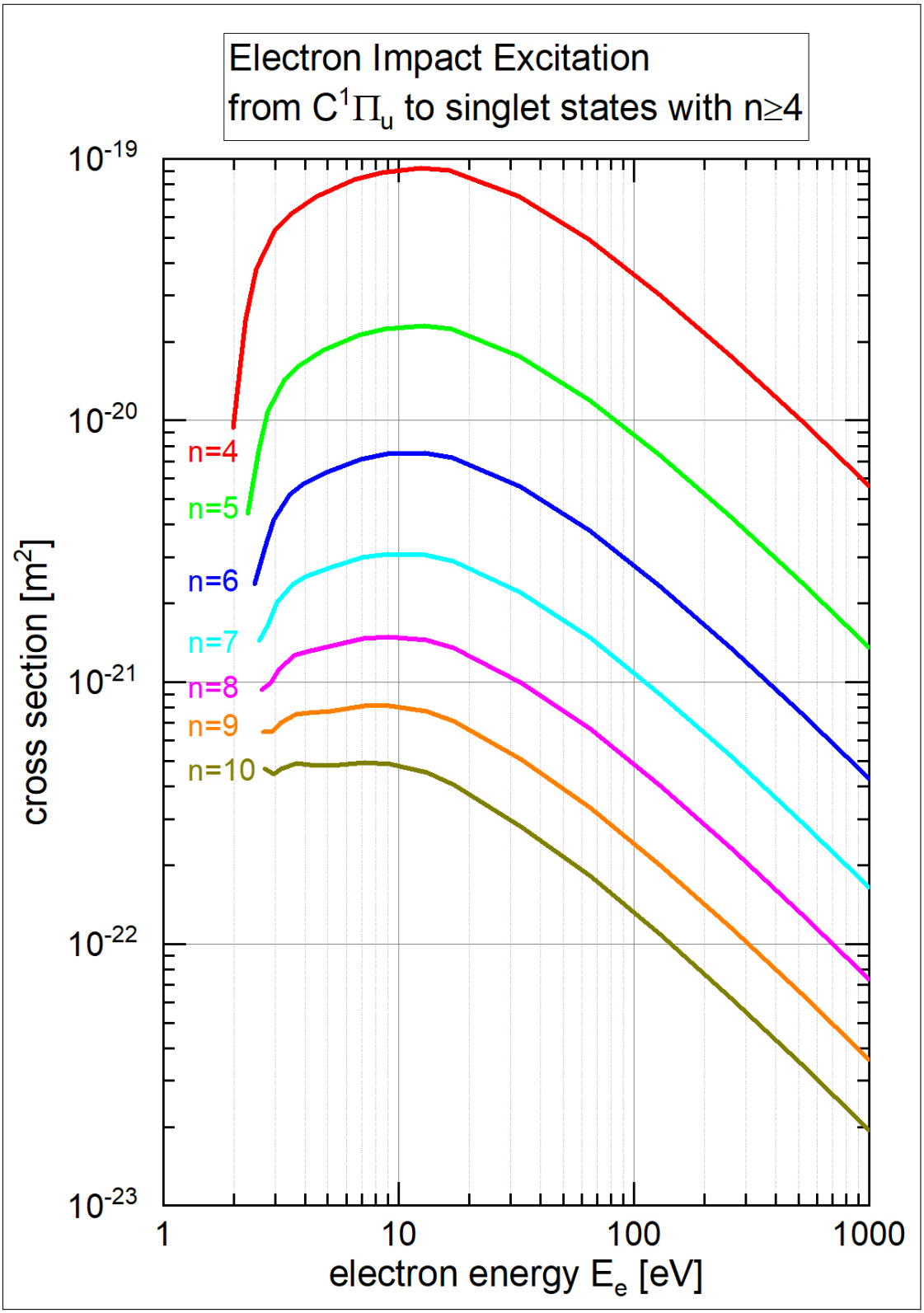
Electron Impact Excitation
from C¹Πu to singlet states with n≥4
cross section [m²]
10-19
10-20
10-21
10-22
10-23
n=4
n=5
n=6
n=7
n=8
n=9
n=10
1
10
100
1000
electron energy Ee [eV]

Non-Dissociative Electron Impact Ionization

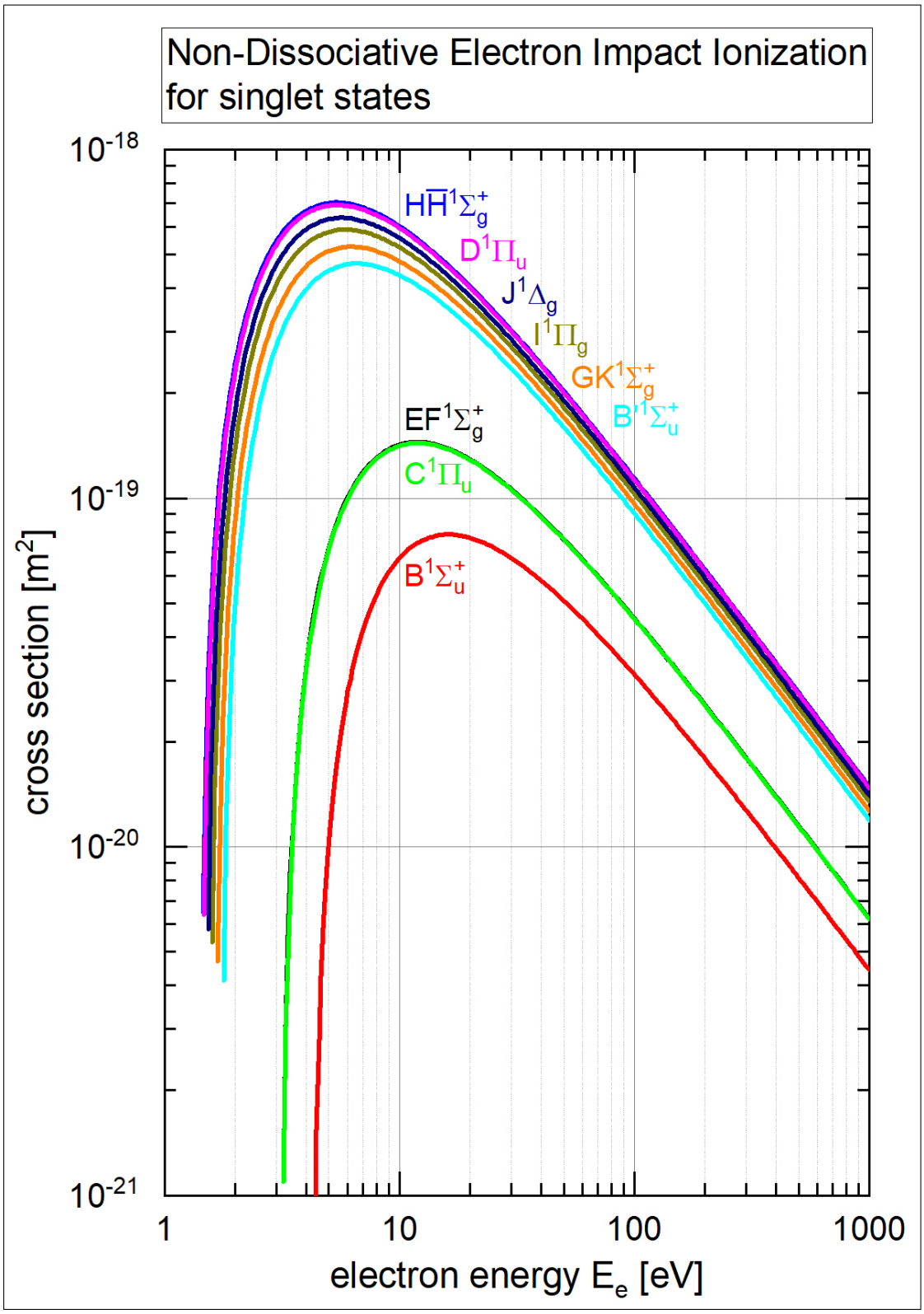

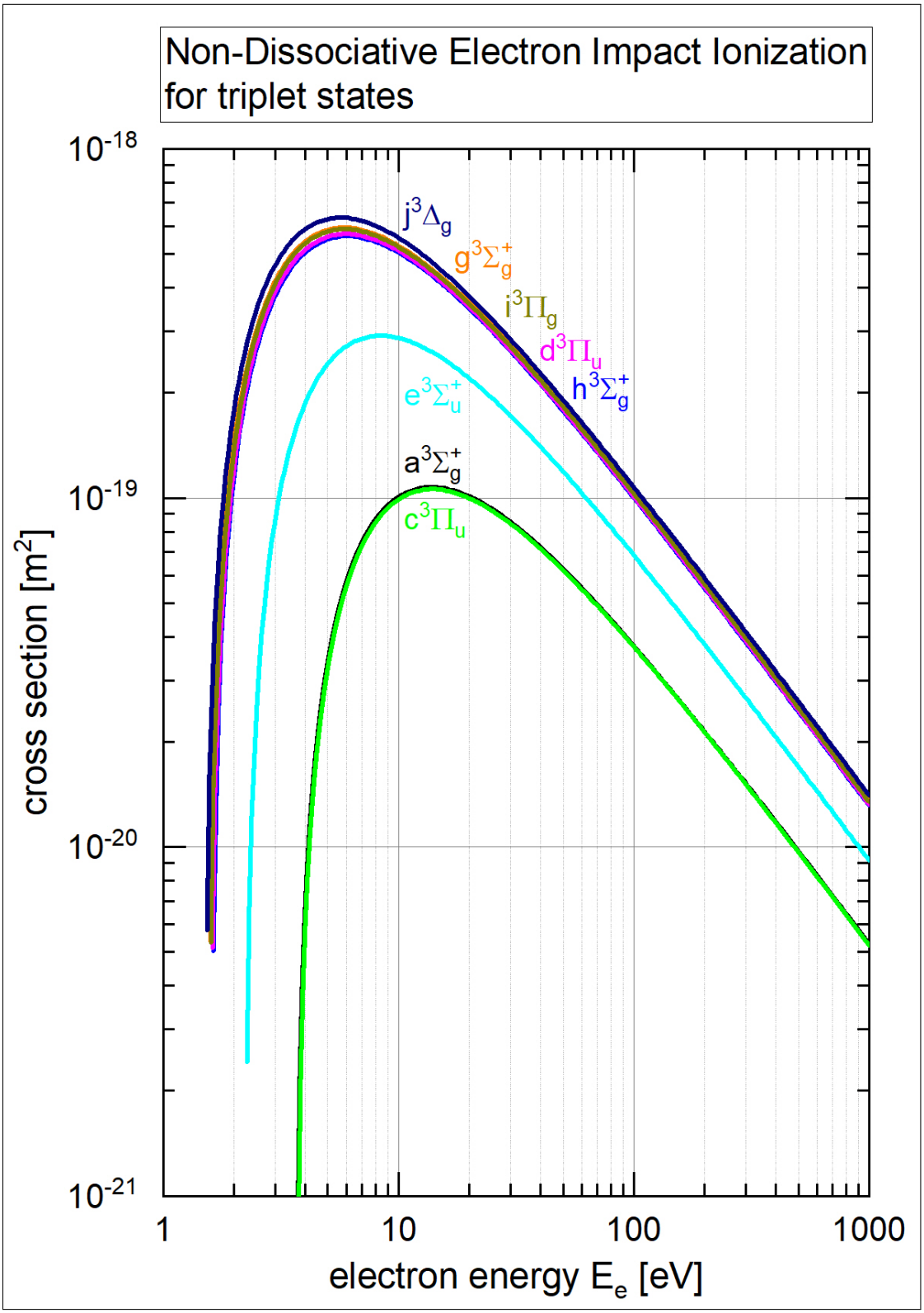
Non-Dissociative Electron Impact Ionization
for triplet states
cross section [m²]
10-18
10-19
10-20
10-21
j³Λg
g³Σ+g
i³Πg
d³Πu
h³Σ+g
e³Σ+u
a³Σ+g
c³Πu
1
10
100
1000
electron energy Ee [eV]

Dissociative Electron Impact Ionization

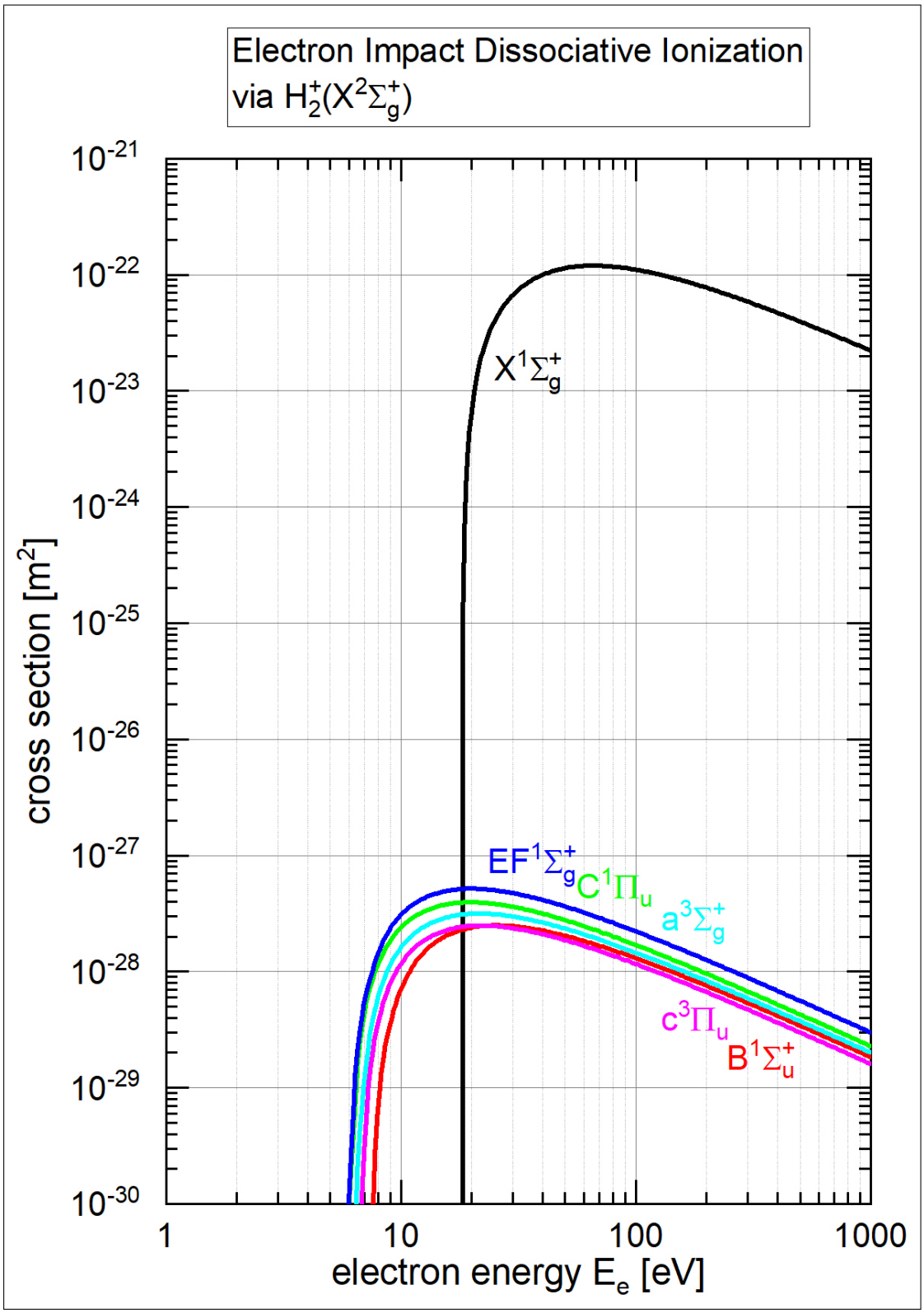

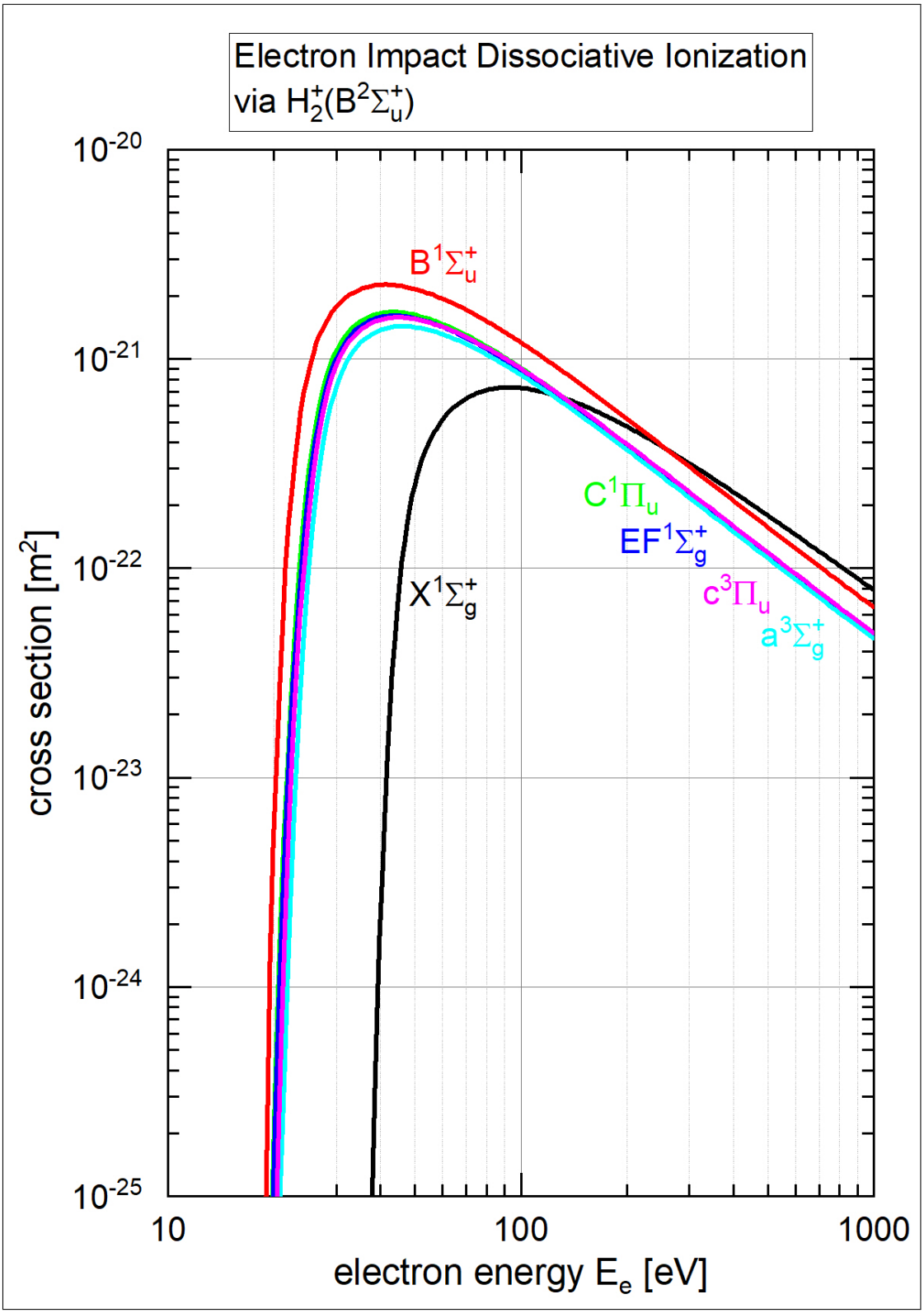
Electron Impact Dissociative Ionization
via $H_2^+(B^2\Sigma_u^+)$
10^{-20}
10^{-21}
10^{-22}
10^{-23}
10^{-24}
10^{-25}
cross section [m^2]
$B^1\Sigma_u^+$
$C^1\Pi_u$
$EF^1\Sigma_g^+$
$c^3\Pi_u$
$a^3\Sigma_g^+$
$X^1\Sigma_g^+$
10
100
1000
electron energy E_e [eV]

Proton Charge Transfer

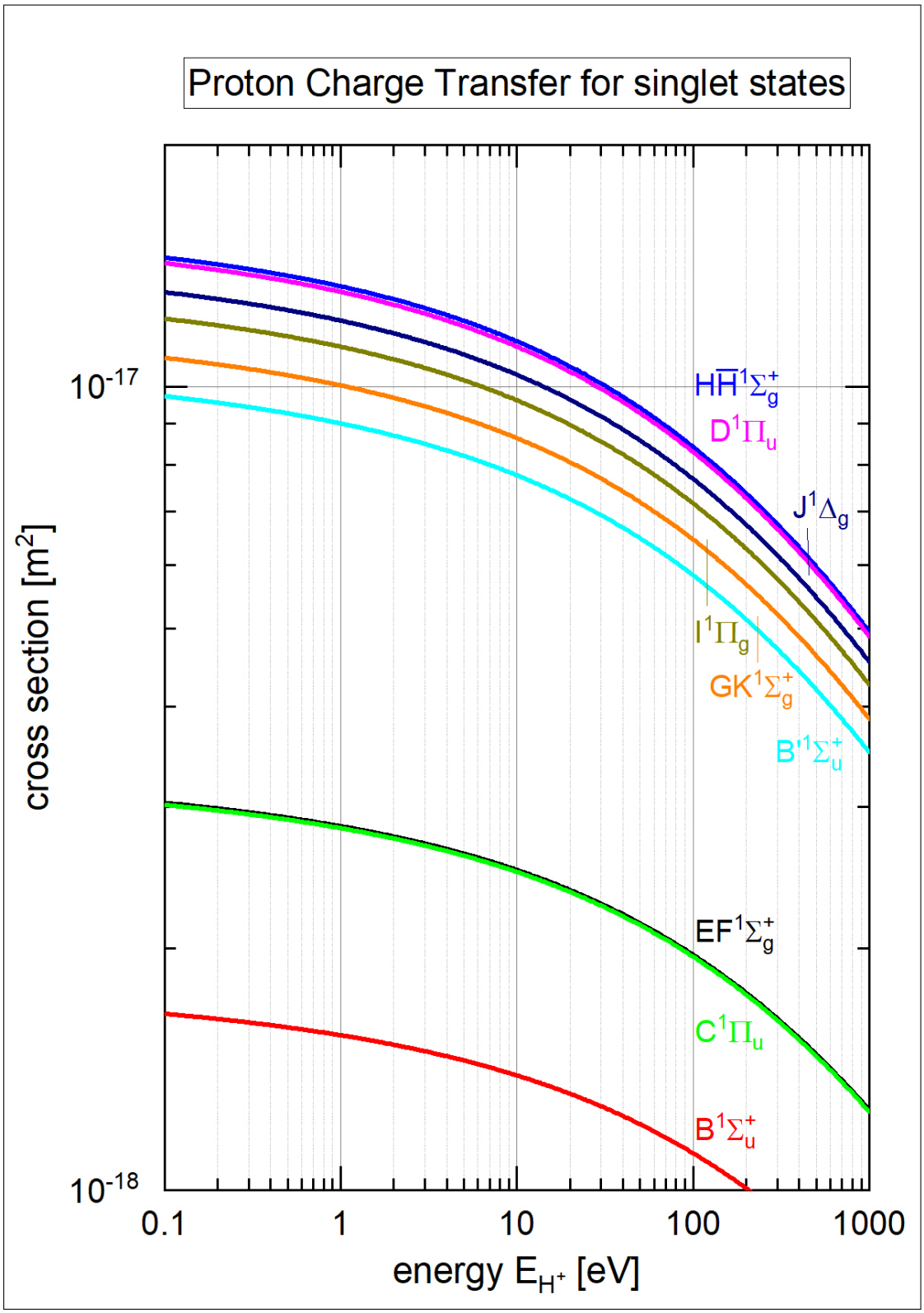

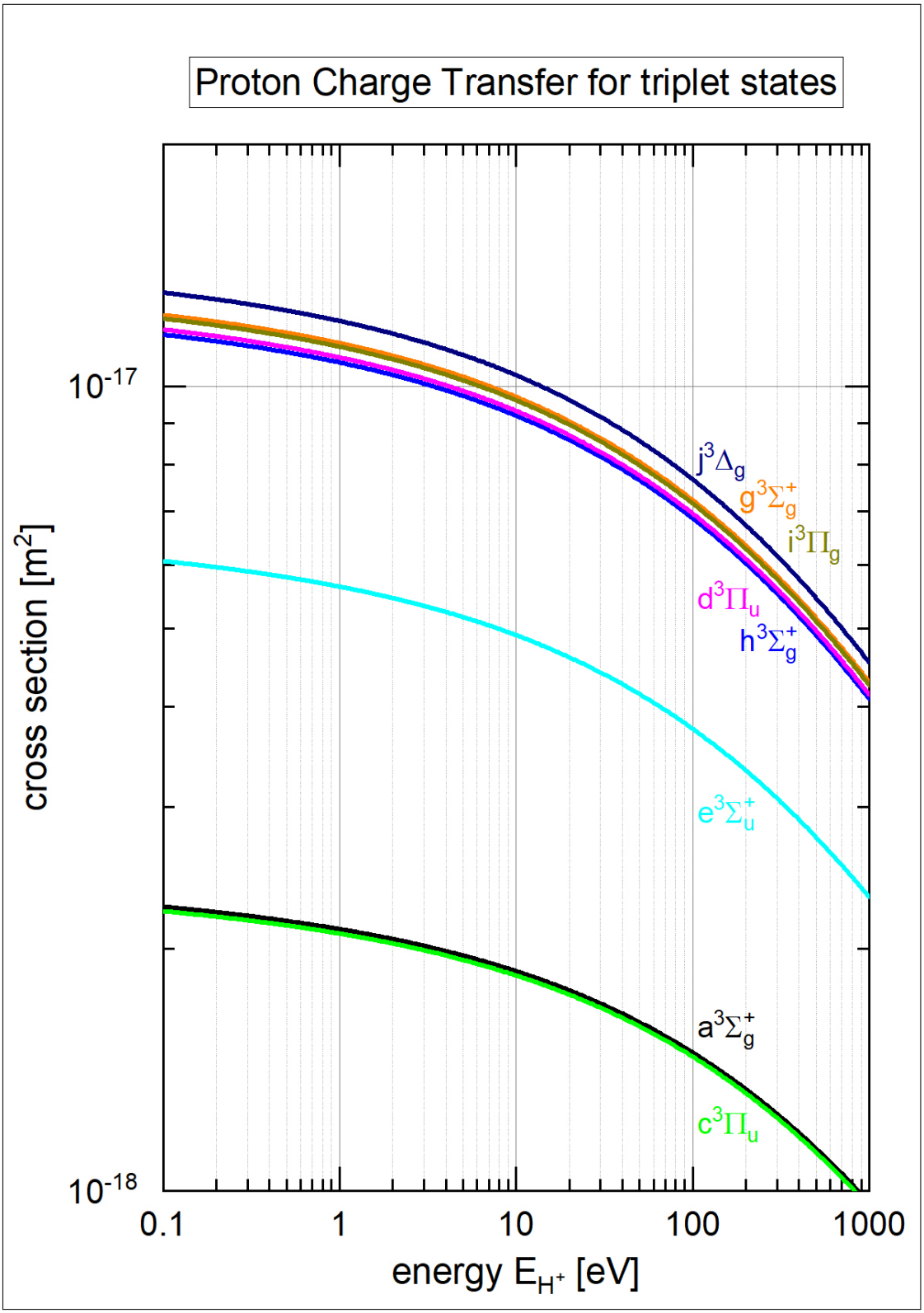
Proton Charge Transfer for triplet states
cross section [m²]
10-17
10-18
0.1
1
10
100
1000
energy E H+ [eV]
j3Δg
g3Σ+g
i3Πg
d3Πu
h3Σ+g
e3Σ+u
a3Σ+g
c3Πu

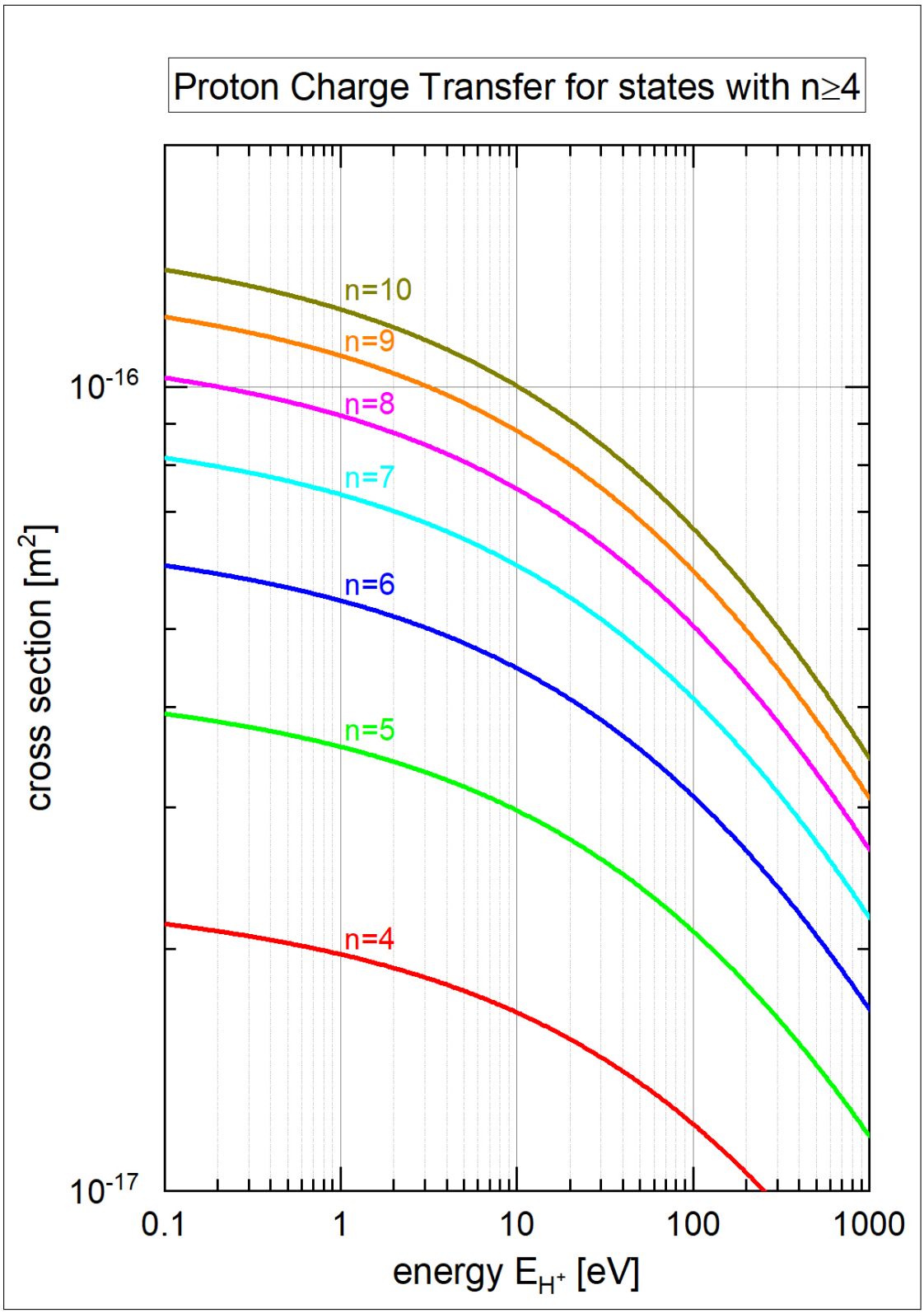
Proton Charge Transfer for states with n≥4
n=10
n=9
n=8
n=7
n=6
n=5
n=4
10-16
10-17
cross section [m2]
0.1
1
10
100
1000
energy EH+ [eV]

B.2 The Yacora $H_2(X^1, v)$ model

Electron Impact Excitation

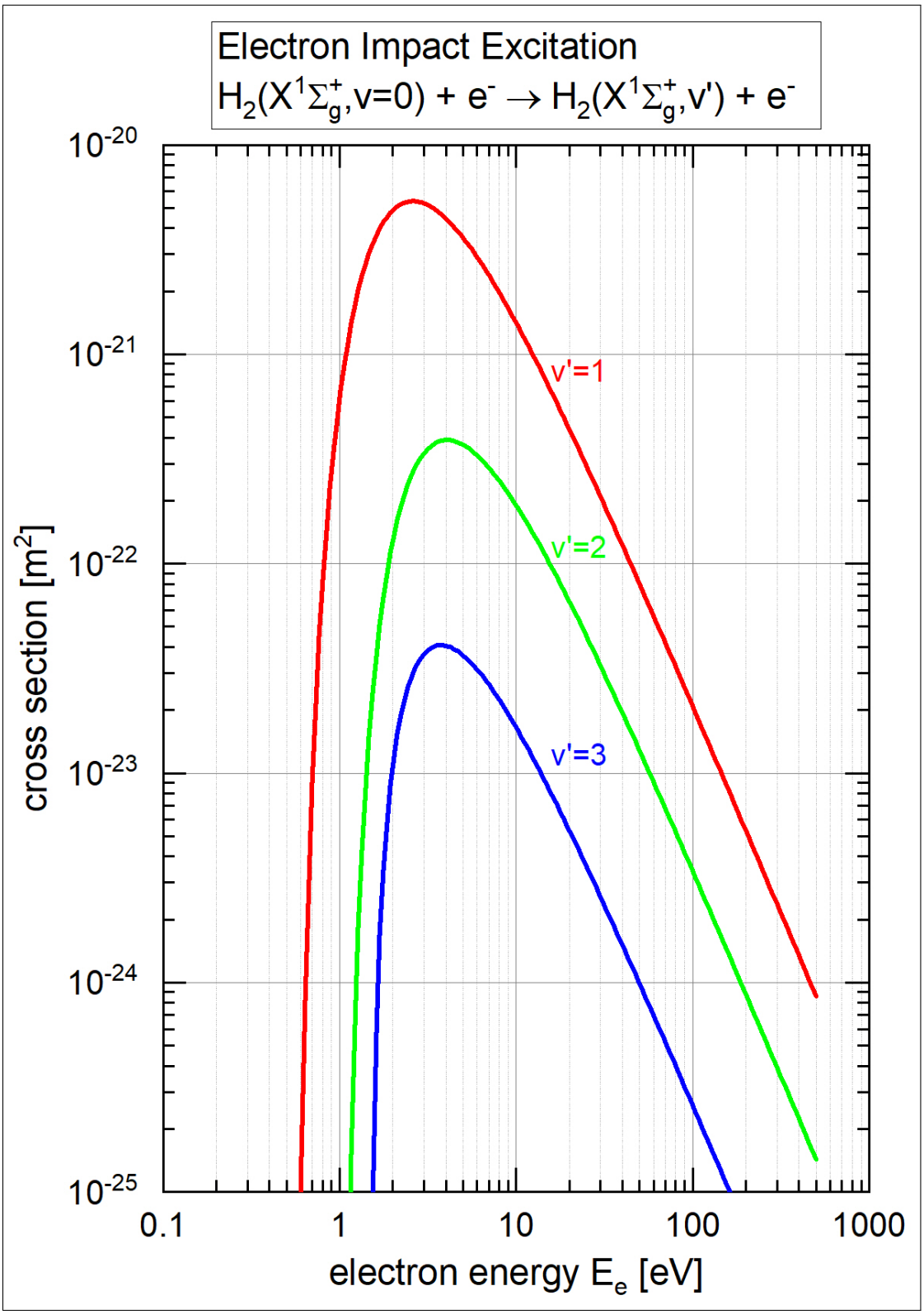

Electron Impact Dissociation

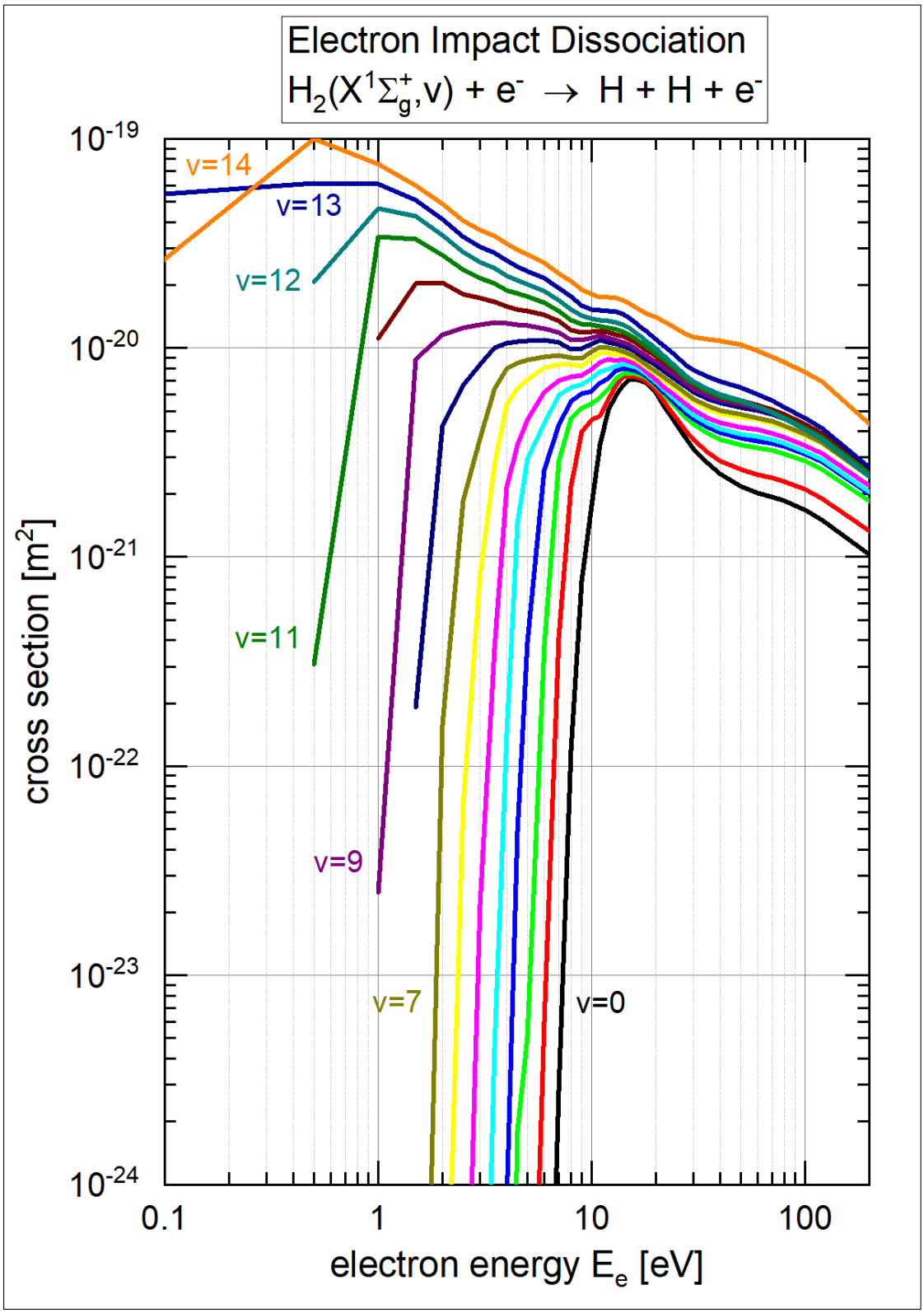

Dissociative Electron Attachment

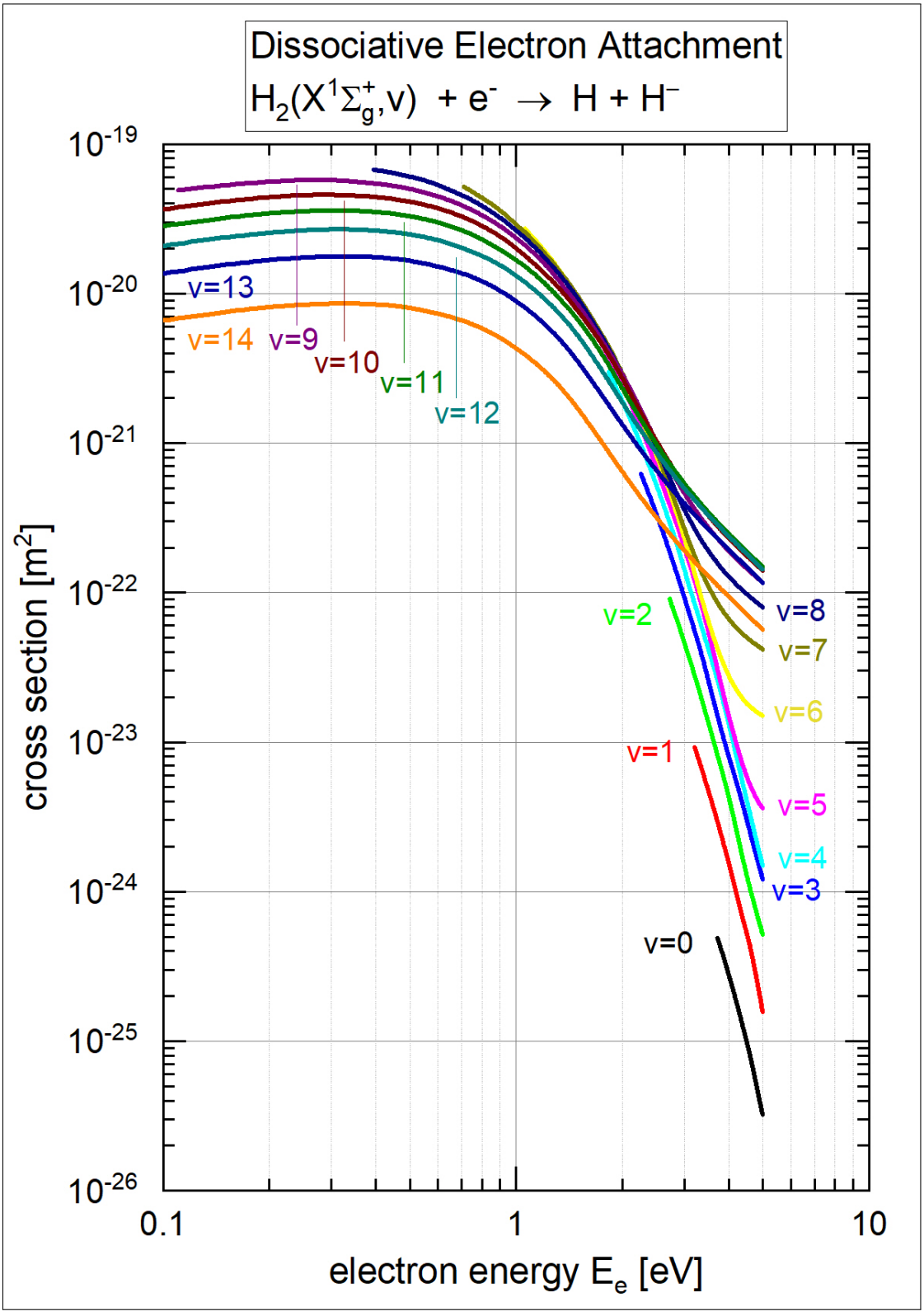

Proton Charge Transfer

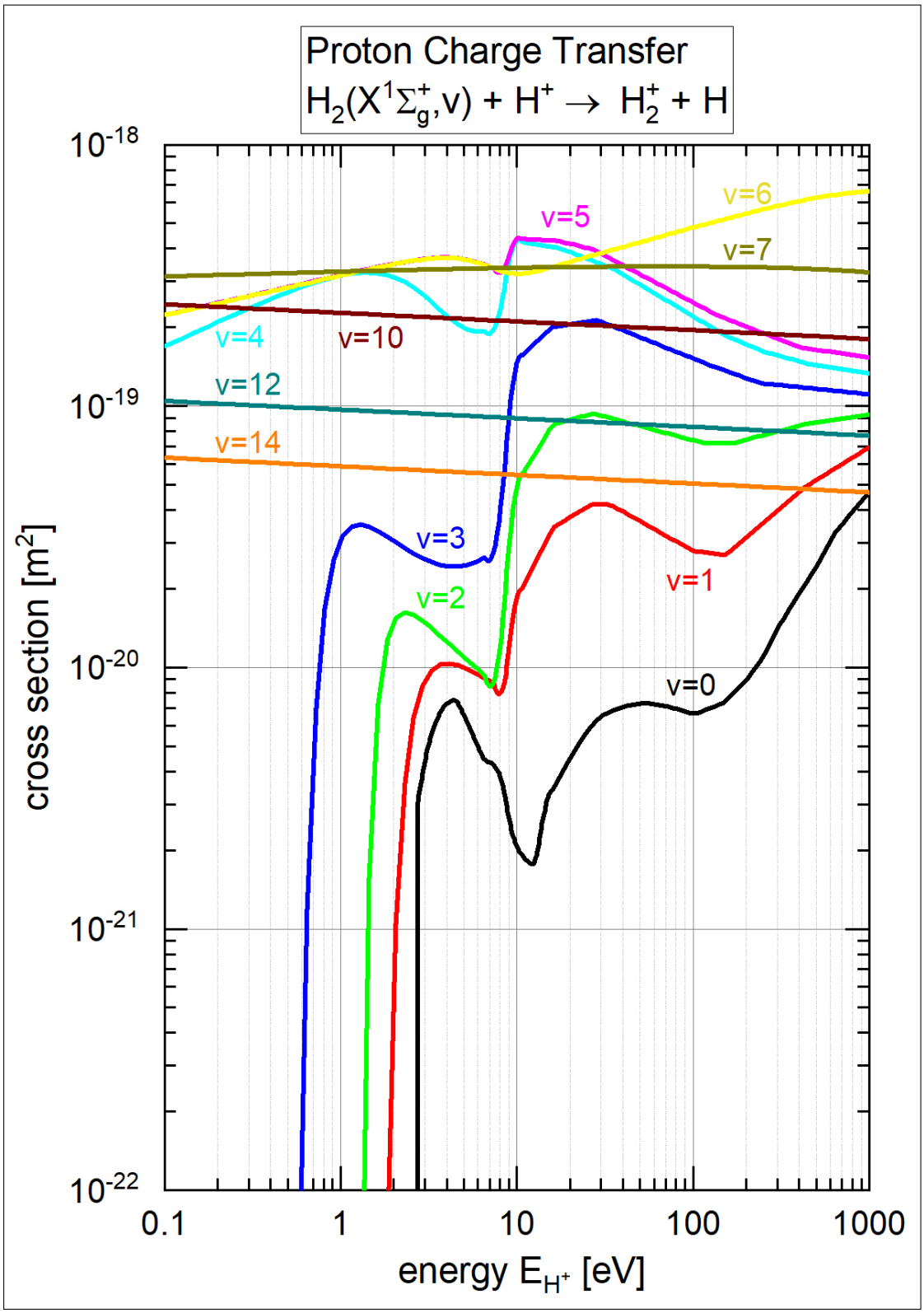

Non-Dissociative Electron Impact Ionization

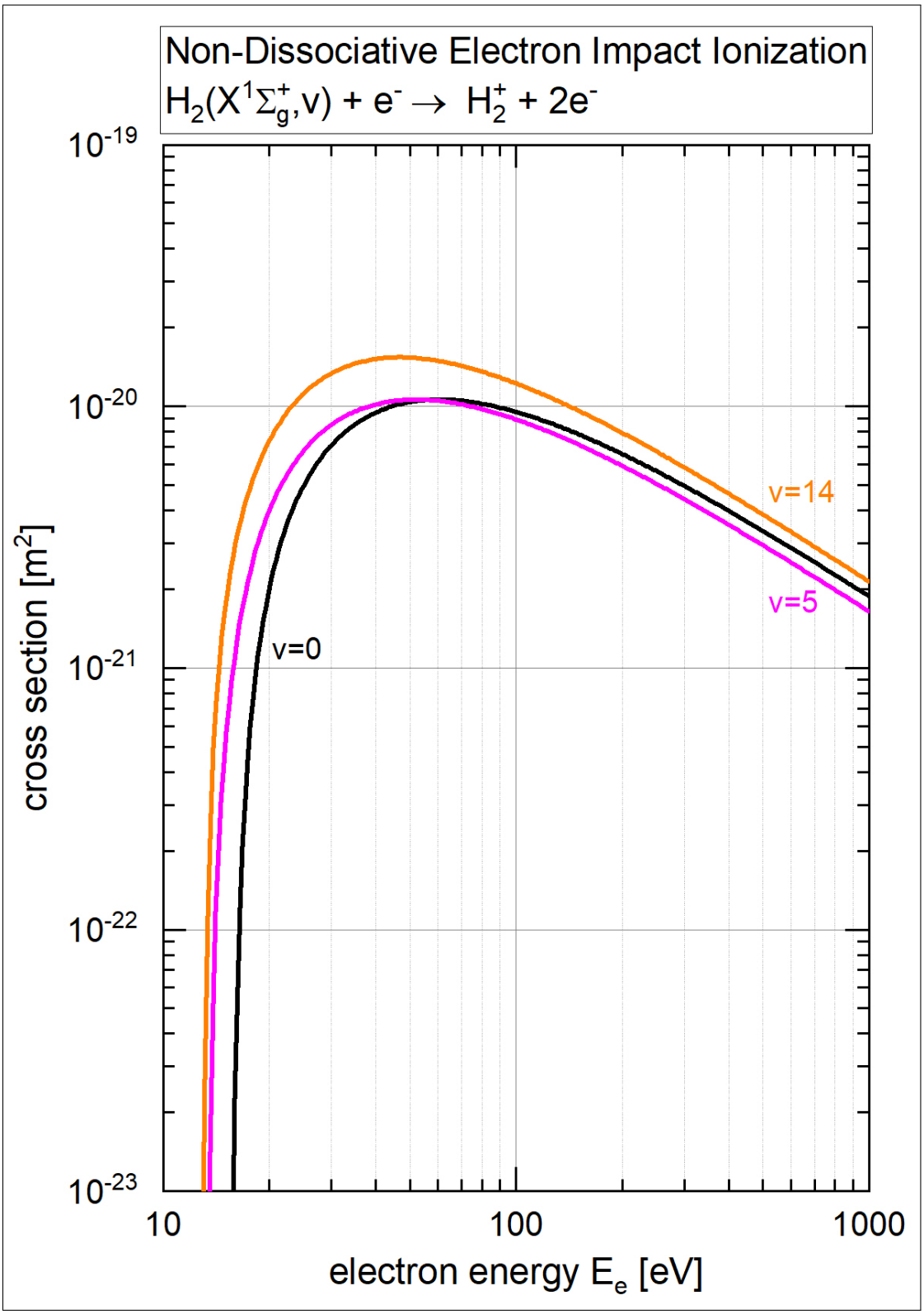

Dissociative Electron Impact Ionization

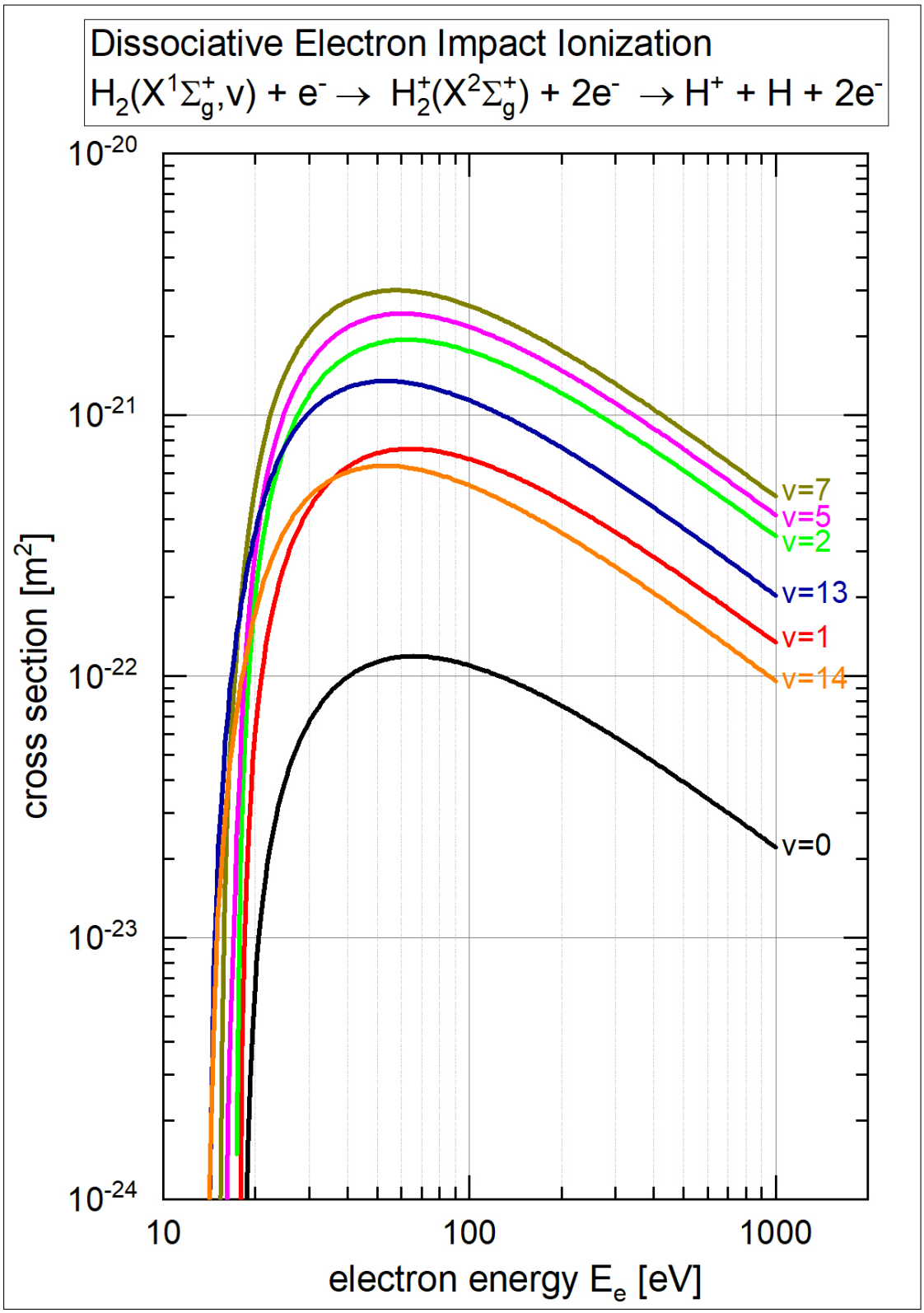

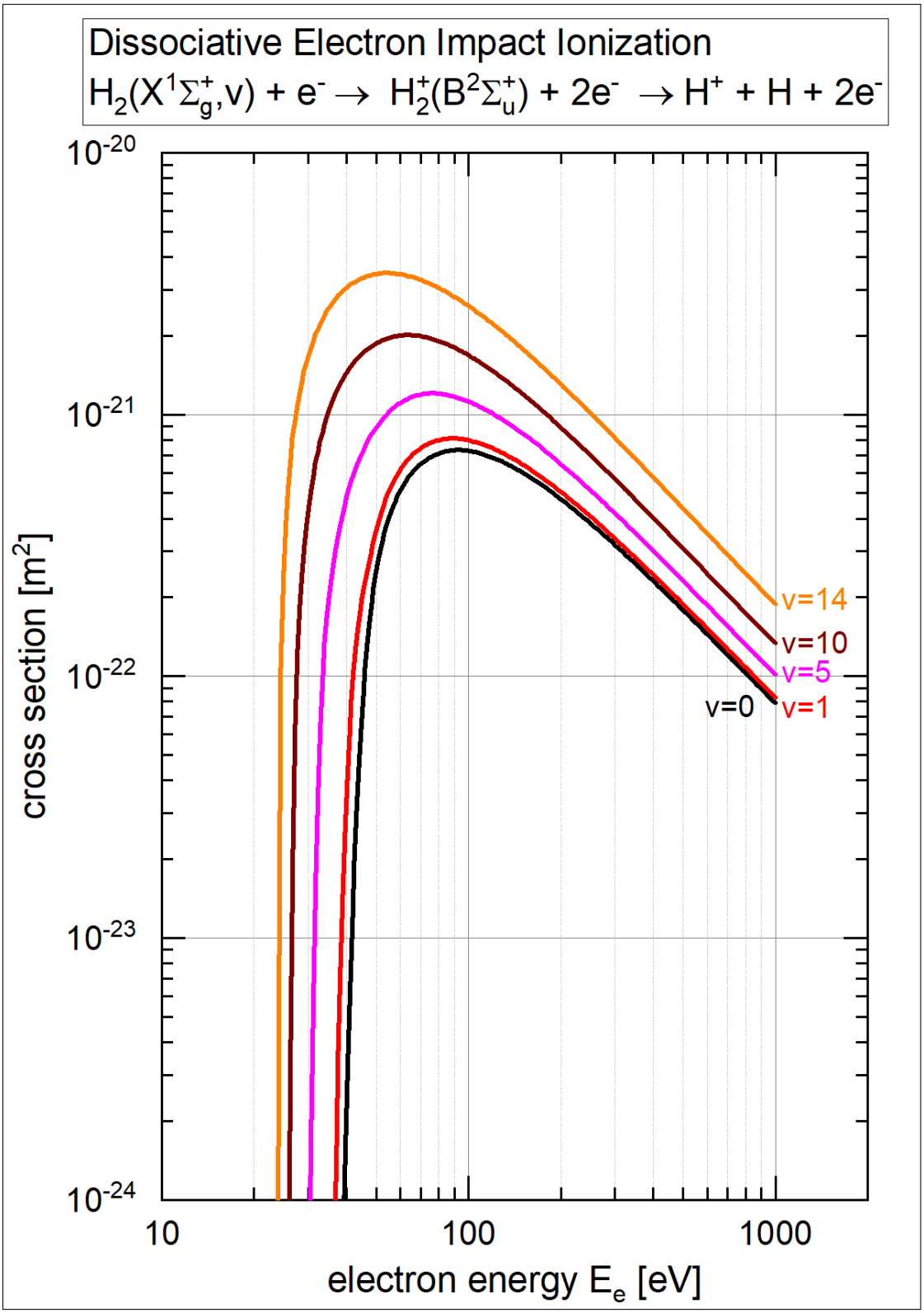
Dissociative Electron Impact Ionization
$H_2(X^1\Sigma_g^+,v) + e^- \rightarrow H_2^+(B^2\Sigma_u^+) + 2e^- \rightarrow H^+ + H + 2e^-$
cross section [m^2]
10^{-20}
10^{-21}
10^{-22}
10^{-23}
10^{-24}
10
100
1000
electron energy E_e [eV]
v=14
v=10
v=5
v=1
v=0

Proton Impact (De-)Excitation

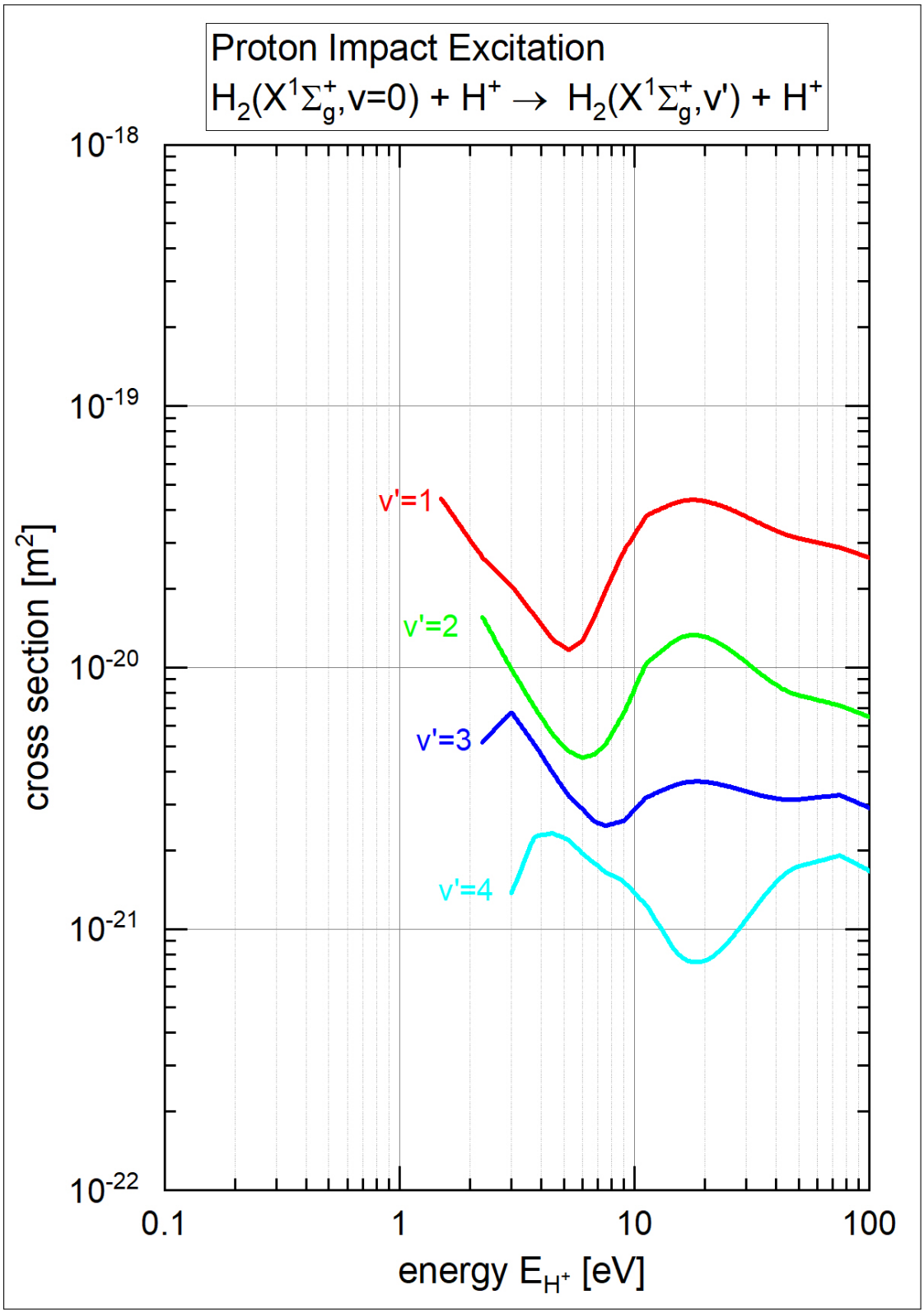

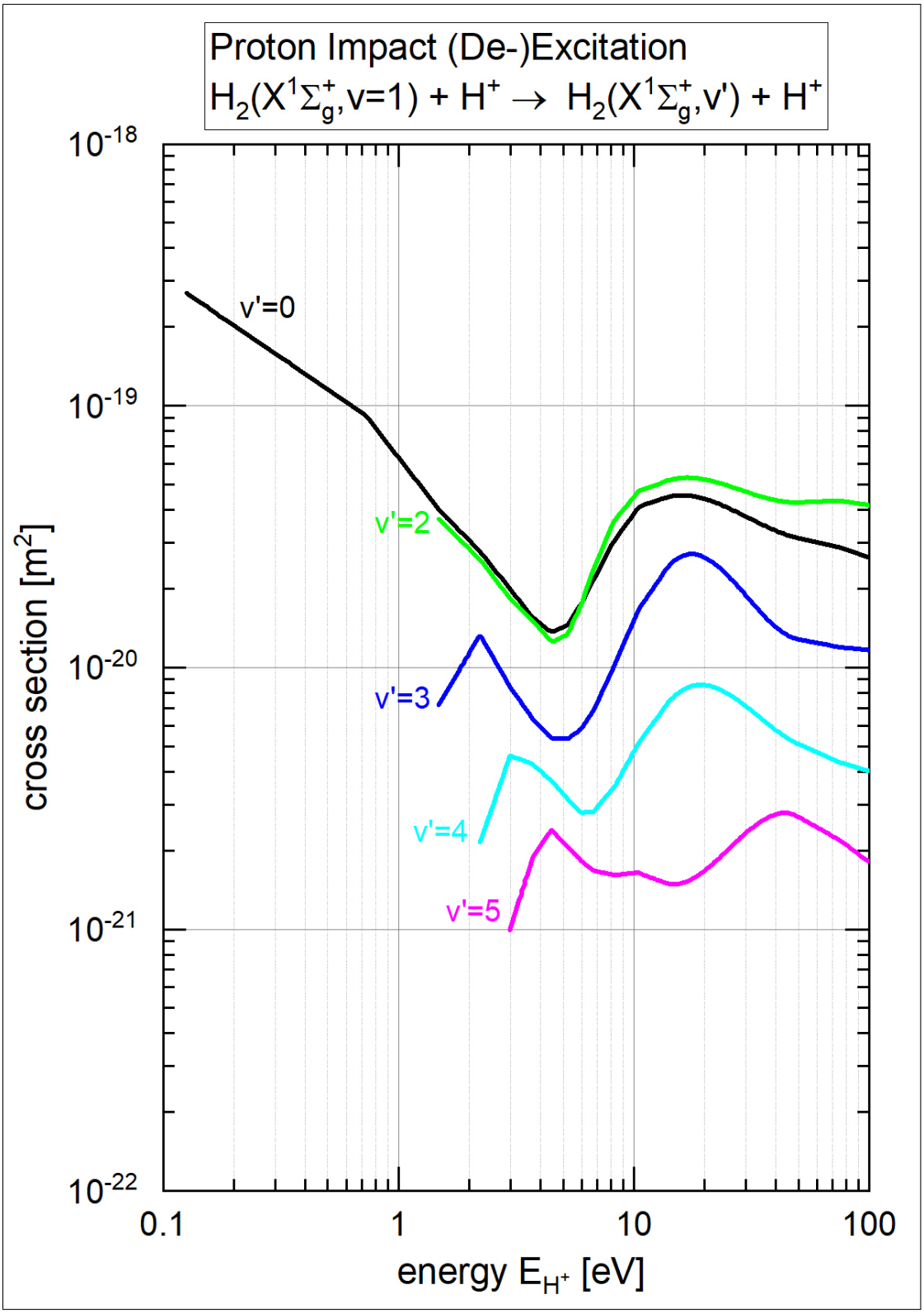
Proton Impact (De-)Excitation
H2(X1Σg+,v=1) + H+ → H2(X1Σg+,v') + H+
cross section [m2]
10-18
10-19
10-20
10-21
10-22
v'=0
v'=2
v'=3
v'=4
v'=5
0.1
1
10
100
energy EH+ [eV]

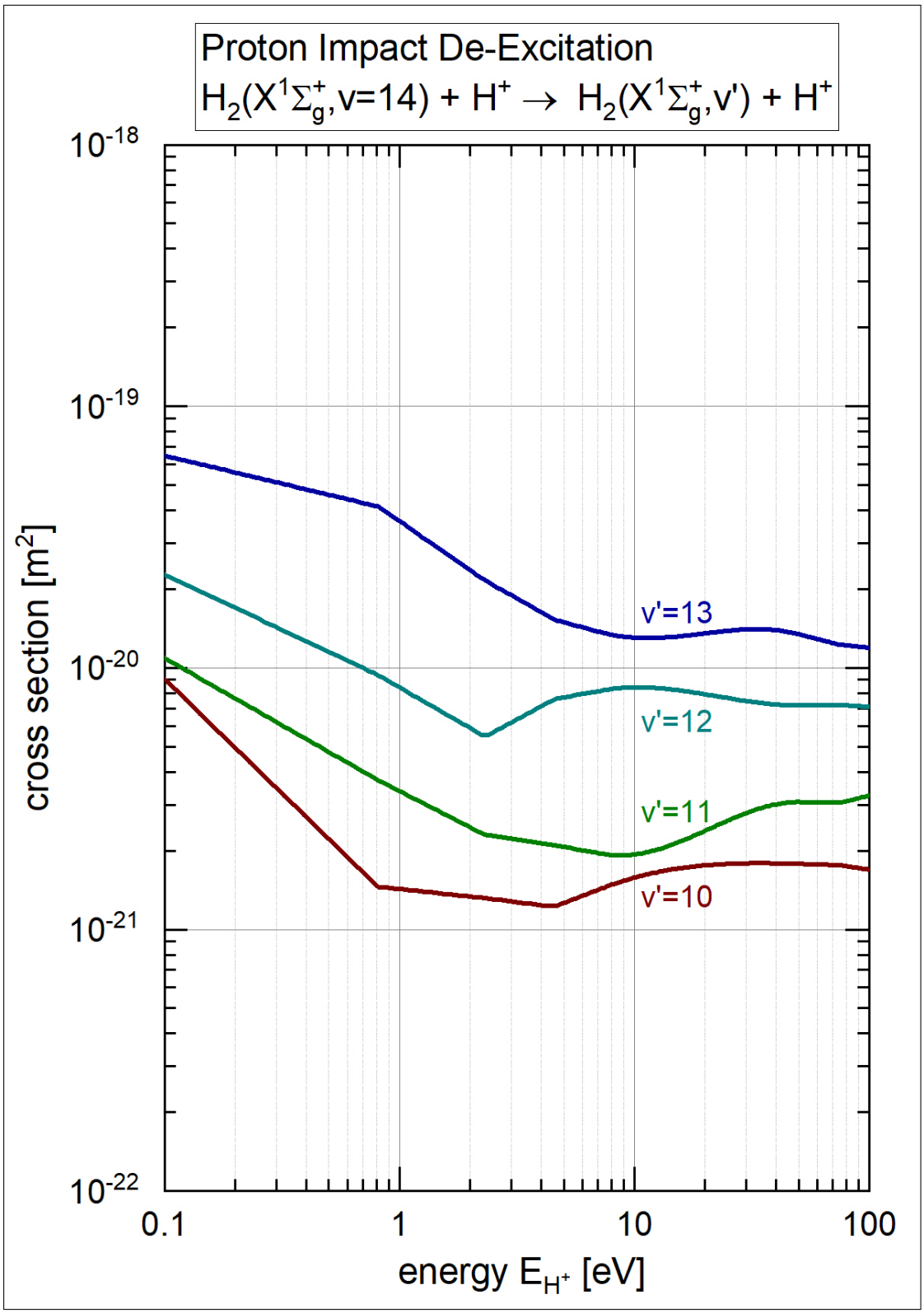
Proton Impact De-Excitation
H2(X1Σg+,v=14) + H+ → H2(X1Σg+,v') + H+
cross section [m2]
10-18
10-19
10-20
10-21
10-22
0.1
1
10
100
energy EH+ [eV]
v'=13
v'=12
v'=11
v'=10

Proton Impact Dissociation

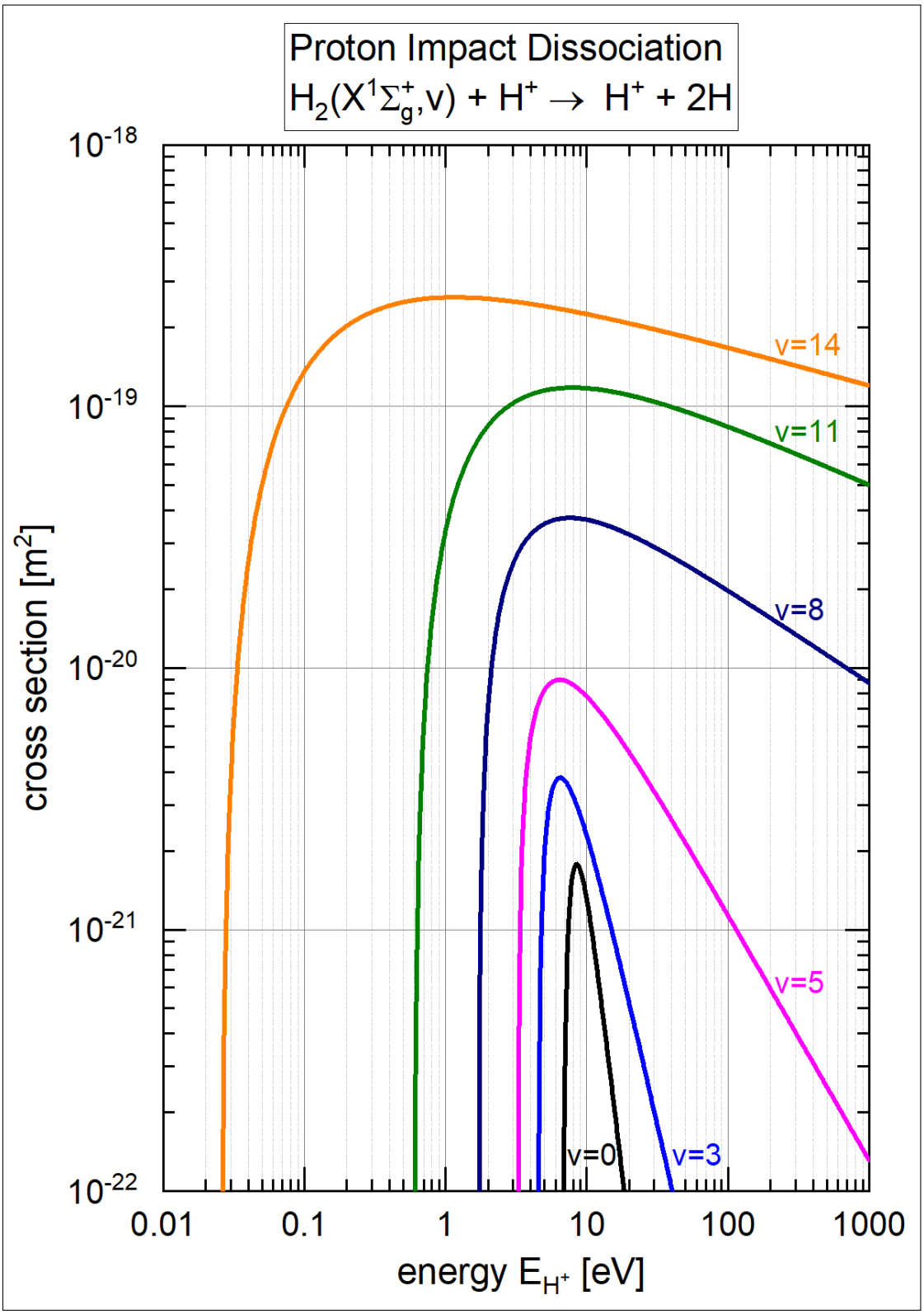

Hydrogen Atom Impact Dissociation

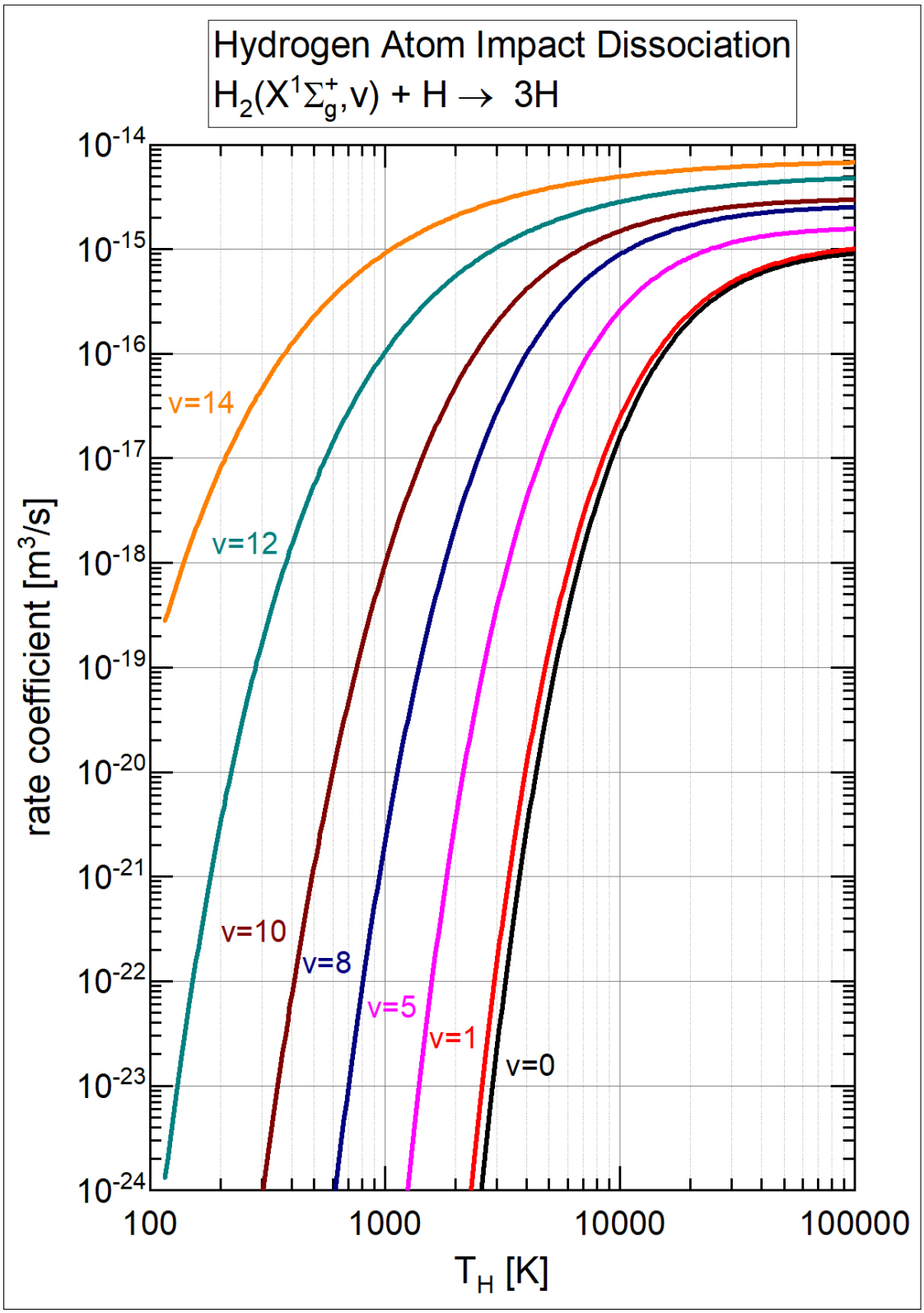

H_3^+ Dissociative Recombination